INVERSE MODELING OF GROUNDWATER FLOW IN THE RHÔNE ALLUVIAL AQUIFER IMPACT OF THE THIRD RHÔNE CORRECTION

Thesis defended on May 13, 2013 at the

FACULTY OF SCIENCES

INSTITUTE OF HYDROGEOLOGY AND GEOTHERMICS (CHYN)

UNIVERSITY OF NEUCHÂTEL

for the degree of

DOCTOR OF NATURAL SCIENCES

presented

by

DAMIAN GLENZ

Accepted by the following Jury:

Prof. Philippe Renard

Prof. Pierre Perrochet

Prof. Philip Brunner

Prof. Ghislain de Marsily

Prof. Peter Huggenberger

Dr. Andrés Alcolea

Alexandre Vogel

unine
UNIVERSITÉ DE NEUCHÂTEL

UNIVERSITÉ DE
NEUCHÂTEL

Faculté des sciences
Secrétariat-décanat de Faculté
Rue Emile-Argand 11
2000 Neuchâtel - Suisse
Tél: + 41 (0)32 718 2100
E-mail: secretariat.sciences@unine.ch

IMPRIMATUR POUR THESE DE DOCTORAT

La Faculté des sciences de l'Université de Neuchâtel autorise l'impression de la présente thèse soutenue par

Monsieur Damian GLENZ

Titre:

"Inverse modeling of groundwater flow in the Rhône alluvial aquifer – Impact of the Third Rhône correction"

sur le rapport des membres du jury:

- Prof. Philippe Renard, Université de Neuchâtel, directeur de thèse
- Prof. Pierre Perrochet, Université de Neuchâtel, co-directeur de thèse
- Prof. Ghislain de Marsily, Université Paris 6, France
- Prof. Peter Huggenberger, Université de Bâle, Suisse
- Prof. Philip Brunner, Université de Neuchâtel
- Dr. Andres Alcolea, Geo-Energie, Suisse
- Alexandre Vogel, Etat du Valais, Suisse

Neuchâtel, le 18 juin 2013

Le Doyen, Prof. P. Kropf

Meinen Eltern, Dionys und Claudia

Acknowledgements

First of all, I would like to thank to my supervisor, Professor Philippe Renard. After my master's thesis, he encouraged me to embark on a PhD thesis. Being initially doubtful about this idea, I got finally convinced by his verve, his brilliancy and his friendly and open manner. Many thanks for his flexibility, for his availability and for leaving me free to go my own way. It was a great opportunity and experience to work with him and I hope we'll stay in touch after this work has been completed.

I am very grateful to those responsible for the project of the Third Rhône correction, both at the Canton of Valais and at the Federal Office for the Environment, for having found the means to fund this work. A special thank goes to Alexandre Vogel, the person in charge of hydrogeological studies at the Third Rhône correction. Not only has his knowledge of the region contributed to my work; he also showed a lot of patience and understanding for that part of the work, whose importance for the project was not immediately apparent. Thanks also to Pascal Ornstein at the Crealp, who made the majority of the data available.

This thesis would not have been possible without the guidance and the help of Pierre Perrochet, Andrés Alcolea and Philip Brunner, co-supervisors in more or less official terms. I thank Pierre for his helpful advices, his support and his presence throughout this work. Thanks to Andrés and Philip for the many discussions and for the thorough reviews of the manuscript. Your assistance on the final straight was invaluable.

A lot of thanks go also to the other members of the thesis committee, Professor Ghislain de Marsily and Professor Peter Huggenberger.

My particular thanks go to Andrea Borghi, fellow sufferer, flat mate and friend, for the good time, the many discussions and last but not least for his precious help, peculiarly with regard to scripting.

I am very grateful for the help of Julien Straubhaar. Many times, discussing with him helped me develop ideas and cleared my thoughts. I hope that he appreciated sharing the office with me as much as I did.

I also wish to say a big thank you to Fabien Cornaton for making his software available to me and especially for offering an incredibly responsive helpline with it. The same can be said of John Doherty. His technical and scientific support was a great help and I have learnt a lot from him.

I would like to thank also to Grégoire Mariethoz, Tristan Ibrahim, Jaouher Kerrou, Ellen Milnes, Giona Preisig, Gregory Deman, Christian Moeck, Daniel Käser, Guillaume Pirot, Fabio Oriani, Mohammed Chaoui and Laetitia Laigre for sharing their scientific experience with me.

Many, many thanks to Dom, Cécile, Cybèle, Lucien, François Negro, Michel, Alice, Pierik, Martin, Axa, Simona, Vanessa, Geoffrey, Lilou, Lorienne, the Baillieux brothers, Marco, Louis, Hubert, Asma, François, Julien, Mehdi, Damien, Claire, Yann and all the staff of the CHYN. I feel lucky to have crossed your ways during the unforgettable time I spent at the CHYN.

I had the opportunity to work in a private company alongside my thesis. I am very appreciative for the extra portion of flexibility and organization which Hermann Rovina and his team afforded due to my small employment.

I am greatly thankful to everyone who has supported me in whatever way during this work: Andrej, Eric, Michu, Oli, Steini, Martinli, Nora, Sili, Patrick, Anka, Oli, Tinu, Simu, Sandra, Franzi, Ruschle, Andy, Benj, Häring, Lantsch, Maria, Ezra, Stefan, Mathieu, Laurent, Yann, Tristan and Marie Caroline, have all contributed to this experience by being wonderful companions, funny flat mates or reliable friends.

Finally, I owe great thanks to my parents and to my sister for their unconditional support and love during all these years. Merci villmal!

Abstract

The main objective of this thesis is the quantitative evaluation of the impact of the Third Rhône correction (PR3) on groundwater within the Rhône alluvial aquifer. PR3 is a river restoration project which aims at improving flood protection and at upgrading the ecologically deficient streambed of the Rhône River (Valais, Switzerland). The approach taken to extend the drainage capacity of the Rhône River is a widening of the streambed, which causes at large a lowering of river stages (of about 0.9 m on average).

The impact of PR3 on groundwater was estimated using a steady state numerical flow model that was calibrated against average hydraulic head. The numerical model allows integrating data and can be used to simulate the system behavior under conditions which differ from the ones of the investigated state. When the model is used to simulate future system behavior, its predictions contain necessarily a certain degree of uncertainty. Two sources of predictive uncertainty were explored herein. On the one hand the non-uniqueness of the solution of the inverse problem, i.e. the estimation of model parameters based on available measurements of hydraulic head; on the other hand the uncertainty as to how the streambed conductance of the Rhône River will be altered as a consequence of the restoration. Predictive uncertainty arising from the non-uniqueness of the inverse problem was assessed by the "null space Monte Carlo" (NSMC) method implemented in PEST; predictive uncertainty associated with the uncertain evolution of the streambed conductance was estimated by a sensitivity analysis of model predictions to streambed conductance.

The model is based upon a conceptual understanding of the system gained through interpretation of available data. Those data clearly suggests that the system is strongly driven by regional controls and that the interaction of groundwater with the Rhône River, as well as with ditches, plays a key role.

The model is consistent with field measurements (head measurements, patterns of SW-GW interaction, exchange flow at ditches). One unexpected result of the model is that high SW-GW exchange flows occur on short stretches of the Rhône River close to gravel pits and at in-stream quarries.

Assuming that streambed properties will return to a stable state identical to the current state (involving the development of a clogging layer), the model predicts that the groundwater table will lower at large in response to the PR3 in the long-term. Modeling results suggest also that drainage ditches considerably attenuate the influence of the restoration, and that furthermore they reduce predictive uncertainty.

The predictive uncertainty arising from the non-uniqueness of the inverse problem is small (q_{90}–q_{10} inter-percentile range of 0.07 m on average), indicating that the predictions made using the calibrated model seem to be very reliable in most parts of the

model. However, this low uncertainty has to be interpreted with care: a simple synthetic example showed that in the context of a nonlinear model, the NSMC methodology potentially underestimates uncertainty. Moreover, parameter uncertainties arising from the non-uniqueness of the inverse problem are considered as low as compared to the uncertain evolution of streambed properties in the restored state. In the upstream part of the model, predictions were found to depend strongly on streambed conductance, to the point that despite the lowering of river stages, already a slight increase of the streambed conductance produces a rising of the groundwater table.

Keywords

Surface water – groundwater interaction, river restoration, groundwater flow simulation, inverse problem, parameter estimation, predictive uncertainty quantification, null space Monte Carlo.

Résumé

Le principal objectif de cette thèse est l'évaluation quantitative de l'impact de la troisième correction du Rhône (PR3) sur l'aquifère alluvial de la plaine du Rhône. Le PR3 est un projet d'aménagement, dont le but est d'une part l'amélioration de la protection contre les inondations, et d'autre part la renaturalisation du lit de la rivière Rhône (Valais, Suisse). L'approche considérée pour améliorer la capacité de drainage du Rhône est l'élargissement du lit de la rivière, ce qui causera un abaissement du niveau de la rivière (d'environ 0.9m en moyenne).

L'impact du PR3 sur les eaux souterraines a été estimé avec un modèle numérique d'écoulement permanent. Ce modèle a été calibré avec des données de charge hydraulique. Le modèle numérique permet d'intégrer les données existantes, et d'étudier ensuite le comportement possible du système lorsqu'il sera soumis à des conditions qui diffèrent de celles investiguées actuellement (état restauré). Quand le modèle est utilisé pour simuler l'état futur du système, ses prévisions contiennent nécessairement un certain degré d'incertitude. Deux sources d'incertitude ont été considérées dans ce travail : d'une part la non-unicité de la solution du problème inverse, qui consiste à estimer les paramètres du modèle sur la base des mesures disponibles de charge hydraulique; d'autre part l'incertitude concernant l'évolution de la conductivité hydraulique du lit du Rhône suite à la restauration. L'incertitude sur les prévisions découlant de la non-unicité du problème inverse a été traitée grâce à la méthode du "null Space Monte Carlo" (NSMC) implémentée dans PEST. L'incertitude induite par l'état futur incertain du lit du Rhône a été traitée avec une analyse de sensibilité des prévisions par rapport à la conductivité du lit de la rivière.

Le modèle est basé sur une compréhension conceptuelle du système, acquise grâce à l'interprétation des données disponibles. Ces données suggèrent clairement que le système est fortement contrôlé par des paramètres à l'échelle régionale, et que les interactions de l'eau souterraine avec le Rhône, ainsi qu'avec les canaux, joue un rôle clé dans le fonctionnement de l'aquifère.

Le modèle est cohérent avec les données mesurées sur le terrain (charge hydraulique, zones d'échanges entre eau de surface et nappe phréatique, flux d'échange dans les canaux). Un résultat inattendu du modèle est que les zones d'échanges importants entre eaux superficielles et souterraines se produit sur de brefs tronçon du Rhône et à proximité des gravières et des carrières dans le lit de la rivière.

En supposant que les propriétés du fond du lit du Rhône vont revenir à un état stable et identique à l'état actuel (ce qui implique le développement d'une couche de colmatation), le modèle prévoit que, à terme, le niveau d'eau s'abaisse à cause du PR3. Les résultats de modélisation suggèrent aussi que les canaux de drainage vont

considérablement atténuer l'influence de la restauration du Rhône, et réduisent de plus l'incertitude sur les prévisions.

L'incertitude des prévisions découlant de la non-unicité du problème inverse est faibles (une gamme de 0.07m en moyenne entre les quantiles q_{90} et q_{10}), ce qui indiquent que les prévisions du modèle calibré semblent très fiables dans la majeure partie du domaine. Toutefois, cette faible incertitude doit être interprétée avec précaution : l'étude d'un exemple synthétique simple a montré que dans un modèle non-linéaire, la méthode NSMC peut sous-estimer l'incertitude. De plus, l'incertitude sur les paramètres découlant de la non-unicité du problème inverse, et calculée avec la méthode NSMC, est considérée comme faible en comparaison de l'évolution incertaine des propriétés du lit de la rivière dans l'état restauré. Dans la partie amont du modèle, il a été remarqué que les prévisions dépendent fortement de la conductivité hydraulique du lit de la rivière à un tel point que, en dépit de l'abaissement du niveau d'eau de la rivière, un léger accroissement de la conductivité du lit de la rivière produit une hausse du niveau piézométrique dans la nappe.

Mots-clé

Echanges nappe/rivière, simulation d'écoulement des eaux souterraines, problème inverse, estimation de paramètres, quantification d'incertitude des prédictions, null space Monte Carlo.

Zusammenfassung

Das Hauptziel dieser Doktorarbeit ist es, den Einfluss der 3. Rhonekorrektion (PR3) auf das Grundwasser des alluvialen Rhonetal-Aquifers quantitativ abzuschätzen. PR3 ist ein Projekt zur Flussrestaurierung der Rhone (Wallis, Schweiz) mit den Hauptzielen, den Hochwasserschutz zu verbessern und den Fluss ökologisch aufzuwerten. Das Projekt verfolgt den Ansatz, die Abflusskapazität des Flusses mittels einer Aufweitung des Flussbettes zu erhöhen; generell bewirkt dies eine Absenkung des Wasserspiegels der Rhone (um ca. 0.9 m im Mittel).

Der Einfluss des PR3 auf das Grundwasser wurde mit Hilfe eines stationären numerischen Grundwasserfliessmodelles abgeschätzt, welches unter Verwendung von Mittelwerten des hydraulischen Potentials im Aquifer kalibriert wurde. Das numerische Modell eignet sich gut zur Integration vorhandener Daten und kann dazu verwendet werden, ein System unter veränderten Bedingungen zu untersuchen. Modellvoraussagen über das Verhalten des Systems in der Zukunft sind notwendigerweise mit einer gewissen Unsicherheit behaftet. In dieser Arbeit wurden zwei mögliche Quellen, aus denen sich Unsicherheiten bezüglich der Modellvoraussagen ergeben, berücksichtigt: einerseits die Unmöglichkeit, die Parameter des Fliessmodelles aus den vorhandenen Messungen des hydraulischen Potentials im Aquifer eindeutig zu bestimmen; andererseits die Ungewissheit darüber, wie die Durchlässigkeit der Rhonesohle sich im Zuge des PR3 verändert. Die Schätzunsicherheit, welche aus der fehlenden Eindeutigkeit des Inversen Problems entsteht, wurde mittels der „null-space-Monte-Carlo-Methode“ (NSMC) in PEST bemessen; die Unsicherheit, welche sich aus der Abhängigkeit der Modellvorhersagen von der unsicheren Entwicklung der Durchlässigkeit der Flusssohle ergibt, wurde mittels einer Sensitivitätsanalyse abgeschätzt.

Das Modell basiert auf einem konzeptuellen Verständnis des Systems, welches durch die Interpretation der vorhandenen Daten gewonnen wurde. Diese Daten deuten eindeutig an, dass das System zu einem bedeutenden Teil durch Prozesse auf regionalem Massstab gesteuert wird und dass die Wechselwirkung von Grundwasser mit der Rhone sowie mit Kanälen eine Schlüsselrolle einnimmt für das Funktionieren des Aquifers.

Das Modell ist konsistent mit Feldmessungen (Messungen des hydraulischen Potentials, Muster der Wechselwirkung zwischen Oberflächengewässer und Grundwasser, Austauschraten an Kanälen). Ein unerwartetes Modellresultat ist das Auftreten von hohen Austauschraten zwischen der Rhone und dem Grundwasser auf kurzen Abschnitten der Rhone in der Nähe von Baggerseen und an Stellen mit Kiesentnahmen aus dem Rhonebett.

Unter der Voraussetzung, dass die Eigenschaften des Rhonebettes langfristig den heutigen entsprechen (was die Entwicklung einer Kolmationsschicht mit einschliesst), sagt das Modell als Folge des PR3 langfristig eine Absenkung des Grundwasserspiegels voraus. Die Modellresultate deuten auch an, dass die Drainagekanäle die Auswirkungen der Restaurierung merklich abmindern und dass deren Präsenz ausserdem die Unsicherheit der Modellvoraussagen reduziert.

Die Unsicherheit der Voraussagen, die aus der Schätzunsicherheit der Parameter resultiert, scheinen die Voraussagen des kalibrierten Modelles an den meisten Stellen des Modells sehr verlässlich (durchschnittlicher x_{90}–x_{10} Interperzentilbereich von 0.07 m). Diese geringe Unsicherheit muss jedoch mit Vorsicht gedeutet werden: ein einfaches synthetisches Beispiel verdeutlichte, dass die NSMC-Methode in nichtlinearen Modellen die Unsicherheit potentiell unterschätzt. Ausserdem wurde die mit der NSMC-Methode ermittelte Schätzunsicherheit als klein eingestuft im Vergleich zur Unsicherheit, die im Zusammenhang mit der ungewissen Entwicklung der hydraulischen Durchlässigkeit der Rhonesohle im restaurierten Zustand besteht. Es zeigte sich, dass die Modellvorhersagen im obstromseitigen Teil des Modells stark von der Durchlässigkeit der Rhonesohle abhängen; so sehr, dass in diesem Bereich schon eine geringfügige Zunahme der Durchlässigkeit der Rhonesohle trotz einer projektbedingten Absenkung des Wasserspiegels der Rhone einen Anstieg des Grundwassers nach sich zieht.

Schlüsselbegriffe

Fluss-Grundwasser Austausch, Simulation des Grundwasserflusses, Inverses Problem, Parameterschätzung, Quantifizierung der Unsicherheit der Vorhersagen, null space Monte Carlo.

Table of contents

Chapter 1

Introduction

1.1 Motivation

The Rhône is a major river system originating in the canton of Valais, in the south-west of Switzerland. As most river systems in Central Europe, the Rhône River has been regulated to prevent floods. The regulation comprises a first (1863 – 1928) and a second (1930 – 1960) stage. As a consequence of the regulation, the Rhône River is channelized by dams to a large extent. In spite of the regulation, the drainage capacity of the Rhône River as well as the condition of the river dams provides insufficient protection against flooding. This became evident during recent flood episodes (1987, 1993 and 2000). An analysis of the drainage capacity of the Rhône River [1] revealed that the Rhône River plain is, in most areas, not protected against a centennial flood.

To alleviate this problem and be better prepared to future flood events, the project of a third restoration of the Rhône River (hereinafter PR3) emerged in the 1990's. It aims at improving flood protection and at upgrading the ecologically deficient riverbed, taking account of socio-economic concerns. The project PR3 is expected to be completed in 2030 with a total budget of approximately 900 million Swiss Francs.

The approach taken to extend the drainage capacity of the Rhône River is a widening of the streambed by a factor of at least 1.6. This implies at large a lowering of the water level in the river. Because the water table of the Rhône alluvial aquifer is in close relation to the water level in the Rhône, this widening of the streambed is expected to result in a lowering of the groundwater table in the alluvial aquifer in the long term. Lowering the groundwater table may induce land subsidence or cause the drying of agricultural fields and therefore involve enhancements of irrigation systems. Moreover, the projected restoration will trigger changes on the geomorphology of the streambed. This may alter the hydraulic conductivity of the streambed and, consequently, impact on the exchange between river and groundwater. It is expected that, in the short term, the hydraulic conductivity will be enhanced by the construction works, thus increasing the exchange between river and groundwater. This enhancement may lead to a rise of the water table in the aquifer. This scenario may eventually cause inundation by groundwater in buildings or swamp formation, to name a few consequences.

For the aforementioned reasons, the restoration must be based on a sound knowledge of surface water–groundwater interactions (hereinafter SW-GW interactions). Despite the large number of studies [2-23] dedicated to the investigation of the Rhône alluvial aquifer, knowledge of SW-GW interactions is still imperfect. Furthermore, the impact of PR3 on groundwater was estimated from a semi quantitative approach during the planning phase of the project. The significance of PR3 and its potential large impact on groundwater deserves a more accurate quantification, which this doctoral study aims to achieve.

1.2 Objectives

The main objective of this thesis is to address the impact of the PR3 on the groundwater of the alluvial Rhône aquifer in a quantitative manner. To that end, additional aims of this work are:

- To contribute to a better understanding of the global behavior of the alluvial aquifer and in particular of the surface water – groundwater system.
- To identify model parameters, uncertain model aspects and to quantify parameter uncertainty.
- To evaluate methods of uncertainty estimation through comparison of different approaches.

These objectives rely on recent advances in the conceptualization, characterization and modeling of SW-GW interactions. A brief summary of the state of the art of this field is given in the following section. The ultimate goal was to make the knowledge and experience gained from this work available to industrial companies.

1.3 State of the art of SW-GW modeling

Interest in SW-GW interactions has increased over the last two decades [24] from scientists in various disciplines. Influential hydrogeological review papers on SW-GW interaction were written by Winter, Harvey, et al. [25], Woessner [26] and Sophocleous [27]. SW-GW interactions are considered complex and involve different temporal and spatial scales [28]. Sophocleous [27] indicated that large-scale hydrological controls like topography, geomorphology, geology and climate also drive the development of SW-GW interactions. On the other hand, the importance of in-stream geomorphic structures such as gravel bars or riffle-pool sequences, or even smaller forms, such as grains and ripples, on the hyporheic exchange flow (i.e. the infiltration of stream water in the sediment and its return to the stream) has been recognized [29]. Implications arising from this observation for restoration projects are the subject of recent studies [30]. As streambed hydraulic properties are influenced by sedimentological and biological processes, which in turn are affected by hydrodynamic factors, streambed hydraulic properties and hence SW-GW interactions typically display temporal variations [31, 32]. Heterogeneity and anisotropy of the streambed and the underlying aquifer are important for SW-GW exchanges at all scales [29, 33, 34]. Heterogeneity may induce the presence of unsaturated zones underneath losing rivers and strongly influence exchange flux [35, 36].

The aforementioned controls of SW-GW interactions may be affected by river restoration measures [37] and estimating the impact of a restoration is often confounded by multiple and interacting variables [38]. An understanding of suspended sediment transport is crucial to predicting the impact of restoration measures on groundwater,

too, as the deposition of fine grained sediments can lead to a decrease in streambed hydraulic conductivity (clogging of the streambed). As a consequence, SW-GW exchange flow in restored reaches may – after an initial increase due to restoration measures – rapidly re-diminish again [30]. Clogging of streambeds is generally influenced by physical, biological and biogeochemical variables [39]. Findings by Fette [14] suggest, that clogging of the Rhône River, is intensified by "hydropeaking". The term "hydropeaking" refers to rapid, unnatural and significant fluctuations in river discharge induced by a release of water from hydropower dams in response to power demand [13].

Various methods have been developed to estimate SW-GW exchange from measurements (see Kalbus, Reinstorf, et al. [40] for a comprehensive review). A frequently used method to quantify SW-GW interactions is numerical modeling. Numerical models are regarded as one of the most powerful tools for quantitative analysis of SW-GW interactions, especially when dealing with large (e.g. reach or basin) scales. These models involve uncertain parameters that need to be calibrated upon existing measurements. Automatic calibration of groundwater models is now a standard in science [41, 42]. Recently, these techniques are increasingly used in models of SW-GW systems. Calibration of leakage coefficients can be based on head losses between the river and the aquifer or on exchange rates, when available. As Fleckenstein, Niswonger, et al. [36] pointed out, regional monitoring networks often lack the necessary spatial density in the vicinity of the river to obtain reliable estimates of local leakage coefficients. However, the uncertainty associated with parameter estimates is not quantified routinely, a deficiency that SW-GW modeling shares with other sub-domains of groundwater modeling [43]. So far, the joint influence of streambed and aquifer heterogeneity has received limited attention. Hydrologists focusing on streambed biogeochemistry and hydroecology typically work on small scales and highlight the importance of streambed heterogeneity. Likewise, groundwater hydrologists typically consider the heterogeneity of the aquifer only, whereas streambeds are often represented as homogeneous zones. While traditionally, groundwater and surface water have been considered as separate elements of the SW-GW system, models coupling surface and groundwater flow are increasingly used to simulate SW-GW interactions in recent years [e.g. 44, 45]. This is in line with the growing conceptual understanding of surface water and groundwater as a single resource [25].

1.4 Methodology and scope

The approach taken herein is to assess the possible consequences of PR3 for groundwater by means of a numerical groundwater flow model. Groundwater modeling solely allows for an integration of available information on the scale considered herein.

The predictive capacity of a model heavily relies on the understanding of characteristic processes within the modeled system. In order to develop a sound knowledge of the functioning of the alluvial aquifer, in *Chapter 2*, available data sets and previous studies are reviewed. The conceptual model of the Rhône system is based on this analysis.

Besides from providing a means to analyze a system, groundwater modeling in principle offers the possibility to make predictions in a setting that differs from the investigated one [46]. Apart from the prerequisite of an appropriate incorporation of key system processes in the model, applying a model for predictive purposes requires that model parameters are correct. In order to integrate the available data and the information encapsulated in measurements of the system state, model parameters are estimated by an inverse solution of groundwater flow herein. Because of the complex nature of the heterogeneous system and the relatively scarce information about it, the solution to the treated inverse problem is non-unique. Therefore, the uncertainty associated with parameter estimates needs to be quantified.

Parameter estimation is carried out by PEST [47] herein, a widely used software for automated nonlinear parameter estimation. Parameter uncertainty in this work is assessed via the null space Monte Carlo (NSMC) methodology, a method that is unique to PEST and which especially in the context of SW-GW modeling is not yet used frequently. In *Chapter 3* a short description of the methods is given. Chapter 3 reports also results of a synthetic modeling study in which the reliance of the NSCM method is tested.

Chapter 4 describes the setup of the numerical model. This includes a description of the extension of the numerical model and its spatio-temporal discretization as well as the definition of boundary conditions.

Parameter estimates resulting from the solution of the inverse problem are presented in *Chapter 5,* along with estimates of their uncertainty. This chapter also includes a discussion of estimated parameter distributions and resulting model outcomes.

In *Chapter 6*, the impact of the PR3 is estimated by means of the numerical flow model described in Chapter 4. A simulation at the scale of the study area is undertaken to estimate the long term impacts of PR3. Furthermore, three small-scale simulations are used to assess the impact of local correction measures. In these simulations,

estimates of worst case scenarios regarding the short-term impacts are given. This chapter closes with a discussion of modeling results.

Chapter 7 holds the main conclusions of this thesis.

Chapter 2

Prior information from available data

2.1 Setting

The study area, situated between Sierre and Evionnaz (Figure 1), is part of the alluvial plain of the upper Rhône River and as such belongs to the upper Rhône catchment. Apart from the part downstream of St-Maurice, the upper Rhône catchment boundaries mostly coincide with the political boundaries of the Swiss Canton of Valais. The study area extends over 60 km and covers a surface of about 90 km^2 with an average width of 1.5 km.

The alluvial fans of St-Barthélemy and Illgraben form natural hydrogeological boundaries within the alluvial aquifer, being built by sediments of a relatively low hydraulic conductivity. This is one reason why they were chosen as limits of the study area. Another reason was that the three basic connection types of surface and groundwater systems, i.e. gaining, losing and losing-disconnected stream, are thought to be present in this area. This is important in order to be able to apply findings of this work to other reaches concerned by the PR3.

The groundwater of the alluvial aquifer plays an important economic role; it is used for drinking, industrial and irrigation purposes (fruit-growing, market gardening). There are more than 40 public pumping wells and numerous unregistered, private irrigation wells present in the alluvial aquifer.

2.2 Tectonics, geology and geomorphology

The Rhône Valley is situated between the Helvetic Nappes to the North and the Penninic Nappes to the South (Figure 2). In the eastern part, north of the Rhône, the crystalline Aar and Gotthard Massifs emerge. In the western part, primarily south of the Rhône, the Mont Blanc and Aiguille Rouge Massifs crop out. The Helvetic and Penninic Nappes are composed of a variety of metamorphosed sedimentary rocks; the Massifs consist of a metamorphic basement with magmatic intrusions [48]. Upstream of Martigny, the axis of the Rhône valley runs in a south-west direction following mainly soft sedimentary sequences. Near Martigny, the valley contains a sharp bend; to the west of this bend, the valley runs north-eastward. It crosses the Aiguilles Rouges and Mont Blanc massifs, the Helvetic Nappes and the Penninic Klippen Nappes in a narrow valley cut through the mountains. After the break through at the narrow gorge of St-Maurice, the valley gets wider and runs to Lake Geneva (Figure 2). Upstream of the “elbow” at Martigny, which formed only in late tertiary [49], the Rhône valley presumably developed along a tectonically weakened zone built by the Rhône-Simplon fault zone [50, 51]. The Rhône-Simplon fault zone is seen as the main expression of an orogen-parallel deformation in the late tectonic history of the western Alps [52]. Indications exist that the system is still active [53]. This would explain the high seismic activity in the Rhône valley amongst the highest in the central Alps [54].

Jaboyedoff, Baillifard, et al. [53] argue that several rock falls and landslides observed in the Valais canton are closely related to a reactivation of the Neogene Rhône-Simplon fault system (e.g. Randa rock fall (1991); Illgraben rock falls and landslides (frequent); Sierre rock fall (1946)).

The present-day landscape of the Rhône valley reveals inheritance of late Pleistocene glaciations [55]. Typical is the U-shaped, overdeepened valleys which have been filled with unconsolidated quaternary deposits. The topography of the bedrock can be estimated from several geophysical studies (seismic reflection surveys: e.g. [56]; [57]; gravimetric measurements: e.g. [58]). Its depth reaches up to 1 km at some places (e.g. [59]; [60]). A longitudinal profile of the bedrock along the Rhône valley drawn by Besson, Marchant, et al. [57] is shown in Figure 3a. A maximum depth to bedrock of about 920 m is observed near Martigny. Further downstream the basin depth decreases until the basement is cropping out in the glacial rock sill at St-Maurice. Downstream of the rock sill at St-Maurice, the sedimentary basin increases in depth again.

Besson, Marchant, et al. [57] identified eight different sedimentary units in the quaternary deposits. They attributed the basin fill to one single deglaciation sequence. A detailed interpretation of the seismic profile shot close to Sion is represented in Figure 3b. The basin fill can largely be summarized as a succession of a top layer of alluvial, mainly fluvial deposits, underlying fluvio-lacustrine and glacio-lacustrine deposits and glacial deposits at the sediment-basement contact ([58]; [49]). Fluvio-lacustrine deposits are considered to form the base of the aquifer studied herein, i.e. only the uppermost sedimentary unit of post-lacustrine sediments is deemed to be relevant in regard to river–groundwater interactions. Based on four vibro-seismic profiles, Finger and Weidmann [61] estimated the maximum thickness of these sediments at 80 m for the Chablais (downstream of St-Maurice). According to Besson, Marchant, et al. [57], the thickness of the alluvial sediments increases from 30 m in the upper part of the study area to 60 – 90 m near St-Maurice. Maximum C^{14} ages of alluvial sediments determined by Finger and Weidmann [61] are about 9'000–10'000 yr BP for sediments sampled at a depth between 30 – 40 m. Based on radiocarbon dating, these authors calculated a mean sedimentation rate of 4-5 m kyr^{-1} in the alluvial plain over the last 12'000 yr. Their estimation of maximum ages of alluvial sediments is in agreement with the finding of Badoux [62] that the Rhône glacier had retreated up to the east of Sierre by 11'000–10'500 yr BP.

The topography is typical of an alpine valley in that it presents a strong relief between high mountains ranging up to more than 4'000 m and the alluvial plain, which has an altitude of 450 and 620 m in the study area. The alluvial plain has a gentle slope of 1.5 ‰ between Sierre and Evionnaz.

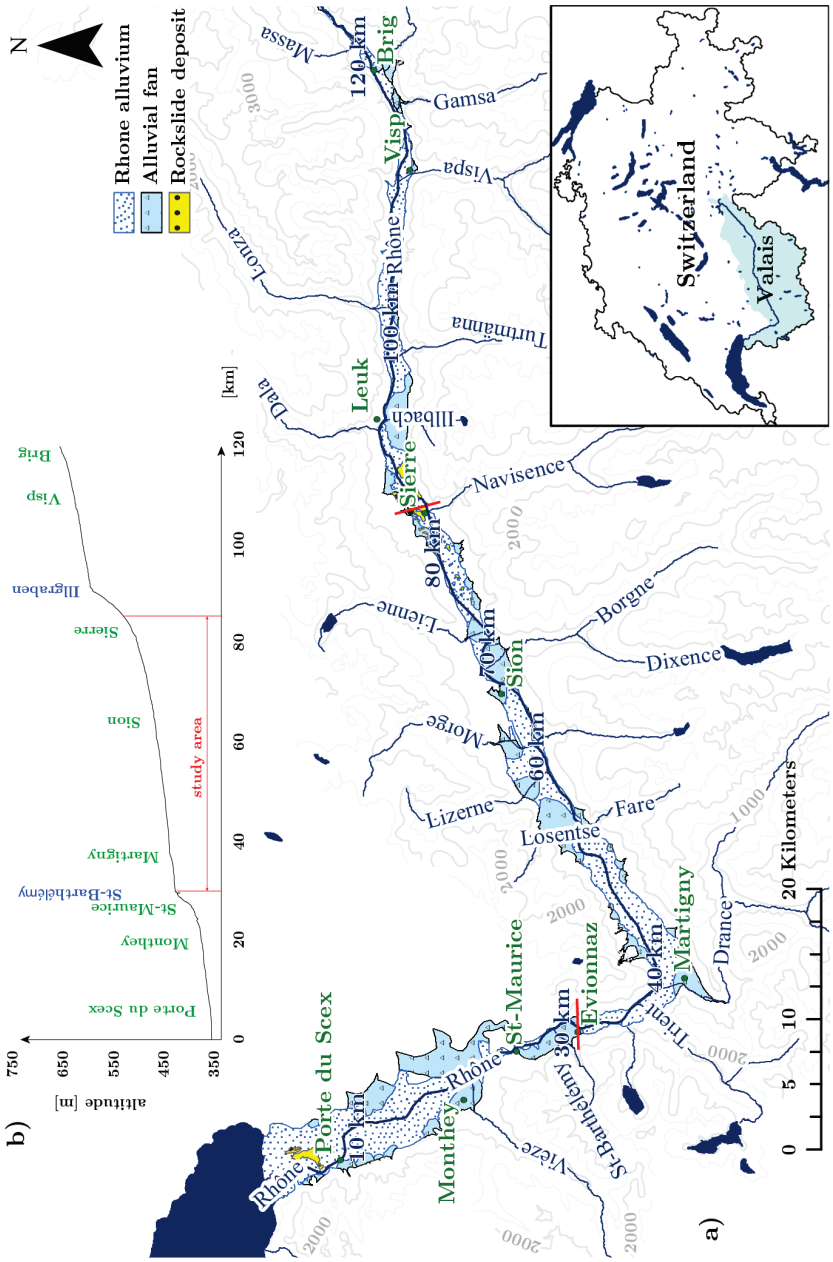

Figure 1 : a) Map of the study site and its surroundings; b) Longitudinal profile.

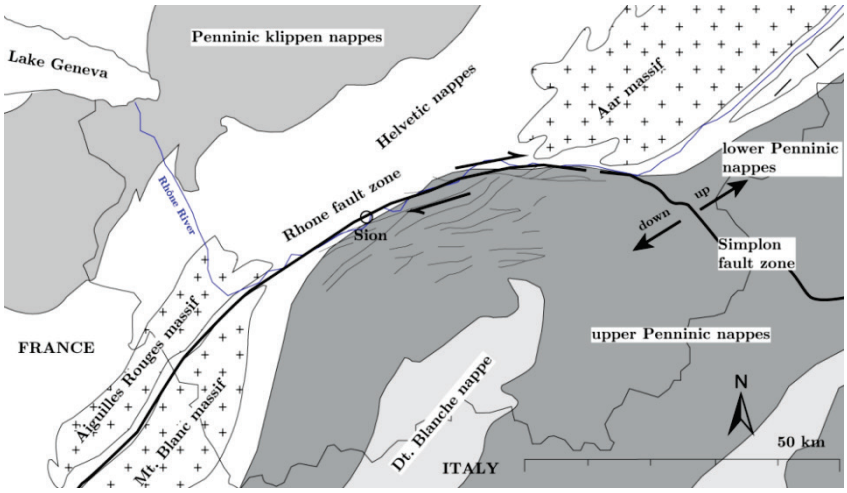

Figure 2 : Major tectonic elements of the northwestern Alps (modified after Maurer, Burkhard, et al. [63]).

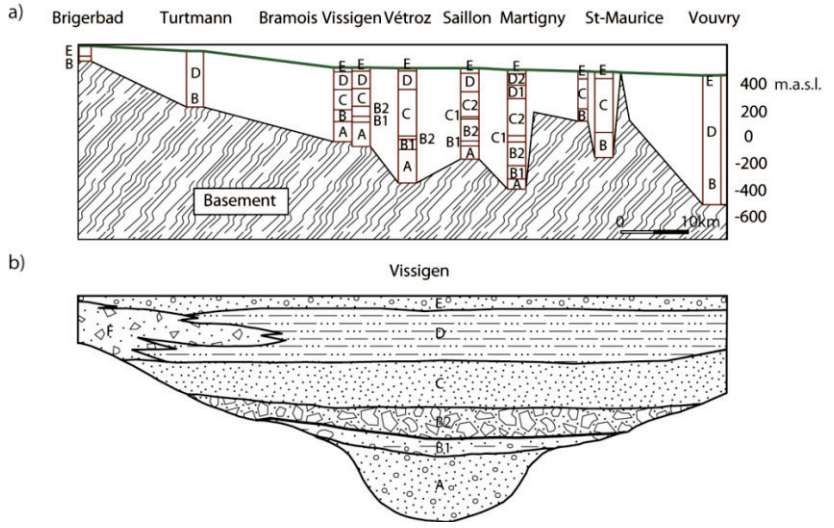

Figure 3 : a) Longitudinal profile incl. bedrock position and interpretation of quaternary sediments (reproduced from [57]). The profile integrates results from reflexion-seismic studies ([57] and [56]), from a gravimetric study [64], from a geolelectrical study [65] and from lithological borehole logs [66]. b) Example of interpretation of a seismic profile (NW-SE seismic profile at Vissigen, near Sion): A: Infraglacial channel deposits; B1: Lodgement till; B2: Meltout till; C1: Proglacial lacustrine deposits; C2: Periglacial lacustrine deposits; D1: Lacustrine deposits (bottom set beds); D2: Lacustrine deposits (forset beds); E: Post-lacustrine deposits; F: Alluvial fan deposits of a tributary.

Two terrain-steps emerge from a longitudinal topographic profile along the Rhône River (Figure 1b): One at about km 30, the other at about km 90. They are related to the large alluvial fans of the tributaries St-Barthélémy and Illbach, respectively. Besides these two large fans, numerous smaller alluvial fans related to tributaries are present. They often deflected the course of the river from one valley side to the other. Hills emerging from the plain in the upper part of the study area, between Sierre and Grône, testify to the large, late glacial Sierre landslide [67].

2.3 Surface Hydrology

2.3.1 General

The present-day hydrology of the Rhône drainage basin is strongly affected by human activity. Major influences are related to flood protection measures and to hydropower use.

Attempts to regulate the destructive forces of the Rhône River date back to middle Ages [68]. However, flood protection then was essentially the municipalities' responsibility and the regulation works prior to 1868 remained isolated and less effective [69]. The age of the large systematic river regulation works in Switzerland began in the early 19th century with the regulation of the Linth, which preceded the first major hydraulic engineering projects of the young Swiss national state: The corrections of the Alpine Rhine (1854), the Jura water and the Rhône (1860s) and the Ticino (1880) [68]. In the case of the Rhône River, it was the dramatic flood of 1860 that ultimately triggered regulation works.

Recent studies, amongst others those by Stäuble and Reynard [70], Zanini, Zanini, et al. [71], Reynard, Evéquoz-Dayen, et al. [49] or also Laigre, Arnaud-Fassetta, et al. [72], have filled the gap in knowledge about the morphology of the alluvial plain before regulation. Based on analysis of historical maps, Stäuble and Reynard [70] found that braided and meandering fluvial styles prevailed (see also extracts of historical maps in Figure 4). Consequently, significant parts of the plain were occupied by the floodplain of the Rhône River (10.9% in 1850 [71]). Prior to regulation inundations of the plain were frequent [68]. The inundated areas remained flooded during long periods and as a consequence marshes and swamps developed (8.2 % of the plain in 1850 [71]).

Once the first stage of regulation (1863 – 1894) was accomplished, the Rhône River had been converted to a sinuous single channel almost all along its path through the alluvial plain, the main exception being the reach crossing the Pfyn forest between Leuk and Sierre. On this stretch the braided character of the river remained largely intact. Despite the straightened and channelized river course, the river bed morphological diversity was largely preserved in the first stage of regulation [73]. The works

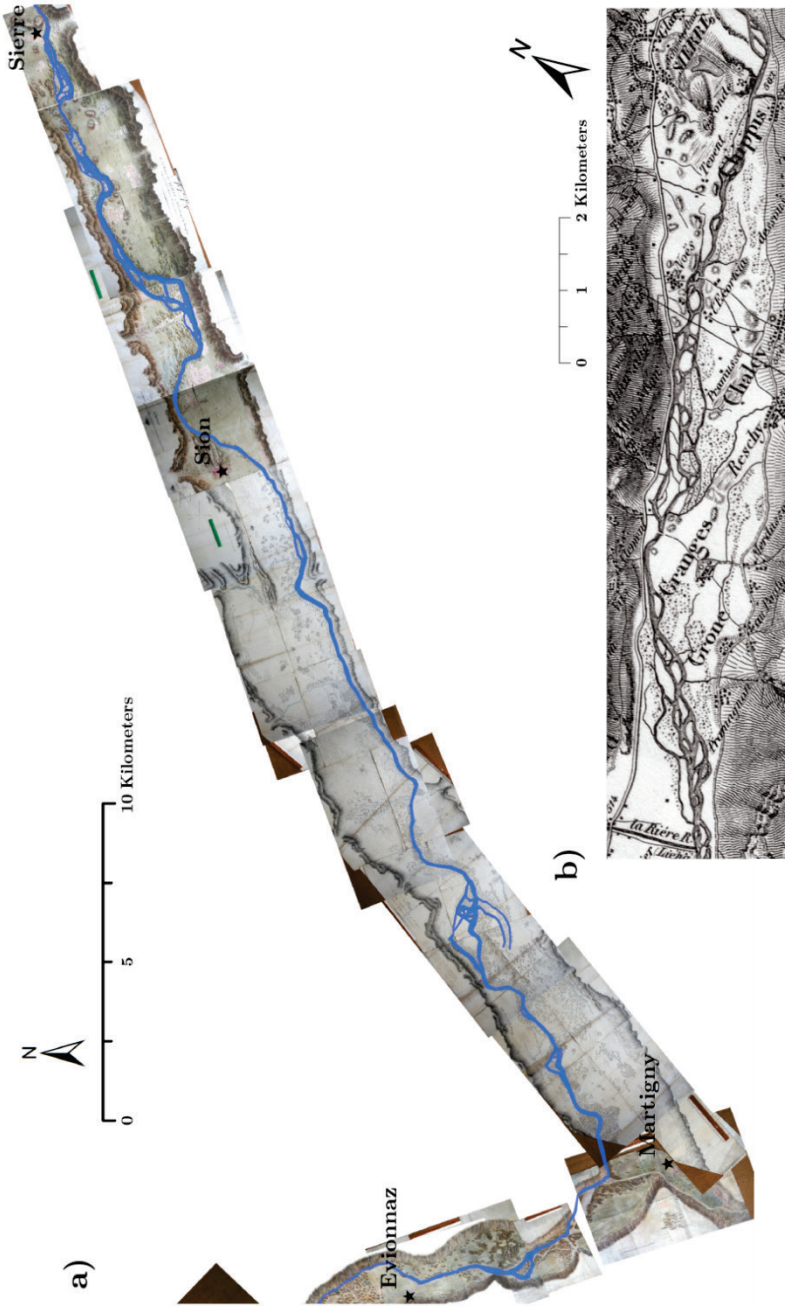

Figure 4 : Extracts of historical maps: a) Map of Napoléon (1802; source: Archives nationales de France, CHAN-F/14/10191 et 10192, photo M. Lechevalier); b) Map of Dufour (1844; source: Federal Office of Topography).

nevertheless caused significant adjustments in terms of river hydrodynamics with repercussions on the river transport regime. For instance, contrary to what had been envisaged, the regulation resulted in a diminishment of the sediment transport capacity of the Rhône River. Accordingly, the level of the streambed rose, at some places by several centimeters per year [74] and finally entailed further regulation works that were accomplished in the second stage of the regulation [49]. Also, many tributaries could not merge the Rhône River any longer due to the dams. They flooded the plain and caused a rising of the groundwater table. These tributaries were therefore repositioned further downstream, where the dam was lower, and ditches were built to drain the inundated plain.

Further changes of the hydrologic system came along with the arrival of industrialization and the inception of hydropower in the early 20th century. Whilst influences remained relatively modest during the first half of the century, the rapidly growing importance of hydropower since the 1950's left a profound imprint on the drainage basin, with most of the large hydropower having been constructed between 1951 and 1975 [12]. Retaining headwaters in dams and by-passing creeks in headrace tunnels leads to significantly altered flow and sediment transport regimes downstream of hydropower dams [13]. Furthermore, the release of water in response to power demand induces rapid, unnatural and significant fluctuations in discharge, a phenomenon termed hydropeaking [13]. Hydropeaking has been identified as one of the main stresses on river ecosystems [e.g. 12, 75, 76, 77]. From a hydrogeological perspective, hydropeaking is important in that the water level fluctuations in the river are transmitted to the aquifer and affect the river-groundwater interactions. It may also accelerate clogging of the streambed [78].

Today, the surface water resources of the Rhône River basin include besides the Rhône River several large man-made mountain reservoir lakes, scores of smaller mountain lakes, tributaries that drain lateral valleys and an extensive network of smaller tributaries, drainage ditches and ponds, scattered throughout the plain. Ditches not only serve for draining but also provide water for agriculture.

2.3.2 Rhône River

Data from the Swiss Federal Environmental Service (FOEN) that maintains seven gauging stations to measure river stage, discharge and temperature, provides an important data base for the following description of the hydrology of the Rhône River. Two of these stations are situated within the study area (Sion, km 64.2 and Branson, km 40). Further measurements are available from stations maintained by the canton of Valais [79]. The stations within the study area are located at Chippis, Sion, Riddes and Fully.

Other important sources of information are various studies conducted by researchers of the Swiss Federal Institute of Aquatic Science and Technology (Eawag) and the Swiss Federal Institute for Forest, Snow and Landscape Research (WSL) as part of the interdisciplinary Rhône-Thur Project [12-18]. Furthermore, a study on the evolution of the suspended sediment load of the Rhône by Loizeau and Dominik [22] and a study on water quality of surface waters in the Valais canton carried out by Bernard, Perraudin - Kalbermatter, et al. [23] were consulted.

The Rhône River originates at Gletsch (km 165, about 1800 m a.s.l). From here it flows westwards, first with a relatively steep slope up to Brig (km 120, 681 m a.s.l), then it levels off in the plain of the main valley up to St-Gingolph (km 0, 386 m a.s.l), where it empties into the Lake of Geneva (s. also Figure 1b).

On an annual average, the discharge of the Rhône River is about 133 m^3/s at Branson (period: 1941 – 2011; data source: [80]) and about 110 m^3/s at Sion (period: 1916 – 2011; data source: [81]). The annual average discharge displays relatively large variations [22]. Seasonal discharge in the Rhône River is controlled by glaciers with low flows during the winter and high flows starting in May and ending with the high altitude freeze in October [22] (Figure 5a). Nowadays, a fifth of the mean annual flow at Porte du Scex – near the mounding of the Rhône into Lake Geneva – is retained by dams during the summer period and released during the winter period [12]. Whilst the flow regime of the Rhône at Porte du Scex could be termed "Glacio-nival" to "Nivo-glaciaire" in its natural state [82], it may today be classified as "Nival de transition" to "Nivo-pluvial préalpin" [12] reflecting the retarding effect of hydropower dams on summer discharge.

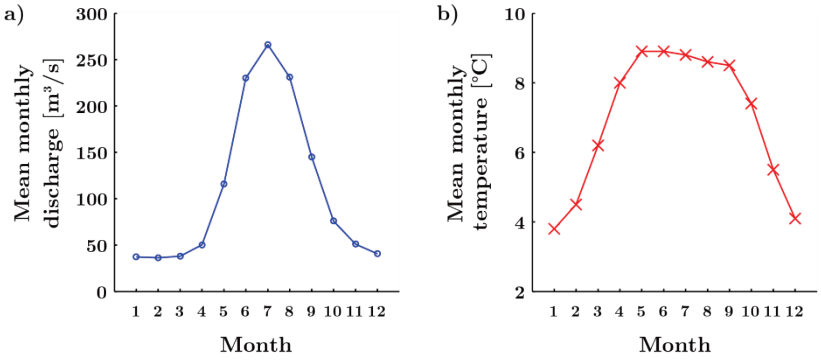

Figure 5 : Monthly mean values of a) discharge (measurement period: 1916 – 2011) and b) temperature (1974 – 2011) of the Rhône at Sion [81].

Natural variations on a yearly scale are hence influenced by the operation of hydro-electric power plants [22]: Their operation leads 1) to an increase in winter discharge and reduction of summer flows, 2) to a reduced intensity and frequency of flooding and 3) to a decrease of suspended solids in the river [14, 15, 22] with consequences on the temperature regime, geochemical cycles, and river and floodplain ecology [15].

Besides the variations on a yearly scale, considerable short-term variations of discharge, river stage and of other parameters such as turbidity [18] and temperature [12, 14, 16, 17] exist in the Rhône River due to the operation of the numerous hydro-electric power plants (hydropeaking). Figure 6 reveals the large influence that the use of hydropower has on the flow regime of the Rhône. Hydropeaking is especially marked on a weekly scale, due to a reduced consumption of electricity during the weekends (Sundays are indicated by vertical lines on Figure 6), but is also visible on a daily time scale: Daily variations of water level in the Rhône River during 2005 are shown in Figure 7 (calculated as the difference between daily extreme values). The measurements at river gauging stations at Branson (km 40.0), Sion (km 64.2) and Chippis (km 80.2) indicate an increasing trend of daily water level variations in downstream direction. The average daily water level variation for 2005 is 0.34 m at Chippis, 0.45 m at Sion and 0.67 m at Branson. This increase is associated with the inflow from several hydro-electric power plants downstream from Sierre, the largest being Cleuson-Dixence, Mauvoisin and Emosson. At the station of Branson, daily water level variations of more than one meter are frequently observed (Figure 7).

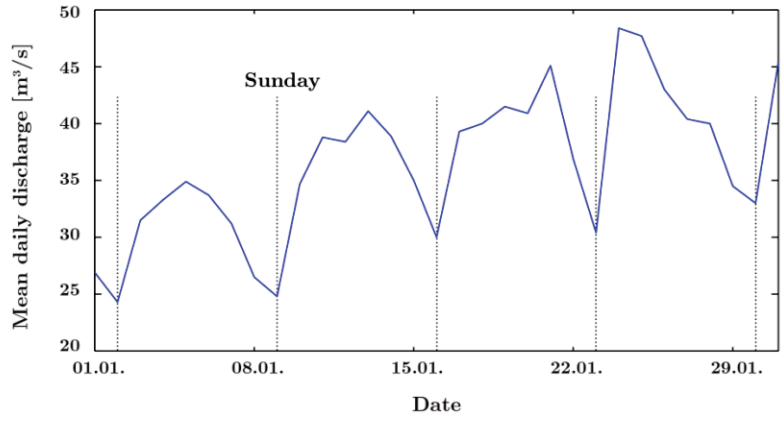

Figure 6 : Mean daily discharge of the Rhône River at Sion, January 2011 (data: [81]).

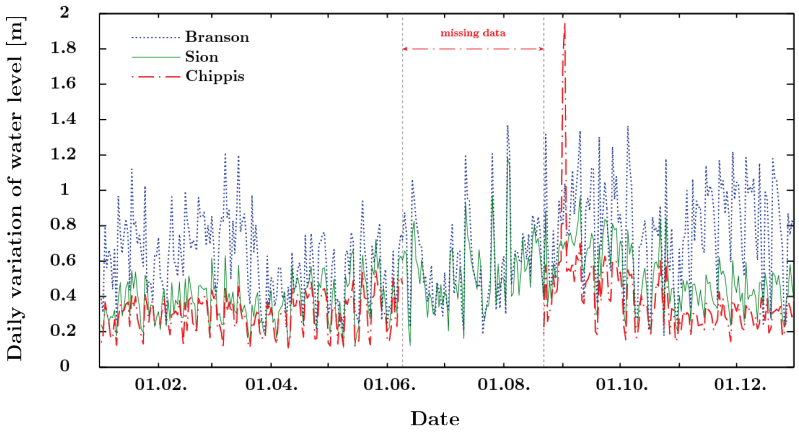

Figure 7 : Daily variations of the water level in the Rhône River during 2005 at Branson, Sion and Chippis (data: [79]).

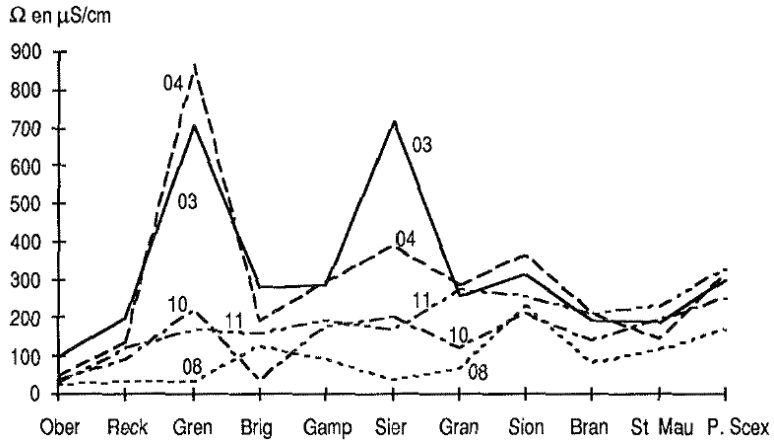

Figure 8 : Evolution of the electrical conductivity in the Rhône River during 1992. Numbers correspond to months; reproduced from [23].

The main dissolved ions in the Rhône River are Ca^{2+}, Mg^{2+}, SO_4^{2-} and HCO_3^- [23]. The concentrations of dissolved ions are generally higher during the winter, when the contribution of surface runoff, low mineralized water from power plants or melting of snow and ice is low [23]. The relatively low mineralization of the Rhône River manifests itself with a low electrical conductivity, the average electrical conductivity is between 100 and 250 µS/cm [83]. Figure 8 shows the evolution of the electrical conductivity along the Rhône River [23]. A slightly increasing trend in the downstream direction should be noted. This was also observed by Brögli [19]. The increase can be

explained by the inflow of water with a higher electrical conductivity from the Rivers Naviscence, Lienne and Borgne [23]. The decrease in electrical conductivity at Branson (Bran) contrasts this trend and may be due to the inflow of lower mineralized waters from dam reservoirs [23].

Melt water draining glacier basins contains high loads of fine material (clay, silt) produced from glacial erosion [84]. Accordingly, suspended load concentration in the Rhône is naturally high during the summer (between 50 mg/l and up to several 100 mg/l). The associated high turbidity has negative effects on the aquatic ecology [18]. Compared to the natural state, concentrations are higher during the winter due to the release of waters from dam reservoirs that are rich in suspended load [12]. The concentrations are nevertheless lower than during the summer (about 10 mg/l to max. 100 mg/l) and are not considered to be ecologically relevant [18].

The average annual water temperature of the Rhône River at the station of Sion is 7.0°C (period: 1974 – 2011; data source: [81]). Highest temperatures are measured in May and June (8.9°C on average), lowest temperatures occur in January (3.8°C on average; Figure 5b). Measurements conducted in 2002 by Meier, Frey, et al. [16] indicate an increase in the average annual temperature in the downstream direction 3°C/120 km between Porte du Scex (7.6 C) and Brig (4.65°C). As Meile, Fette, et al. [31] report, temperature changes can amount to 2.4°C/h as a consequence of hydropeaking.

The Rhône River in its current state is considered as ecologically deficient [85]. The monotonous in-stream structure, which was mainly induced by the second stage of regulation (1930 – 1960) [73] is together with hydropeaking seen as the main reason for the ecological deficits [12, 73, 86]. The consequences of morphological changes can – in the case of the Rhône River – not entirely be separated from the hydrological disturbance of the natural state by hydropeaking, because they occurred more or less simultaneously [12]. The population density of fish is generally low and fish fauna is unvaried (dominated by brown trout) [86]. As a consequence of the pavement and clogging of the river bed, the high hydraulic stress and the lack of morphological diversity, the benthic flora and fauna are degraded [73]. Repercussions of channelizing the river course are the almost complete absence of a Riparian zone [86] and poorly developed longitudinal and lateral floodplain connectivity [87].

2.3.3 Tributaries

The principal tributaries of the Rhône River are shown in the overview map given in Figure 1. At their juncture with the alluvial plain, most often alluvial fans have formed. As a consequence, the tributaries lie several meters above the level of the alluvial plain of the groundwater table. Their streambeds are most often channelized and are often considered clogged [88].

2.3.4 Drainage ditches

In order to drain the alluvial plain, especially after regulation works had led to flooding by tributaries (see section 2.3.1) and by groundwater, a drainage system was set in place in which the plain was divided into eight sub-basins. Every sub-basin was then drained by several secondary ditches leading to one main ditch which then evacuated the water to the Rhône River [89]. Additional drainage ditches were constructed during the period of the Second World War.

This drainage system is still playing an important role for the hydrology of the plain. The drainage is partly effected by hidden drain pipes leading the water to the observable open ditches. The positions of the hidden drains are not known. The figure below gives an overview of the numerous ditches in the study area.

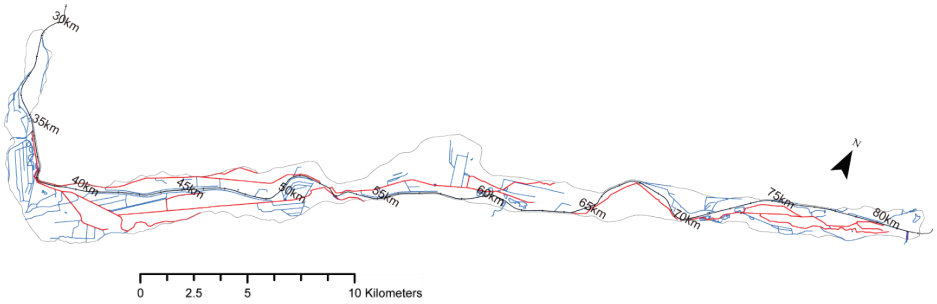

Figure 9: System of drainage ditches in the study area; Main ditches are highlighted in red.

2.4 Subsurface hydrology

2.4.1 Groundwater flow

The description of groundwater flow in the alluvial aquifer given in this section is on the one hand based on measurements that were carried out as part of the Hydro-Rhône project in the mid-1980s [2]. In contrast to the characterization available in the project reports, where the study area is divided into seven stretches that are described in detail, this section aims at giving a coherent description of the Rhône alluvial aquifer on a regional scale. Amongst the data sampled by the Hydro-Rhône project, hydrochemical and hydrophysical measurements were considered in order to recognize hydrogeological boundaries. On the other hand, bi-annual measurements of hydraulic head in the alluvial aquifer were consulted in this work to gain an insight in the functioning of the alluvial aquifer. These measurements were carried out over 10 years (1994 – 2003) in the study area on a measurement network comprised of about 730 piezometers. The piezometers were measured twice a year during low water (HW; February – March) and high water (HW; July – August) conditions of the Rhône River. The

Crealp, a research center on alpine environment, compiled this data to mean hydraulic heads during HW and LW to establish piezometric surfaces for both seasons [90].

Figures 10 and 11a show mean hydraulic heads during HW in a longitudinal section and in a map view. Mean hydraulic heads during LW are not given here, because their representation on a regional scale yields a very similar outcome as the plot of heads during HW. Hydraulic heads during HW and LW are depicted as heights relative to the water level of Rhône River and relative to the altitude of the streambed in Figure 12.

As mentioned before, the study area lies between two large alluvial fans, the fan of the Illbach to the east and of St-Barthélémy (and L'Aboyeu) to the west. These lend themselves as limits of the study area because they correspond to natural boundaries of the alluvial aquifer: Both alluvial fans almost entirely occupy the alluvial plain and cause an exfiltration of groundwater to the Rhône River due to their low hydraulic conductivity. The uppermost part between Sierre (km 82) and the Illgraben fan (km 90) was nevertheless not included in the study area, because no restoration measures are planned on this stretch due to the largely natural character of the streambed. Studies by Schürch [91] and Steiner [20] revealed the complexity of hydrogeological conditions in this part, both in terms of aquifer properties and boundary conditions. Immediately downstream of the fan the groundwater table in the alluvial aquifer lies far below the ground surface at a depth of more than 5 m. Strong recharge of the alluvial aquifer by the Rhône River and through lateral inflow from the southern valley side leads to a rising of the groundwater table within a short distance.

The upstream end of the study area is located near Sierre (km 82). Here, the groundwater table is depleted by public and industrial pumping wells (Figures 10 and 12). Downstream of Sierre the groundwater table rises, but it remains beneath the water level of the Rhône River down to Sion, where it reaches the height of the Rhône level on a short stretch (km 65 – 70). Further downstream – down to Vernayaz (35 km) at HW and to Saxon (47 km) at LW – the level of the Rhône River is again above the groundwater table. Still further downstream, the groundwater table is at the height of the river level or above (Figures 10 and 12). Here the aforementioned influence of the alluvial fan of St-Barthélémy engenders an exfiltration of groundwater to the Rhône River.

It is interesting to notice that this sequence of losing to gaining river can also be observed outside from the study area. It is repeated at least three times within the alluvial Rhône aquifer between Brig and the Lake of Geneva and is related to the presence of sub basins separated from each other by low permeable or impervious natural morphological elements (alluvial fans of Illgraben, St-Barthélemy; rock sill at St-Maurice).

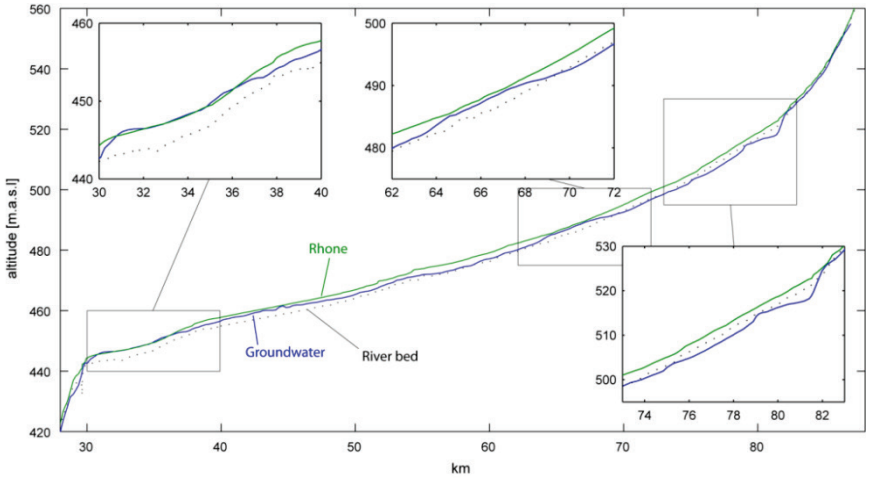

Figure 10 : Longitudinal profile of the streambed elevation of the Rhône River, of river stages and of hydraulic heads in the aquifer underneath the river (water levels during high waters; data PR3 [1]).

Lying generally at shallow depths (often between 1 and 2 m depth), the water level in the alluvial aquifer mirrors at large the topography of the valley floor (Figure 10). The aquifer is mainly unconfined, and groundwater flow is roughly parallel to the Rhône River and to the axis of the valley. Compared to the rest of the study area, the hydraulic gradient is relatively high near Sierre, reaching values of about 7 ‰; to the west it decreases progressively. On average, the hydraulic gradient between Sierre and Evionnaz is about 1.5 ‰. An increase may be noted at km 52, where the aquifer narrows (Figure 11a).

As indicated in Figure 11b, annual head variations can be of more than four meters. In most areas, however, they are less than one meter. Highest variations are observed in the most upstream part (km 79–80), in the region of the alluvial fan of Borgne River (km 65–70) and in the region upstream of the "neck" at Martigny, in the southern part of the plain (about km 42). In all but the latter region, large variations are synchronous to the variation of the flow regime of the Rhône River. Variations in the aquifer amount to about 50 percent of the variations of the Rhône River between km 30 and km 75. Further upstream this value increases. On large reaches, head variations are highest on a strip along the Rhône River. This provides evidence that in these areas, variations are induced by the Rhône River. In areas with drainage ditches, head variations tend to be low.

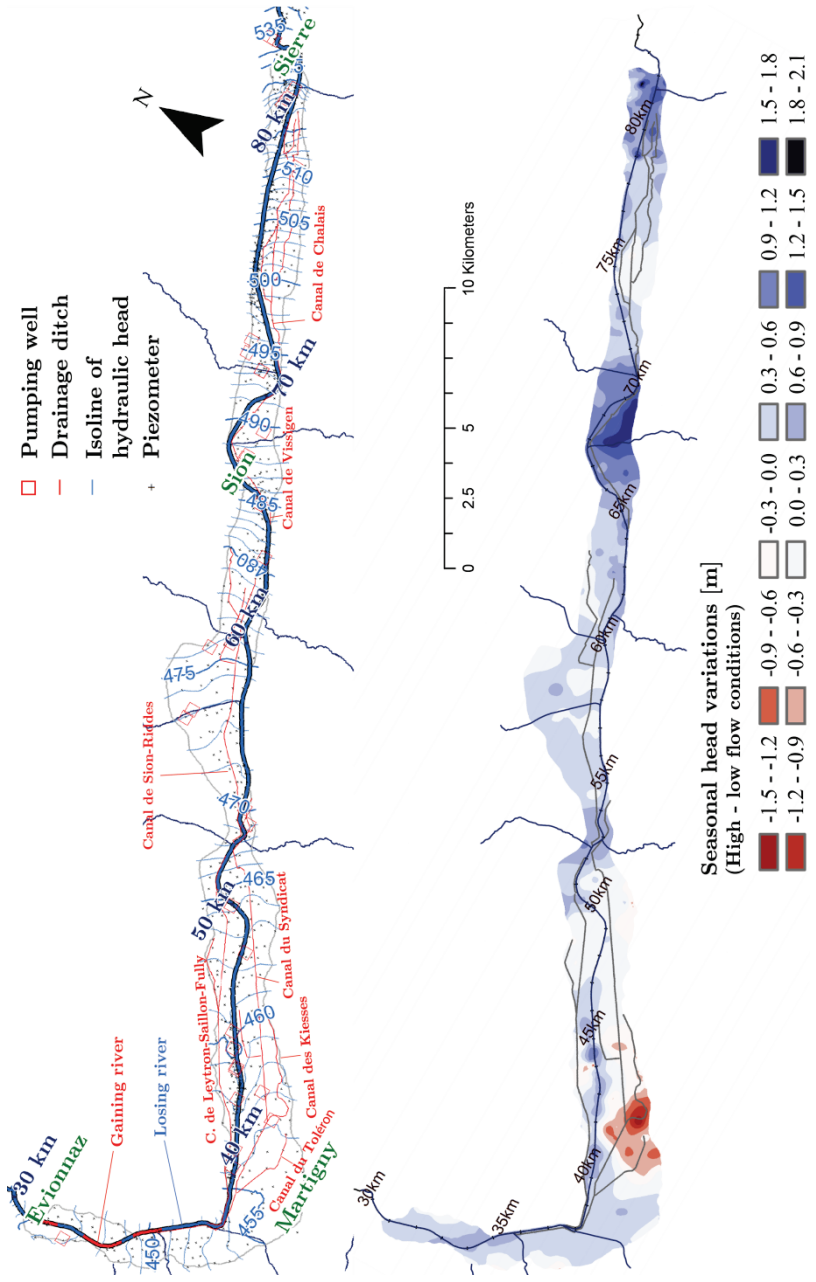

Figure 11 : Average water levels in the aquifer 1995 – 2004: a) Contour map of groundwater heads during HW including major drainage ditches b) Seasonal head variations (difference between average levels during high and low waters, 1995 – 2004).

Apparently, ditches are one cause for head variations to be attenuated. Other causes might be the presence of low permeability sediments or other driving forces which outplay the influence of the Rhône River on the aquifer. For instance, the asynchronous variations in the above cited area are thought to be caused by an inflow from the southern valley slope.

Géoval [2], in their analysis of time series of hydraulic heads in the aquifer, found that in general, precipitation plays a considerable role in the recharge of the Rhone alluvial aquifer. Regarding its relative importance compared to recharge by the Rhône River, it may be notable, that the effect of precipitations in piezometers close to the Rhône River was found to be masked by variations in river stages.

2.4.2 Groundwater – surface water exchange

Two basic flow regimes exist between surface waters and groundwater: either the surface water body drains the aquifer (gaining river, exfiltrating conditions), or it recharges the aquifer (losing rivers; infiltrating conditions). On a losing stretch, the hydraulic head in the river is higher than in the aquifer. In contrast, heads are lower in the river than in the aquifer on a gaining stretch [27].

As indicated in Figure 11 and Figure 12, infiltrating conditions prevail in the SW-GW system of the Rhône River and the alluvial aquifer: The water level in the Rhône River is to the largest part higher than the hydraulic head in the aquifer[1], and the Rhône River is losing water into the aquifer. During HW, the only section where the Rhône River is gaining water from the aquifer is between km 31 and 36 (Figure 11a, Figure 12). From km 30 to 70 the altitude of the streambed is lower than the potential head in the aquifer during HW. Upstream from km 70 the streambed lies above the groundwater level.

As explained in Brunner, Simmons, et al. [92], lowering of the groundwater table causes an increase in infiltration flux, unless the groundwater table drops below a critical depth. If the groundwater table is lowered further, an unsaturated zone may develop between the river and the groundwater table and the infiltration flux approaches an asymptotic value. If the groundwater table lies at a depth, at which a further lowering does not induce a further increase of the exchange flow, a hydraulic disconnection of the stream occurs. A disconnection of the groundwater table is possibly occurring near Sierre, near km 82, where the difference between water levels in the Rhône River and the groundwater table amounts to about 5 m.

On some stretches, the influence of the Rhône River on groundwater is clearly reflected in the shape of contour lines of groundwater heads (Figure 11a): For instance,

[1] As extracted from the piezometric surface at the Rhône axis.

the downstream flection of contour lines in the section between km 40 and km 50 testifies to an infiltration of the Rhône River. This section also illustrates that drainage ditches have an influence on groundwater flow: The flection of the contours to the upstream direction can be taken as a sign of exfiltration of groundwater to the Canal de Syndicat.

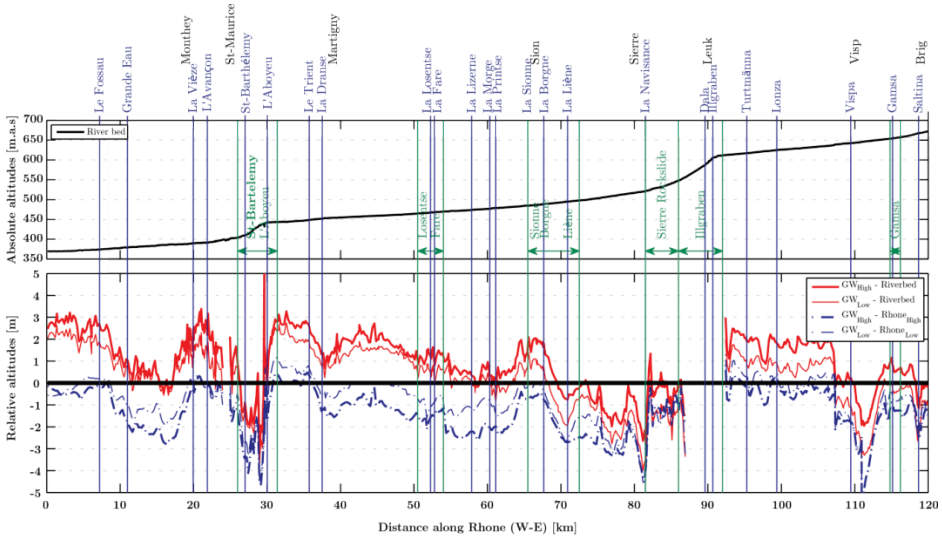

Figure 12 : Longitudinal profile of topography along the Rhône River (above) and of hydraulic heads in the aquifer relative the water level in the Rhône River (below).

2.5 Hydrochemistry

Analyses that were carried out as part of the Hydro Rhône project [2] on a uniquely dense measurement network in 1985/86 are used herein for a short description of hydrochemical properties of the groundwater. The entire dataset consists of 1341 samples and includes measurements of temperature, electrical conductivity, pH, major cations (Ca^{2+}, Mg^{2+}, Na^{+}, K^{+}, NH^{4+}, Fe^{2+}, Mn^{2+}), major anions (Cl^{-}, HCO_3^{-}, SO_4^{2-}, NO_3^{-}, NO_2) and dissolved oxygen from surface waters and groundwater during HW and LW.

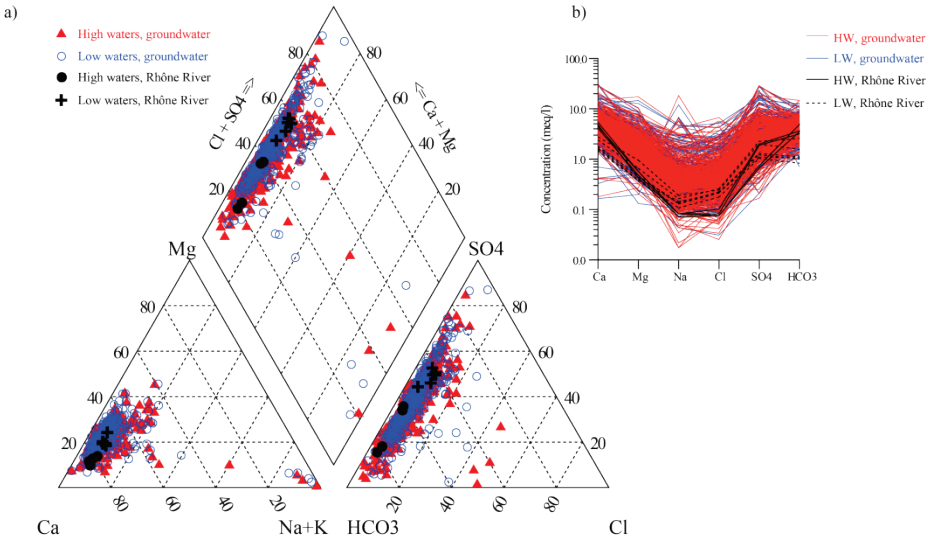

Figure 13 : Composition of the water of the alluvial aquifer in terms of main ions represented in a) a Piper plot; b) a Schoeller plot (Figure b includes data of the Rhône River; data: Hydro Rhône project [2]).

On the cations' side, the waters are mainly dominated by Ca^{2+} and to a lower extent by Mg^{2+}, the major anions are HCO^{3-} and SO_4^{2-} (Figure 13). The data suggest a stable hydrochemical composition of the aquifer throughout the year. At large, waters of the Rhône River and the aquifer have a similar chemical composition (Figure 13a). As shown in Figure 13b, the water samples of the Rhône River are however in general less mineralized.

The spatial distribution of two variables is regarded in more detail: Dissolved oxygen and the electrical conductivity (EC; Figure 14). These variables were helpful environmental tracers to clarify the conceptual model for groundwater flow.

Highly oxygenated waters are generally associated with recharge waters [93]. In the study area, concentrations of dissolved oxygen are always related to the presence of surface waters. Dissolved oxygen is therefore considered as an indicator of recharge of the alluvial aquifer by losing surface waters herein.

In the area of certain alluvial fans, e.g. of rivers Lienne, Borgne, Dranse and Trient, where amongst the highest concentrations are measured (> 8 mg/l; Figure 14b), the groundwater table lies at a relatively large depth (Figure 14a). It is conceivable that in these alluvial fans, recharge of the Rhône aquifer takes places through an unsaturated and aerated zone. This process has been suggested to explain high concentrations of dissolved oxygen in the Thur aquifer [94]. The general trend of decreasing concentrations from the top of the study area down to the "neck" of Martigny might be explained by the same process: in the upstream part, where head losses between the Rhône River and the groundwater are relatively high (Figure 12), the probability that an unsaturated zone develops underneath the Rhône River is higher compared to areas further downstream, where head losses tend to decrease and infiltration occurs preferentially through saturated flow. As a consequence, aquifer waters are depleted of dissolved oxygen (3-4 mg/l) in a large area between Vétroz and the alluvial fan of Losentse River (km 55–58) and further downstream between Riddes and Martigny (km 39–54). On the lowermost stretch, where exfiltrating conditions prevail, relatively high concentrations of dissolved oxygen possibly testify to hyporheic exchange flow.

EC can be taken as an analogue of the concentration of total dissolved solids (TDS), given the strong correlation[2] that exists between these two parameters. Here, EC is preferred over TDS, because its data set is more complete.

A positive correlation between EC and both Ca^{2+}+Mg^{2+} and HCO_3^-+SO_4^{2-} exists, as shown in Figure 15 and there is evidence that high values of EC coincide with recharge of the aquifer by inflow of highly mineralized water from karstified valley slopes. For instance, the area between Charrat and Riddes (about km 40–50), where several springs of the type Ca–HCO_3–SO_4 [95] – including the thermal mineral spring of Saxon – emerge, is marked by the presence of the highest EC in the study area (Figure 14c). On the same stretch, on the northern valley side, high values of EC are observed at Leytron, and at Saillon. In this area, a number of indices for the presence of thermal water exists, as the thermal spring of Leytron and the drill holes capturing thermal waters in Saillon [96]. High values of EC north of the Rhône River in the area of Aproz (km 60–63) are possibly related to an inflow of highly mineralized water at

[2] Pearson correlation coefficient of r = 0.99.

the southern valley side, as suggested by the presence of sulfate-rich mineral springs [14]. A sulfate-rich spring also exists at “Pouta-Fontana” [2], an area also character-

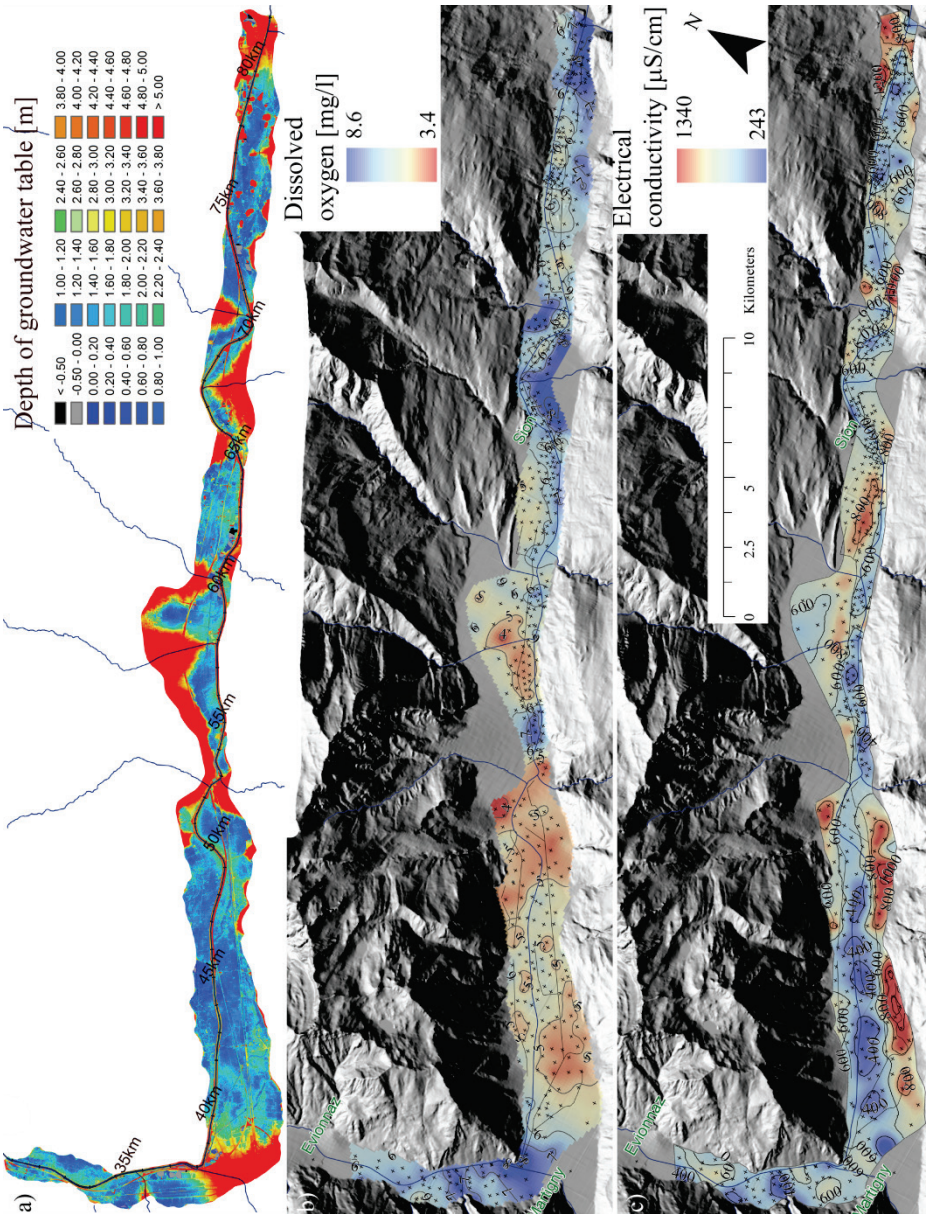

Figure 14: a) Depth of groundwater table during HW (mean values during HW, 1995-2005 data: [79]); b) Concentrations of dissolved oxygen; c) Electrical conductivity (data: HW 1985 [2]).

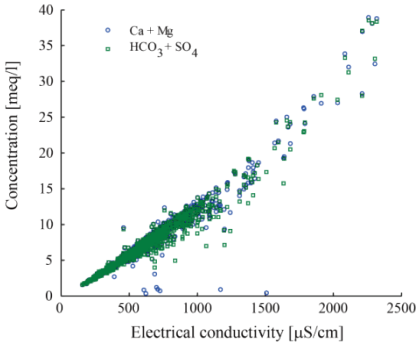

Figure 15 : Scatterplot of Ca^{2+}+Mg^{2+} and HCO_3^-+SO_4^{2-} against electrical conductivity (at 20°C).

ized by high EC values. North of "Pouta-Fontana", an area of higher EC can be observed in Figure 14c. It is located right in front of the subterranean karst lake at St-Léonard. High mineralization may not only be the result of recharge of the aquifer by mineralized water from karst systems but may also develop through dissolution of rocks and their deposits. This can be considered as a possible reason for the relatively high values of EC in the uppermost study area, where low permeable deposits of the Sierre rockslide are present that are partly cemented by precipitations of calcite [67].

On a large part of the study area, the river is environed by a strip of relatively low EC and the lowest values of EC are found close to the Rhône River, too. Given the low mineralization of the Rhône River[3], this can be taken to indicate that the Rhône River loses water to the aquifer[4]. In agreement with high values of dissolved oxygen, low values of EC occur furthermore in alluvial fans of rivers Lienne, Borgne and Trient. In contrast, EC in the area of the alluvial fan of the Dranse River is not low, as might be expected from low values of EC in the Dranse River [97] and from high values of dissolved oxygen. The reason for this is not understood and has not been investigated herein. The fact that low ECs do not always coincide with high values of dissolved oxygen (e.g. km 39–54) may be explained by the consumption of oxygen by microbial activity. The map of EC clearly highlights the functioning of the drainage ditches: Main drainage ditches on large stretches form sharp barriers between higher and lower mineralized waters.

[3] Mean value of all measures: 190 µS/cm.
[4] Mean value of 654 µS/cm.

2.6 Characterization of the alluvial aquifer

2.6.1 Composition of the uppermost aquifer

Data from 886 boreholes were available for the uppermost layers of the Quaternary deposits. All logs are organized in the database "BD-for" [98]. The bores are typically located along the axis of former highway projects. Most of the bores were drilled to less than 30 m deep. The grain size of drilling cores in BD-for is described by a code consisting of three fields (primary, secondary and complementary lithological type[5]).

The data analysis performed herein provides an insight into the lithological composition of the uppermost layers of the Quaternary fill. The data is analyzed by means of vertical proportion curves (VPN). They were introduced by Matheron, Beucher, et al. [99] in the context of simulations of fluvio-deltaic reservoirs as a tool to condition the simulations and are nowadays a basic tool in reservoir characterization. Basically, a VPN is simply a plot of the cumulative distributions of the variable that is examined (lithofacies etc.) at every level against depth (or altitude).

The study area was subdivided into subsections along overarching geomorphologic elements (Figure 16). The subsections are (from west): 1) The alluvial plain between Evionnaz and Martigny (point where the direction of the Rhône valley changes); 2) The alluvial plain between Martigny and Riddes; 3) The alluvial fans of the Rivers Fare and Losentse; 4) The alluvial plain between Ardon and Sion; 5) The alluvial fans of the Rivers Borgne and Lienne; 6) The part between St-Léonard and Chalais, where alluvial deposits alternate with deposits of the Sierre rockslide; 7) The part between Chalais and Salgesch, where surface deposits of the Sierre rockslide prevail over alluvial sediments. Figure 16 shows cumulated relative proportions of the primary lithological types per section and a map of the study area displaying the positions of the bores. Figure 17 gives relative proportions of the most abundant lithological types. In both figures the depth is limited to a range for which a minimum of 15 boreholes is available.

Amongst primary lithologies, gravel is predominant over the whole study area (Figure 16, 64% of the total drilled length). Other common sediments are silt (16%) and sand (13%). Clay as a primary lithology practically only occurs in the section with rockslide deposits near Sierre (section 7, 1% of the total drilled length). Analysis indicated that the uppermost part of the vertical profiles is dominated by silt and mold. With increasing depth, their proportion rapidly decreases. At a depth of 1 to 1.5 m, coarse grained sediments become predominant (Figure 17). Below that depth,

[5] See Table 1 for an overview on the codification (p. 34).

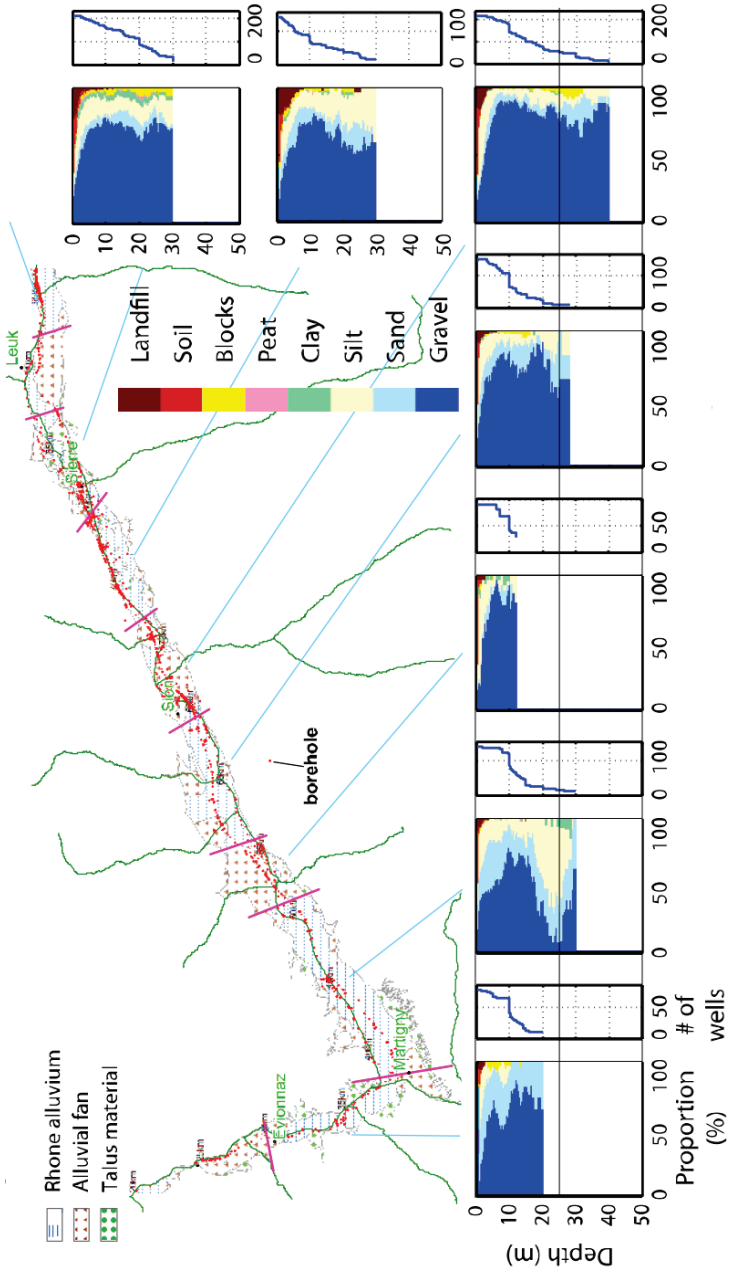

Figure 16 : Proportions of lithologies per section as a function of depth (primary lithological types).

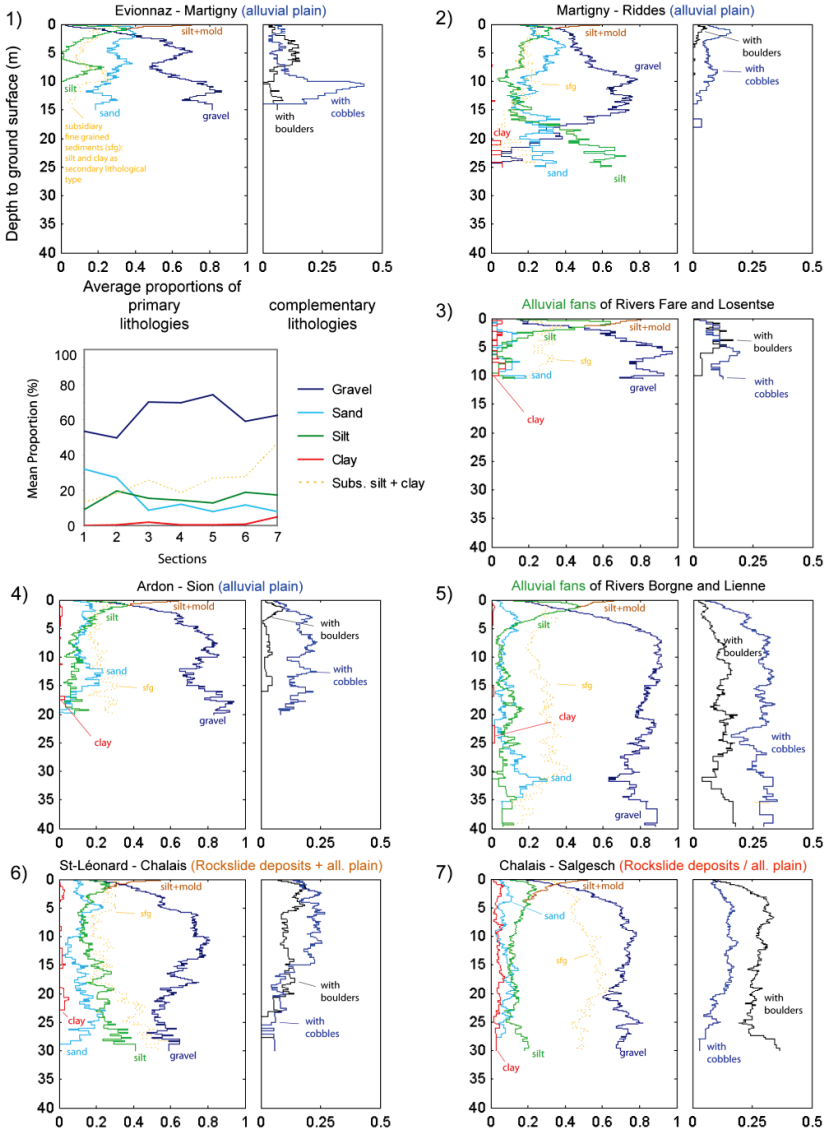

Figure 17 : Proportions of lithologies as a function of depth, per section.

often more than 80% of the drill cores are made of coarse grained sediments. Sand makes up about 30% in average in the sections 1 and 2, further upstream in the sections 3 to 7 its content is lower (Figure 17, see also inset describing zonal means). In the part between Riddes and Martigny (section 2, see Figure 17) the proportion of silt further increases at a depth of about 15 m and becomes the most important grain size

fraction at a depth of about 18 m. An increase of silt with depth can also be observed in section 6 (St-Léonard – Chalais). In all profiles, a decrease of the gravel fraction can be observed in the uppermost 5 – 10 m that is mainly compensated by an increase of the silt fraction.

Coarse grained sediments partly contain fine fractions as subsidiary lithologies, with mean zonal proportions of subsidiary silt or clay tending to increase in the upstream direction (Figure 17; inset of zonal means). Proportions of boulders increase in the upstream direction as well, which may be interpreted as a sign of an increase in depositional energy in the upstream direction. Section 7 (Chalais – Salgesch), where rockslide deposits prevail, is characterized by a relatively high proportion of subsidiary fine grained lithologies as well as by a high proportion of boulders. Apart from at section 7, the proportion of cobbles exceeds the proportion of boulders. The highest proportion of cobbles is reached in the part with the alluvial fans of Rivers Borgne and Lienne (section 5).

The important points of this analysis are 1) that in general, bores are too short to allow determining the base of the aquifer and that 2) the sediment record in the drill cores testifies to predominantly high-energy depositional conditions on the explored depth (max.: about 40 m), aside from the uppermost few meters, where fine sediments prevail.

The observed increase in fine grained sediments in section 2 (Martigny – Riddes) at a depth of about 15 m marks the transition to lower-energy depositional conditions in this area. The data suggests that this transition was temporary and does not mark the transition to the lacustrine depositional environment which is supposed to underlay the fluvial deposits [57]. The predominance of fine grained sediments at a depth of about 18 m therefore can, at best, be considered as the minimum local aquifer thickness.

The available data were only analyzed with the purpose to answer the above questions considering the vertical extent and the vertical heterogeneity of the alluvial aquifer. It would however be interesting to further explore the data set for example to investigate what the causes for the shift in the depositional energy on the uppermost 5 – 10 meters are[6], or to study the reason for the outstandingly high proportion of cobbles in section 1, between 10 m and 15 m.

[6] Referring to sedimentation rates determined by Finger and Weidmann [61], this thickness corresponds to 1000 – 2500 yr.

2.6.2 Hydraulic conductivity of the aquifer

Beside the lithological description BD-for contains also the results of hydraulic tests. The results of small-scale hydraulic tests served to establish a distribution of hydraulic conductivities for the main lithofacies[7] (Figure 18). Basic statistics of the most important lithofacies are given in Table 1.

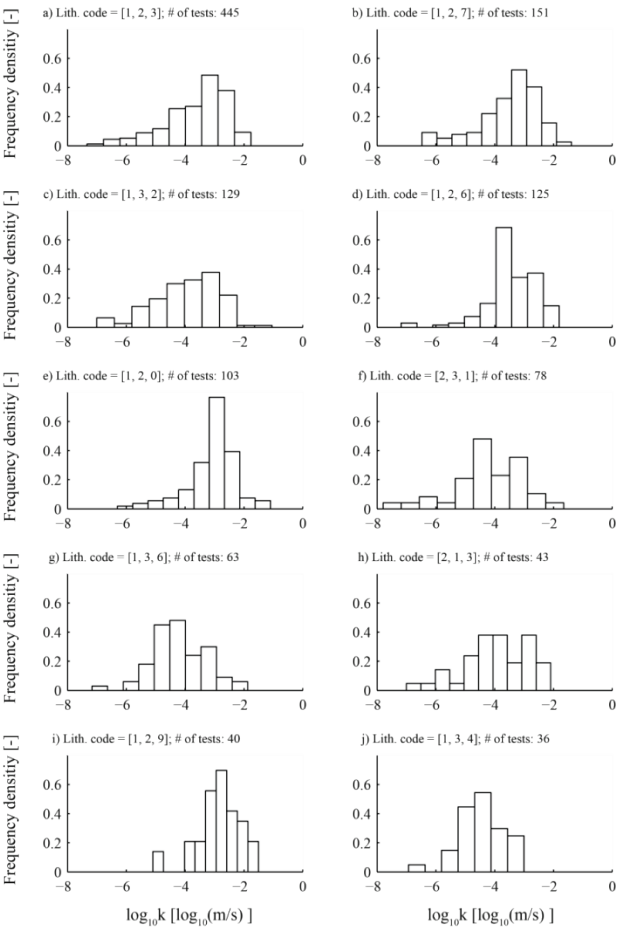

Figure 18 : Hydraulic conductivities of lithofacies with more than 30 hydraulic tests (results of hydraulic tests in BD-for [98], e.g. Lith. code = [1, 2, 3] corresponds to a sandy gravel that contains silt).

[7] Any combination of the three primary fields describing the geology in BD-for is considered a "lithofacies" herein.

Table 1 : Main lithofacies and corresponding hydraulic conductivities derived from hydraulic testing (sorted in increasing order of k values; >15 samples; data: BD-for [98][8]).

Facies description	**Code**	**Mean**		**Variance**	**N. samples**
	(in BD-for)	k(m/s)	$\log_{10}$(k)	$\log_{10}$(k)	-
Gravel, sandy, with pebbles	[1 2 9]	1.4E-03	-2.86	0.57	40
Gravel, sandy	[1 2 0]	8.3E-04	-3.08	0.74	103
Sand, gravelly	[2 1 0]	5.6E-04	-3.25	0.82	17
Gravel, sandy, with blocks	[1 2 6]	3.6E-04	-3.44	0.77	125
Gravel, sandy, with clay	[1 2 4]	3.4E-04	-3.47	1.33	21
Gravel, sandy, with boulders	[1 2 7]	2.9E-04	-3.53	1.05	151
Sand, with gravel	[2 0 1]	2.5E-04	-3.61	0.98	23
Sand, gravelly, with boulders	[2 1 7]	2.4E-04	-3.62	0.80	17
Gravel, sandy, with silt	[1 2 3]	2.3E-04	-3.63	1.10	445
Gravel, silty, with sand	[1 3 2]	1.2E-04	-3.90	1.25	129
Sand, gravelly, with silt	[2 1 3]	1.1E-04	-3.96	1.25	43
Gravel, silty, with boulders	[1 3 7]	6.2E-05	-4.21	1.46	26
Gravel, silty, with blocks	[1 3 6]	6.1E-05	-4.21	0.93	63
Sand, silty, with gravel	[2 3 1]	5.8E-05	-4.24	1.46	78
Sand, with silt	[2 0 3]	4.8E-05	-4.32	0.75	15
Silt, clayey, with sand	[3 4 2]	4.0E-05	-4.39	2.11	17
Gravel, silty, with clay	[1 3 4]	2.6E-05	-4.59	1.05	36
Sand, silty	[2 3 0]	2.3E-05	-4.63	1.22	24
Sand, silty, with clay	[2 3 4]	1.5E-05	-4.82	1.62	27
Gravel, clayey, with boulders	[1 4 7]	1.4E-05	-4.86	1.55	19

Visual inspection of Figure 18 suggests that the common assumption of log-normality of hydraulic conductivities is hardly justifiable for most distributions; the mean and the standard deviation are hence of limited value in describing the distributions.

While these distributions and statistics may potentially be of interest for regional hydrogeologist, they are here not discussed further. In chapter 5, Table 1 will be used as a base for the calculation of mean hydraulic conductivities at each bore.

[8] *Primary* lithological types: Gravel (1), Sand (2), Silt (3), Clay (4), Peat (5), Blocks (6), Rock (7), Soil (8), Gypsum (9), Landfill (10);
Secondary lithological types (adjective): Gravel (1), Sand (2), Silt (3), Clay (4);
Complementary lithological types (containing…): Gravel (1), Sand (2), Silt (3), Clay (4), Peat (5), Blocks (6), Boulders (7), Gypsum (8), Pebbles (9);

2.7 Characterization of the streambed

Results from in-stream hydraulic tests are available from sites near Lalden (outside from the study area; km 112) and near Fully (km 44) [5, 100]. Besides hydraulic testing, the analysis of the streambed properties at these sites included a grain size analysis of sediment samples. Sediment samples stem from drilling cores of bores in which hydraulic tests were performed and were taken from sediments previously investigated by hydraulic testing.

According to Badertscher [5] and Rovina and Glenz [100], the lithological descriptions of the drilling cores don't reveal any superficial clogging layer in the streambed. Layers of fine grained sediments, which might correspond to a clogging layer, were present only in one out of seven drill cores. The deposits are mainly coarse grained and characterized by gravel or sand in a sandy and partly silty matrix.

The available data from the 26 slug tests have been synthesized in Figure 19a. Values of streambed conductivity range between 1.3e-7 m/s and 4.0e-5 m/s. At both sites a general decrease of the hydraulic conductivity can be observed with increasing depth. For a given depth, values at Lalden are about one order of magnitude lower than at Fully.

Grain size distributions were also used for an estimate of streambed conductivity based on the widely accepted Kozeny-Carman equation [5, 100].

Figure 19b shows that the hydraulic conductivities from grain size analysis are in general lower than those from hydraulic testing (by a factor of 2 on average), but range most often within the same order of magnitude.

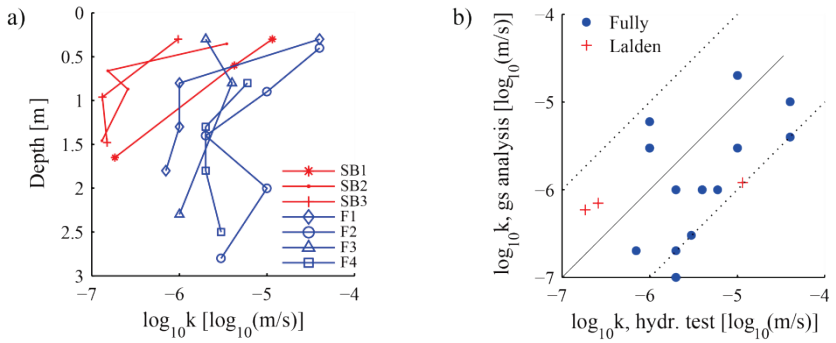

Figure 19 : a) Results of slug tests at Lalden (SB1-SB3) and Fully (F1-F4) as a function of depth. b) Comparison of the hydraulic conductivities from grain size analysis and slug tests.

2.8 Climate

The Rhône valley is shielded against precipitation both from the north and the south. This leads to a contrasted distribution of precipitations with generally dry conditions in the plain and high precipitation depths in the mountains. In the central Valais region an average precipitation amount of less than 700 mm/year is observed [101]. The mean annual precipitation amounts to 599 mm at Sion, the mean annual temperature at Sion is 9.2°C [101]. Within the study area, precipitations are high in the western part and decrease to the east (Figure 20).

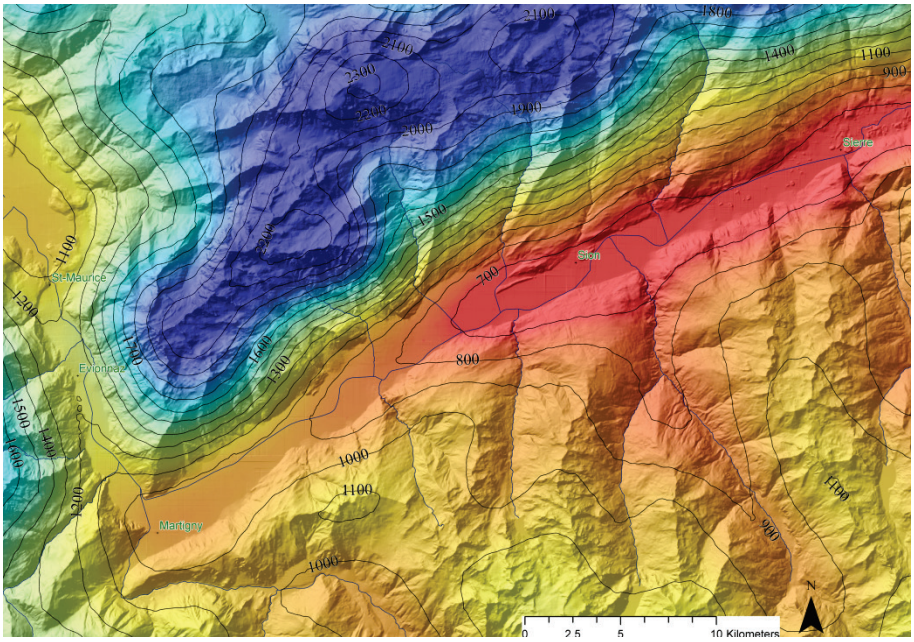

Figure 20 : Mean annual precipitation depth (Isolines in mm/yr; red: low values / blue: high values; data source: FOEN [102]).

2.9 Synthesis of data analysis

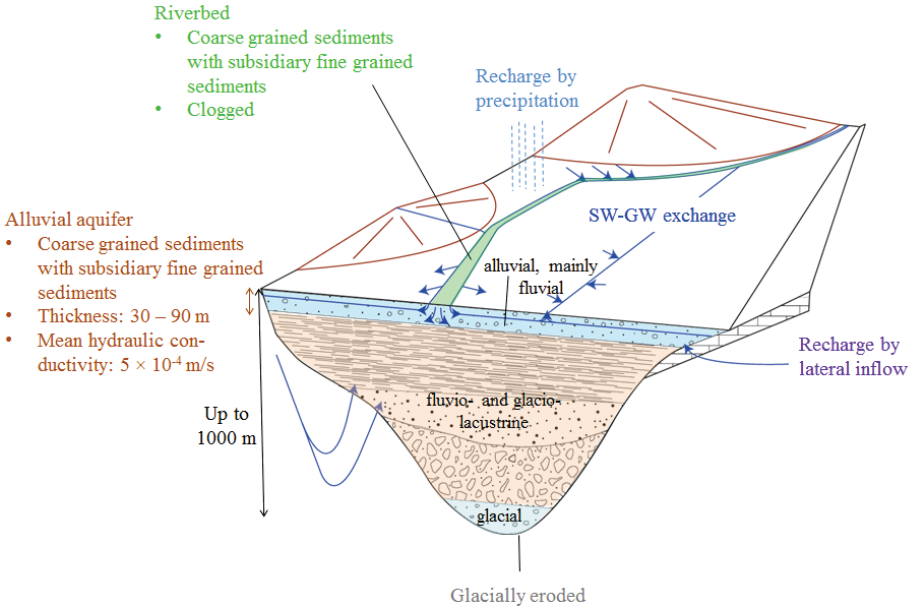

Figure 21 : Conceptual aquifer model of the Rhone alluvial aquifer including the major elements and drivers of the hydrosystem.

Figure 21 shows a sketch of the conceptual model of the Rhone alluvial aquifer as developed through the analysis of the available data.

1) The uppermost layer of the up to 1 km thick valley fill can be considered as the alluvial aquifer herein. The data analysis of drilling logs confirms the widely accepted understanding that the alluvial Rhône aquifer is heterogeneous and mainly built up by highly permeable coarse-grained quaternary gravels and sands. The thickness of the alluvial aquifer cannot be determined because bores are not reaching deep enough. For the modeling study, the thickness is estimated to be 40 m. This corresponds to the maximum explored depth (in section 5).

2) The presence of a fine matrix in the generally coarse-grained streambed sediments implies that the clogging of the streambed postulated by previous research occurs as inner colmatation, i.e. by the deposition of fine sediments within the coarse-grained material. Outer colmatation of the streambed, i.e. the accumulation of fine grained particles on streambed material, is not indicated by field data (drilling cores, sediment samples).

3) Surface water – groundwater (SW–GW) interactions are the major driving force of subsurface hydrology of the Rhône alluvial aquifer. This can safely be concluded by analysis of groundwater flow patterns, of the distribution of hydrophysical and hydrochemical parameters. Besides the Rhône River, drainage ditches are an important element of the SW–GW system.

4) At and near the upstream limit, on the stretch between Charrat and Riddes, at Saillon, at Martigny, at Conthey and at four other places with minor contributions, recharge of the aquifer by lateral inflows from valley slopes and small lateral alluvial aquifers is indicated by piezometric, hydrochemical and hydrophysical data. The hydraulic conductivity of the lacustrine deposits underlying the aquifer is thought to be too low to allow major contributions to aquifer recharge by deep groundwater circulations.

5) The system is largely driven by regional controls, with low water tables in the aquifer downstream of the low permeable Illgraben fan and increasing heads in the downstream direction due to recharge by the Rhône River. At the downstream limit; the low permeable alluvial fan of St-Barthélémy is meant to force groundwater to exfiltrate into the Rhône River.

Chapter 3

Parameter estimation and uncertainty quantification: Overview and preliminary tests

3.1 General

A detailed treatment of the theory of inverse problems and of inverse solution techniques is beyond the scope of this work. This section is limited to a brief introduction that highlights some important aspects.

Solving the inverse problem in hydrogeology consists to an important part in estimating system parameters based on measurements of the system state[9]. Any system property, including distributed parameters such as hydraulic conductivity, specific yield, porosity, boundary conditions and sources/sinks of water, may be estimated. Measurements of the system state commonly consist of steady-state or transient head data, but other variables such as flow and/or concentration may be involved as well. Besides parameter estimation, solving the inverse problem always involves model identification. This refers to identifying the nature of the model, such as governing equations, heterogeneity patterns or the time regime of the system [42]. In principle, an inappropriate representation of one of these items may be identified in the calibration process and subsequently, the conceptual model may be rejected. The question of which model constitutes an appropriate conceptual model is related to the decision of what is considered a good-enough data match and is thus subjective.

According to Neuman [103], inverse solution techniques can be classified as either direct or indirect. In the *direct* approach, model parameters are formally derived by solving the flow equation based on measured heads. The *indirect* approach is essentially an automated version of a trial-and-error procedure that seeks to minimize some error criterion, often termed objective function. Most automated inverse solution techniques are based on the indirect approach. Minimization of the objective function, a mathematical expression that measures the closeness of model outcomes to measurements, is often achieved based on a Gauss-Newton or a gradient search approach. As most inverse problems in hydrogeology are nonlinear, parameter estimation in inverse groundwater modeling is carried out by repeatedly solving the forward problem with iteratively updated parameter values until some termination criterion is met.

Inverse problems in groundwater modeling are commonly ill-posed in the sense of Hadamard, i.e. if there is any solution to them, there is commonly not one unique solution to them but many and/or the solution is highly sensitive to small variations in the input data [41]. Approaches to make ill-posed problems tractable within the framework of a least squares approach are referred to as regularization [104]. The most commonly used methods of regularization of ill-posed problems are Tikhonov regularization and truncated singular value decomposition [105]. Certain iterative

[9] The terms *parameter estimation* and *model calibration* are used interchangeably herein.

solution methods, as for instance the Levenberg–Marquardt algorithm, have regularizing effects on the estimation process, too.

Aside from the above methods, uniqueness can also be achieved by adopting the implicit regularization strategy of using a reduced parameter set. One such method to reduce the number of unknowns is zonation [106]. As an alternative, de Marsily [107, 108] proposed the pilot points method. While zonation has traditionally often been used in groundwater modeling, nowadays the pilot points method has become standard in nonlinear inversion [42]. While originally designed as a parameterization device to reduce the number of parameters and to optimally integrate measured field data of model parameters [107], the pilot points method has been further developed [109-111] and allows the formulation of over-parameterized problems that include a regularization criterion. Regularization may be formulated such that either non-homogeneity [e.g. 112] or the departure of model parameters from their prior information [e.g. 113] is penalized. In this method, the parameters of the inverse problem are assigned to points distributed throughout the model. Parameters of the forward problem are then derived by interpolation from pilot points to the model grid, e.g. based on kriging. Compared to zonation, the pilot points method offers a number of advantages including an easier and more pleasant representation of heterogeneity and releases the modeller from the obligation to define tentative zones of piecewise constancy ahead of the parameter estimation process [112].

In a Bayesian framework, the frequent ill-posedness of inverse problems is faced by identifying a distribution of parameters instead of one single parameter set, as classical parameter estimation methods do. Bayesian methods that are known to correctly quantify the parameter uncertainty arising from the non-uniqueness of solutions to inverse problems are Rejection Sampling and Markov Chain Monte Carlo [114]. Besides these exact methods, other approximate methods exist for quantifying uncertainty, for instance the gradual deformation method [115], the probability perturbation method [116], the simulated annealing method [117] or also the pilot points method, when applied to conditional simulation [110].

Regularized inversion using the pilot points method was adopted herein because it has proven to be robust and flexible and it is furthermore implemented in the widely used and open source code PEST, contrary to the above methods.

3.2 Parameter estimation and uncertainty quantification using PEST

The following sections are intended to provide a brief overview on the solution methods available for regularized inversion and the methods of uncertainty quantification available in PEST. An extensive documentation about underlying concepts and algorithmic details of PEST, including practical considerations of its usage, are extensively documented elsewhere [e.g. 47, 104, 118, 119].

3.2.1 Parameter estimation

In PEST, the solution to the inverse problem is derived based on principles of least-squares minimization. The objective function which PEST attempts to minimize depends on the nature of the considered problem. As far as no regularization is included in the problem, e.g. because it is over-determined, the objective function Φ corresponds to the sum of squared weighted residuals between model outcomes and observation data [47]:

$$\Phi = (\mathbf{c} - \mathbf{Xb})^t \mathbf{Q_m} (\mathbf{c} - \mathbf{Xb}) = \sum_{i=1}^{m} (w_i r_i)^2 \qquad [3.1]$$

with **c** the vector comprising observation data, **X** the model function; **b** is the vector of model parameters, $\mathbf{Q_m}$ a diagonal matrix with squared observation weights w_i, r_i the residuals and *m* the number of observation data.

If more parameters are estimated than can be constrained uniquely by observations, the problem needs to be regularized. If Tikhonov regularization is considered as a regularization mechanism, the estimation is constrained to a unique solution by incorporating prior knowledge of system parameters in the optimization process. This implies that the objective function changes to [47]:

$$\Phi = \gamma \Phi_m + \Phi_r = \gamma (\mathbf{c} - \mathbf{Xb})^t \mathbf{Q_m} (\mathbf{c} - \mathbf{Xb}) + (\mathbf{d} - \mathbf{Zb})^t \mathbf{Q_r} (\mathbf{d} - \mathbf{Zb}) \qquad [3.2]$$

with Φ_m the measurement objective function, Φ_r the regularization objective function, γ a multiplier, **d** the regularization observations, **Z** the matrix expressing the regularization equations and $\mathbf{Q_r}$ a diagonal matrix with squared regularization weights.

In PEST, minimization of Equation [3.2] is achieved by minimizing Φ_r under the constraint that Φ_m is suitably low. In the context of a nonlinear model, minimization of Equation [3.2] is a sequential process in which parameters are iteratively updated. PEST has a number of methods implemented to compute parameter updates, including the Levenberg-Marquardt method, truncated singular value decomposition (TSVD), or alternatively the LSQR method [120] and SVD-assist.

TSVD belongs to a family of subspace methods in which instead of adding prior information to the problem, as is the case with Thikhonov regularization, numerical stability of an ill-posed problem is achieved by reducing the number of unknowns within the problem. Estimable parameters are determined by a singular value decomposition of the Jacobian matrix, the sensitivity matrix of model outcomes with respect to model parameters [121]. Parameter combinations for which the respective singular values are larger than a given threshold are considered estimable and to belong to the solution space. The remaining parameter combinations are assigned to the null space of the problem[10].

Using SVD-assist [123] as the solution method of the inverse problem, super parameters are estimated instead of the native model parameters. Super parameters correspond to projections of native parameters onto the solution space of the problem. The solution space is defined ahead of the optimization process using a singular value decomposition of the Jacobian matrix. This considerably reduces the number of parameters estimated and hence alleviates the numerical burden of calculating the sensitivity matrix. As for the estimation of native parameters, Tikhonov regularization may be included in order to consider the prior knowledge of the modeled system.

Apart from using Tikhonov regularization in any of the above methods, prior knowledge on parameters can be included in constraining the permissible parameter range by limits.

3.2.2 Uncertainty quantification using null space Monte Carlo

As explained by Doherty [119], uncertainties associated with predictions are related to two sources, namely (1) to measurement noise and (2) to structural noise, i.e. noise that arises from the imperfect nature of a model, for instance due to conceptual, spatial and temporal simplifications. PEST provides both linear and nonlinear methods for uncertainty estimation. Linear approaches, based on the analysis of the Jacobian matrix, have the advantage of being computationally more efficient than nonlinear approaches. Outcomes of linear analysis are however in general less exact than those of nonlinear uncertainty analysis. Two nonlinear methodologies of uncertainty quantification are available in PEST, constrained maximization/minimization [124] and a technique for calibration constrained Monte Carlo analysis, referred to herein as the "null space Monte Carlo" (NSMC) method [125]. The second approach is used herein, because it is considered more robust [119].

The NSMC methodology provides an efficient means to produce calibration-constrained parameter sets. The first step of the NSMC methodology consists in the

[10] In linear algebra, the null space of A consists of all vectors x such that Ax = 0 [122].

calibration of the model. Stochastic parameter fields are then created based on a user-supplied geostatistical model, which is deemed to appropriately represent parameter variability. These random parameter sets are then projected to the null space of a linearization of the solution set about the calibration solution. This step is intended to sample the null space about the calibration solution. The solution space component of the random field is then replaced by the solution space component of the calibration solution, while the null space component is retained [126]. In the context of a linear model, this procedure produces parameter sets, whose model outcomes perfectly reproduce the outcomes of the calibrated model. In a nonlinear model however, this results in slightly de-calibrated models. Therefore, NSMC parameter fields generally need to be re-calibrated. In summary, in the context of a non-linear model, the NSMC approach consists in 3 steps: It involves 1) a calibration step, 2) the identification of the null space of the linearized inverse problem and the sampling of it and 3) generally a re-calibration step.

3.3 Comparison of PEST's NSMC with a Bayesian approach

3.3.1 Introduction

In this section, a comparison of PEST's NSMC methodology for estimating parameter uncertainty and Rejection Sampling (RS), a Bayesian approach, is carried out. The comparison of NSMC to a reference method is motivated by the lack of such a comparative study.

At the very beginning, the Bayesian approach used herein is briefly described. We consider a very simple flow model based on five zones. Using this model, potential difficulties in using the NSMC approach are investigated and discussed. A very basic problem is considered. This has the advantage that the problem can be analyzed easily through a graphical representation.

3.3.2 Bayes theorem

The Bayesian approach of parameter inference is extensively described in the literature [127-129]. This section gives a short overview of the approach and serves to introduce the rejection sampling method.

Within this approach, solving the inverse problem consists in seeking the distribution of system parameters conditioned to measurements of the system state. In a Bayesian perspective, the conditional parameter distribution, also termed the posterior parameter distribution, is inferred by updating the knowledge prior to data collection by using the information gained through measurements of the system state. The formal expression of Bayes theorem is:

$$f(\mathbf{m}|\mathbf{d}) = \frac{f(\mathbf{d}|\mathbf{m})\, f(\mathbf{m})}{f(\mathbf{d})} \qquad [3.3]$$

where $f(\mathbf{m}|\mathbf{d})$ is the conditional parameter distribution, $\mathbf{m}$ is a vector of unknown system parameters, $\mathbf{d}$ is a vector of measured data of a system state variable, $f(\cdot)$ denotes a probability density function and $|$ indicates conditionality.

The prior knowledge on system parameters is encapsulated in the prior parameter distribution $f(\mathbf{m})$. Although efforts have been made to derive objective priors, its choice remains subjective most of the time [130]. Updating of the prior information is mathematically done by a convolution with $f(\mathbf{d}|\mathbf{m})$, often referred to as the likelihood function ($L(\mathbf{m})$). It defines the probability of measuring observations of the system state $\mathbf{d}$ given that a certain set of model parameters $\mathbf{m}$ is true. The likelihood expresses the correspondence of model outcomes with measurements of the system state and can be regarded as a measure of the closeness of a given parameter set $\mathbf{m}$ to the true system parameters. Different likelihood functions can be chosen. The choice can be informed by knowledge of the structure of measurement errors, or assumptions

on it, or can be subjectively taken [131]. The term $f(\mathbf{d})$ describes the probability of observing the data $\mathbf{d}$.

3.3.3 Bayes theorem by the rejection method

Several numerical techniques of Bayesian inference exist. Within stochastic methods, the family of Markov Chain Monte Carlo (MCMC) methods ranges among the most widely used, despite a number of practical issues related to the convergence of Markov chains. Alternatively, more basic methodologies can be used if models are not too complex, for instance Rejection Sampling (RS) which was used for this comparative study. Compared to MCMC methods, RS has the advantage of yielding uncorrelated and independent samples of the posterior [114]. It does furthermore not require identifying the initial burn-in period and throwing away respective samples, a requirement commonly encountered when using MCMC methods. RS demands hence less attention regarding convergence issues and its implementation is straightforward.

RS can be used to generate samples from any target probability density function (PDF) that can be evaluated up to a proportionality constant [114]. The main idea is to draw a candidate sample from a relatively simple proposal PDF and then to apply a test to decide whether to accept the sample or not. The decision is based on the compatibility of the sample with measurements of the system state, which is – as stated above – evaluated through a likelihood function. The principle of RS can be understood, when Bayes equation [3.3] is written as:

$$\frac{f(\mathbf{m}|\mathbf{d})}{af(\mathbf{m})} = \frac{L(\mathbf{m})}{af(\mathbf{d})} \qquad [3.4]$$

If a value a is found such that $af(\mathbf{m}) \geq f(\mathbf{m}|\mathbf{d})$ for all $\mathbf{m}$, the denominator on the right of Equation [3.4] is equal to the maximum value that can be achieved by $L(\mathbf{m})$ (L_{max}). Accepting a sample $\mathbf{m}$ with the probability expressed through Equation [3.4] then allows to sample from $f(\mathbf{m}|\mathbf{d})$.

Practically, $f(\mathbf{d})$ is not known and the estimation of a is made via an estimate of the maximum likelihood $L_{max} = af(\mathbf{d})$ in the RS method. The requirement to estimate an adequate value of L_{max} is the main limitation of RS [132]. Note that a high value of L_{max} causes the method to be inefficient, a too low value leads to a wrong target distribution. More generally, the efficiency of RS depends strongly on how well the proposal PDF approximates the target PDF. If the first is a close envelope of the latter, RS is efficient. There are however no general methods to construct adequate proposal PDFs and RS is generally very inefficient. Highly parameterized models thus become practically intractable. Here, this method is used, because it is easy to implement and yields a correct sample of the posterior PDF.

The RS scheme that we adopted herein consists of four steps.

1. It begins by drawing a sample from the prior distribution of model parameters.
2. Then one assesses the acceptability of the sample by evaluating the likelihood function $L(\mathbf{m})$ based on residuals between model outcomes and conditioning data.
3. The probability of accepting the sample is then computed as the ratio of the likelihood $L(\mathbf{m})$ to an estimate of the maximum likelihood L_{max} that is expected to be encountered during the sampling procedure.
4. Finally a uniform random number u drawn in [0, 1] is compared to the relative likelihood $p = L/L_{max}$. If $p \geq u$, the sample is accepted as a draw of the posterior distribution, otherwise, it is rejected. The process is repeated until the posterior distribution has been sampled sufficiently.

3.3.4 Convergence analysis of sample moments

We analyzed convergence of constraint Monte Carlo simulations by assessing the stability of statistical moments of the posterior distribution of parameters. Stability was on the one hand assessed qualitatively by visual inspection of plots of running means and variances versus the number of accepted simulations. Furthermore it was assessed via uncertainties of sample moments, which were estimated following the methodology proposed by Ballio and Guadagnini [133]. This method uses confidence intervals for the first two statistical moments as an indicator of the uncertainty associated with the computed sample mean and variance. If the sample mean follows a normal distribution, the confidence intervals for the sample mean [3.5] and the variance [3.6] can be estimated:

$$Pr\left[\bar{\Re}_N - t_{N-1}\left(1-\frac{\alpha}{2}\right)\frac{S_N}{\sqrt{N}} \leq \mu \leq \bar{\Re}_N + t_{N-1}\left(1-\frac{\alpha}{2}\right)\frac{S_N}{\sqrt{N}}\right] = 1-\alpha \qquad [3.5]$$

$$Pr\left[\frac{N-1}{\chi^2_{N-1}(1-\alpha/2)}S_N^2 \leq \sigma^2 \leq \frac{N-1}{\chi^2_{N-1}(\alpha/2)}S_N^2\right] = 1-\alpha \qquad [3.6]$$

where $1-\alpha$ is the probability that the value of the ensemble mean μ (or variance σ^2) lies within the confidence interval around the sample mean $\bar{\Re}_N$(or variance S_N); N is the number of accepted simulations; $t_{N-1}(p)$ is the p-quantile of the Student distribution with (N–1) degrees of freedom; $\chi^2_{N-1}(p)$ is the p-quantile of the chi-square distribution with (N–1) degrees of freedom. We plotted confidence intervals calculated from Equations [3.5] and [3.6] on top of running moments in order to refine the assessment of the stability of statistical moments.

3.3.5 A simple groundwater flow model

3.3.5.1 Introduction

For this comparative exercise, we first built the simple 1D flow model represented in Figure 22. Using this model, we compared the results of an uncertainty analysis using different implementations of the NSMC methodology with results from RS on the one hand and with results from a global optimization on the other. The prime purpose of this study was a methodological comparison of uncertainty associated with model parameters. We completed the comparison in examining how the parameter uncertainty affected the estimation of predictive uncertainty.

3.3.5.2 Problem setup

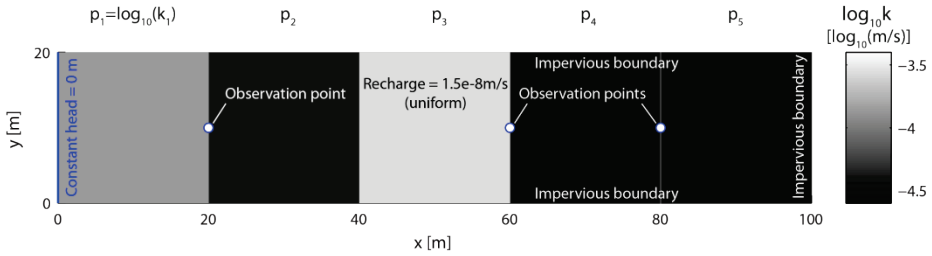

Figure 22 : Setup of the synthetic groundwater flow model.

Steady state groundwater flow in a single-layer unconfined aquifer was simulated on a 1 x 5 grid of square 20 x 20 m cells. A constant head boundary of 0 m was specified on the left side of the model. The right, top, and bottom model limits formed no flow boundaries conditions. We applied a uniform recharge of 1.5e-8 m/s on the model domain using a source term. Hydraulic conductivity was parameterized on a cell-by-cell basis. It was the only variable to be estimated in the inverse problem. As the inset in Figure 1 indicates, logarithms (to base 10) of the hydraulic conductivities (**p**) were estimated in the inverse problem rather than native parameters (**k**). A reference parameter set was created by randomly drawing 5 samples from a uniform distribution in [-5.5, -2.5]. We created conditioning data by performing a forward model run based on reference parameters. Hydraulic heads at $x = 20$, 60 and 80 m were then used to condition the inverse problem. Predictive uncertainty was evaluated with regard to hydraulic heads at $x = 40$ m (h_{40}).

3.3.5.3 Uncertainty estimation using rejection sampling

Likelihood function

Observation data was contaminated by normally distributed and independent random errors with a uniform standard deviation ($\sigma = 0.02$ m) and an expected value of zero. Under these circumstances the likelihood function $f(\mathbf{d}|\mathbf{m})$ takes the form:

$$f(\mathbf{d}|\mathbf{m}) = L(\mathbf{m}) = \prod_{i=1}^{m} f(d_i|\mathbf{m}) \qquad [3.7]$$
$$= \prod_{i=1}^{m} \frac{1}{\sqrt{2\pi\sigma^2}} exp\left(-\frac{\varepsilon_i^2}{2\sigma^2}\right)$$
$$= \frac{1}{(2\pi\sigma^2)^{m/2}} exp\left(-\frac{\sum_{i=1}^{m}\varepsilon_i^2}{2\sigma^2}\right)$$

with σ the measurement error, $\varepsilon_i = (\mathbf{Gm})_i - d_i$ the residual between observation d_i and the corresponding model outcome, $\mathbf{G}$ the mathematical model, $\mathbf{m}$ the model parameters and m the number of observations. We used a value of $L_{max} = 1$ as a maximum value for the likelihood function in this synthetic example.

Prior distribution

We aimed at assigning an equal probability to each portion of the parameter space, i.e. we wanted to use a prior distribution that would not favor some parameters over others. Tarantola [127] terms such a distribution *homogeneous.* He shows that for positive parameters that occur as reciprocal pairs (as for instance conductivity and resistivity) the homogeneous probability distribution corresponds to a uniform distribution of the logarithm of the parameters. Log-transformation of such parameters, which he terms *Jeffreys parameters,* leads to a definition of distance in parameter space that has the desirable properties to be invariant under translations and rotations and to treat symmetrically the pairs of parameters. This is the very reason why hydraulic conductivity was log-transformed in this study.

We considered the same prior distribution as the one, from which the reference parameters had been drawn. Knowing the true prior is, of course, a favorable setting that is typically not encountered in practice. In real-world modeling problems, a badly chosen prior may for instance not even encompass the “true” parameter set.

Prior uncertainty by unconstrained Monte Carlo

In order to evaluate the variability of flow solutions induced by variation of the model parameters, an unconstrained Monte Carlo analysis was first performed. This allowed furthermore defining an a priori predictive uncertainty for h_{40}. Numerical values of model parameters were created according to the prior distribution specified above using a random number generator in MATLAB [134]. Numerical flow simulation was carried out using a MATLAB code based on the finite element approach. The notion 'unconstrained' means that contrary to the remainder of this study, the procedure does not include conditioning to measurement data.

3.3.5.4 Uncertainty estimation using PEST

Calibration

The first step in the NSMC methodology for uncertainty analysis is model calibration. Calibration here was implemented using PEST [47] employing TSVD to minimize the objective function [47]:

$$\Phi = \sum_{i=1}^{m} (w_i r_i)^2 \qquad [3.8]$$

with r_i the residuals between model outcomes and observation data, w_i the weights of observation data and m the number of observation data.

Procedures for estimating parameter uncertainty

Uncertainty analysis using PEST was carried out in four different ways herein. The first three variants correspond to different implementations of the NSMC methodology. In a linear model context, the NSMC method produces parameter sets, which calibrate the model to the same degree as the calibration parameter set chosen as the base for the null space projection. Applying the NSMC methodology in nonlinear models corresponds to exploring the null space of a local linearization of the nonlinear problem. Draws from the null space, itself a linear subspace, do generally not calibrate the model and at least one re-calibration step is usually required. The three different implementations of the NSMC procedure tested herein differ in the manner in which drawing from the null space was accomplished and/or in how re-calibration was accomplished. The variants are only briefly summarized in this section; a more detailed description of the different implementations of the NSMC procedure follows in the next two subsections.

The *first* variant corresponds to the "standard" NSMC procedure as suggested in Doherty [119][11]. In the *second* variant, simulations of measurement noise were added to calibration data prior to undertaking post-NSMC-re-calibration. Consideration of measurement noise is often not crucial in real case models, because in reality measurement noise is often dominated by structural noise [135]. It may however have its place in this methodological comparison based on a synthetic case. In the first and the second variant, uncertainty analysis was performed by exploring the null space about a single calibrated solution. It is known that in nonlinear models contexts, the NSMC methodology does not necessarily yield parameter sets which constitute a sample of the posterior PDF in a strictly Bayesian sense [136]. This problem may be addressed by repeating the NSMC procedure about several calibrated solutions [137].

In the *third* variant, we propose a novel approach to address the problem of model nonlinearity. We designed the uncertainty analysis as a sequence of repeated null space projections with subsequent re-calibrations. Along this sequence, the null space is continuously updated by re-calibration steps (see also Figure 29b and associated text).

In the *fourth* variant, a global optimization was performed by running local optimizations from multiple starting points (MSP). This method has been widely applied to quantify uncertainty in parameter estimation problems with pilot points parameterization [137]. As in the second variant, measurement noise was explicitly taken into account in the third and fourth variant. The following table summarizes the different variants of uncertainty analysis using PEST. Note that the table doesn't mention the very first step of all NSMC procedures, which consists in finding a particular solution by calibration.

Table 2 : Variants of uncertainty analysis using PEST

Var.	Description	Procedure	Null space draws	Meas. noise
1	Standard NSMC	1) Sample null space (NS) at 1 solution → 2) Re-calibrate	Project a sample of the prior onto NS	no
2	" with noise	"	"	yes
3	Sequential NSMC	1) Draw from NS → 2) Re-calibrate + update NS → 1)	Directly draw from NS	yes
4	MSP	1) Sample prior → 2) Calibrate	-	yes

[11] NSMC method 1 – Using the existing parameterization scheme.

Sampling the null space

In the *first* and *second* implementation of the NSMC procedure, drawing from the null space was undertaken by projecting random parameters onto the null space. We used a random number generator to create a sample of the same uniform distribution that had been used in the Bayesian approach. Then, we projected these random parameters onto the model null space and added them to the solution space component of the calibration parameter set[12]. In the *third* variant, the null space was sampled in a different manner because, as the following example illustrates, the drawing procedure used in variants 1 and 2 may unwittingly lead to an inhomogeneous sampling of the null space (Figure 23a–c).

> Consider the underdetermined linear problem $\mathbf{Xp} = y$ where $\mathbf{X}$ has dimensions 1 x 2, $\mathbf{p}$ is a 2 x 1 matrix and y is a scalar. As described above, the procedure begins by the search for a solution $\mathbf{p_0}$. It continues by drawing random parameter sets from a given distribution. In this example we draw from a uniform distribution bounded by [$\mathbf{p}^{min}$, $\mathbf{p}^{max}$] (Figure 23a). These random parameters are then projected onto the null space and added to $\mathbf{p_0}$, the calibration parameter set (Figure 23b). Parameters that fall outside the parameter bounds are not considered, of course. Figure 23c illustrates that a larger number of random parameters maps to the area denoted with "A" than to the area denoted with "B", when subjected to projection onto the null space translated to $\mathbf{p_0}$ ($\mathbf{N_p}$). This means that $\mathbf{N_p}$, is not sampled homogeneously, as it might be intended to be.

In the *third* implementation of the NSMC procedure, we therefore directly drew from $\mathbf{N_p}$ instead of projecting random parameters onto it. The only difficulty to attain this resides in the requirement to limit the sampling of the null space to the domain within the parameter bounds. We limited ourselves to solving this challenge in an approximate way that is outlined in Figure 23d–e: First all corners of the hyperbox built by parameter bounds are projected onto $\mathbf{N_p}$, the null space translated to the current solution $\mathbf{p_i}$. Here the index "i" refers to the sequential character of the procedure. An individual of $\mathbf{N_p}$ is then drawn from $\mathbf{p_i} + \mathbf{V_2 u}$ with $u_i \in [-d_j, d_j]$, where d_j is the maximum distance between the current solution and the projected corners, j indexes corners of the hyperbox of parameter bounds and i is the index of basis vectors $\mathbf{v_2^i}$ of the null space $\mathbf{V_2}$. Note that this technique ensures full coverage of the null space within the range limited by parameter bounds. However, it produces individuals from

[12] Using the PEST utility PNULPAR

outside the parameter bounds, too (Figure 23e), a drawback that it shares with the traditional null space sampling method. This may yield the sampling inefficient in high

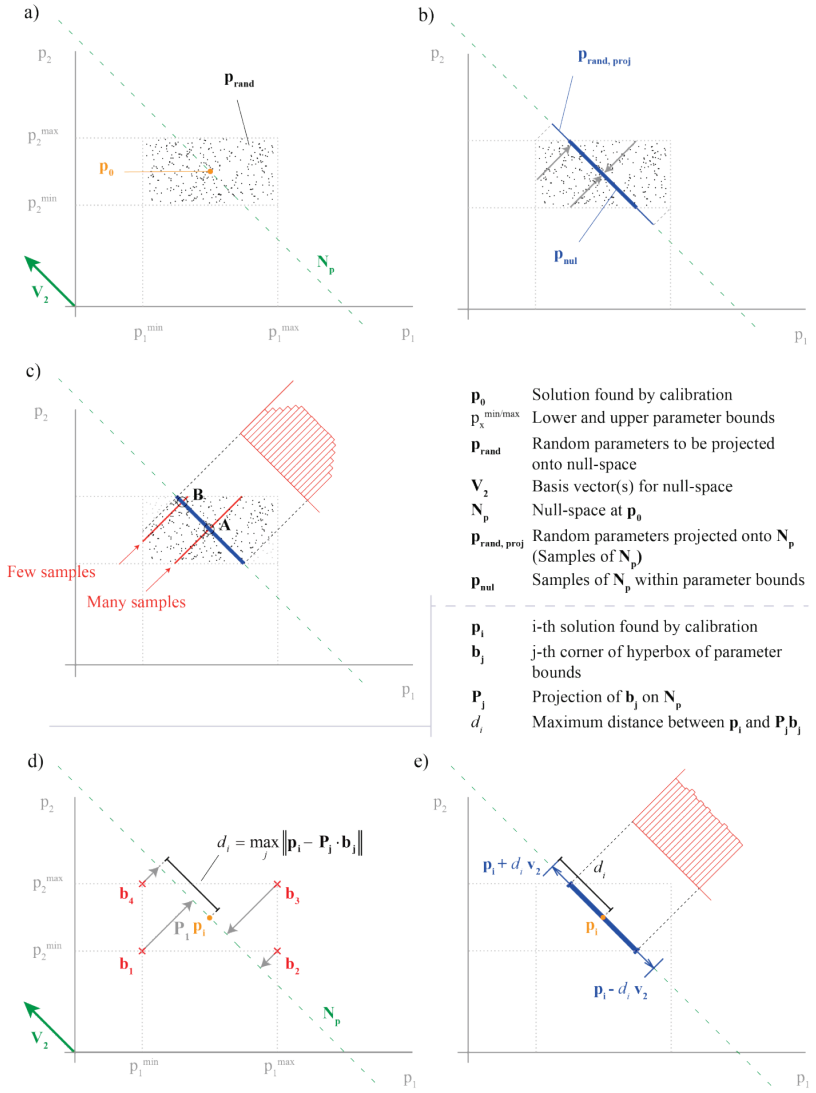

Figure 23 : Upper part: Sampling of the null space by projection of random parameters: a) Find a solution, create random parameter sets; b) Project random parameter sets to null space and add them to the solution; c) Resulting histogram of a sample of the null space at the solution; Lower part: Direct sampling of the null space: d) Project corners of the hyperbox built by parameter bounds onto the null space at the solution; e) Draw from the null space at the solution on a range defined by the maximum distance between the current solution and the projected corners; Resulting histogram of a sample of the null space at the solution.

dimensional problems. Also, computation of all possible combinations of parameter bounds and their projection to the null space may quickly become a time-demanding task if more than a few variables are involved.

In order to be able to control the size of the null space steps, we introduced an additional variable: the maximal step size in terms of parameters which have a component lying in the solution space (l_s). In the results presented herein, we drew from the null space according to $\mathbf{p_i} + \mathbf{V_2 u}$ with $u_i \in [-l_s, l_s]$ and $l_s = 1$.

Re-calibration

In the first variant, measurement noise was accounted for by defining a minimum threshold for the objective function in accord with measurement noise. Once the measurement objective function fell below this threshold, the objective function was not further reduced. As in all other variants too, we weighted observation data by the (dimensionless) inverse of measurement noise and provided PEST with a threshold value[13] to implement this strategy. According to the definition of the measurement objective function (3.7) a value of 35 × 1 = 35 was chosen, where 35 is the number of observation data and 1 is the mean weighted residual. This strategy ensured that the model-to-measurement misfit of the resulting simulations was in the order of measurement noise. In addition to this, measurement noise was explicitly taken into account in all other variants. This was done by adding white Gaussian noise with a uniform standard deviation of $\sigma = 0.02$ m to conditioning data prior to undertaking post-NSMC-re-calibration.

Re-calibration was undertaken by adjustment of the solution space components of random parameters. Subdivision of the parameter sets into solution space and null space components was achieved by singular value decomposition of the Jacobian matrix, which contains sensitivities of model outcomes to parameters at the solution found in the calibration step. The dimensionality of the solution corresponds to the number of significantly non-zero singular values found through singular value decomposition.

Here, the dimension of the solution space agreed with the number of observation points (= 3). This is the maximum possible dimensionality of the solution space. Because individual observation points often contain redundant information, the solution space dimensionality is generally lower than the number of observation points. Note that the dimension of the null space is given by the difference between the dimension of the parameter space and the solution space dimensionality. Here, the null space hence had a dimension of 5 – 3 = 2.

[13] via the variable PHISTOPTHRESH

3.3.5.5 Results and discussion

Unconstrained Monte Carlo

Figure 24a shows nodal heads resulting from an unconstrained Monte Carlo analysis based on 10'000 realizations of hydraulic conductivity. Inspection of the figure shows that the model outcomes display a large scatter and do, as expected, generally not coincide with the conditioning data. Figure 24b depicts the histogram for h_{40} as predicted by the unconstrained Monte Carlo analysis. The figure reveals that the parameters selected as the reference parameters lead to a prediction that has a relatively high probability to occur.

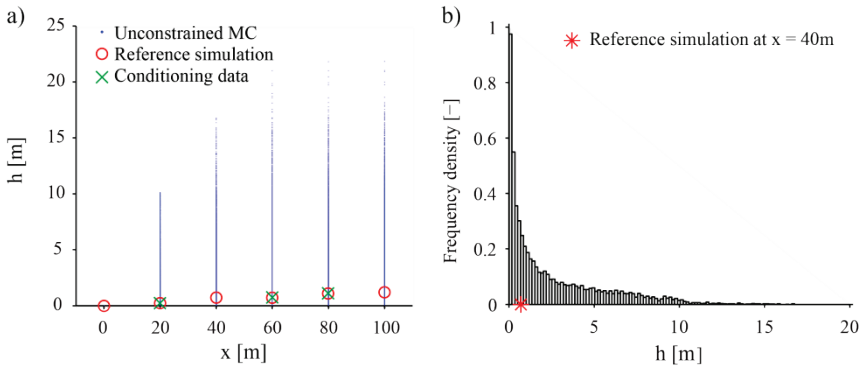

Figure 24 : a) Hydraulic heads resulting from 10'000 unconstrained Monte Carlo simulations; b) Histogram of predicted heads at x = 40 m (h_{40}) based on the unconstrained Monte Carlo analysis.

Convergence assessment for RS

An extensive suite of nearly 2e+8 simulations was performed to generate a sample of the posterior by RS (sample size: 2638). Figure 25 shows the running means and variances of accepted parameters together with the respective confidence intervals calculated according to Equations [3.5] and [3.6]. After several hundred accepted simulations, the moment curves appear to be more or less stable. By about 1'000 accepted simulations, the width of the confidence intervals has sufficiently decreased for our purpose and the comparison with the NSMC methodology and the MSP approach was therefore undertaken based on a sample size of 1'000.

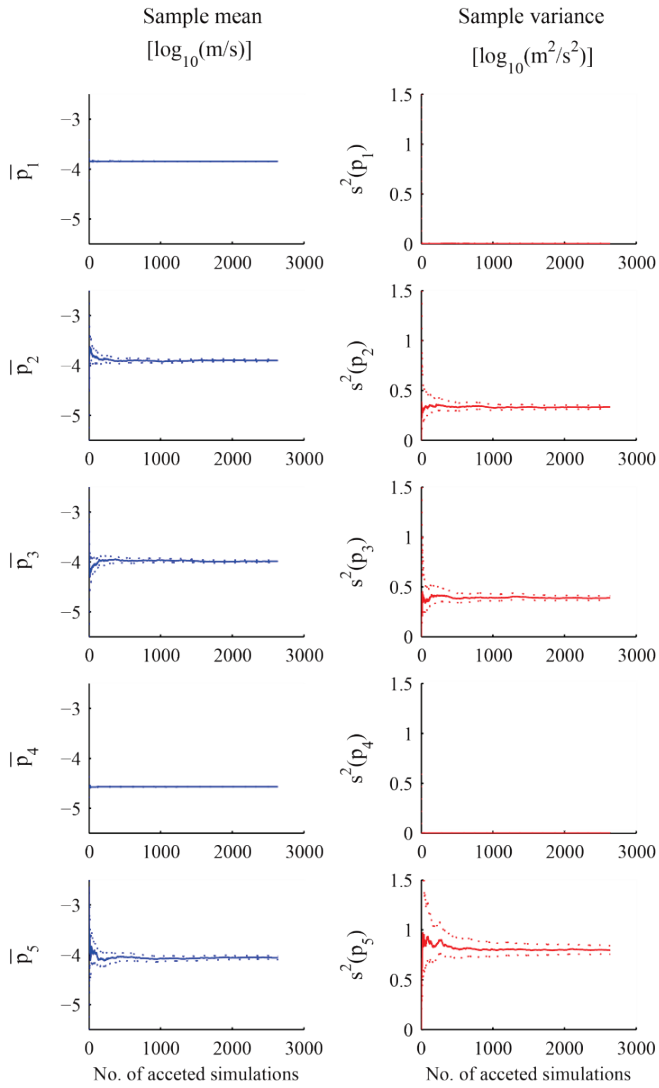

Figure 25 : Evolution of posterior means (left) and variances (right) of hydraulic conductivity and the respective 95% confidence intervals as a function of increasing number of accepted parameter sets.

Model performance

Figure 26 represents the hydraulic heads arising from parameter sets that were accepted by RS. Note that in spite of the good agreement between model outcomes at observation points and conditioning data, predictive uncertainty remains considerable.

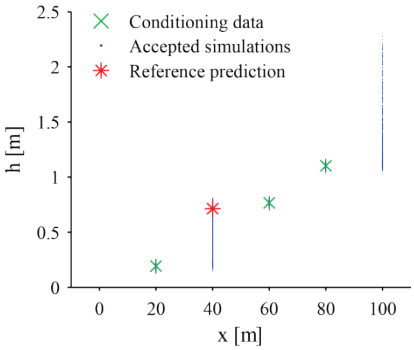

Figure 26: Hydraulic heads of 1'000 simulations accepted by RS.

Histograms of the objective function based on the residual heads at observation points are compared in Figure 27. Except from the first, all variants yield very similar distributions of objective functions, to the point that they can barely be distinguished on the plot.

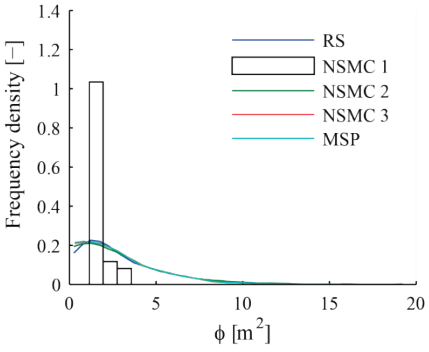

Figure 27 : Assessment of model performance using parameter sets by RS, by different NSMC procedures and by MSP.

Parameter uncertainty

Based on the experience on convergence of the posterior sample made with RS, uncertainty analysis in all variants involving PEST was done on 1'000 parameter sets. Figure 28 compares the posterior parameter distribution given by RS with parameter

distribution arising from uncertainty analyses conducted with PEST. Note that the range of the x-axis represents the width of the prior distribution. Figure 28 thus immediately pictures the worth of conditioning data in reducing the parameter uncertainty. Inspection of the results given by RS (Figure 28a) shows that the uncertainty associated with parameters p_1 and p_4 has been significantly reduced by constraining the inverse problem by observation data. This is also indicated by their low sample variance in Figure 25. In comparsion, p_2 and p_3 are only moderately informed by the conditioning data and as a consequence, the respective parameter uncertainty remains relatively high. From the last plot of Figure 28a one could conclude that the data doesn't contain any information with regard to parameter p_5 as its uncertainty remains the same as in the prior. It should however be noted that the prior is most probably not fully encompassing the posterior distribution and there might possibly be some information in the data regarding p_5 that would solely be perceived outside of the parameter bounds. It is worth noting that the reference parameter values are always included in the posterior as given by RS (Figure 28a). For parameters p_1, p_2 and p_4, the modes approximately correspond to the reference values. The low uncertainty of p_1 and p_4 can be explained by the vicinity of conditioning data, of the constant head boundary and the observation point at $x = 20$ m in the case of p_1 and the observation points at 60 m and 80 m in the case of p_4.

Figure 28b reports parameter distributions that result from the standard NSMC procedure. A comparison with the results of variant 2 (Figure 28c), where measurement noise was added before re-calibration, reveals that halting the optimization process at a threshold value is not sufficient to guarantee propagation of measurement noise into parameters (s. plots for p_1 and p_4). For parameters p_1, p_2, p_4 and p_5, results of variants 1 and 2 are at large consistent with results by RS. The tail of the distribution of parameter p_3 towards high values however is not detected in variants 1 and 2. Results of the sequential NSMC procedure (Figure 28d) as well as of MSP (Figure 28e) compare very well to those by RS.

In general, the non-unique set of solutions to an inverse problem geometrically corresponds to some curve or surface in parameter space. Figure 29 represents solution sets for this synthetic case in parameter space (p_1, p_2, p_3). Figure 29a reveals that only a part of the parameter space can be explored by the gradient-based optimization algorithm implemented in PEST, when starting from the null space of the linearized problem at the solution $\mathbf{p_0}$. This explains the undersampling of p_3 observed in implementations 1 and 2 of the NSMC procedure. Obviously, the re-calibration step brings all parameters sets of the null space at $\mathbf{p_0}$ with values of $p_3 < -4.0$ to an area with values of p_3 of a little below -4.0. This causes the peak in the histograms of p_3 in Figures 28b and 28c.

The problem of the undersampling of p_3 in implementations 1 and 2 of the NSMC procedure is related to the nonlinear posterior correlation of p_2 and p_3 illustrated by the curve of the solution set in Figure 29a. Figure 29b indicates that the sequential NSMC procedure tested in variant 3, manages to deal with these challenging circumstances. It should be mentioned that the sequential NSMC procedure tends to be computationally more expensive than the standard NSMC procedure, since the computation of the Jacobian matrix – a process which demands as many model runs as there are estimated parameters – is mandatory for updating the null space, while it is not imperatively required in the standard NSMC procedure.

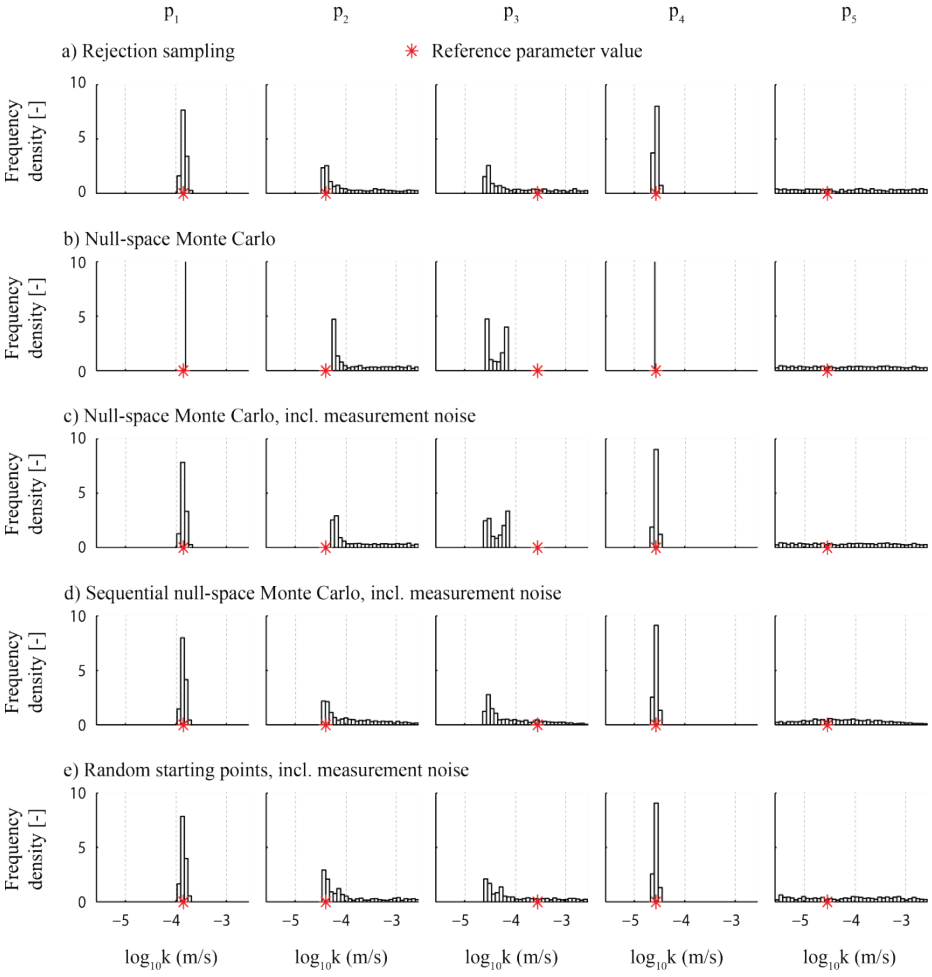

Figure 28 : Comparison of parameter distributions arising from the different methods of uncertainty estimation tested herein.

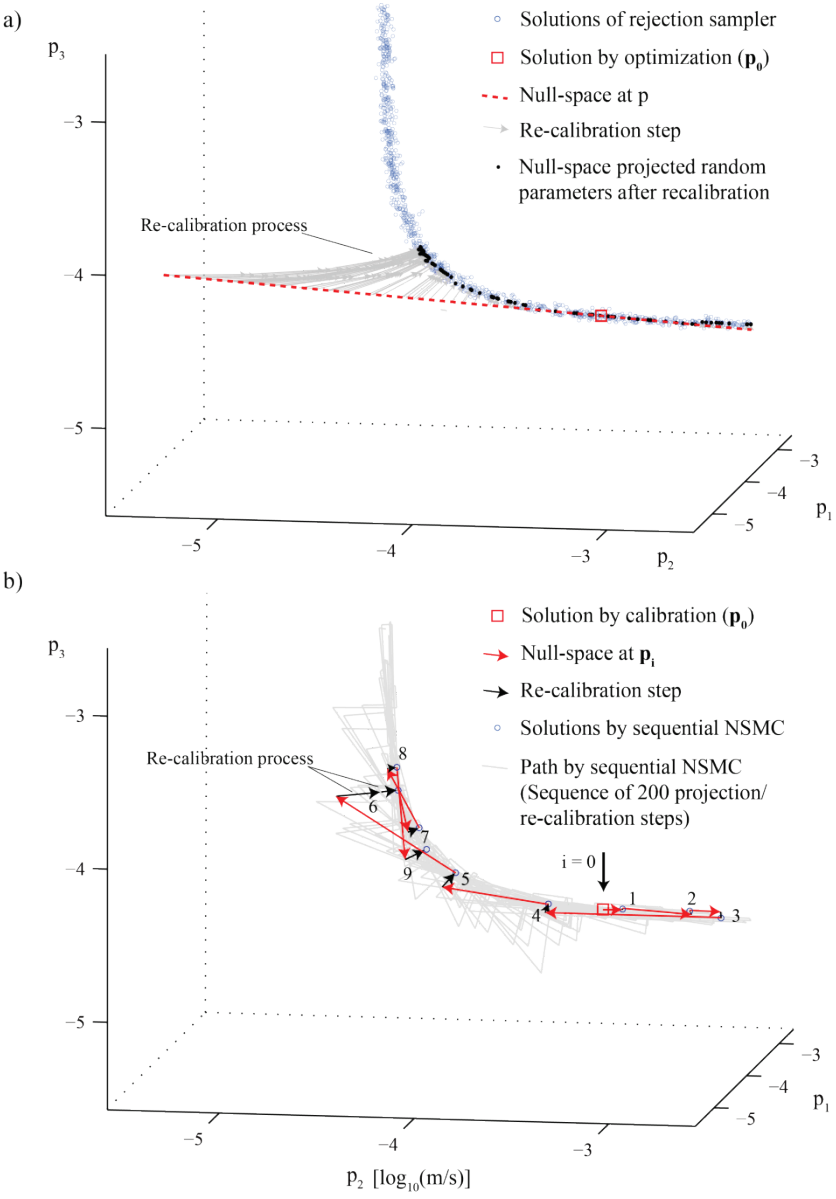

Figure 29 : Realizations of NSMC procedures in parameter space (p_1, p_2, p_3): a) Procedure as implemented in variant 1 (superposed to solutions found by RS); b) Procedure as implemented in variant 3 (the first 10 members of the sequence are highlighted).

However, the burden may be alleviated by the fact that the computation of the Jacobian matrix is not always necessary: Provided the sequence runs across a "flat" area of the solution set, the definition of the null space can be passed from one step to the next throughout the sequence. Here, in about 27% of the steps, the null space definition of the previous step could be re-used. Note also that thanks to the choice of relatively short null space steps, re-calibration could be achieved within a few optimization runs, as indicated by the length of the re-calibration steps in Figure 29b.

Computational burden

Table 3 reports the number of model runs required for finding 1'000 solutions that reproduce the conditioning data. Only those techniques are considered which correctly sampled the posterior PDF. In this example, sequential NSMC was about 10'000 times more efficient than RS and about four times more efficient than MSP.

Table 3 : Efficiency of methods reproducing correctly the posterior PDF

Method	Model calls for 1'000 parameter sets
Rejection sampling (RS)	71'724'891
Multiple starting points (MSP)	32'726
Sequential NSMC	8'830

Predictive uncertainty

As stated earlier, the predictive uncertainty for h_{40} remains considerable, despite the good data fit of model outcomes using accepted parameter sets. As a comparison between Figures 24a and 30 reveals, the predictive uncertainty is nevertheless clearly lower than if measurements had not been included: while values range between 0.02 and 16.76 m in the unconstrained MC analysis (Figure 24a), the range of predictions using the posterior parameter distribution is reduced to 0.15 – 0.81 m (Figure 30). Interestingly, a bimodal distribution can be observed for h_{40} with one mode at 0.22 m and another mode at 0.74 m. Whereas the NSMC implementations based on a single solution clearly fail at reproducing the upper mode and hence underestimate the predictive uncertainty (Figures 30a and b), the results from sequential NSMC and the MSP approach are in good agreement with results from RS (Figures 30c and d). The upper mode corresponds to simulations with relatively high values of p_3 and with relatively low values for p_2, as indicated by Figure 31. The underestimation of predictive uncertainty in implementations 1 and 2 of the NSMC procedure is thus a direct consequence of the undersampling of p_3 in these variants.

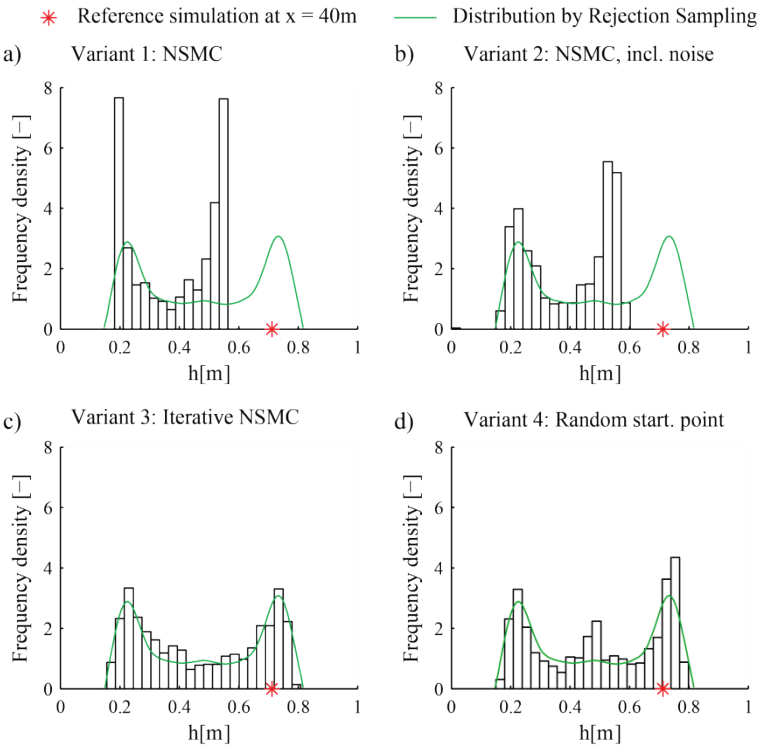

Figure 30 : Histograms of predicted heads at x = 40 m (h_{40}) resulting from different variants of uncertainty estimation by PEST compared to a smoothed histogram of results given by RS.

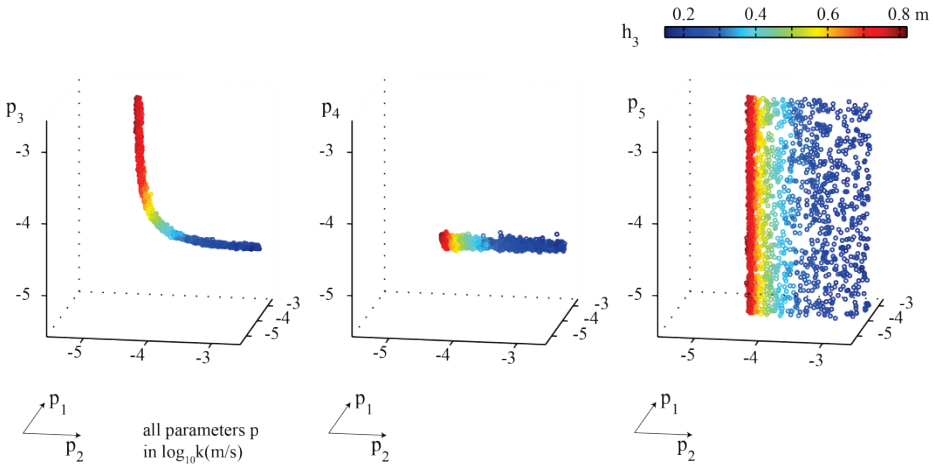

Figure 31 : Set of logarithms of hydraulic conductivities solving the inverse problem according to RS in 3D model parameter space; Points are colored according to the predictive value of h_3.

3.3.5.6 Conclusions

This section compares the Null Space Monte Carlo (NSMC) approach to Rejection Sampling (RS), a Bayesian approach, and to the Multiple Starting Point (MSP) method. Three different implementations of the NSMC procedure were tested herein; two that were based on a single calibrated model and one, where – similar to the MSP method – several calibrated models were used. The methods were applied to a very simple inverse groundwater flow problem comprising only five estimable parameters and three observations, and compared with regard to their estimate of parameter and predictive uncertainty. Predictive uncertainty was evaluated by the estimation of the hydraulic head at a given point. The outcomes of the uncertainty quantification by the RS method were considered as the reference herein. The ability of the other methods to reproduce the results by RS was taken as the criterion to evaluate their reliability in quantifying uncertainty. The comparison was based on 1'000 parameter sets yielded by the different methods. All these parameter sets fulfilled the requirement to belong to a given prior distribution and to produce model outcomes that are consistent with conditioning data.

In this synthetic example, including measurement noise in the re-calibration step proved to be necessary in order to correctly propagate measurement noise into parameters.

We showed that the null space is not necessarily sampled in a homogeneous way, if sampling is undertaken by projection of random parameter sets onto the null space. For low dimensional problems, an alternative method is proposed herein.

This study demonstrated in an illustrative way that in the context of a nonlinear model the NSMC method may underestimate parameter uncertainty, if it is based on a single calibrated model only.

This finding is neither surprising nor is it new. For instance, Yoon, Hart, et al. [137], in their comparative study between the NSMC method and MSP, recently found that the NSMC methodology may provide a computationally efficient alternative to MSP, but only if it is based on multiple initial parameter sets. The implications of a potential underestimation of parameter uncertainty are often not discussed in practical applications, because people are primarily concerned with the quantification of predictive uncertainty rather than of parameter uncertainty. It is however clear that depending on the problem, a wrong estimate of parameter uncertainty may lead to a poor quantification of predictive uncertainty. The example given herein has been demonstrated to be such a case. In this study a new implementation of the NSMC procedure was tested to overcome the difficulties that NSMC displays in a nonlinear context. Uncertainty analysis was designed as a sequential process of null space projection with subsequent re-calibration. This scheme has the advantage to adapt the

search direction (i.e. the direction of the null space steps) in "curved" portions of the solution set, while in "flat" portions of the solution set, it takes profit of the efficiency of the NSMC methodology. In a linear model, the proposed sequential NSMC would hence turn to the standard NSMC procedure. As the MSP approach, sequential NSMC was able to reproduce the results of the uncertainty analysis done by RS. In this example, sequential NSMC demanded about four times less computational effort than MSP. Compared to MSP, sequential NSMC has the advantage to release the modeler from the task to choose different starting points to base NSMC uncertainty analyses on. Clearly, the proposed strategy needs to be tested in other circumstances, too, and it is for instance questionable if it would be more efficient than MSP in problems with discontinuous solutions sets. Systematic tests on the influence of the maximum length of the null space steps would be required, too. It is evident that this parameter is highly influent on the performance of the sequential NSMC procedure both in terms of efficiency and of the capacity to sample form the posterior PDF correctly. Sequential NSMC might possibly be more efficient if this parameter was optimized.

Chapter 4

Numerical flow model of the Rhône alluvial aquifer

4.1 Introduction

The strategy to assess the possible consequences of PR3 for groundwater by a numerical groundwater flow model has been motivated in Chapter 1. This chapter describes how the conceptual model of the Rhône alluvial aquifer presented in Chapter 2 was applied to a numerical framework.

The chapter starts with a short note on why *GroundWater* (*GW* hereinafter) is the selected software to solve the groundwater flow problem. Then a relation between the streambed conductance, an important physical parameter for the current study, and the respective model parameter is developed. The extension of the numerical model and its spatio-temporal discretization are described in section 4.4. Section 4.5 develops how and where boundary conditions were defined. For boundary conditions that are not subjected to parameter estimation, as is the case with extraction rates at pumping wells and river stages, it is then explained how values for boundary conditions were derived.

Chapter 5 will discuss the parameters being estimated, i.e. hydraulic conductivity of the aquifer, stream bed conductance, recharge by precipitation and in- and outflow through outer model limits.

4.2 Numerical code

The numerical model was initially built using *FEFLOW*, a standard software for groundwater flow and contaminant transport modeling. However, it was found that parameter estimation and uncertainty estimation of the highly parameterized model presented herein was computationally intensive and required the parallelization of the estimation process on a Linux cluster. Parallelizing *FEFLOW* was not feasible, given the limited number of *FEFLOW* licenses available at the CHYN[14]. To overcome this problem, the groundwater flow problem was translated to *GW*. *GW* allows to simulate variably saturated flow, mass transport and heat transfer in the coupled surface and sub-surface media using the finite element method [138]. The capacities of *GW* are similar to those of *FEFLOW*.

Steady state 2D groundwater flow in a heterogeneous isotropic unconfined aquifer is considered in the model of the Rhône aquifer (see section 4.4.1 for a justification of the approach). Provided the density of the fluid is homogeneous, transient 2D flow can be approximated by the Boussinesq equation [139]:

[14] Institute of Hydrogeology and Geothermics at the University of Neuchâtel

$$\frac{\partial}{\partial x}\left(\mathbf{K}h\frac{\partial h}{\partial x}\right)+\frac{\partial}{\partial y}\left(\mathbf{K}h\frac{\partial h}{\partial y}\right)+i=S_y\frac{\partial h}{\partial t} \qquad [4.1]$$

where h is hydraulic head (L), t is time (T), i is a fluid source and sink term (LT^{-1}), $\mathbf{K}$ is hydraulic conductivity (LT^{-1}), and S_y is the specific yield (−).

4.3 Streambed conductance and its model parameterization

The relevance of the Rhône River to the underlying alluvial aquifer has already been highlighted in previous chapters. Like other surface water bodies (i.e. drainage ditches, tributaries), the Rhône River was implemented in the model using a leakage boundary (also termed Cauchy or mixed type boundary condition). This type of boundary condition is defined by the water level of the surface water and a transfer coefficient related to the streambed conductance [140]. The streambed conductance is defined as the hydraulic conductivity of the streambed divided by its thickness [27]. The flux across the boundary between the streambed and the aquifer is calculated from the head loss between the specified surface water level and the model-calculated head in the aquifer. It is assumed that storage is negligible in the streambed and therefore the transfers are occurring instantaneously.

GW assumes a linear relationship between nodal flow and head losses. If the river is conceptualized as a single line – as it is herein - and if an unconfined aquifer is modeled, the nodal flow at a river boundary condition as computed by *GW* is:

$$Q=2\varphi\cdot(H-h)\cdot L_N\cdot(h-z_0) \qquad [4.2]$$

where Q (L^3T^{-1}) is the flow across the boundary, φ (T^{-1}) is the transfer rate, H (L) is the hydraulic head in the river, h (L) is the head in the aquifer, z_0 (L) is the base height of the aquifer, and L_N (L) is the range of influence of the modeled grid node. If a linear surface water body is being modeled, the range of influence corresponds to the sum of half the distances to all neighboring nodes which define the river profile (e.g. $L_N = x_1/2 + x_2/2$ in Figure 32). If a surface water body is modeled, the ponderation is a function of its area.

From a conceptual view, the transfer rate φ in Equation [4.2] is related to the streambed conductance in the following manner. Based on Darcy's law, the flow between a surface water body and the aquifer can be estimated by [141]:

$$Q=k'\cdot A\cdot\frac{H-h}{e'} \qquad [4.3]$$

where Q (L^3T^{-1}) is the flow across the streambed, A (L^2) is a contact surface, k' (LT^{-1}) is the hydraulic conductivity of the streambed and $e'(L)$ being its thickness. Using for A the control surface of node N $(A = L_N \cdot W)$ and comparing Equa-

tions [4.2] and [4.3] yields the desired relation between the transfer rate φ and the real-world hydraulic conductivity of the streambed *k'* (Figure 32):

$$\varphi = \frac{1}{2} \cdot \frac{k'}{e'} \cdot \frac{W}{h - z_0} = \frac{1}{2} \cdot \frac{k'}{e'} \cdot \frac{W}{h_s} = \kappa \cdot \frac{W}{2h_s} \qquad [4.4]$$

where $h_s = h - z_o(L)$ is the saturated thickness and κ (T^{-1}) the streambed conductance. The transfer rate can be formulated for inflowing and outflowing conditions by means of specific values, i.e. $\varphi = \varphi_{in}$ if $H > h$ and $\varphi = \varphi_{out}$ if $H < h$.

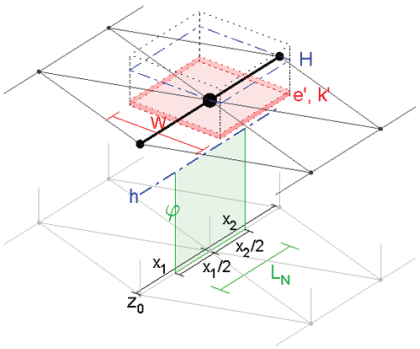

Figure 32 : Parameters relating the real-world streambed conductance to its model counterpart: *H*: head in the river, *h*: head in the aquifer, z_0: base height of the aquifer, L_N: range of influence of the node, x_1, x_2: distances to neighboring nodes, φ: transfer rate, *W*: river width, k': hydraulic conductivity of the clogging layer, e': thickness of the clogging layer.

The relation between the hydraulic parameter and the transfer rate depends on the model type (confined or unconfined), the model dimension, the mesh type (triangular or rectangular), the grid cell size, as well as on the dimension of the river as implemented in the model. Table 4 lists relationships which we derived for 2D confined flow models. If the river is modeled as a 2D feature, the boundary condition is assumed to be running on 3 parallel lines with a uniform spacing Δx (hence the river width $W = 2\Delta x$) and a uniform cell size in the direction of the river axis Δy. Dividing the right hand side of the equations in Table 4 by the saturated thickness readily yields the equations for the unconfined case. Figure 33 presents a comparison between the numerical results of flow calculation at a linear river boundary condition in a 2D unconfined flow model and the analytical results. This test was made to verify the validity of equation [4.2], because the user's guide of *GW* does not detail how flow through the streambed is calculated in such cases. Observed results compare very well with the analytical solution.

Table 4 : Relation between real-world and model parameter of streambed leakage

Dimension of river	Mesh-type	Equation
1D	Rectangular/Triangular	$\varphi = \frac{k'}{2e'} W$
2D	Rectangular	$\varphi = \frac{k'}{2e'} \frac{\Delta x \Delta y}{(\Delta x + \Delta y)}$
2D	Triangular	$\varphi = \frac{k'}{2e'} \frac{\Delta x \Delta y}{\left(\Delta x + \Delta y + 1/2\sqrt{\Delta x^2 + \Delta y^2}\right)}$

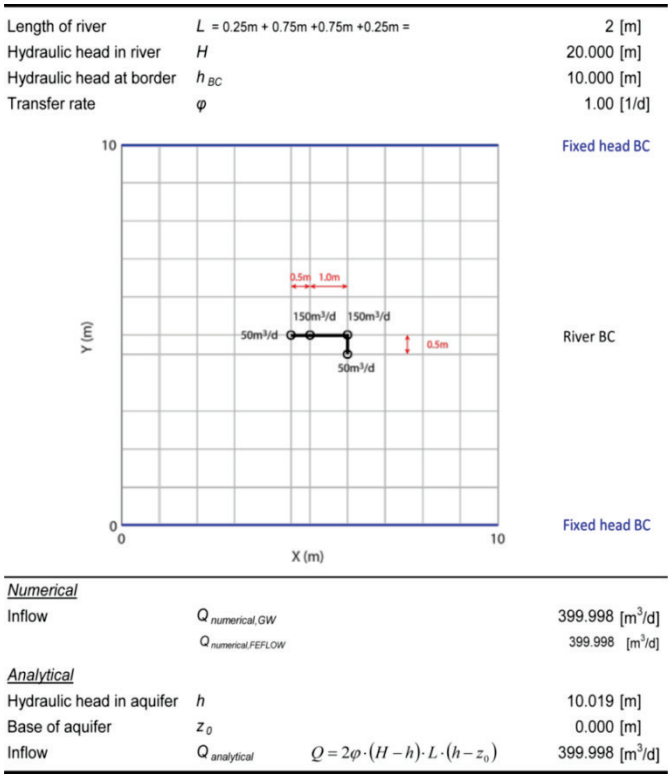

Figure 33: Comparison of numerical and analytical results for flow calculation at a river boundary. The results using *GW* compare very well to those obtained from the analytical solution as well as to those obtained with *FEFLOW*.

4.4 Model discretization

4.4.1 Model limits and dimension

The limits of the Rhône alluvial aquifer are defined by the topographic conditions and by the contacts between the unconsolidated sediments of the alluvial aquifer and the valley slopes, mainly formed by impervious hard rock. These contacts can be easily detected by observing the large contrast in hydraulic conductivity between sediments and hard rock.

At the upstream and the downstream, i.e. at the east and west borders of the model, the model limits cut the flood plain in a curve that follows a contour line of the piezometric surface. Near Martigny and near Vétroz, small alluvial plains running into lateral valleys are cut by the model boundary. Highly permeable alluvial fans are also integrated in the numerical model. Less permeable alluvial fans (e.g. the alluvial fan of La Losentse between km 50 and 55) are not considered because their contribution to the overall hydraulic behavior of the alluvial aquifer is small. Due to their relatively small extent, deposits of the Sierre landslide are also included in the model, even though their hydraulic conductivity is low [67].

As stated in Chapter 2, the alluvial aquifer is underlain by a thick succession of fluvio-lacustrine deposits. They are considered as the base of the aquifer; hence only the uppermost sedimentary unit of post-lacustrine sediments is comprised by the numerical model. Its vertical extent is only vaguely known. We assumed a uniform thickness of 40 m (see conceptual model in Chapter 2).

The 2D geometry of the numerical model is justified upon the large longitudinal and lateral extents of the model compared to the relatively small vertical extent.

4.4.2 Spatial discretization

The software *Triangle* [142] was used to generate a mesh of triangular finite elements. The mesh was conditioned to all inner boundary conditions using lines for drainage ditches and points for pumping wells. Furthermore, the mesh grid was conditioned to observation points for higher accuracy. The mesh contains 54’974 elements and 28’332 nodes, resulting in an average edge length of about 60 m. As a quality measure, 97.9 percent of all triangles meet the Delaunay criterion.

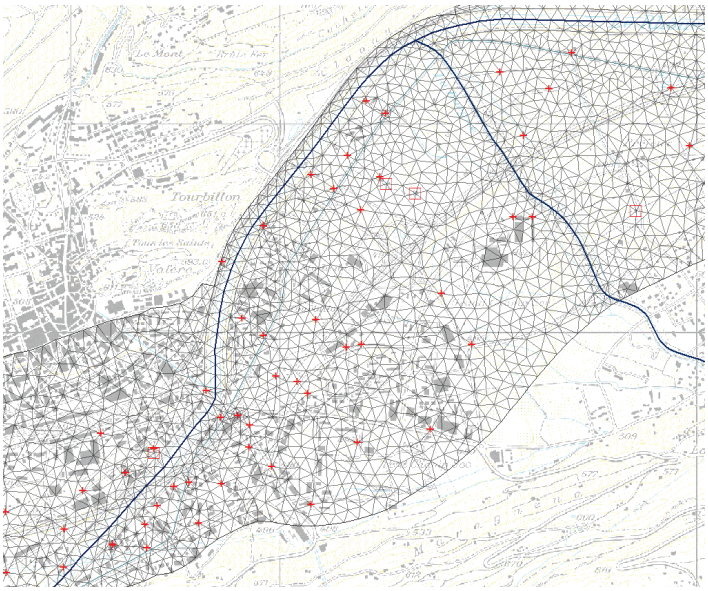

Figure 34 : Representation of the finite element mesh near Sion: The figure indicates the conditioning of the mesh grid to surface waters, pumping wells and to observation points (Background map: Swiss National Map 1: 25'000 (source: Federal Office of Topography)).

4.4.3 Temporal considerations

In most of the calculations, a steady-state regime was considered because the primary goal of the model is to produce long-term predictions. Modeling of the long-term state is based on the assumption that the flow system will return to a stable state in the long run, after the inherent alterations due to restoration works. Seasonal variations of heads will still be present in such a stable future state and natural variations cannot be accounted for when using a steady state model (Figure 35). The shortcoming of such an approach seems however not to be substantial to the needs of the project, because on the scheduled duration of the restoration works (~ 30 years), natural variations are expected to lie within the range of uncertainty related to predictions. Actually, the possibility for other influences on groundwater to arise within such a time horizon must not be neglected and contributes to predictive uncertainty.

It is self-evident, that the postulated re-equilibration process of the system cannot be modeled by simulating transient groundwater flow. Doing that in an appropriate manner requires the modeling of sedimentation processes. Alternative assumptions can be made on the amount of time required to attain a stable state. Here, such assumptions would be highly speculative given the lack of knowledge on the sedimentation processes in the Rhône River at the reach-scale. They were therefore not considered herein.

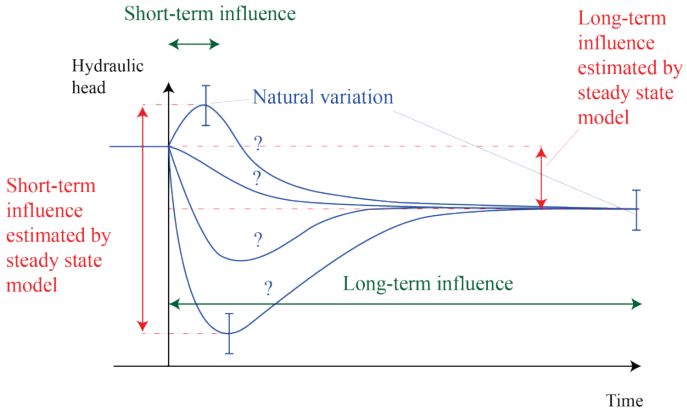

Figure 35 : Sketch illustrating time-dependencies of the groundwater flow problem presented here.

Regarding the short-term behavior, it is believed that worst-case scenarios may be reasonably simulated using a steady state approach, even if the influence of natural variations is not taken into account. This assumption is based on the close hydraulic coupling between the Rhône River and the aquifer, observable through a fast transmission of water level changes in the Rhône River to the aquifer. Less dynamic phenomena like the draining of peat may be addressed through analytical approaches.

One reason for using a transient model could be that transient data possibly contain important information that is not present in steady state data. The gaining of using transient data may however be counterbalanced by the further unknowns that are brought into play and it is difficult to evaluate a priori whether considering transient data would lead the inverse problem more or less unique. Anyhow, a sound parameter estimation with a transient model demands transient boundary conditions, particularly in a case like this, where groundwater flow is highly influenced by surface waters. Transient data, e.g. to model boundary conditions at the Rhône River but also at drainage ditches, was not readily available.

4.5 Boundary conditions

4.5.1 Setting boundary conditions

Outer model boundaries are mainly no flow boundaries, representing the contact of the alluvial aquifer with impermeable hard rock. However, some boundaries where lateral inflow is thought to occur are modeled as prescribed (but unknown) flow boundaries. A prescribed flow is used to model inflow conditions upstream from the model. A prescribed head boundary condition was set at the downstream limit representing the constant head imposed by the river power station at Lavey. As mentioned above, surface waters were modeled by mixed type boundary conditions. Extraction wells were implemented by means of the "well boundary condition" intended for this purpose in *GW* [138]. An areal source term was used to account for effective recharge by precipitation.

Different types of data have been used to identify locations where a boundary condition was set (see Chapter 2). Figures 36a and b summarize how boundary conditions were identified. In Figure 36a dissolved oxygen contents are represented in classes of one or two standard deviations above the mean value[15]. High anomalies of dissolved oxygen were considered as potential indicators for aquifer recharge. Similarly, low and high anomalies of electrical conductivities were regarded as indicators of zones with aquifer recharge. Figure 36b displays electrical conductivities in classes of one or two standard deviations above or below the mean value[1]. The analysis of flow patterns based on contour lines of piezometric heads[16] (Figures 36a), time series analysis of hydraulic heads and knowledge of local hydrogeology completed the process to identify model boundaries. Figure 36c represents the locations and types of boundary conditions employed in the flow model.

[15] Data from HW in 1985.
[16] Mean hydraulic heads during HW (1994 – 2004).

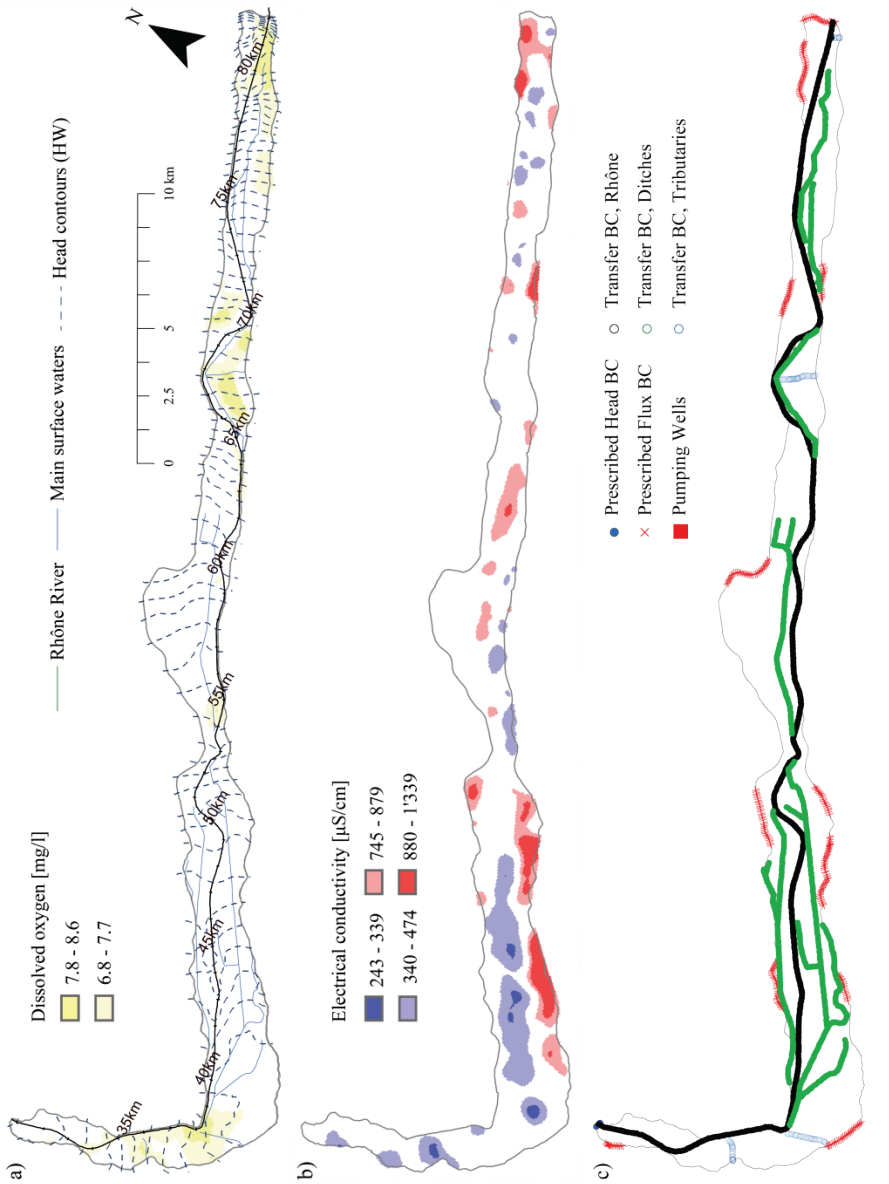

Figure 36 : Simplistic representation of how model boundary conditions are identified: a) Map of dissolved oxygen[17] together with contour lines of piezometric surface[18]; b) Map of electrical conductivity[6]; c) Locations and types of boundary conditions in the model.

[17] Data from HW in 1985.

4.5.2 Surface water levels

4.5.2.1 Rhône River

We used the result of a one dimensional hydraulic model (HEC-RAS) to represent water stages along the Rhône River. The hydraulic modeling was made by Niederer + Pozzi Umwelt AG based on a measurement of stream discharge using cross-sectional profiles at an average distance of about 140 m. From average stages during HW and LW that were available through cantonal authorities (data from PR3 [1]), we calculated average water stages that were used to prescribe the profile of heads at the Rhône River. Heads where calculated according to:

$$M^* = \alpha H_{mean} + \beta B_{mean} \qquad [4.5]$$

where M^* (L) is the estimated mean head, H_{mean} (L) and B_{mean} (L) are the mean water levels during HW and LW. α and β weight the contribution of high and low water levels to the mean. The parameters were determined using mean water levels at Sion and Branson [80, 81] obtaining α = 0.3333 and β = 0.6666. Water stages at cross-sectional profiles were linearly interpolated to mesh nodes.

4.5.2.2 Drainage ditches

From the extensive network of drainage ditches that is present in the alluvial plain, only main ditches were considered in the model. Available measurements of water levels were used to impose boundary conditions at ditches in the region between Martigny and Riddes, namely at the Canal du Syndicat, the Canal du Toléron, the Canal des Quiess, the Canal des Marais Neufs, the Canal des Chavannes, the Canal de Leytron-Saillon-Fully and the Canal de Gru. For other important drainage ditches, the Canal de Sion-Riddes, the Canal de Chalais and the Canal de Vissigen, as well as for tributaries, that were included in the model, too, water levels were not at disposition during the construction of the model. Water levels for these surface waters were extracted from a LiDAR (laser screen) based DTM. DTM are considered a potential source to obtain surface water elevations [143].

Figure 37 indicates that extracting data from the DTM along a ditch may lead to an irregular streambed elevation. The presence of noise is explained by the fact that ditches typically have a width that is in the range of the resolution of the DTM or even below it. Extracted values may thus partly be influenced by the topography of the surroundings, which generally have a higher elevation than the water level of the ditch. Raw data were smoothed by subsampling the noisy curve and leveling it to

[18] Mean hydraulic heads during HW (1994 – 2004)

local minima. As demonstrated for the Canal de Syndicat in Figure 37, the applied procedure is able to produce elevations that compare well to measured data. Water levels were linearly interpolated to mesh nodes of the model mesh grid.

In a DTM, the elevation of the water surface is recorded at the moment of the aerial survey. For the DTM used herein [144], surveys were carried out in spring (March – May [145]). It is clear that a DTM thus offers at best a snapshot of time variant water levels of surface waters which is not representative for the mean value. Values of boundary conditions at surface waters extracted from the DTM are therefore subject to a relatively high uncertainty.

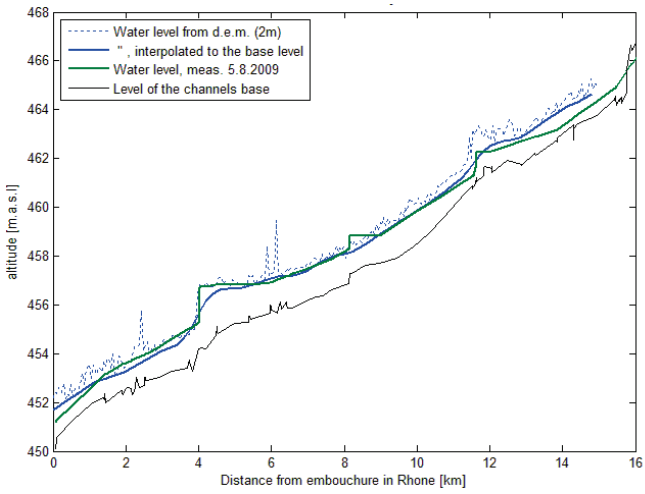

Figure 37 : Comparison of measured water levels in the Canal du Syndicat with topographical values from the DTM [144].

4.5.2.3 Lakes

The numerous small ponds scattered throughout the plain were not represented by boundary conditions, because they have been proven to be part of the groundwater flow system [14, 146].

4.5.3 Flux constraints on surface waters

At ditches, influx was constrained by a maximum infiltration rate. This became necessary because there are places where the PR3 induces an inversion of the hydraulic conditions in that gaining ditches turn to losing. The simulation of the future state then uses a transfer rate which has not been calibrated. As a consequence, a high inflow may result. The maximum infiltration rate was calculated according to Osman and Bruen [147] and Brunner, Cook, et al. [148]. In this approach, the unsaturated

properties of the aquifer underneath a losing surface water body are considered in the calculation of the hydraulic gradient, in addition to the hydraulic properties of the clogging layer. The head losses required for the calculation of the maximum infiltration rate were estimated from the DTM [144] and the water level in the aquifer.

Table 5 : Properties of ditches and the underlying aquifer used for the calculation of the maximum infiltration rate at ditches.

Saturated properties:		
Hydraulic conductivity of aquifer:	5e-4	[m/s]
Hydraulic conductivity of clogging layer:	5e-6	[m/s]
Thickness of clogging layer:	0.3	[m]
Depth of water table	2	[m]
Van Genuchten function parameters:		
Residual water saturation	4.5e-2	[m^3m^{-3}]
Alpha (power index)	14.5	[m^{-1}]
Beta (power index)	2.68	[-]
Pore connectivity	0.5	[-]

4.5.4 Pumping wells

Locations and abstraction rates of wells that were considered in the groundwater flow model are listed in Table 6. Locations of pumping wells were available from cantonal authorities. Abstraction rates were retrieved from persons in charge of water supply at municipalities. The data quality is inconsistent and sometimes questionable. It ranges from annual mean values based on several years of monthly measurements to estimates made during a personal communication by phone call.

Uncertainties related to abstraction rates were nevertheless a minor concern because we estimated the contribution of pumping wells to the overall hydraulic balance to be relatively small. For the same reason, abstraction rates were not calibrated.

It can be assumed that there are abstractions present in the model area which have not been considered in the model, presumably mostly for agricultural purposes. Based on irrigation needs for agricultural land in Switzerland [149] and on a contribution of 16% of groundwater to the agricultural water demand in Valais [150] we estimated the maximum amount of additional abstractions to be about 2300 m^3/d on an annual average. This is in the order of magnitude of one large pumping well and can be neglected in a regional scale model.

Table 6 : Geographical positions and abstraction rates of pumping wells used in the model

Municipality	Pumping well	X	Y	Q (m^3/d)
Evionnaz	Station de pompage n° 3	568200	112400	5'500
Fully	Puits de Branson	573430	108410	590
	Puits de Barillet	574020	108688	790
	Puits d'Yvaud	575600	109500	390
	Puits des Places, aval	576520	110050	790
	Puits des Places, amont	576580	110098	790
	Puits de Mazembre	577110	110520	390
	Puits de Lantzes	577630	110820	200
Charrat	Station de pompage de Lettray	576275	108860	980
Saxon	Station de pompage du Vacco	580280	111850	310
Saillon	Aux Marais Neufs	581490	113115	1'140
Ardon	Puits du Nayas	586480	117900	130
Vétroz	Puits du Botza	586830	117820	520
	Puits Séba	588615	116740	190
Conthey	Les Poujes	589100	118400	270
Sion	Ronquoz	592810	118310	1'200
	Sainte-Marguerite 1	594400	119420	600
	Grand-Champsec 1	595513	120710	540
	Grand-Champsec 2	595654	120665	540
	Station de pomp. de Préjeux/Bramois	596710	120580	150
	Uvrier 1	598530	121720	150
St-Léonard	Station de pompage 2	599310	122575	810
Sierre	Station de pompage de Chalais	605450	124300	500
	P7 (industriel)	607200	125850	2'760
	P5 (industriel)	607370	125800	1'950
	P8 (industriel)	607850	125750	2'860

Chapter 5

Parameter estimation and uncertainty quantification

5.1 Introduction

This chapter deals with parameter estimation and quantification of the uncertainty associated with the estimate.

The chapter begins with a description of parameterization schemes through which parameters are represented in the model. Assumptions that were made to constrain the parameter estimation process are next laid out. Constraining the inverse problem by including regularization was necessary in order to make the underdetermined problem solvable. The estimation of parameters of a nonlinear model is an iterative process and requires the definition of initial parameter values. Concepts are presented based on which initial parameter values were determined together with respective numerical values. Furthermore, values for parameter bounds are given and justified.

Section 5.3 describes how average values for hydraulic heads, which were used as conditioning data herein, were derived. An estimate of the uncertainty related to conditioning data is given, too, and observation weights are derived based on it. In the following, details are given on the solution method of the inverse problem and on how the uncertainty analysis was implemented.

In section 5.6, the model performance is evaluated in terms of its capacity to reproduce calibration data, both for the calibration solution and NSMC realizations. Section 5.7 treats parameter estimates and related uncertainties in detail. Then, in section 5.8 simulated flow rates and water balances are presented.

After a comparison of model outcomes to data that have not been included in the calibration in section 5.9, the chapter closes with a discussion.

5.2 Spatial Parameterization

5.2.1 Parameterization schemes

Throughout the work on the model, the inverse problem was adapted in an iterative process involving re-adjustment of the conceptual model, of model parameterization and of inversion parameters. The parameters that finally were estimated are:

– hydraulic conductivity of the aquifer;
– stream bed conductance of the Rhône River, of drainage ditches and of tributaries;
– recharge by precipitation;
– in- and outflow through model limits.

Table 7 gives an overview on the estimated parameters and on the respective parameterization device used herein.

Table 7 : Parameterization of the flow model.

Model parameter	Transformation	Scheme	No.
Hydraulic conductivity	Log	Pilot points	375
Transfer rate			
Rhône River	Log	Pilot points	103
Ditches	Log	Pilot points	136
Tributaries	Log	Pilot points	14
In-/Outflow at model limits			
Upstream limit	Log	Line with prescribed fluxes	1
Downstream limit	None	Line with prescribed heads	1
Lateral limits	Log	Line with prescribed fluxes	12
Recharge by precipitation	Log	Zones	11
Total number of model parameters[19]			906

The choice of the parameterization scheme was made based on the degree of heterogeneity typically encountered in parameters. Hydraulic conductivity and streambed conductance were expected to vary considerably and were thus parameterized using pilot points. Compared to zones of constant property values, pilot points allow a more realistic representation of geological heterogeneity.

Given the small variability of climatic forcing functions, recharge was assumed to be relatively homogeneous and was parameterized by large zones of uniform values.

[19] Transfer rates can be defined for in- and outflow conditions and are hence counted twice.

Areas with potential in- or outflow in the flow model in Figure 36c are isolated and relatively small. Parameterization of the inverse problem was therefore based on the parameterization of the forward problem, as shown in the representation of parameters of the inverse problem in Figure 38.

Kriging was chosen as the interpolation method to interpolate from pilot points to the model grid. It has the advantage to honor prescribed values at pilot points and to provide the best linear unbiased estimate between pilot points [104].

In order to extract a maximum amount of information from the conditioning data set, our strategy here was to set up a highly parameterized model. Besides the fact that uncertainty tends to be underestimated when using a small number of parameters, using a highly parameterized model has the advantage that structural noise incurred by lumping of real-world parameters into model parameters can be reduced to a minimum.

5.2.2 Parameter transformation and offset

All parameters, but the downstream boundary condition, were log-transformed[20]. This often speeds up the estimation process [47]. Parameters for which the lower bound was defined as zero cannot be log-transformed once their values fall to their lower bound. These parameters were provided with an offset to assure that they remain positive.

5.2.3 Regularization scheme

In the present model the number of model parameters exceeds the number of observation points. As stated earlier, the solution of such underdetermined problems is generally non-unique in that several solutions exist which all reproduce the observation data equally well. To make such ill-posed problems solvable, they need to be reformulated in making additional assumptions, such as adherence of parameters to preferred values or smoothness of parameter fields.

Here, the inverse problem was regularized through the combined use of a subspace method (truncated singular value decomposition) and of prior information. This combination is unique to PEST and is termed “SVD-assist” in PEST parlance [47] (see section 3.2.2 for an brief overview of the methodology).

[20] Logarithmic transformation is undertaken to the base 10 in PEST.

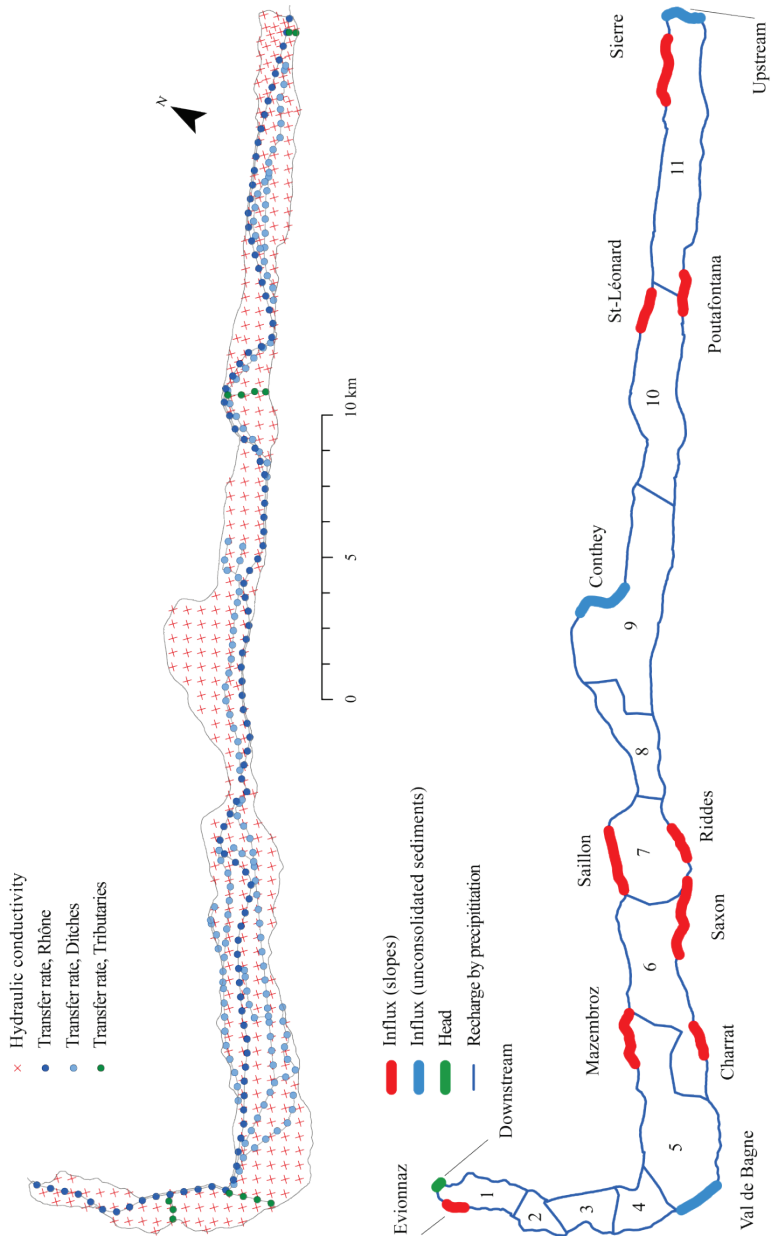

Figure 38 : Overview on model parameters of the inverse problem.

To in-/outflow parameters as well as to zones of recharge by precipitation, preferred-value regularization was applied, referring to initial values as the preferred state. For hydraulic conductivity and streambed conductance, we defined homogeneity as the preferred state. This was implemented in specifying differences of zero between parameters of the same group as the preferred condition. Using a preferred-difference strategy of regularization offers the possibility of constraining an undetermined inverse problem in a context, where preferred values are not well known. Using preferred-value regularization in such cases presents the risk that the regularization term of the objective function biases the estimation to a wrong solution [111]. This formulation was chosen because of the limited confidence in initial values of hydraulic conductivity and of streambed conductance.

For parameters implemented through pilot points, regularization weights ascribed to prior-information equations were calculated based on the variograms used for interpolating parameters from pilot points to the model grid[21]. Regularization constraints for zones of recharge were assigned relative weights proportional to their area. Regularization equations applied to in- and outflows were weighted uniformly.

In PEST, each regularization equation is assigned to a regularization group, according to the parameter group to which the concerned parameters belong[22]. Inter-regularization group weights adjustment here was undertaken in such a way that the total composite sensitivities[23] of all regularization groups were the same[24], i.e. regularization constraints of each parameter group were considered to be of equal importance at the parameter group level.

5.2.4 Hydraulic conductivities

In Chapter 2, a look-up table for the most abundant lithofacies present in the Rhône alluvial aquifer was established based on lithological data and results of hydraulic testing. In order to integrate this 3D data in the 2D flow model, an average hydraulic conductivity was calculated at each bore. To achieve this, we made the simplifying assumption of a vertically stratified aquifer with predominantly horizontal groundwater flow. It is well established that the equivalent hydraulic conductivity of the subsurface is given by the arithmetic mean of hydraulic conductivities of individual layers in such a setting [e.g. 63]. Head measurements most often were measured at a depth of

[21] Using the PEST groundwater utility PPKREG.
[22] Each of the different parameter types in Table 7 was assigned to a different parameter group.
[23] Prior information equations are regarded as additional observations in PEST. The composite sensitivity of a particular prior information equation is a measure of the sensitivity of that "observation" to all parameters involved in the estimation process [47].
[24] By setting the PEST variable IREGADJ to 1 (Changing the inter-regularization group weights does not affect the relative weighting within each group [47]).

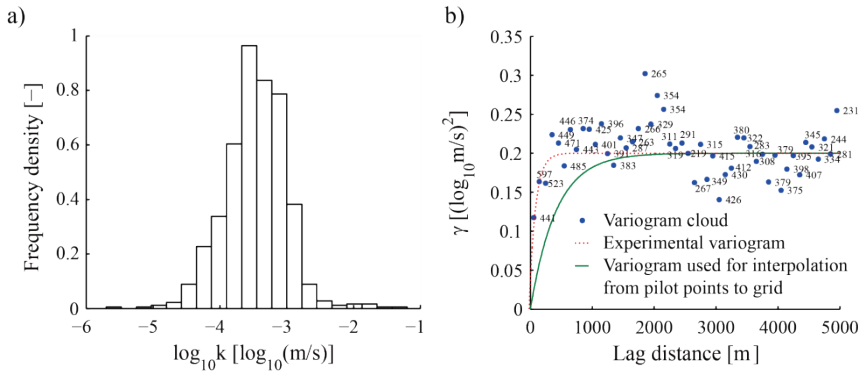

Figure 39 : a) Histogram of vertical averages of hydraulic conductivities at bores; b) Variogram of vertical averages of hydraulic conductivities at bores.

less than 20 m. The average was thus computed on the saturated part of the uppermost 20 m of the aquifer.

Interpolated values of average hydraulic conductivities at bores were considered as initial parameter values for the parameter estimation process. Lower and upper parameter bounds (6e-7 m/s and 1e-1 m/s) were chosen such as to encompass the histogram of average hydraulic conductivities at bores shown in Figure 39a. Figure 39b shows the experimental variogram of the average hydraulic conductivities at bores. From this experimental variogram, the sill of the variogram for interpolating hydraulic conductivities from pilot points to the model grid was determined (to 0.2). In order to honor prescribed values at pilot points, a nugget of zero was used for the interpolation between pilot points.

The experimental variogram in Figure 39b displays a short range, indicating a short correlation length typical of heterogeneous alluvial aquifers. If a range as short as that exhibited by the experimental variogram would be assumed for the interpolation between pilot points, adequate discretization of the hydraulic conductivity field[25] would lead to a very high number of pilot points and would make the problem computationally difficult to handle. Instead, the range of the interpolation variogram was defined as 2.5 times the distance between pilot points[14].

Parameterization of hydraulic conductivity was based on a regular grid of 500 m x 500 m (Figure 38). This pilot point density was regarded as high enough to capture the heterogeneity of hydraulic conductivity as resolved by the observation data at

[25] Obeying the rule of thumb, which states that about 2-3 pilot points per correlation length are needed for the pilot points method to work [151].

most places. A higher pilot point density was considered to face the relatively complex hydrogeological setting in the uppermost part of the model. At a few places, additional pilot points were added to avoid large gaps. Locations of pilot points were kept fixed during the estimation process.

5.2.5 Transfer rates

Equation [4.4] states that in an unconfined 2D aquifer the transfer rate, i.e. the transfer coefficient related to the streambed conductance, depends on the hydraulic conductivity of the streambed, its thickness, the river width and the saturated thickness of the underlying aquifer, if the river is being modeled as a single line. Falling head tests carried out in the streambed yielded values of hydraulic conductivity between 1.3e-7 m/s and 4.0e-5 m/s. Values estimated from grain size analysis of sediment samples taken from the streambed varied between 2.1e-6 m/s and 9.7e-5 m/s (see Chapter 2). Inspired by this, minimum and maximum values of 1.3e-8 m/s and 7.5e-5 m/s (3.8e-4 m/s for exfiltrating conditions) were assumed for the computation of parameter bounds of transfer rates of the Rhône River (Table 8). This large prior uncertainty, typically encountered when dealing with hydraulic conductivities of streambed materials [152], is additionally augmented by the uncertainty on the other parameters involved in the definition of the transfer rate. For the thickness of streambed sediments a range of 0.1 – 5 m was assumed. The high value for the upper limit is motivated by the results of infiltration tests (see Chapter 2) which indicate a decrease of hydraulic conductivity down to depth of several meters (~ 3 m in the tests). The width of the Rhône River varies between 30 m and 75 m. According to lithological information from drill-logs (see Chapter 2) a range of 30 – 50 m was considered for the saturated thickness of the aquifer.

Prior information on the hydraulic conductivity of the streambed is relatively sparse. For this reason, uniform initial values were used. Referring at large to mean hydraulic conductivities found from hydraulic testing and from sediment samples (mean values of 6e-6 m/s and 1.8e-5 m/s respectively) a value of 1.0e-5 m/s was used to compute initial parameter values of transfer rates of the Rhône River for infiltrating conditions. Because streambed clogging is typically stronger for infiltrating conditions than for exfiltrating conditions [153], a higher conductivity was generally considered for the computation of maximum and initial values for exfiltrating conditions (five times higher).

For other surface water bodies, information on hydraulic properties is limited to rough estimates based on visual inspection. The bed of drainage ditches in the study area is often built up by a several tens of centimeters thick mud layer [154]. Consequently, a low hydraulic conductivity of 1.0e-6 m/s was assumed for calculating initial values of transfer rates (Tables 9 and 10). This is largely in agreement with falling

head tests performed in a drainage ditch in the upper part of Valais that yielded hydraulic conductivities of 1.8e-6 m/s and 3.1e-6 m/s [10]. As a consequence of the frequently encountered pavement, streambeds of tributaries are considered as being of relatively low permeability, too. Parameter bounds for transfer rates of tributaries and ditches were based on assumed ranges of river width, of hydraulic conductivity of the streambed and of its thickness.

Pilot points for transfer rate were placed at regular distances of 500 m along surface waters. At some places additional points were added to better represent the geometry of surface water bodies (Figure 38). Given the lack of information on the spatial correlation of streambed conductance, the same variogram as for hydraulic conductivity was used for the interpolation between pilot points.

Table 8 : Initial values and parameter bounds of transfer rate for the Rhône River.

Parameter		Infiltration			Exfiltration		
		Initial	Min.	Max.	Initial	Min.	Max.
Streambed conductance	k' (m/s)	1.0E-05	1.3E-08	7.5E-05	5.0E-05	1.3E-08	3.8E-04
Thickness exchange layer	e' (m)	0.25	5	0.1	0.25	5	0.1
River width	W (m)	52.5	30	75	52.5	30	75
Saturated thickness	h_s (m)	40	50	30	40	50	30
Transfer Rate	ϕ (s^{-1})	2.6E-05	7.5E-10	9.4E-04	1.3E-04	7.5E-10	4.7E-03

Table 9 : Initial values and parameter bounds of transfer rate for ditches.

Parameter		Infiltration			Exfiltration		
		Initial	Min.	Max.	Initial	Min.	Max.
Streambed conductance	k' (m/s)	1.0E-06	1.3E-08	3.8E-06	5.0E-06	1.3E-08	7.5E-05
Thickness exchange layer	e' (m)	1	2	0.1	1	2	0.1
River width	W (m)	1.5	1	2	1.5	1	2
Saturated thickness	h_s (m)	40	50	30	40	50	30
Transfer Rate	ϕ (s^{-1})	1.9E-08	6.3E-11	1.3E-06	9.4E-08	6.3E-11	2.5E-05

Table 10 : Initial values and parameter bounds of transfer rate for tributaries.

Parameter		Infiltration			Exfiltration		
		Initial	Min.	Max.	Initial	Min.	Max.
Streambed conductance	k' (m/s)	1.0E-06	1.3E-08	3.8E-06	5.0E-06	1.3E-08	3.8E-05
Thickness exchange layer	e' (m)	1	2	0.5	1	2	0.5
River width	W (m)	17.5	15	20	17.5	15	20
Saturated thickness	h_s (m)	40	50	30	40	50	30
Transfer Rate	ϕ (s^{-1})	2.2E-07	9.4E-10	2.5E-06	1.1E-06	9.4E-10	2.5E-05

5.2.6 Recharge by precipitation

The maximum value of recharge by precipitation was estimated as the difference between the mean annual precipitation depth [1951 – 1980, 102] and the mean annual actual evaporation [1973 – 1992, 155] herein. Surface runoff was neglected due to the very small slope of the plain of a few per mill. The data is available as grids of 2 x 2 km^2 (precipitation data) and 1 x 1 km^2 (evaporation data). The coarse resolution leads to an effective precipitation depth which is unreasonably inhomogeneous on the scale of the model. The result was therefore filtered by a moving average (window size 5 km).

Eleven zones were delimited to parameterize recharge by precipitation (Figure 40). Mean and maximum values of effective precipitation of each zone were chosen as initial values and as upper parameter bounds. The lower bound was set to zero. Table 11 gives an overview of numerical values used herein.

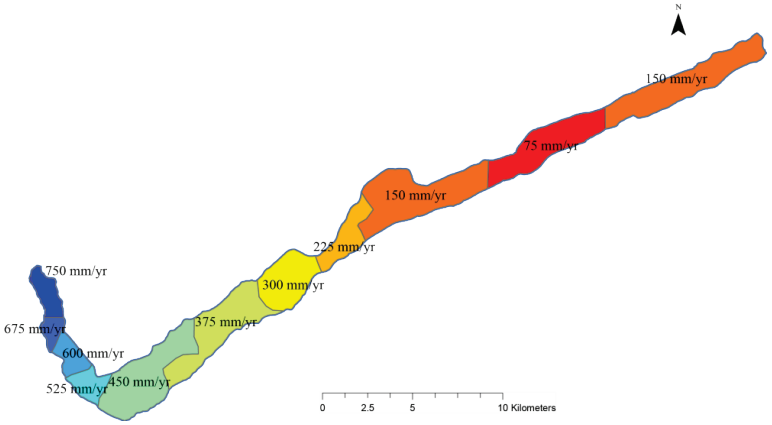

Figure 40 : Mean annual net precipitation depth (moving average; window size 5km), divided into classes of 75 mm (data from FOEN [102, 155]).

Table 11 : Initial and bounding values for recharge by precipitation.

Zone	Initial values		Maximum values	
	mm/yr	m/s	mm/yr	m/s
1	712.5	2.3E-08	750.0	2.4E-08
2	637.5	2.0E-08	675.0	2.1E-08
3	562.5	1.8E-08	600.0	1.9E-08
4	487.5	1.5E-08	525.0	1.7E-08
5	412.5	1.3E-08	450.0	1.4E-08
6	337.5	1.1E-08	375.0	1.2E-08
7	262.5	8.3E-09	300.0	9.5E-09
8	187.5	5.9E-09	225.0	7.1E-09
9, 11	112.5	3.6E-09	150.0	4.8E-09
10	37.5	1.2E-09	75.0	2.4E-09

5.2.7 Head at the downstream boundary

Interpolated heads during LW and HW were considered as the lower and upper parameter bound of the prescribed head at the downstream limit of the model. The initial head was set according to the equation used to estimate mean values for the Rhône (Equation [4.5]) given the high influence of the Rhône on groundwater in this area.

Table 12 : Initial and bounding values heads at the downstream limit.

Parameter		Head			Unit
		minimal	maximal	initial	
Hydraulic head	h	445.27	445.53	445.35	(m)

5.2.8 Influx at model limits

5.2.8.1 Lateral valley slopes

Red lines in Figure 41 indicate areas of potential recharge of the alluvial aquifer by lateral influx from valley slopes that had been identified (see also Figure 38). The approach followed herein to derive parameter bounds for prescribed fluxes, by which lateral influx was parameterized in the model, is simple: water fluxes were considered proportional to the area of schematic drainage basins of recharge zones and to effective precipitation (see section 5.2.6). Drainage basins were drawn in a schematic way based on topography. The followed approach is certainly very simplistic. To account for the uncertainty related to such a simple approach, influx parameters were allowed to move on a large range.

The maximum influx at each location was calculated from the maximum effective precipitation on the corresponding drainage basin and considering an infiltration rate of 20%. For the initial influx, the minimum effective precipitation on the corresponding drainage basin and an infiltration rate of 1% were considered. This relatively low value has been chosen to account for the importance of surface runoff in the present context of an accentuated topography. A zero flux was assumed as the lower parameter bound.

Table 13 gives an example of how the initial and bounding values were calculated for the area near Saxon. Table 14 shows initial and bounding values for areas with potential recharge by lateral influx.

Table 13 : Calculation of initial and bounding values for lateral influx near Saxon.

Parameter		Flux			Unit
		minimal	maximal	initial	
Infiltration rate	R	0	0.2	0.01	*(-)*
Effective precipitation	P	0	800	500	*(mm/yr)*
			2.5e-8	1.6e-8	*(m/s)*
Width of drainage basin	W	0	4500	3000	*(m)*
Length of drainage basin	L	0	5000	3000	*(m)*
Influx	$Q = R \cdot P \cdot W \cdot L$	0	1.1e-1	1.4e-3	*(m^3/s)*
		0	9'863	123	*(m^3/d)*
Width of discharge area	x	0	2718	2718	*(m)*
Nodal flux GW	$q = Q / x$	0	4.2e-05	5.3e-07	*(m^2/s)*

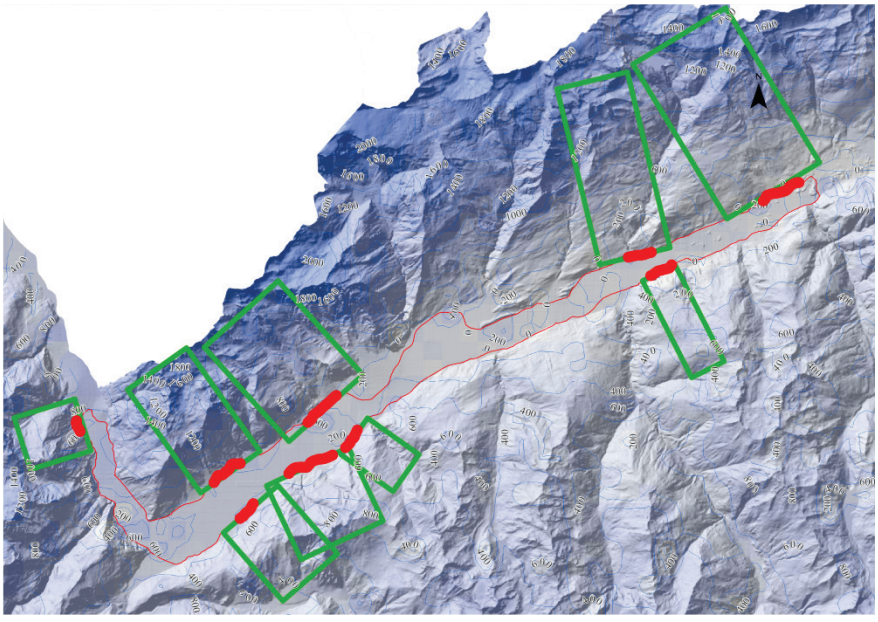

Figure 41 : Areas with potential lateral influx from valley slopes and their schematic drainage basins. The colored background map and the isolines represent effective precipitation depth (light blue: low values, dark blue: high values).

Table 14 : Initial and bounding values for zones with recharge by lateral influx (in blue: locations with a lateral alluvial plain).

Location		Initial values		Minimum		Maximum	
		m/s	m^3/d	m/s	m^3/d	m/s	m^3/d
1	Evionnaz	4.0E-08	88	0	0	2.1E-06	4'603
2	Val de Bagne	3.3E-08	177	0	0	2.0E-06	10'639
3	Charrat	1.1E-08	41	0	0	2.8E-06	10'959
4	Fully-Mazembroz	6.1E-09	41	0	0	3.4E-06	23'014
5	Saxon	1.3E-08	123	0	0	1.1E-06	9'863
6	Saillon-Leytron	3.1E-08	230	0	0	4.2E-06	31'644
7	Riddes	1.2E-08	49	0	0	9.4E-07	3'836
8	Conthey	7.5E-08	622	0	0	1.3E-07	1'106
9	Pouta-Fontana	7.2E-09	33	0	0	1.0E-06	4'603
10	St-Léonard	9.4E-09	41	0	0	3.5E-06	15'342
11	Sierre	2.2E-08	173	0	0	6.2E-06	49'315
12	Upstream boundary	7.5E-07	2'974	1.0E-07	455	3.0E-06	14'515

5.2.8.2 Upstream boundary and lateral alluvial plains

Based on the analysis of piezometric maps, an influx to the alluvial Rhône aquifer from small lateral alluvial aquifers was assumed at Martigny and Conthey (Figure 42, see also Chapter 3).

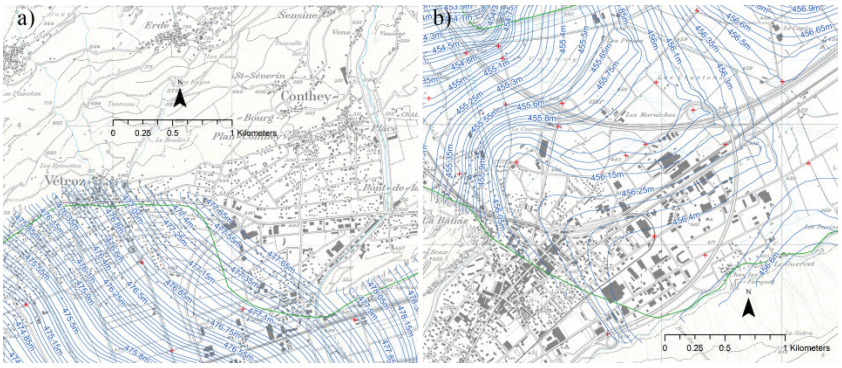

Figure 42 : Contour lines of mean piezometric head during HW at Conthey (a) and at Martigny (b) (Lines are drawn at an interval of 5 cm).

As for the upstream boundary condition (Table 15), initial values and parameter bounds for fluxes were calculated from the hydraulic gradient, the hydraulic conductivity, the width of the contact area and the saturated thickness, as shown in Tables 16 and 17 below. For the upstream boundary, minimum and maximum values were calculated based on hydraulic gradients at LW and HW respectively. For lateral alluvial

plains, the maximum influx was calculated based on an estimate of the maximum hydraulic gradient across the model limit in the corresponding area. The minimum influx here was set to zero. Values of hydraulic conductivity and of aquifer thickness were estimated based on lithological information and hydraulic tests in BD-for [98].

Table 15 : Initial and bounding values for lateral influx at the upstream limit.

Parameter		Flux			Unit
		initial	minimal	maximal	
Hydraulic gradient in GW	i	5.0E-03	4.0e-03	6.0e-03	*(-)*
Hydraulic conductivity	k	1.5E-04	6.0e-05	4.0e-04	*(m/s)*
Width of aquifer	L	1'290	1'290	1'400	*(m)*
Saturated thickness	h_s	40	17	50	*(m)*
Area of cross section	$A = L \cdot h_s$	51'373	21'925	70'000	*(m^2)*
Influx	$Q = k \cdot A \cdot i$	3.9E-02	5.3e-03	1.7e-01	*(m^3/s)*
		3'329	455	14'515	*(m^3/d)*
Nodal flux GW[26]	$q = Q / L / h_s$	7.5e-07	1.0e-07	3.0e-06	*(m/s)*

Table 16 : Initial and bounding values for lateral influx at Martigny.

Parameter		Flux			Unit
		initial	minimal	maximal	
Hydraulic gradient in GW	i	3.3e-04	0	1.0e-03	*(-)*
Hydraulic conductivity	k	1.0e-04	0	2.0e-03	*(m/s)*
Width of aquifer	L	1'539	0	1'539	*(m)*
Saturated thickness	h_s	40	0	40	*(m)*
Area of cross section	$A = L \cdot h_s$	24'243	0	63'494	*(m^2)*
Influx	$Q = k \cdot A \cdot i$	2.1e-03	0	1.2e-01	*(m^3/s)*
		177	0	10'639	*(m^3/d)*
Nodal flux GW	$q = Q / L / h_s$	3.3e-08	0	2.0e-06	*(m/s)*

Table 17 : Initial and bounding values for lateral influx at Conthey.

Parameter		Flux			Unit
		initial	minimal	maximal	
Hydraulic gradient in GW	i	1.0E-03	0	1.3e-03	*(-)*
Hydraulic conductivity	k	7.5E-05	0	1.0e-04	*(m/s)*
Width of aquifer	L	2'400	0	2'400	*(m)*
Saturated thickness	h_s	40	0	40	*(m)*
Area of cross section	$A = L \cdot h_s$	96'000	0	96'000	*(m^2)*
Influx	$Q = k \cdot A \cdot i$	7.2E-03	0	1.3e-02	*(m^3/s)*
		622	0	1'106	*(m^3/d)*
Nodal flux GW	$q = Q / L / h_s$	1.0E-03	0	1.3e-07	*(m/s)*

[26] Assuming a saturated thickness of 40 m.

5.3 Conditioning data

5.3.1 Calculating average hydraulic heads

The groundwater flow model presented herein is meant to represent mean flow conditions of the Rhône alluvial aquifer at the long term. Head measurements, which are used herein to condition the inverse problem, are available as continuous time series and as bi-annual measurements during LW and HW. At observation points with continuous data, averages of the time series were used as conditioning data. Because observation points with continuous measurements are too sparse (74 observation points) to allow for a good spatial coverage, bi-annual measurements needed to be considered for the construction of the conditioning data set of average heads. A simple model was built, in which it is assumed that the average head at a given measurement point can be estimated from bi-annual measurements by a linear combination of these:

$$M^* = \frac{1}{N}\sum_{i=1}^{N} M_i{}^* = \frac{1}{N}\sum_{i=1}^{N}(\alpha H_i + \beta B_i) = \alpha H_{mean} + \beta B_{mean} \qquad [5.1]$$

where M^* is the estimated average hydraulic head, $M_i{}^*$ the estimated average hydraulic head for year *i*, H_i and B_i the hydraulic heads during HW and during LW for year *i*, with H_{mean} and B_{mean} the average hydraulic heads during HW and LW (arithmetic mean over *N* years), and with α and β the uniform model parameters. Numeric values for α and β were obtained by minimizing the variance of residuals between true and modeled average hydraulic heads $\mathrm{Var}(\mathbf{R}) = \mathrm{Var}(\mathbf{M} - \alpha\mathbf{H} - \beta\mathbf{B}) = f(\alpha, \beta)$ subject to the constraint that the expectance of the residuals $\mathbb{E}[\mathbf{R}] = \mathbb{E}[\mathbf{M}] - \alpha\mathbb{E}[\mathbf{H}] - \beta\mathbb{E}[\mathbf{B}] = \varphi(\alpha, \beta)$ be zero. The variance of the residuals **R** may be written as:

$$\begin{aligned}\mathrm{Var}(\mathbf{R}) = \mathrm{Cov}(\mathbf{R},\mathbf{R}) &= \mathrm{Cov}(\mathbf{M} - \alpha\mathbf{H} - \beta\mathbf{B}, \mathbf{M} - \alpha\mathbf{H} - \beta\mathbf{B}) \\ &= \mathrm{Cov}(\mathbf{M},\mathbf{M}) - 2\alpha\mathrm{Cov}(\mathbf{H},\mathbf{M}) - 2\beta\mathrm{Cov}(\mathbf{B},\mathbf{M}) \\ &+ 2\alpha\beta\mathrm{Cov}(\mathbf{H},\mathbf{B}) + \alpha^2\mathrm{Cov}(\mathbf{H},\mathbf{H}) + \beta^2\mathrm{Cov}(\mathbf{B},\mathbf{B})\end{aligned} \qquad [5.2]$$

A solution to the constraint minimization was found using the Lagrangian multiplier method. We defined the Lagrangian as:

$$\mathcal{L}(\alpha, \beta, \lambda) = f - 2\lambda\varphi \qquad [5.3]$$

The gradient of the Lagrangian is then:

$$\nabla\mathcal{L} = \left(\frac{\partial f}{\partial \alpha} - 2\lambda\frac{\partial \varphi}{\partial \alpha}, \frac{\partial f}{\partial \beta} - 2\lambda\frac{\partial \varphi}{\partial \alpha}, -2\varphi\right) \qquad [5.4]$$

Setting $\nabla\mathcal{L}$ to zero yields:

$$\begin{pmatrix} \mathrm{Cov}(\mathbf{H_k},\mathbf{H_k}) & \mathrm{Cov}(\mathbf{H_k},\mathbf{B_k}) & \mathbb{E}[\mathbf{H_k}] \\ \mathrm{Cov}(\mathbf{H_k},\mathbf{B_k}) & \mathrm{Cov}(\mathbf{B_k},\mathbf{B_k}) & \mathbb{E}[\mathbf{B_k}] \\ \mathbb{E}[\mathbf{H_k}] & \mathbb{E}[\mathbf{B_k}] & 0 \end{pmatrix} \begin{pmatrix} \alpha \\ \beta \\ \lambda \end{pmatrix} = \begin{pmatrix} \mathrm{Cov}(\mathbf{H_k},\mathbf{M_k}) \\ \mathrm{Cov}(\mathbf{B_k},\mathbf{M_k}) \\ \mathbb{E}[\mathbf{M_k}] \end{pmatrix} \quad [5.5]$$

At some observation points, time series with continuous measurements as well as measurements at HW and LW are available. Measurements of time series longer than five years (59 observation points) were considered to calculate "true" average hydraulic heads and to derive values for α (0.2588) and β (0.7411) in solving Equation [5.5]. Average heads were then estimated according to Equation [5.1].

5.3.2 Calculating observation weights

5.3.2.1 Approach

When parameter estimation is carried out using PEST, a weight is assigned to each observation. The more reliable an observation is, the larger its contribution should be to the objective function and the larger hence its weighting should be. Weights that are inversely proportional to the standard deviation of observations are often (e.g. [47]) considered the most appropriate.

In order to estimate observation weights, an uncertainty analysis of observations was undertaken. We identified three sources of uncertainties present in the conditioning data set. The quality of estimates of average hydraulic heads depends first on the capacity of Equation [5.1] to estimate the average hydraulic head on the basis of average values during HW and LW. This uncertainty was quantified by the standard deviation of residuals between estimates and true values derived from continuous measurements. A second source of uncertainty arises from the fact that the available average water levels at HW and LW do not correspond to true, long-term average values, given that the period for which average heads at HW and LW are available covers 10 years at a maximum. This was addressed by using a confidence interval for estimated average heads. Thirdly, measurement noise is present in observations due to inaccuracies of measuring devices. Measurement noise was estimated based on experience. An estimate of the overall uncertainty was then made based on individual uncertainties. From this, observation weights were calculated.

5.3.2.2 Uncertainty of estimation method for average hydraulic heads

In Figure 43 estimates of average values computed using Equation [5.1] are compared to average values derived from continuous data (Figure 43). The error of the estimated average head values is centered on zero and has a standard deviation of $\sigma_{model} = 0.12$ m. This value was retained as an estimate of the error related to the method by which average heads are calculated.

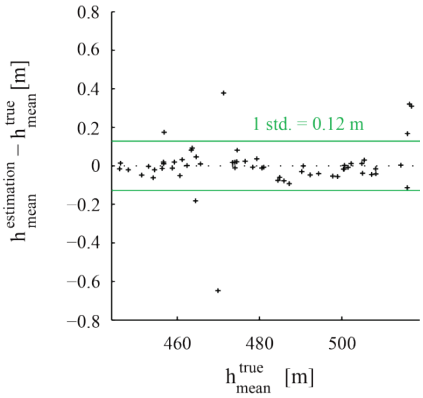

Figure 43 : Residuals between true and estimated average heads at observation points with continuous measurements.

5.3.2.3 Uncertainty of averages

The estimation of the uncertainty related to averages of hydraulic heads due to the limited sample size herein is based on the assumption of normally distributed sample means. If this condition is met, the confidence interval of the sample mean can be estimated [133] as:

$$Pr\left[\bar{\Re}_N - t_{N-1}\left(1-\frac{\alpha}{2}\right)\frac{S_N}{\sqrt{N}} \le \mu \le \bar{\Re}_N + t_{N-1}\left(1-\frac{\alpha}{2}\right)\frac{S_N}{\sqrt{N}}\right] = 1-\alpha \qquad [5.6]$$

where $1-\alpha$ is the probability that the value of the ensemble mean μ lies within the confidence interval around the sample mean $\bar{\Re}_N$; S_N is the sample standard deviation; N is the sample size; $t_{N-1}(p)$ is the p-quantile of the Student distribution with (N–1) degrees of freedom; $\chi^2_{N-1}(p)$ is the p-quantile of the chi-square distribution with (N–1) degrees of freedom.

Using Equation [5.6] requires knowledge of the sample standard deviations. Standard deviations of annual average values were used to estimate the sample standard deviation. The former turn out to be proportional to the latter , but underestimate it, as shown in Figure 44a or also in the example in Figure 45. We limited ourselves to matching true standard deviations of annual averages (Figure 44b) for the estimation of the uncertainty of average values. As the equation in Figure 44b indicates, standard deviations of estimated annual average heads tend to overestimate values derived on the basis of true annual average heads. After removal of this trend standard deviations of estimated annual average heads were used to compute the confidence interval of the sample means at the 95 percent level ($\sigma_{sample\ moment}$) according to [5.6].

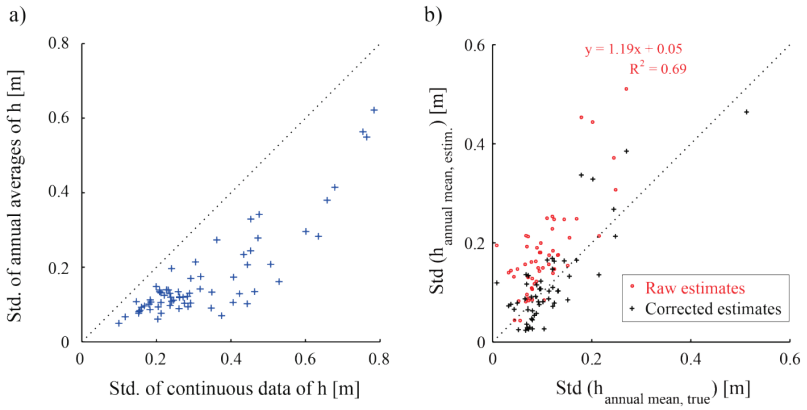

Figure 44 : a) Comparison of sample standard deviations evaluated from continuous head data and standard deviations of average annual heads (computed from continuous data); b) Comparison of standard deviations of annual averages of hydraulic head calculated from continuous data (x-axis) and calculated from annual measurements during low and high water conditions (y-axis).

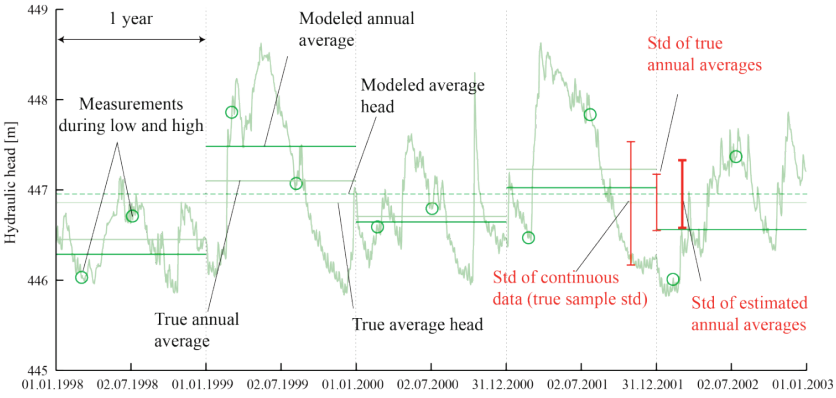

Figure 45 : Example of a time series of continuous measurements of hydraulic heads with true and estimated sample moments (the estimate of the sample standard deviation is drawn bold).

5.3.2.4 Uncertainty due to inaccuracies of measuring devices

For manual head measurements at HW and LW, a measurement error of σ_{device} = 2 cm was assumed. Continuous measurements were considered to be error-free.

5.3.2.5 Overall observation uncertainty and observation weights

If various quantities $x_1, \cdots, x_n$ display small uncertainties $\delta x_1, \cdots, \delta x_n$, then the uncertainty of the sum and difference of the quantities $q = x_1 + \cdots + x_n$ is $\delta q =$

$(\delta x_1 + \cdots + \delta x_n)^{-1/2}$ [156]. If it is assumed that individual error terms sum up to a total error, the overall uncertainty can be computed as:

$$\sigma = \sqrt{{\sigma_{model}}^2 + {\sigma_{sample\ moment}}^2 + {\sigma_{device}}^2} \qquad [5.7]$$

5.3.3 Calibration target

Based on Equation [5.7], observation weights were calculated as inversely proportional to the estimated measurement uncertainty using a proportionality constant of 1:

$$w = \frac{1}{\sigma} = \frac{1}{\sqrt{{\sigma_{model}}^2 + {\sigma_{sample\ moment}}^2 + {\sigma_{device}}^2}} \qquad [5.8]$$

The measurement objective function being defined as $\Phi = \sum_{i=1}^{m}(w_i r_i)^2$ [47], with r_i the model-to-data residuals, w_i the weights of observation data according to Equation [5.8] and m = 604 the number of observation data, a value of 604 was then specified as the calibration target[27]. PEST attempts to lower the model-to-measurement misfit to the target objective function but will not reduce it below that level. This ensures that the model-to-measurement misfit of the resulting simulations is in agreement with the estimated measurement uncertainty. Under the premise that the measurement uncertainty has been estimated correctly, this strategy is a measure to prevent the estimation process from overfitting, i.e. from fitting to measurement noise.

Because structural noise typically displays a high degree of correlation, using a weighting scheme with spatially independent measurement noise, as done herein, implicates that no structural noise is present in the model. This assumption is always violated to a greater or lesser degree, given that a model contains always a minimum amount of structural noise introduced through parameter simplification. Often structural noise is even more important than measurement noise [135]. In order to find a minimum predictive error variance solution, an observation covariance matrix is theoretically required in the presence of correlated structural noise [118]. An observation covariance matrix is however rarely supplied in practice [118], because neither the magnitude nor the structure of the correlation are known. Adopting the strategy suggested by Doherty and Welter [135] to reduce structural noise incurred through parameter simplification, a relatively dense spatial parameterization was used in the model presented herein and uncertain system stresses were included in the parameter estimation process.

[27] Via the PEST variable PHILIM.

5.4 Solution method

As stated earlier, SVD-assist was used herein to solve the inverse problem in an efficient manner in terms of computing time. SVD-assist requires the definition of super parameters (see section 3.2). Here the number of super parameters was estimated based on a pre-inversion optimization run undertaken for the purpose of calculating derivatives of observations with respect to model parameters. In this pre-inversion run, regularization constraints were removed and the Marquardt parameter was set to zero in order to calculate the derivatives with respect to model parameters in a "pure" way. Following Doherty [47], a singular value decomposition (SVD) of the sensitivity matrix can be used to select the number of super parameters: It is estimated as the number of singular values for which singular values drop to about 10^{-7} to 10^{-8} of the highest singular value.

Here, this would correspond to 434 – 475 super parameters. A lower number may be used to avoid numerical instability or overfitting. Here, 400 super parameters were estimated (value of highest to lowest eigenvalue: 5.5e-7). Figure 46 shows singular values for each eigen component. The fact that the number of uniquely estimable parameters is lower than the number of observation points indicates redundancy of information encapsulated in the observation data set.

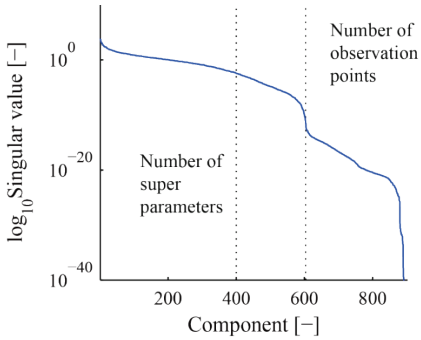

Figure 46 : Determination of number of super parameters based on a SVD of the sensitivity matrix of the pre-inversion optimization run.

5.5 Implementation of the NSMC procedure

Quantification of parameter uncertainty herein was undertaken using the NSMC methodology [47]. A summary of this method is given in section 3.2.2.

The NSMC procedure as used for the present model of the Rhône alluvial aquifer follows the instructions given by Doherty [119] for the implementation based on the existing parameterization scheme. Besides this method, PEST offers the possibility to perform a NSMC uncertainty analysis at the level of the model grid. The inclusion of fine – scale parameter variability is not thought to noticeably increase the uncertainty of predicted head changes induced by PR3.

As mentioned earlier, a null space projection of random parameters is undertaken as part of the NSMC procedure. Random parameters used for this purpose were assumed to follow a normal distribution centered on the calibration solution. Random realizations of pilot-point based parameters, i.e. hydraulic conductivity and transfer rates, were generated based on their prior covariance matrix[28]. Other parameters (i.e. recharge through precipitation and boundary conditions at model limits) were assumed to be uncorrelated and a standard deviation of one fourth of the range between upper and lower bounds was considered to assess their prior parameter uncertainty[29].

SVD-assisted re-calibration of null space projected parameters is accomplished by adjusting their solution space components [47]. For the uncertainty analysis, the same solution space dimensionality as in the calibration step was used (i.e. 400). Super parameters were re-defined for the uncertainty analysis based on sensitivities of model outputs towards model parameters calculated at the calibration solution. As for the definition of super parameters prior to calibration (section 5.4), care was taken to calculate sensitivities in a "pure" way[30].

1'000 random parameter sets were generated and subjected to null space projection. After replacement of the solution space component of null space projected parameters by calibrated values[31], one optimization run was then carried out for each set. No regularization constraints referring to prior information were included in the problem. However, regularization was implemented employing truncated singular value decomposition.

---

[28] Using the PEST utility RANDPAR.
[29] 95.4% of the values of a normally distributed variable lie within 4 standard deviations of the mean.
[30] To this end, regularization constraints were removed from the problem and the Marquardt parameter was set to zero.
[31] Using the PEST utility PNULPAR.

5.6 Data match

5.6.1 Calibration performance

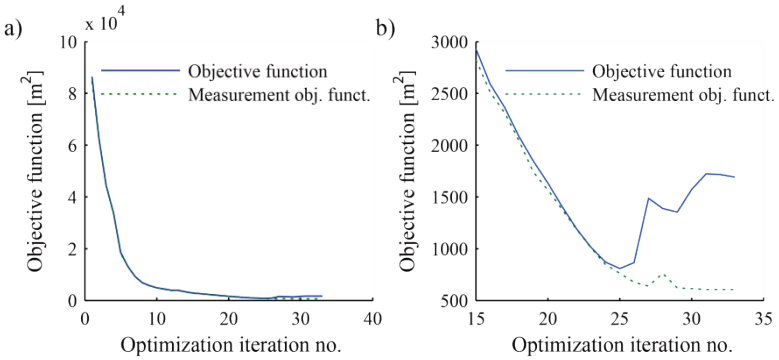

Figure 47 : Evolution of the objective function during the optimization process: a) Overview; b) Zoom to last iteration steps.

Figure 47 displays the evolution of the objective function during the optimization process. As the figure shows, the objective function reaches the minimum at iteration 25 before it begins to rise again. This rise is related to an increase of the contribution from the regularization objective function to the overall objective function. The measurement objective function could be reduced further at the prize of violating the regularization constraints of preferred homogeneity. The optimization process was stopped upon achievement of the target objective function of 604 after 33 optimization iterations[32]. The regularization component of the objective function here was mainly introduced in order to lead the inverse problem stable rather than as a plausibility term. Meeting the condition of preferred homogeneity was not a prerequisite in the given hydrogeological context of an alluvial aquifer. Therefore, the parameter set of the last optimization iteration was considered the best fit solution, even though the objective function is not at its minimum value.

In Figures 48 – 51, the capacity of the model to reproduce the system state is evaluated. In Figure 48a, residual heads between observation data and model outcomes are shown as a scatter plot. In Figure 48b, the histogram of residual heads is drawn. In both representations no systematic error in matching the data can be detected.

The spatial distribution of data misfit is quantitatively assessed in Figure 49. In Figure 49a residuals of heads at observation points are plotted in a map view. In Fig-

[32] 22'803 model runs (Duration of 1 model run ≈ 50 seconds of CPU time).

ure 49b, residuals are normalized by the estimated measurement error. This provides a means to assess how well the model matches the calibration target. Data misfits lie mostly within two standard deviations of measurement errors (95 percent of observation points). Although in general the misfit doesn't display a clear spatial structure, the data match tends to slightly improve in the downstream direction. Also clusters of observation points with large misfits can be observed at a few places: The calibrated model produces relatively large misfits in the area near the pumping well of Evionnaz and in the area near the pumping wells of Sierre. Whilst misfits near Sierre are not systematic, modeled heads close to the pumping well of Evionnaz are systematically lower than conditioning data. It cannot be excluded that abstraction rates for this well are too high in the model. The misfits near Sierre are possibly due to the relatively complicated hydrogeological setting of this area. Relatively high levels of misfits are also present next to the Canal de Vissigen (Figure 49 a and b). Here modeled heads are systematically higher than conditioning data. It is evident that one potential cause for this would be too high values of heads assigned to the boundary condition representing the Canal de Vissigen. This explanation remains however speculative, as the ones given above for other locations with large misfits.

It should be stressed that both conditioning data and the associated errors are estimations and are hence subject to uncertainty. An underestimation of the measurement error might for instance be at the origin of isolated occurrences of relatively large misfits such as near km 37 or km 55 (Figure 49b).

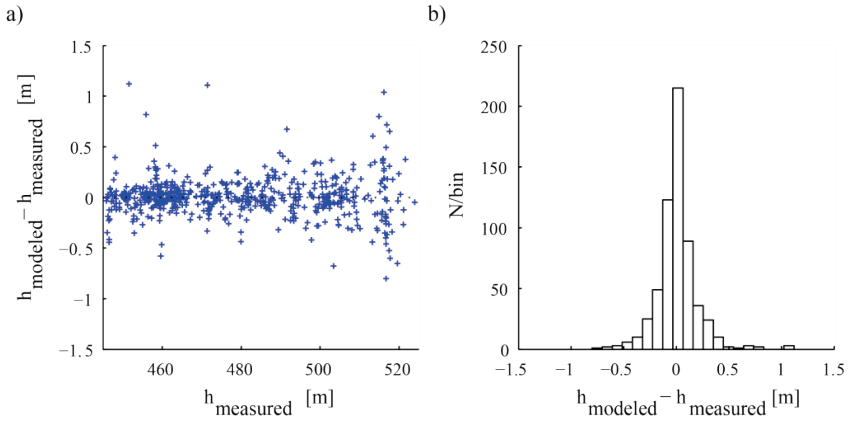

Figure 48 : Residuals between measured and modeled hydraulic heads: a) Scatterplot of residual heads; b) Histogram of residual heads.

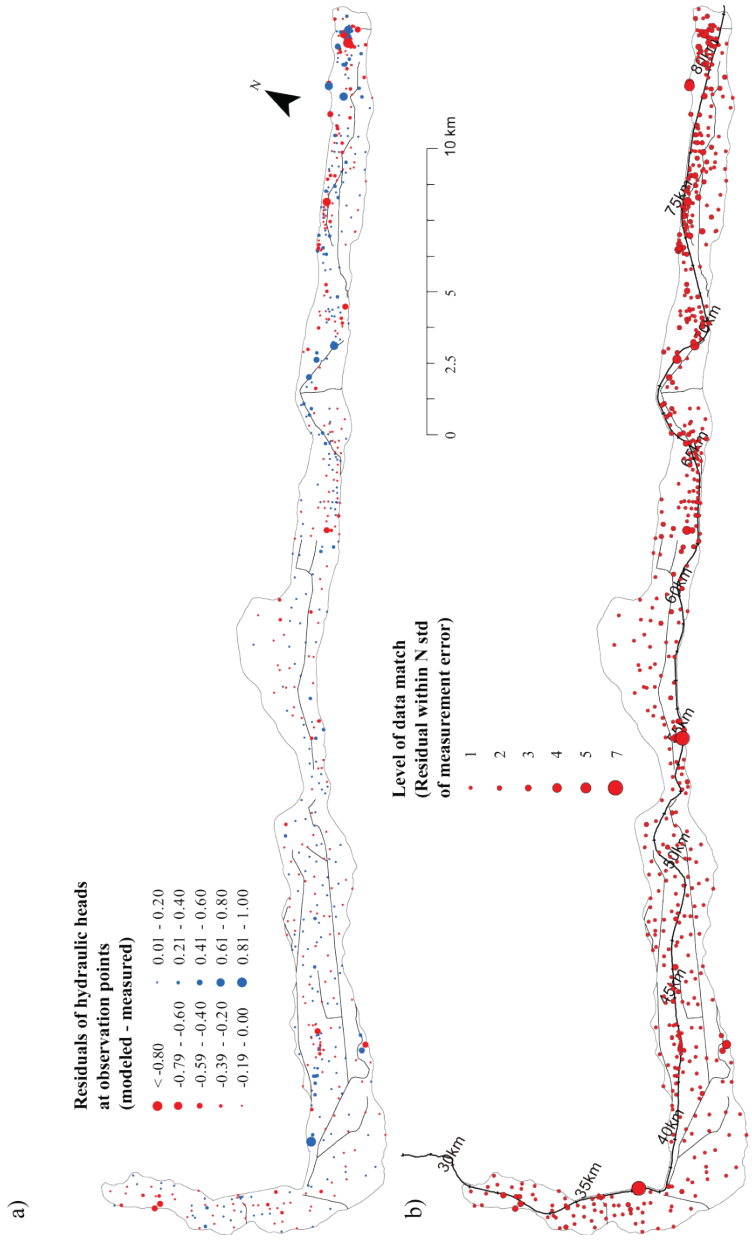

Figure 49 : Residuals between measured and modeled hydraulic heads: a) Absolute values of residual heads; b) Level of data match: Residual heads relative to measurement error (Level 1 = within 1 standard deviation of measurement error).

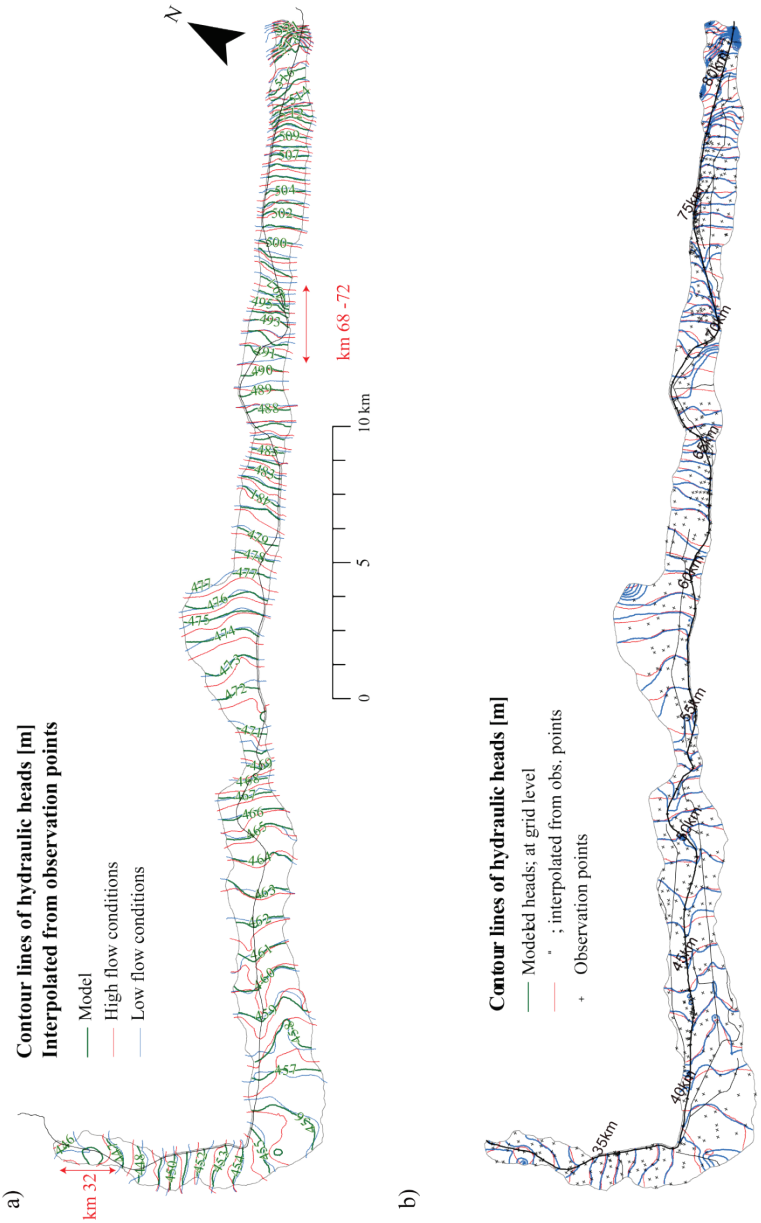

Figure 50 : Contour lines of hydraulic heads; a) Piezometric surfaces of modeled and measured heads interpolated from observation points; b) Piezometric surface of modeled heads at the model grid level superimposed to heads interpolated from observation points.

The comparison between piezometric contour maps of measured and modeled heads in Figure 50a gives a qualitative representation of the distribution of the data match. Contour lines of modeled heads were interpolated by Kriging, based on values at observation points. A geostatistical structure was used similar to the ones used for establishing contour maps of high and low waters [90][33]. The modeled contour lines compare well to measurements, in that flow patterns are generally reproduced and in that contour lines most often fall between corresponding contour lines of measured heads during high and low flow waters. The main exceptions to the good agreement between model outcomes and measurements are the stretch near the pumping well of Evionnaz (~ km 32) and the part at km 68 – 72 near St-Léonard (red arrows in Figure 50a). In the former case, drawdown induced by pumping is exaggerated in the model. In the latter case, the contour lines of modeled heads at the southern limit of the aquifer are deflected towards the aquifer due to inflows from the Rhône River and from the lateral boundary at "Pouta-Fontana".

In Figure 50b, the contour map of heads at the model grid level is superimposed to a contour map interpolated from modeled heads at observation points[34]. This figure illustrates the importance of a good spatial coverage by observation points for a valid identification of hydrogeological boundaries. For instance the influence of River Dranse in the model (~ at km 39) is only barely visible based on head measurements at observation points used as conditioning data herein.

In Figure 51 heads in the aquifer underneath the Rhône River are presented in a profile view. Values of both measured and modeled heads were interpolated from heads at observation points of the conditioning data set, as for Figure 50a. Heads in the aquifer for high, mean (model) and LW are plotted relative to corresponding water levels of the Rhône River in Figure 51a and relative to the elevation of the river bed in Figure 51b. In both plots, modeled heads run to a large part between curves of measurements during high and low water conditions. With regard to the hydraulic relation, steady state GW-SW interactions between the Rhône River and the alluvial aquifer are thus adequately reproduced by the model.

[33] A linear variogram with $\gamma(h) = 1\,h$ and a range of 1000 m was considered.
[34] Green lines in Figure 50a correspond to red lines in Figure 50b.

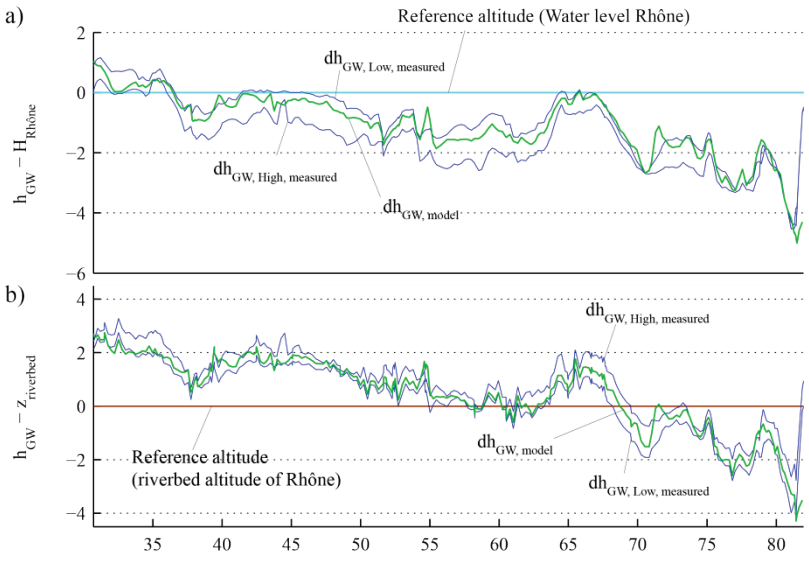

Figure 51 : Comparison of interpolated values of measured and modeled groundwater heads along the Rhône River relative to a) the water level of the Rhône River and b) the elevation of the streambed (data PR3).

5.6.2 Performance of NSMC realization

Results of the NSMC analysis were post-processed in that simulations for which re-calibration did not occur within one optimization run, were filtered out. Choosing a threshold value for which re-calibration is considered achieved always involves a certain degree of subjectivity, especially in the presence of structural noise [119]. Here simulations that yielded an objective function of more than 1'200 were filtered out.

Because the objective function quantifies the average misfit, simulations may be accepted that display a poor fit in some part of the model, if the filter step is limited to setting a threshold value. Therefore, an additional requirement for a simulation to be accepted was that all residuals be within 5 standard deviations of measurement noise.

Figure 52a shows residuals between calibration data and model outcomes of the 535 accepted stochastic realizations. In Figure 52b the histogram of objective functions of accepted realizations is displayed. Figure 53 shows that outcomes of the accepted NSMC realizations are slightly biased towards higher values, especially in the uppermost 2 km of the model.

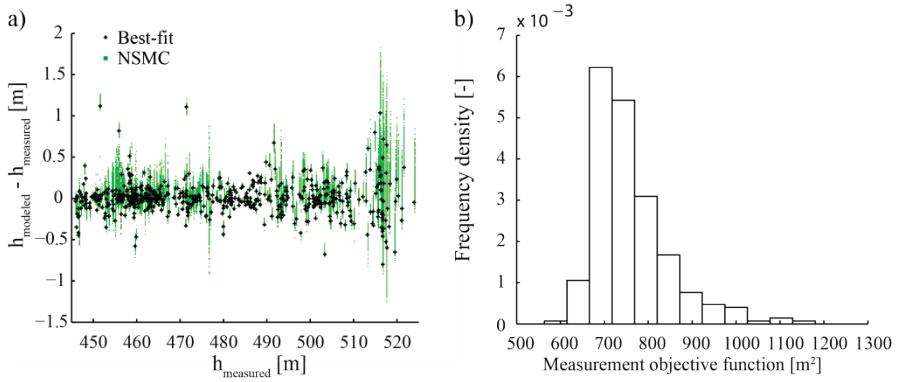

Figure 52 : Data match of accepted simulations: a) Scatter plot of residuals; b) Histogram of objective functions.

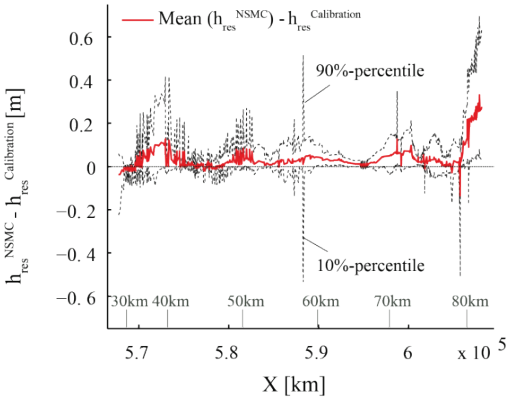

Figure 53 : Comparison of residual heads at observation points resulting from NSMC realizations (h_{NSMC}) and from the calibration solution ($h_{calibration}$). Ideally the mean of h_{NSMC} would correspond to $h_{calibration}$ (kilometer values refer to running kilometers of the Rhône River).

5.7 Parameter estimates

5.7.1 Calibration solution

Figures 54 – 56 display parameters of the calibrated model in different forms. Figure 54 gives an overview of parameters in map view. Figure 55 re-traces the evolution of parameters of the inverse problem along the optimization process. Figure 56 shows histograms of pilot-point-based parameters at the model grid level.

For the calibration solution, influx across model limits is highest at the upstream model limit, as shown by the inset in the upper left corner of Figure 54. The relatively high value is in agreement with the estimate made prior to the optimization run (Table 14). The optimized value is higher than the initial guess and is close to what has been considered as the maximum reasonable value (Figure 55b)[35]. In the calibration solution, fluxes at other outer boundary conditions are at least one order of magnitude smaller than the one at the upstream limit and optimized values are often close to initial guesses. Exceptions to this occur at boundary conditions north of Sierre and near Conthey, where fluxes rise along the optimization process and reach relatively high values (Figure 55b). For the boundary near Conthey, the optimized value is at the upper parameter bound. Because the lengths of lateral boundaries are relatively homogeneous, a similar picture as for fluxes results regarding flow rates at model limits, as will be shown below in section 5.8.1.

Figures 59 and 55 lack a representation of heads at the downstream boundary condition. This parameter displays almost no variability along the optimization process and its optimized value corresponds to the initial value.

Recharge by precipitation in the calibration solution largely follows the prior distribution with high values in the western part and low values in the eastern part (Figure 54). A closer look on parameter values reveals that for the four westernmost zones parameters hit the upper bound. On the contrary, values are at the minimum of zero for zones 8, 10 and 11 in the eastern part. In the remaining zones (5, 6, 7 and 9), estimated parameter values are close to initial values.

[35] Solving the Darcy law assuming an average hydraulic gradient of 5e-3 (Table 14) yields a hydraulic conductivity of 3e-4 m/s at the upstream boundary.

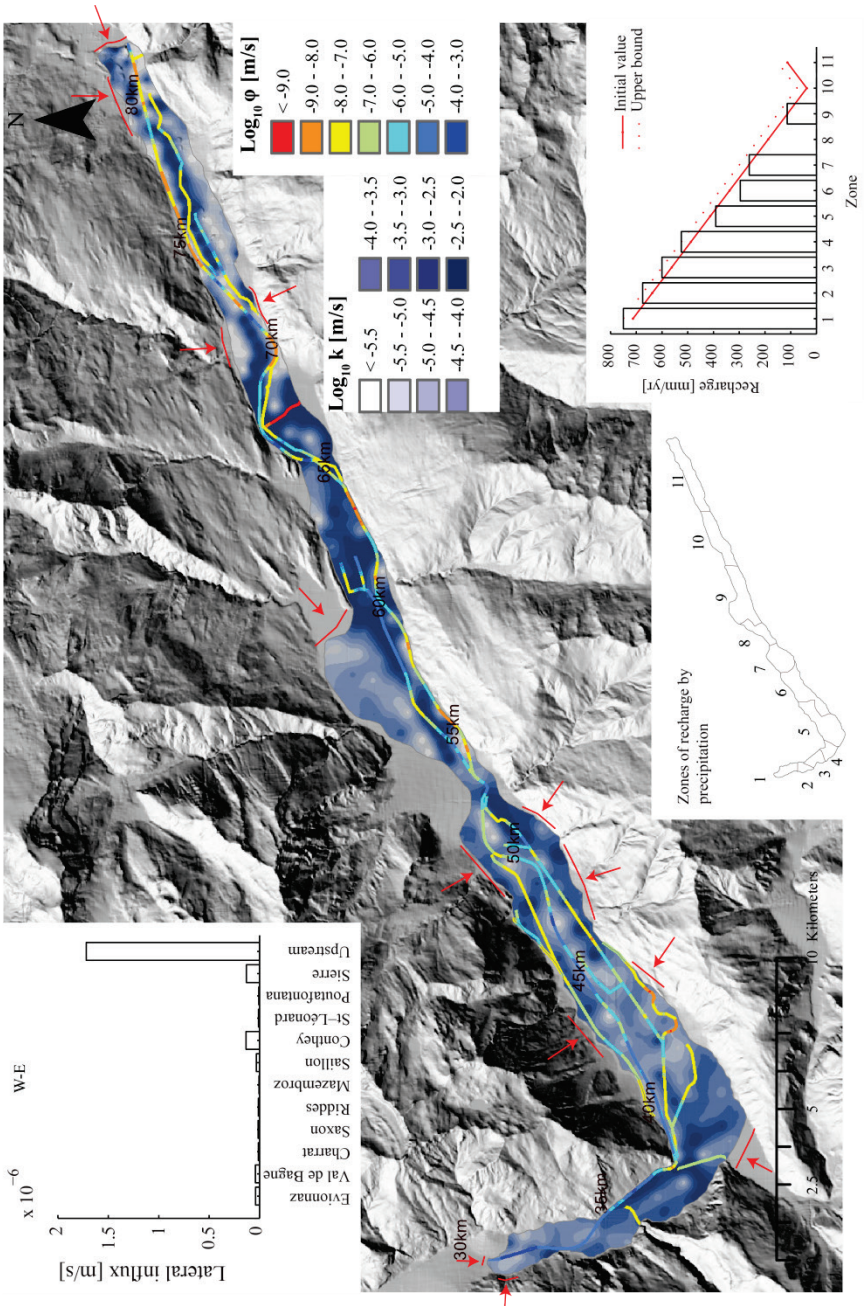

Figure 54 : Overview map of best-fit parameter values (background map: greyscale hillshade of the DTM [144]).

On a very schematic level, the best-fit hydraulic conductivity field can be described as follows (Figure 54): the uppermost 10 – 15 km are characterized by low[36] and very low permeability zones often running parallel to the valley which stand in sharp contrast to areas of high to very high hydraulic conductivity. This part is followed in the downstream direction by a considerably more uniform stretch where high to very high values of hydraulic conductivity prevail (km 54–70), the main exception being the part at the northern model limit between Conthey and the alluvial fan of Losentse, where hydraulic conductivities are predominantly low to moderate. This zone gives way to a transitional zone with an overall moderately permeable area running along the center axis of the valley and being flanked to the north and south by zones of high to very high conductivities (km 45–54). The part between km 40 and km 45 is dominated by rather low to moderately permeable sediments. The area around the "elbow" near Martigny is heterogeneous and displays a branched zone of high to very high hydraulic conductivities (km 35–40). Toward the downstream limit, hydraulic conductivities tend to decrease.

The histogram of logarithms of the best-fit parameter field of hydraulic conductivities is presented in Figure 56a. It displays two modes that lie around the mode (and the mean) of the histogram of prior estimates of hydraulic conductivity (see section 5.2.4). The histogram looks as if it was cut laterally, which indicates that the estimation was constrained by parameter bounds. This appears also from Figure 55a, which shows that during the optimization process many of the pilot point parameters hit parameter bounds. At the end of the optimization process, the optimized value of almost a third (29%) of all pilot points lies at the upper or lower bound. As Figure 57 shows, many of the concerned points are located in the upper part of the model.

Transfer rates of the Rhône River vary over the entire range specified by parameter bounds (Figures 56c and d). Both for infiltrating and for exfiltrating conditions, the modes of the histograms lie slightly below initial values. At a few places with infiltrating conditions, parameters are at the lower parameter bound (Figure 55c); the histogram for infiltrating conditions in Figure 56c seems to be constrained by the lower parameter bound.

---

[36] The terminology defined in this section to describe hydraulic conductivities (k) is:

Very high :	$k \geq$ 1e-2 m/s
High :	1e-3 m/s $\leq k <$ 1e-2 m/s
Moderate – rather high :	1e-4 m/s $\leq k <$ 1e-3 m/s
Rather low :	1e-5 m/s $\leq k <$ 1e-4 m/s
Low :	1e-6 m/s $\leq k <$ 1e-5 m/s
Very low :	$k <$ 1e-6 m/s

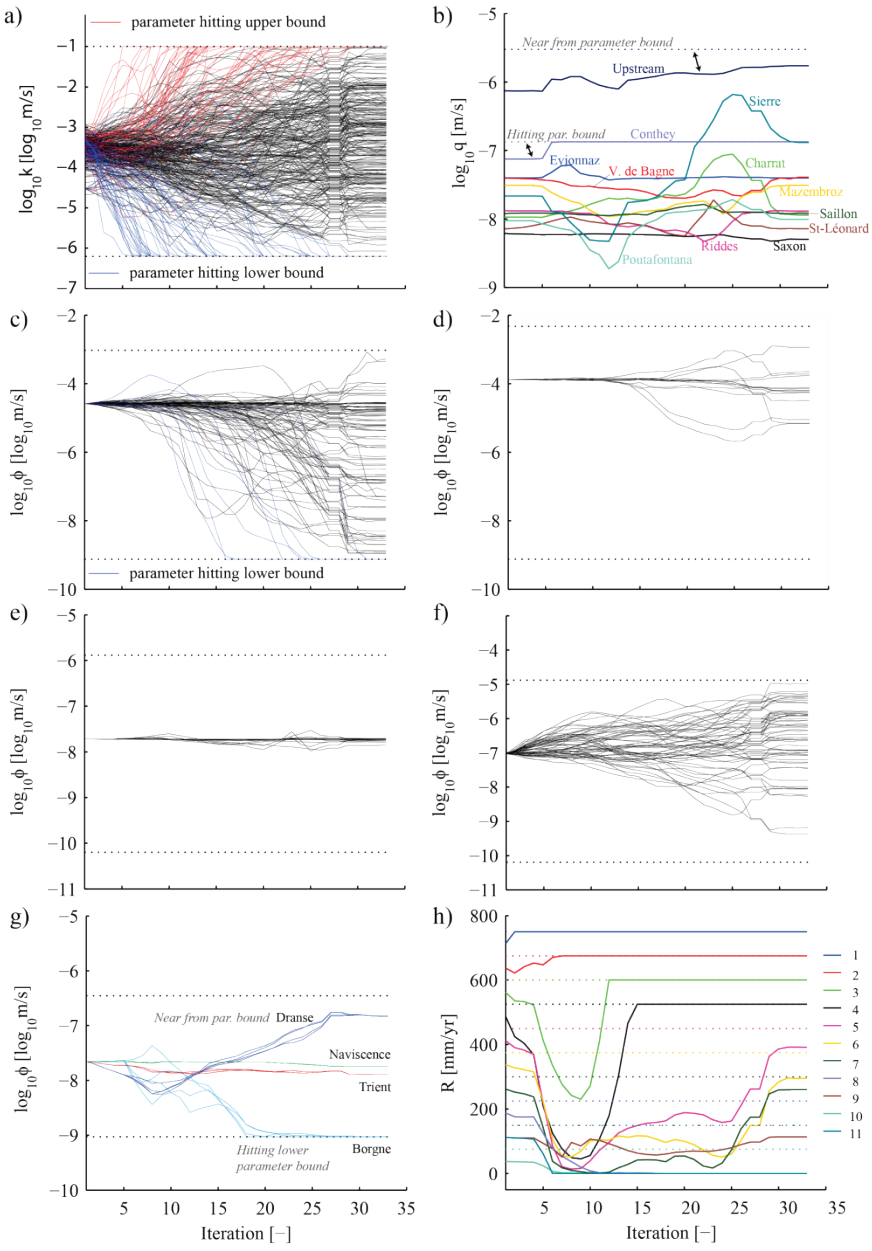

Figure 55 : Evolution of parameters along the optimization process; a) Hydraulic conductivity; b) Nodal flux across model limit; c) Transfer rate, Rhône River, in; d) Transfer rate, Rhône River, out; e) Transfer rate, ditches, in; f) Transfer rate, ditches, out; g) Transfer rate, tributaries, in; h) Recharge through precipitation.

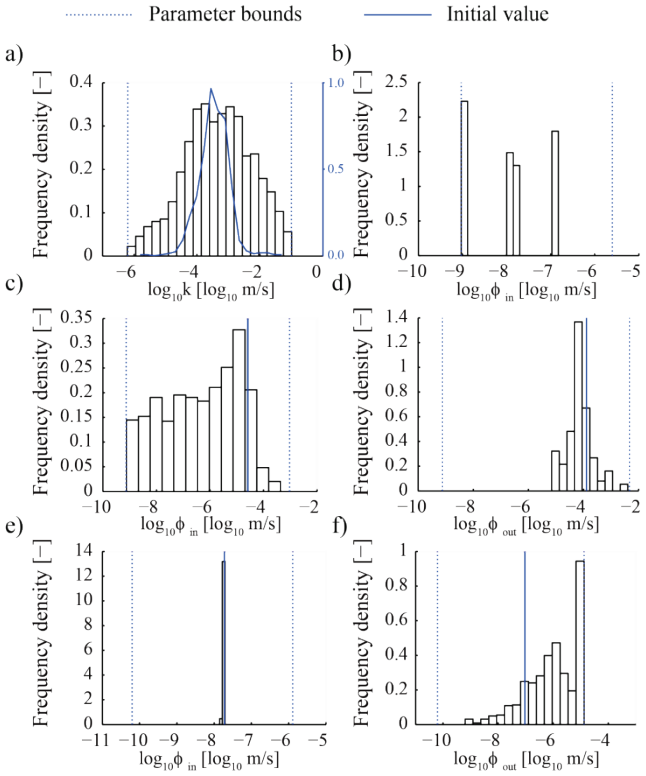

Figure 56 : Histograms of model parameters parameterized trough pilot points at the grid level; a) Hydraulic conductivities; b) Transfer rates of tributaries (infiltrating conditions); c) Transfer rates of Rhône River for infiltrating conditions; d) Transfer rates of Rhône River for exfiltrating conditions; e) Transfer rates of ditches for infiltrating conditions; f) Transfer rates of ditches for exfiltrating conditions.

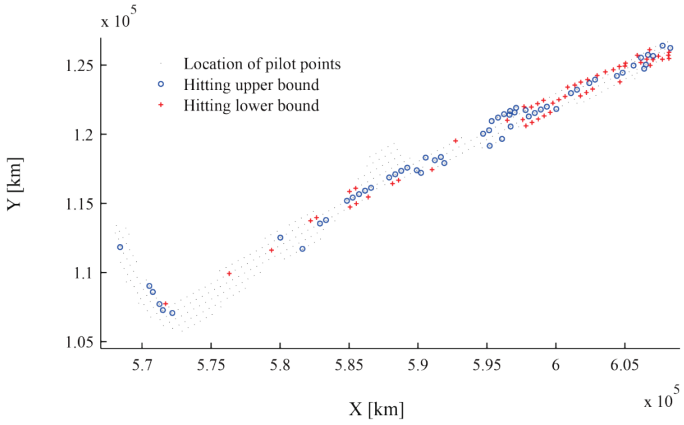

Figure 57 : Location of pilot points where values of aquifer conductivity are at parameter bounds.

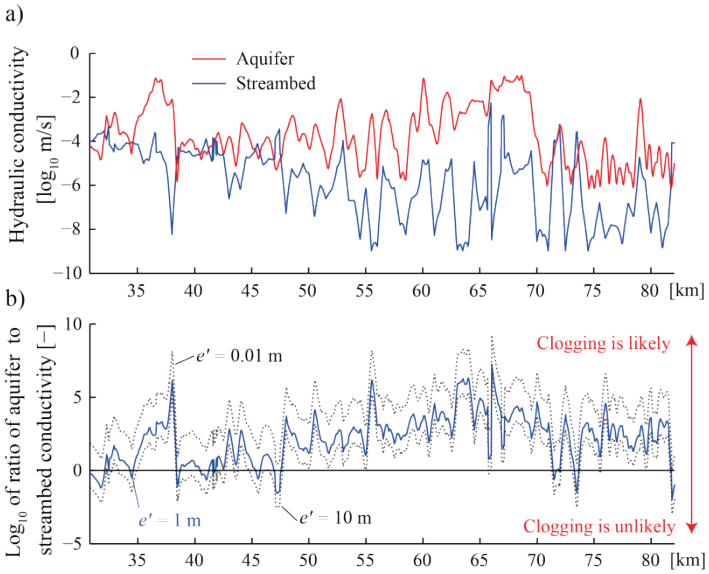

Figure 58 : a) Comparison of hydraulic conductivities of the streambed and the aquifer underneath the Rhône River; b) Ratio of aquifer conductivities over streambed conductivities.

Figure 58 compares estimated hydraulic conductivities of the streambed of the Rhône River with conductivities of the underlying aquifer. Hydraulic conductivities of the streambed were calculated using the relation between the streambed conductivity and the transfer rate derived in Chapter 4. Solving Equation [4.4] for k' yields:

$$k' = \frac{2\varphi e' h_s}{W} \qquad [5.9]$$

where φ is the transfer rate (LT^{-1}), k' (LT^{-1}) is the hydraulic conductivity of the streambed and $e'(L)$ its thickness, W (L) is the river width and h_s (L) is the saturated thickness. Streambed conductivities shown in Figure 58a were calculated assuming $W = 60$ m, $h_s = 40$ m and $e' = 1$ m. It can be observed that streambed conductivity exhibits an increasing trend in the downstream direction and that it is mostly lower than aquifer conductivity. Aquifer and streambed conductivity seem to be loosely connected, even if no clear correlation can be detected from a scatterplot of these parameters. In Figure 58b the ratio of aquifer conductivity k to streambed conductivity k' is represented (k/k'). The y-axis is scaled logarithmically because the ratio is very high in some places. The lower the ratio, the less likely is the presence of a clogging layer and vice versa. Values below zero indicate stretches on which the streambed conductivity is higher than the hydraulic conductivity of the aquifer. Here different values of streambed thickness (0.1 m, 1 m and an extreme value of 10 m)

were considered to account for the uncertainty related to that property. It can be seen that as judged by calibrated parameters, large parts of the streambed are clogged.

While transfer rates of ditches vary considerably for exfiltrating conditions (Figures 55f and 56f), they remain practically unaffected by the optimization process for infiltrating conditions and stuck at the initial value (Figures 55e and 56e). The histogram in Figure 56f indicates that the estimation of transfer rates of ditches for exfiltrating conditions has been considerably constrained by the upper parameter bound.

Transfer rates of tributaries are homogeneous for each tributary. Values of Rivers Naviscence and Trient are only weakly altered in the optimization. Transfer rates of River Dranse increase along the optimization before stabilizing at values that are relatively close to the upper bound. In contrast, initial values at River Borgne are decreased by PEST and reach the lower bound.

As the discussion on parameter estimates has to be held in the light of their uncertainty, parameter estimates will be revisited in the next section which deals with parameter uncertainty. It will become clear that some of the parameters are poorly informed by the conditioning data set and that respective estimates are thus uncertain. To complete this preliminary discussion on parameter estimates, a summary of modes and mean values of distributions of pilot-point based parameters has been provided in Table 18.

Table 18 : Modes and mean values of distributions of pilot-point-based parameters in the calibration solution.

	Mode(s)		Mean	
	[$\log_{10}$ m/s]	[m/s]	[$\log_{10}$ m/s]	[m/s]
Hydraulic conductivity	-3.75 / -3.02	1.8e-4 / 9.4e-4	-3.33	4.7e-4
Transfer Rate, Rhône, in	-4.91	1.2e-5	-6.34	4.6e-7
Transfer Rate, Rhône, out	-4.18	6.6e-5	-4.14	7.2e-5
Transfer Rate, Ditches, in	-7.74	1.8e-8	-7.73	1.9e-8
Transfer Rate, Ditches, out	-5.89 / -5.03	1.3e-6 / 9.3e-6*	-6.03	9.4e-7

** Mode resulting from the accumulation of values at the upper parameter bound.*

5.7.2 Uncertainty of estimated parameters

Results of the NSMC uncertainty analysis represented in Figure 59 indicate that lateral fluxes coming from the alluvial plain of "Val de Bagne" and from valley slopes near Saxon, Riddes, Saillon and Mazembroz are poorly informed by the calibration data, compared to influx at other places. In comparison to other places, influxes at the upper model limit and from the slope north of Sierre display a low variability if outliers are not considered. Influx at Evionnaz, Charrat, St-Léonard and "Pouta-Fontana" seems to be relatively well informed by calibration data. The calibration solution lies

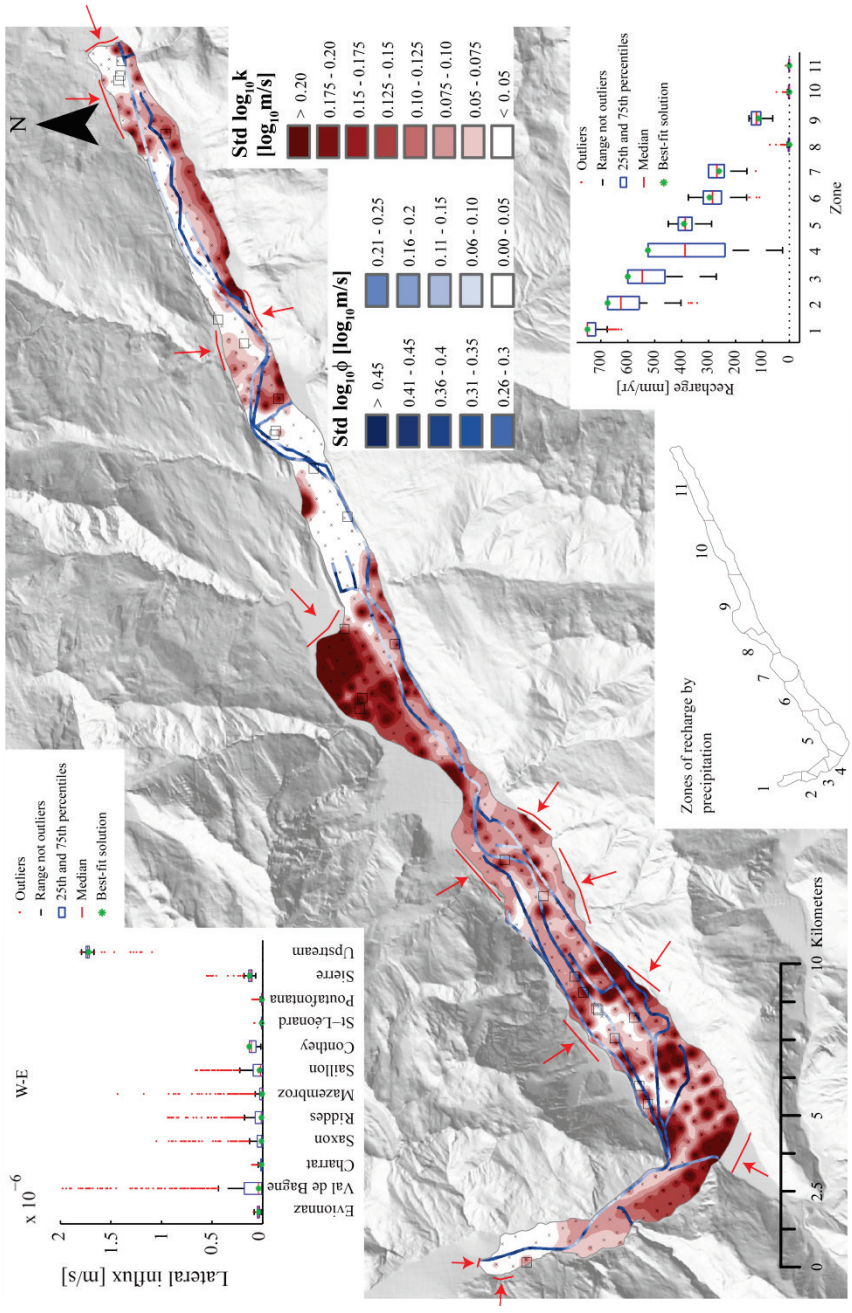

Figure 59 : Overview map of parameter uncertainty quantified by a NSMC analysis (background map: greyscale hillshade of the DTM [144]).

in all cases close to the median of the distribution resulting from the NSMC analysis.

Uncertainty of recharge by precipitation is generally smaller in the upper part of the model (zones 8 – 11). A high uncertainty results for zones 2 – 4 downstream of Martigny, with whiskers extending over almost the entire range between the upper and lower bound for zone 4. In zones with a high uncertainty (zones 2 – 4), the median of parameters yielded by the NSMC analysis is lower than the best-fit parameter. For other zones, best-fit estimates are close to the median.

Uncertainty of aquifer conductivity is expressed through the standard deviation of logarithms of hydraulic conductivity in the map view in Figure 59. Values of standard deviations range between 0.01 and 0.42 $\log_{10}$ m/s. The mean standard deviation is 0.10 $\log_{10}$ m/s[37]. The map of mean values is not presented herein, because it closely resembles the map of the calibration solution. Large coherent zones of small parameter uncertainty are present near the lower model limit downstream from Dorénaz, in the center part of the model between Aproz and Borgne River (km 62 – 68) and close to the upper model limit. In the upper part of the model between St-Léonard and Chalais (km 70 – 78), the uncertainty increases from low values close to the Rhône River to relatively high values when moving away from the river. A zone of small parameter uncertainty can also be observed near Fully. In this area however, zones of small uncertainty alternate with zones of high uncertainty within a small range. Uncertainty is overall relatively high around the "elbow" at Martigny, besides a small strip following the aforementioned highly conductive zone appearing in this area. On a regional scale, high uncertainties are also indicated for the area around Charrat (km 41 – 45) along the southern model limit and for the northern part of the area between Conthey and the alluvial fan of Losentse (km 55 – 59). Uncertainties are also comparingly high in the area of the alluvial fan of Sionne River, at Sion, in the upstream part of the alluvial fan of the Borgne River and at local spots in the area between km 40 and km 60.

Compared to aquifer conductivity, transfer rates generally display a higher uncertainty with standard deviations of 0.03 – 1.38 $\log_{10}$ m/s and a mean value of 0.25 $\log_{10}$ m/s. Uncertainties are generally higher in the downstream part of the Rhône River. Transfer rates are uncertain in the lowermost part of the model (< km 33.5), on the stretch between Martigny and Saxon (km 38 – 48; with an interruption around km 43 – 44), and near Sion (km 65 – 68). In contrast, low uncertainties arise on short

[37] A calculation example:
$\log_{10} k$ = -3.3 + 0.1 [$\log_{10}$ m/s] → k = $6 \cdot 10^{-4}$ m/s
$\log_{10} k$ = -3.3 - 0.1 [$\log_{10}$ m/s] → k = $4 \cdot 10^{-4}$ m/s

stretches around km 34, 35, 43 – 44, 48 – 49, 53, 62 and 64.5, as well as on a long stretch in the upstream part between "Pouta-Fontana" and Sierre (km 73 – 81).

Uncertainties of transfer rates at drainage ditches tend to be higher than for the Rhône River and display a large variability. Transfer rates at tributaries are generally rather high, especially for the Trient River and the Naviscence River.

A sensitivity analysis about the calibration solution was performed in order to compare the "identifiability" of parameter groups between each other. Indices of "parameter identifiability" of parameters were computed as the length of the solution space projection of a given parameter compared to its length in parameter space[38]. A value of zero means that the given parameter lies entirely in the calibration null space and is not identifiable. On the opposite, a value equal to one signifies that a parameter lies entirely in the solution space and that it can – besides the contribution of measurement noise to its estimation error – be entirely identified.

Figure 60 presents parameter identifiability indices clustered according to their belonging to parameter groups. Referring to the median value of indices, recharge by precipitation is all in all the best informed parameter group, followed by hydraulic conductivity. Boundary conditions at model limits and transfer rates are less well identifiable, especially for tributaries and – to a lesser degree – for ditches.

While no clear quantitative relation exists between the local availability of measurements and parameter uncertainty, Figure 61a indicates that high uncertainties of hydraulic conductivities are always related to a low density of observation points, and

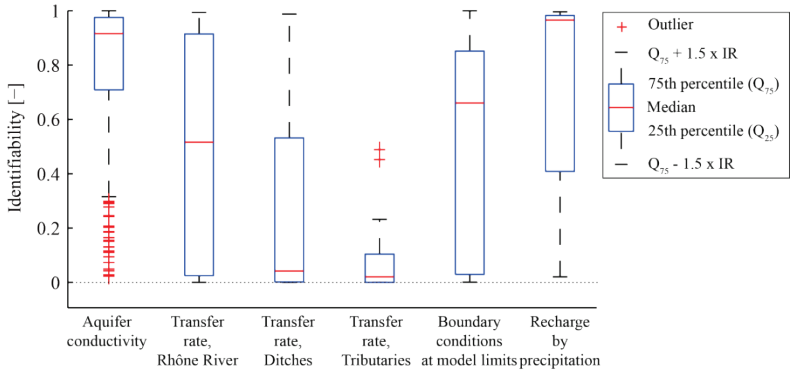

Figure 60 : Parameter identifiability for different parameter groups (Heads at the downstream limit and fluxes at the upstream limit and at lateral limits are grouped in the class 'Boundary conditions at model limits').

[38] Using the PEST utility IDENTPAR.

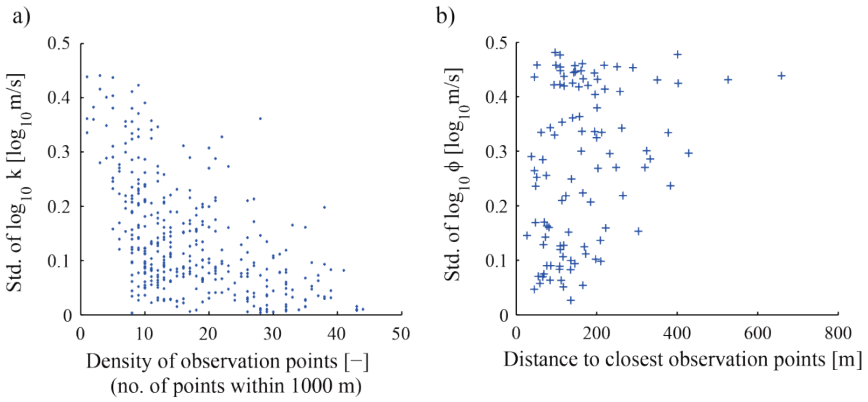

Figure 61 : Influence of data availability on parameter uncertainty a) Uncertainty on aquifer conductivities at pilot points vs. density of observation points in the surroundings (no. of points within a radius of 1'000 m). b) Uncertainty on aquifer conductivities at pilot points vs. distance to closest observation point.

Figure 61b shows that low uncertainties of transfer rates at the Rhône River occur exclusively where the nearest measurement point is located nearby.

In section 5.9, it will become clear that within the range of uncertainty related to abstraction rates at wells, parameters can actually only be estimated in a relative manner based on the given calibration data. This means that if all model parameters – apart from boundary conditions involving hydraulic heads – are multiplied by a given factor, the very same flow fields emerges. This underlines the importance of well-chosen prior parameter estimates and parameter bounds.

5.8 Simulated flow rates

5.8.1 Water balance

As stated earlier, surface water – groundwater exchange is thought to be an important component of the water balance of the Rhône alluvial aquifer. This conceptual understanding is well represented in the numerical model, as can be seen by the water balance given in Figure 62a: river infiltration represents 86% of the mean aquifer recharge of accepted NSMC realizations. Recharge by precipitation is the second most important source of aquifer recharge. The by far largest contribution to river infiltration is made by the Rhône River followed by a relatively non-significant contribution made by infiltration at the Dranse River (Figure 62b and e). Tributaries as well as ditches are all in all of minor importance for recharge. Similarly, inflow from valley slopes or lateral alluvial plains is marginal, the largest proportion coming from the up-

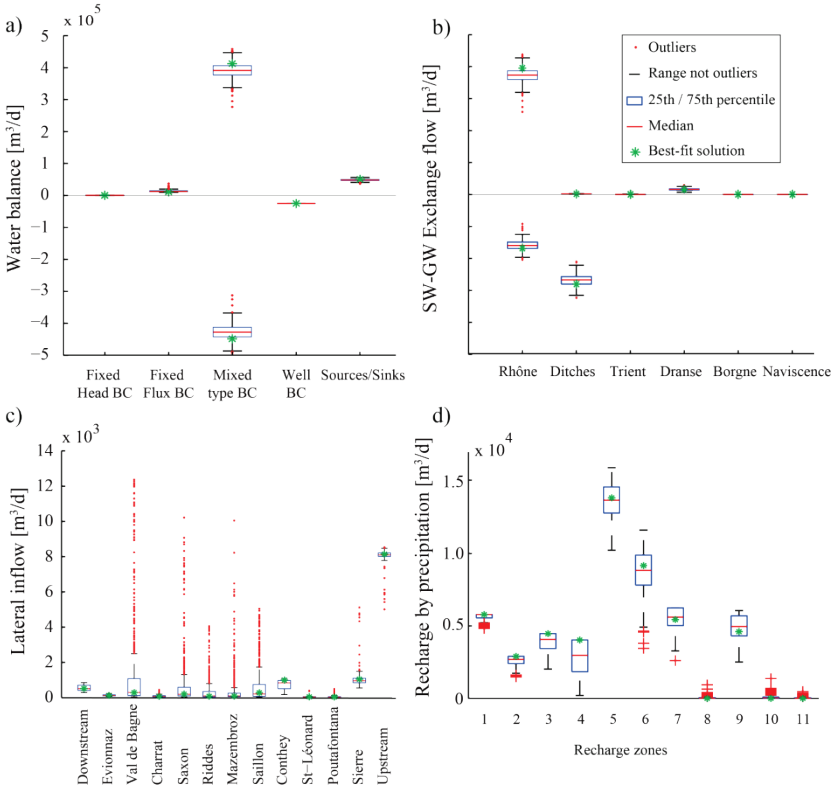

e)

Boundary Type	Inflow		Outflow	
	[m³/d]	[% in]	[m³/d]	[% out]
Downstream head	558 ± 144	0.1	-13 ± 11	0.0
Fluxes at model limits	13'167 ± 3'286	2.9	-	-
Rivers	390'970 ± 21'410	86.3	-427'800 ± 22'289	94.5
Rhône River	*373'054 ± 20'434*	*82.4*	*-159'263 ± 13'988*	*35.2*
Ditches	*1'758 ± 393*	*0.4*	*-268'537 ± 17'081*	*59.3*
Tributaries	*16'160 ± 3'718*	*3.6*	-	-
Well boundary conditions	-	-	-25'040 ± 0	5.5
Recharge by precipitation	48'165 ± 2'808	10.6	-	-
Total	452'860 ± 22'290	100.0	-452'853 ± 22'289	100.0
Imbalance	7 ± 19	0.002	-	-

Figure 62 : Simulated water balance for the current state resulting from the calibration solution and from NSMC realizations; a) Flux according to boundary condition types; b) Detail of fluxes at mixed type boundary conditions (rivers); c) Detail of fluxes across model limits; d) Detail of fluxes from recharge by precipitation; e) Table of fluxes resulting from NSMC realizations (Surface of the model: 84 km^2).

stream model limit. The occurrence of an inflow at the downstream limit is rather unexpected and might be related to too a high abstraction rate at the nearby pumping well of Evionnaz. Exfiltration by surface waters is, by far, the most important draining process of the aquifer. Corresponding to 59% of the outflow, ditches have – according to modeling results – a major influence on groundwater flow in the alluvial Rhône aquifer. The other main contribution to outflow is made by the Rhône River (36% of the total outflow). Compared to exfiltration by surface water, abstraction rates at wells are relatively small. The small error in the water balance (0.002 %) can be taken as an indication that the code correctly solves the flow problem [140].

The NSMC analysis yielded a total inflow of 452'860 ± 22'290 m^3/d; the total inflow could thus be estimated with an uncertainty of 5%. The same uncertainty results for infiltration and exfiltration rates at the Rhône River.

Similarly to the Rhône River, the Thur River in the Canton Thurgau is currently undergoing restoration. As in the case for the flow model presented herein, the restoration project motivated the construction of a groundwater flow model. As both projects are scientifically supported by the "Rhône-Thur River project" [21], we had access to inverse modeling results of the Thur alluvial aquifer [157]. It is – as a side note – interesting to notice that elements of the water balance of the Rhône alluvial aquifer arising from the flow model established herein closely resemble the results of the Thur model, as shown in Table 19. This is possibly explained by the hydrogeological setting of unconsolidated alluvial deposits that is common to both sites. It must be stressed however, that no detailed comparison between the hydrogeological characteristics of both sites has been established. Therefore, the good agreement of the water balances has to be interpreted with caution.

Table 19 : Comparison of water balances calculated using calibrated flow models of the Rhône and the Thur alluvial aquifers.

	Rhône (Surface: 84 km^2)				Thur (Surface: 64 km^2)			
	In		Out		In		Out	
	[m^3/s]	[m/s]	[m^3/s]	[m/s]	[m^3/s]	[m/s]	[m^3/s]	[m/s]
SW - GW exchange	4.77	*5.7E-08*	-5.19	*-6.2E-08*	3.50	*5.5E-08*	-3.62	*-5.7E-08*
Recharge	0.58	*6.9E-09*	0	*0*	0.43	*6.7E-09*	0	*0*
Lateral in-/outflow	0.13	*1.6E-09*	0.00	*-1.8E-12*	0.05	*7.8E-10*	0	*0*
Abstractions	0	*0*	-0.29	*-3.4E-09*	0	*0*	-0.36	*-5.6E-09*

5.8.2 Nodal flow rates and SW–GW exchange

The map in Figure 63a exposes recharge and discharge of the groundwater – surface water system and recharge by lateral inflows. The represented flow rates have no direct physical meaning because they correspond to nodal flow rates of the flow model and depend on the size of model cells.

Simulated flow rates of SW-GW exchanges exhibit a large spatial variability. Exchange flow at the Rhône River is concentrated in a few locations at km 37–38, 53, 60, 62, 66–70, 72 and at km 79. At these spots, 85% of the total simulated infiltration flow at the Rhône River and 90% of the total simulated exfiltration flow at the Rhône River take place. It is notable that the stretches at km 37–38, 60, and 62 are located in the immediate vicinity of flooded gravel pits "Le Rosel" and "Les Iles" (Figure 64a and c). The spot at km 72 lies next to the wetland of the natural reserve of "Pouta-Fontana" (Figure 64e). The spots at km 53 and at km 79 (Figure 64b and f) coincide with quarries in which gravel is excavated from the streambed of the Rhône River. The stretch on km 66–70 lies in the alluvial fan of the Borgne River.

Similarly to the Rhône River, large values of exfiltration rates at drainage ditches occur on relatively short sectors: At the uppermost stretches of "Le canal du Syndicat" (around km 50) and "Le canal Sion-Riddes" (around km 58–60) as well as of "Le canal de Chalais" around km 75. It may be noted, that pronounced curvatures of contour lines in the downstream part of Canal du Syndicat (around km 42) are not related to large exchange rates. Their appearance may be explained by the rather low to moderate hydraulic conductivity in this region.

In Figure 63b, maps of hydraulic relations between the Rhône River and the aquifer during HW and LW are presented. The maps were derived based on interpolations of average heads in the aquifer during HW and LW [90] to the axis of the Rhône River and on modeled water stages in the Rhône River for respective conditions (data PR3). As already stated in the comment to Figure 51, GW-SW interactions between the Rhône River and the alluvial aquifer are satisfyingly reproduced by the model.

Figure 65 represents mean values and standard deviations of specific SW – GW exchange rates per meter of surface water bodies. Characteristics of exchange flow are very similar to those arising from the calibration solution (Figure 63a) with high values concentrated at the above cited locations. Figure 65b indicates that uncertainty in absolute terms is highest at places where values themselves are high. This suggests that the uncertainty relative to the quantity is homogeneous.

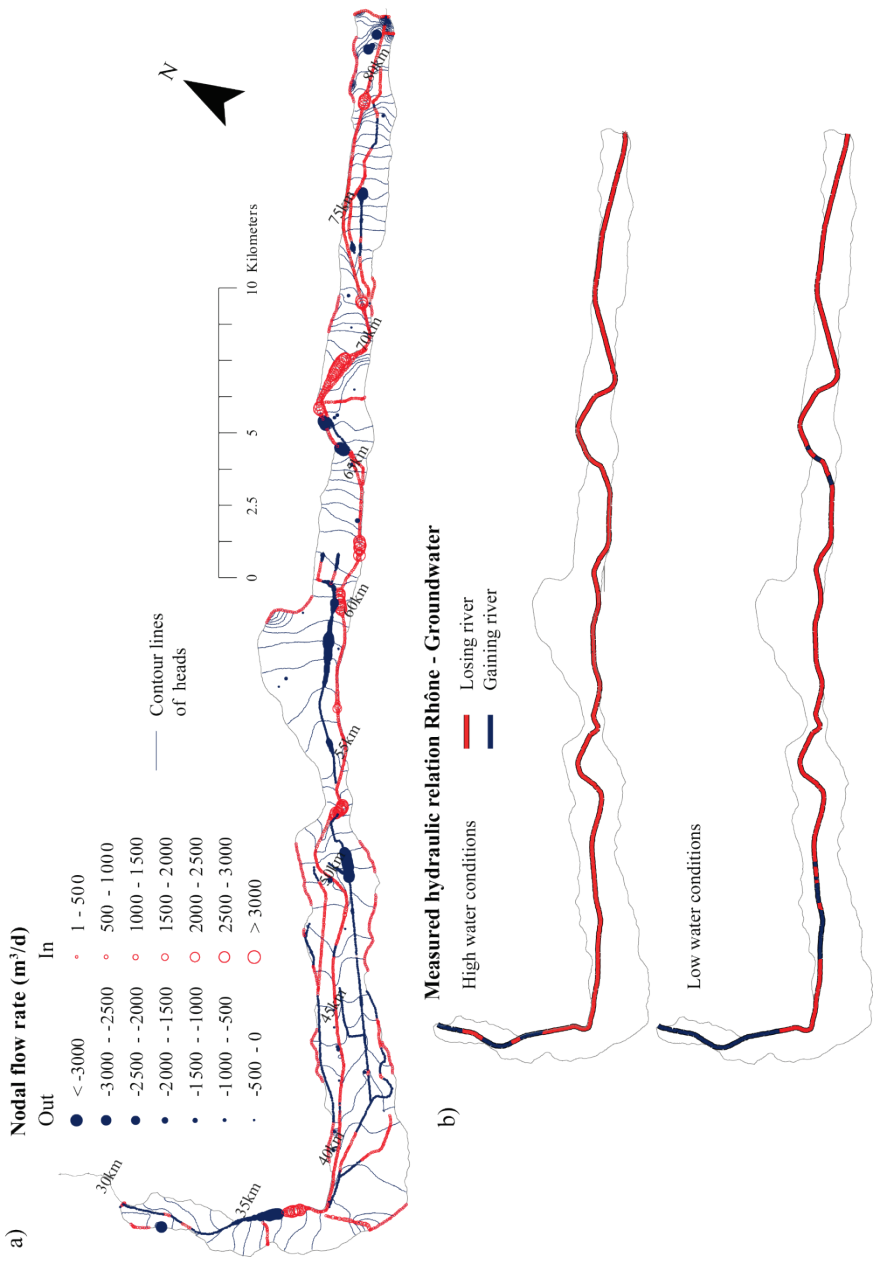

Figure 63 : a) Map of nodal flow rates of resulting with the calibration solution (superimposed to a contour map of heads); b) Hydraulic relation between the Rhône River and groundwater.

Specific SW – GW exchange rates per meter of the Rhône River are also represented in a profile view in Figure 66, along with other quantities. The profile view underlines the observation that simulated exchange flows are concentrated on a few locations (Figure 66d).

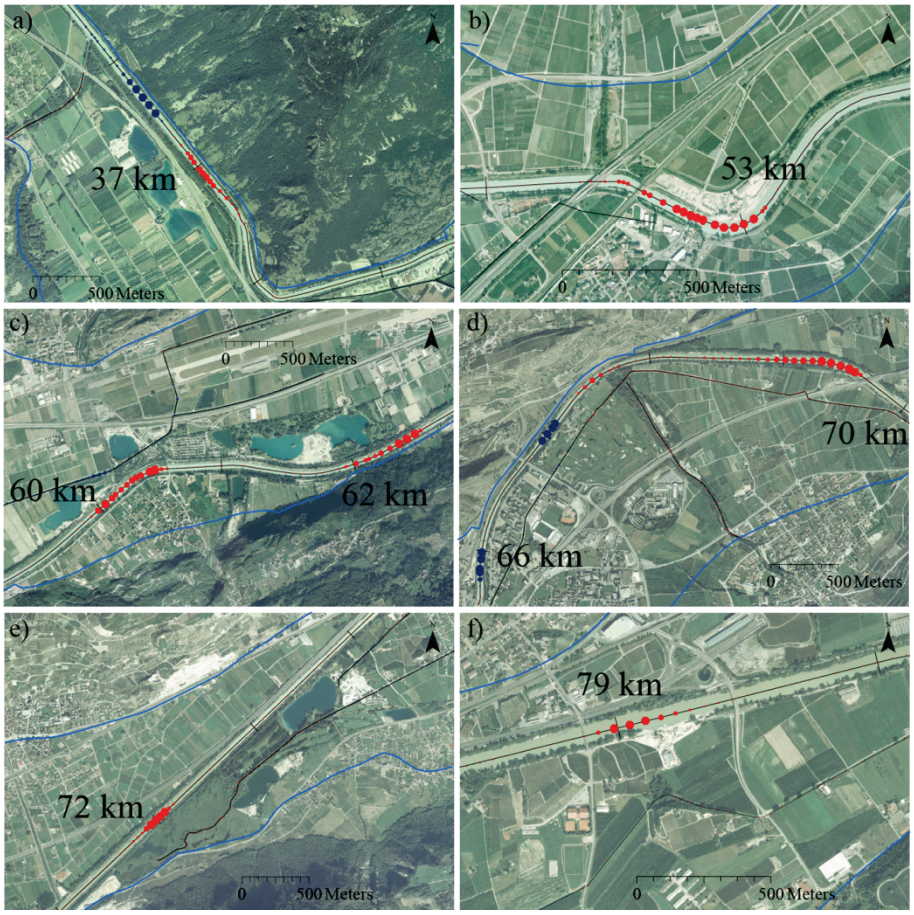

Figure 64 : Sites with high exchange rates between the Rhône River and the alluvial aquifer at a) km 37–38 (“Le Rosel”); b) km 53; c) km 60–62 (“Les Iles”); d) km 66–70 (Alluvial fan of Borgne River); e) km 72 (“Pouta-Fontana”); f) km 79 (background: orthophotos SWISSIMAGE (source: Federal Office of Topography)).

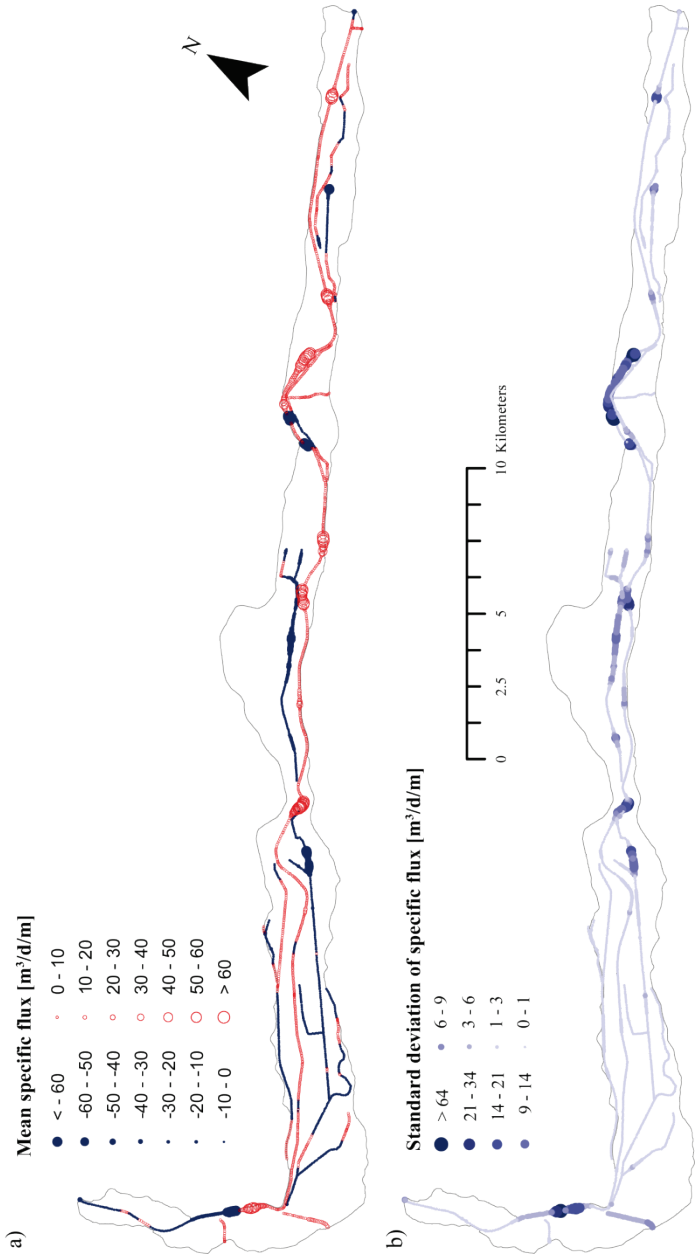

Figure 65 : Mean (a) and standard deviation (b) of specific flow rates (flux per meter of surface water body).

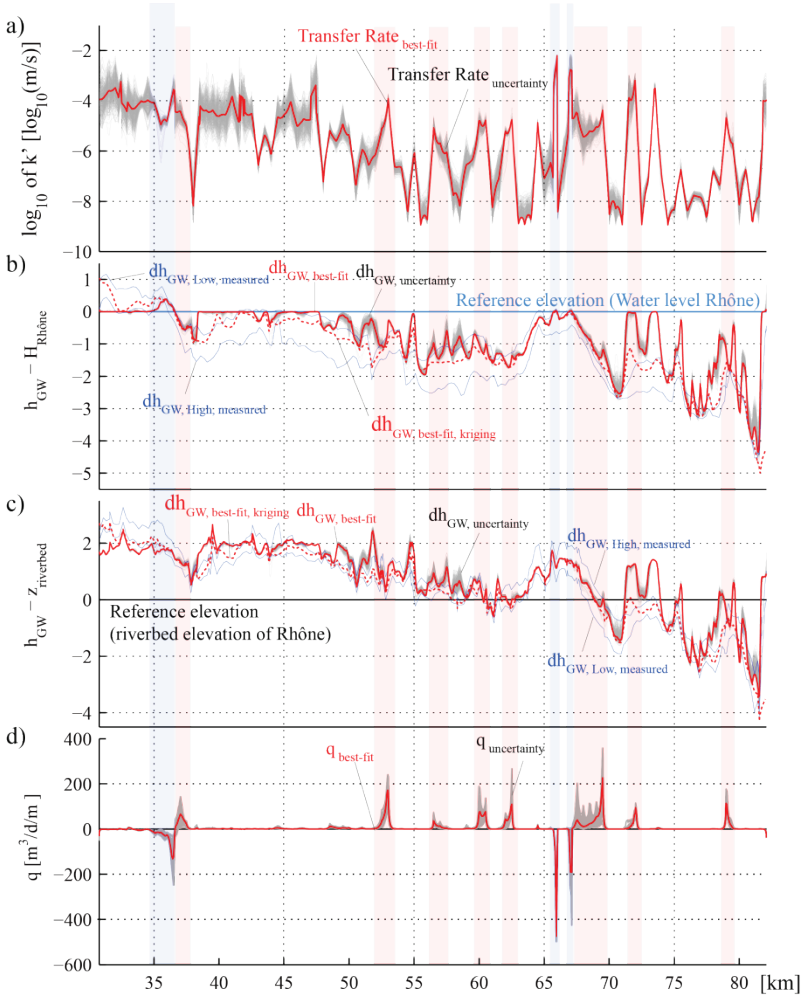

Figure 66 : Profile view of several variables at the Rhône River: a) Transfer Rates; b) Comparison of measured and modeled groundwater heads along the Rhône River relative to the water level of the Rhône River (data from PR3) and c) relative to the elevation of the streambed (data from PR3); d) Specific flow rates per meter of river (river width: about 50 – 60 m).

5.9 Comparison of model outcomes to other data

5.9.1 Exchange rates at ditches

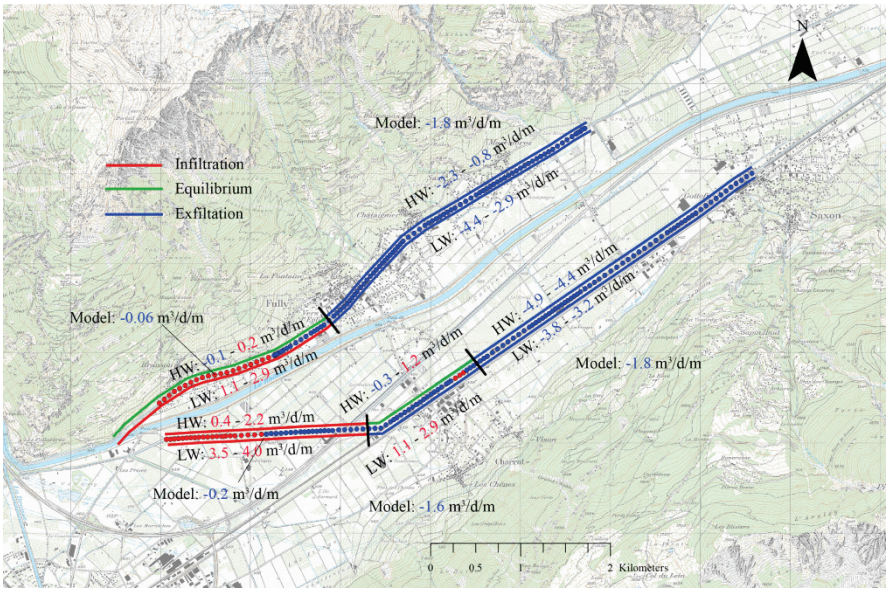

Figure 67 : Comparison between measured and modeled specific exchange rates at drainage ditches at Canal de Leytron – Saillon – Fully (at the North) and Canal du Syndicat (at the South). (Measurement dates: Low waters (LW): 01.03.2010; High waters (HW): 22.05.2010 [9] ; background map: Swiss National Map 1: 25'000 (source: Federal Office of Topography).

In 2010, discharge measurements at the Canal du Syndicat and the Canal de Leytron-Saillon-Fully were performed during low and high water conditions using current meters [9]. Figure 67 compares measured flow rates to values resulting in the model[39]. Hydraulic relations between drainage ditches and the groundwater are similar in the flow model as in measurements. Infiltration is less pronounced in the model, which results in a net exfiltration on the most downstream stretches of both ditches, whereas measurements indicate a net infiltration on these stretches. Exchange rates on stretches with exfiltrating conditions correspond for both ditches satisfyingly well to measured values, even though simulated values are a little lower than values derived from measurements.

[39] Recall that the mean system state, which is represented in the flow model, is closer to LW than to HW, as the period of high waters is shorter than the period of low waters (see Chapter 2).

Based on tracer tests Badertscher [8] calculated specific exfiltration rates of 1.7 m^3/d/m (LW) and of 3.5 m^3/d/m (HW) for the exfiltrating stretch of Canal de Vissigen near Sion. He reports that other studies yielded higher values for HW for periods in which the ditch had been cleaned shortly before (up to 14.6 m^3/d/m). The model calculated value of 4.3 m^3/d/m is slightly above measured values.

The fact that exchange flow rates at ditches compare satisfyingly well to estimations based on measurements is very important for the trust that can be made in model predictions, because within the range of uncertainty related to abstraction rates at wells, head data do not contain any information with regard to absolute parameter values, but allow only their relative estimation. This is illustrated by Figure 68a, where nodal heads of the calibration model are compared to nodal heads calculated based on multiples of calibrated parameters (Multiples of 0.5 and 2)[40]. Obviously, all three parameter sets result in the very same head distribution and none of the three sets can therefore be preferred over another based on calibration data. As they are proportional to flow parameters, flow rates do vary in response to a multiplication of flow parameters, contrary to hydraulic heads. Figure 68b presents results of a sensitivity analysis of exchange flow at the above cited three drainage ditches with regard to a multiplication of model parameters and abstraction rates by factors of 0.33 – 3, covering at large the estimated uncertainty on abstraction rates. The misfit between model outcomes and annual averages of measured flow rates, expressed through the objective function in Figure 68b, was calculated as the sum of squared residuals weighted

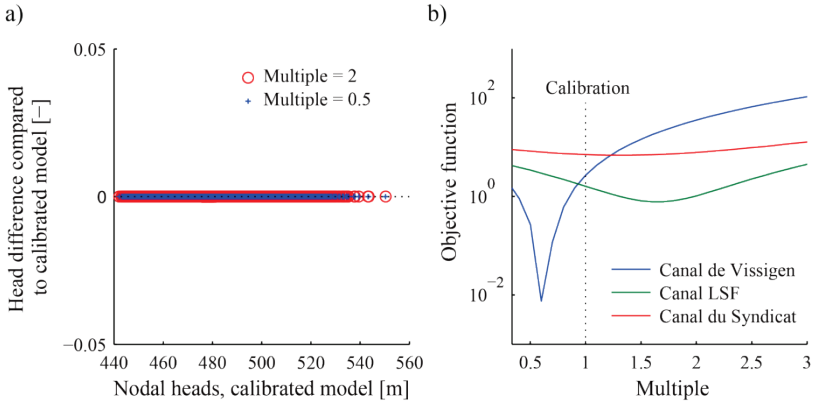

Figure 68 : Model outcomes using multiples of calibrated parameters: a) Nodal heads using multiples of the calibration parameter; b) Misfit on exchange flows at ditches.

[40] Hydraulic-head boundary conditions and mixed type boundary conditions were not altered.

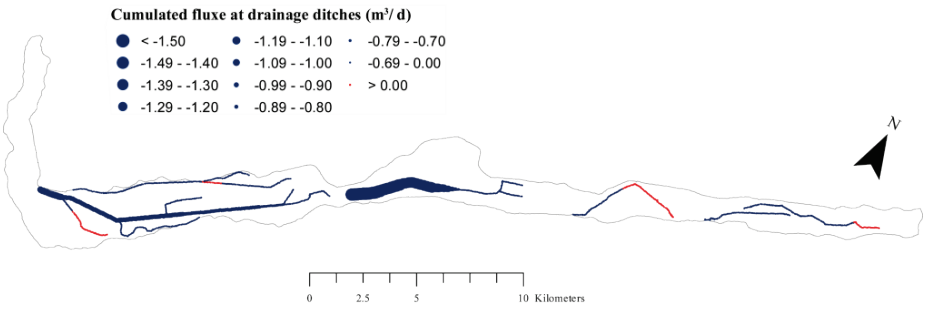

Figure 69 : Cumulated flow rates at ditches as calculated with the calibration solution.

by the relative length of the sections of each ditch. The figure indicates that the objective function is lowest using factors around 1 (0.6 – 1.6). This means that exchange rates are nearly best reproduced by the calibration solution.

Figure 69 represents cumulated flow rates at ditches as calculated in the model. Exchange flows are clearly highest for the Canal de Sion – Riddes, for which according to a simulation with the calibration model a flow rate of about 1.5 m^3/d results at its mounding in the Rhône River. Unfortunately, no measurements are available to verify the validity of this calculation. The value seems however to be high, as an absolute value, and also when compared to other ditches.

5.9.2 Annual head variations

Based on calibration parameters of the steady state model, a transient verification test was performed with the purpose to compare model calculated annual variations to differences between average heads at HW and LW. Since the Rhône River is the major driving force of the system, only water stages at the Rhône River were considered as time-dependent. A uniform storativity of 0.15 was applied. The construction of transient boundary conditions at the Rhône River is based on a continuous time series of river stages at Sion (Figure 70, [79]). From these data, a model shape curve with a temporal discretization of one month was derived. This was achieved by resampling a 1-month moving average of the time series at a monthly interval. At every node of the boundary condition at the Rhône River, this model curve was then shifted to the corresponding average annual river stage and scaled to the average river stages during HW and LW (see examples in Figure 71). In the model, annual head differences were calculated as the difference between heads at the beginning of August and at the beginning of March.

Resulting annual head variations at observation points are presented in a scatter plot against measured data in Figure 72. The plot indicates that if observation points close to the upper boundary, which is also varying in reality, are removed, modeled

head variations compare fairly well to measurements, given that no calibration of storativity has been undertaken.

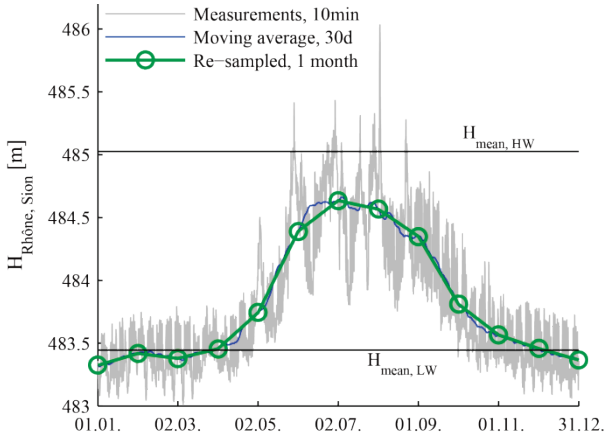

Figure 70 : Derivation of the prototype model curve for time-dependent boundary conditions at the Rhône River.

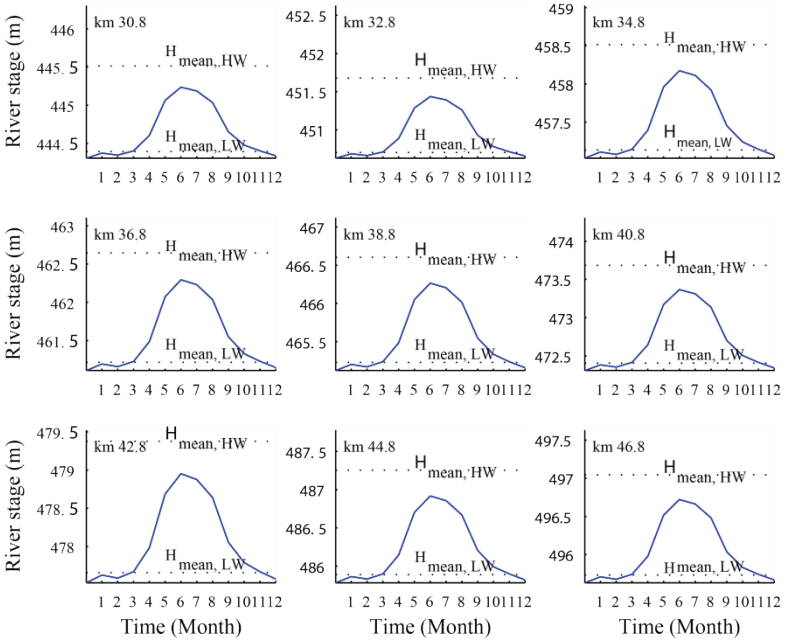

Figure 71 : Examples of boundary conditions at the Rhône River. Values of the boundary condition vary both in space and in time.

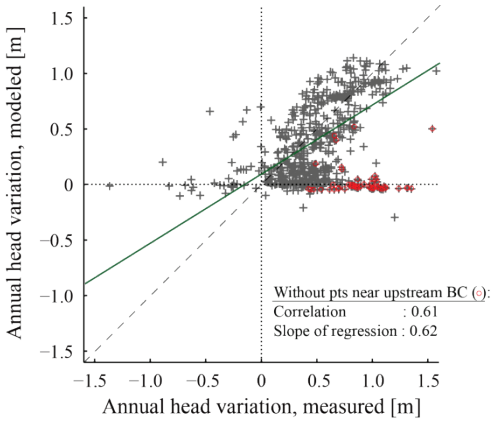

Figure 72 : Comparison of model computed and measured annual head variations (calculated as the difference between high and low water levels).

5.10 Discussion

Amongst all parameter groups, parameter bounds are considered the most certain for recharge by precipitation, because its value cannot be less than zero and because the upper limit is thought to be reliably determined by effective precipitation. Estimated parameters are therefore considered plausible.

Estimated hydraulic conductivity is in an order of magnitude that can generally be expected for an alluvial aquifer and its spatial variability is considered to be realistic in the given hydrogeological context. At many places, hydraulic conductivities are in agreement with the local hydrogeology. For instance, the stretches at km 40 – 45, at km 55 – 59, between Conthey and the alluvial fan of Losentse, and at km 73 – 80 in the southern part of the plain are known to be less permeable [2]; the area of the alluvial fan of Borgne River is known to be highly conductive [2].

While the mean value of hydraulic conductivity estimated by inverse modeling compares well to the prior estimate based on field data (Figure 56a), no correspondence between prior estimates and modeled parameters is found at the level of bores from which prior information was calculated (Figure 73). This may on the one hand be explained by the small support volume for which available hydraulic properties are representative. Furthermore, the spatial variability of hydraulic properties is often underestimated in a numerical flow model, due to the parameterization of the inverse problem or even due to the spatial discretization of the model. This brings issues related to the up-scaling of real-world parameters to model parameters into play. It is for instance not uncommon that model parameters are different from physical aquifer properties because of their need to compensate for an undersampling of the aquifer heterogeneity in the model.

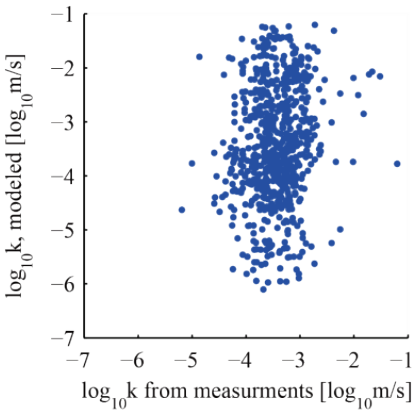

Figure 73 : Comparison between prior estimates derived from lithological information at bores and values of the calibration solution at corresponding locations.

One part of the highly conductive zone near Martigny mentioned in the description of parameter estimates (section 5.7.1) concerns a longitudinal strip along the Rhône River[41]. In this area, gravel pits are present that are flooded by groundwater. This may explain the high to very high hydraulic conductivities, because the ponds correspond to highly conductive zones. Furthermore, they testify to coarse–grained deposits. West of the neck at Martigny, a zone of high hydraulic conductivity has also been identified at the southern model limit. This contrasts somewhat with geographical names for that area indicating the former presence of marshes[42]. Estimated high values of hydraulic conductivities are possibly related to the presence of infiltration ditches in that area which were not considered in the model due to their small size. The above cited highly conductive zone extends to the area upstream of the neck of Martigny where it passes a flooded gravel pit[43] and branches out into three arms. It is notable that the central arm roughly follows an ancient secondary arm of the Rhône River, historically termed “Le Petit Rhône” [158] (surface water body running from km 40 to SE and then to E on Figure 74). A correspondence between highly conductive zones and such old river courses seems to exist elsewhere, too, as suggested by Figure 74, where the map of Dufour is superimposed to the hydraulic conductivity field of the calibration solution. For instance the zone between km 55 – 65 corresponds to an area in which in 1844, when the map of Dufour was drawn, the Rhône River exposed a braided fluvial style.

[41] « Le Rosel »
[42] « Les Marais »
[43] « Gravière du Verney »

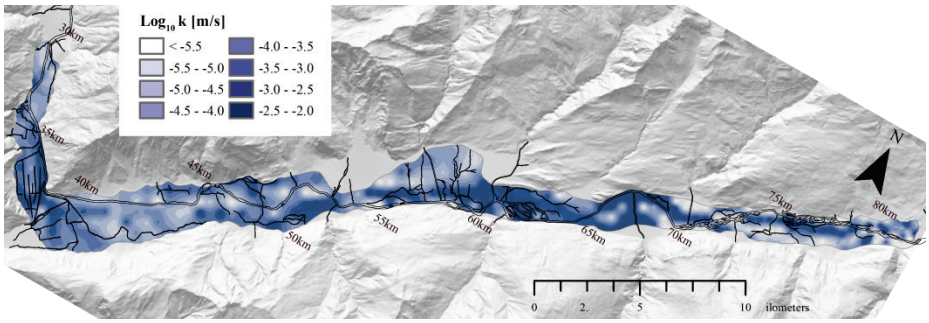

Figure 74 : Map of Dufour (1844) superposed to map of estimates of hydraulic conductivities (background map: hillshade of DTM [144]).

Plausibility of transfer rates is difficult to assess since available measurements are rare, restricted to the Rhône River and they yield very local estimates only. On the other hand, streambed clogging, which is indicated by transfer rates of the Rhône River, has been postulated by several authors [e.g. 12, 14]. The reason for increasing uncertainties of transfer rates at the Rhône River in the downstream direction is seen as a consequence of the decrease of head losses between the Rhône River and the aquifer in the downstream direction (Figure 66a and b).

Specific infiltration rates at the Rhône River amount to 0.14 $m^3d^{-1}m^{-2}$ [44] on average, with maximum values of about 4 $m^3d^{-1}m^{-2}$ [45]. Compared to values given by Hoehn [159] for rivers in Switzerland, the mean value is rather low, whereas the maximum value lies slightly above the given range of 0.05 – 3 $m^3d^{-1}m^{-2}$. Meile, Fette, et al. [12] report maximum values of specific infiltration rates of 2.8 $m^3d^{-1}m^{-2}$ in their synthesis report on hydropeaking in the Rhône River. Although being higher than reference values, the maximum value found herein by inverse modeling is not considered unrealistic, given that it results from hydraulic gradients between the Rhône River and the aquifer that are close to measurements (Figure 51) and from transfer rates that correspond to streambed conductivities that are moderate (about $1 \cdot 10^{-4}$ m/s, Figure 66a, km 69). Average specific exfiltration rates at the Rhône River of 0.47 $m^3d^{-1}m^{-2}$ [46]are considered plausible with respect to the above cited values for specific infiltration rates. Maximum values of specific exchange flow rates for exfiltrating conditions occurring at km 66 arise from transfer rates being at a value that has been considered as the maximum.

[44] On a total length with infiltrating conditions of 44 km.
[45] Figure 66d at km 69, assuming a river width of 50 m.
[46] On a total length with exfiltrating conditions of 6 km.

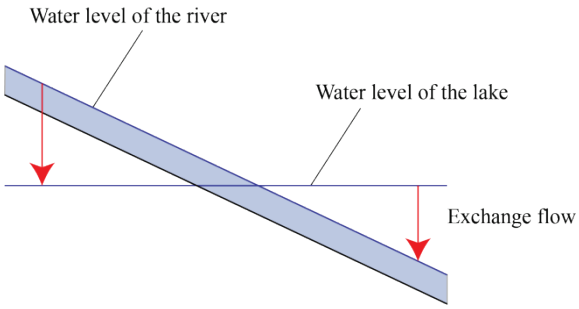

Figure 75 : Principle of exchange flow in a connected river-lake system.

Model results indicate that SW-GW exchange flow preferentially occurs at a few sites. While this finding was unexpected, high exchange rates can tentatively be explained by the hydrogeological setting. An explanation of the phenomenon that high exchange flow results in each of the three areas in which the Rhône River passes close to a pond, is illustrated in Figure 75. In the upstream part of a lake passed by a river, high gradients may induce a flow from the river to the lake given that a hydraulic connection exists between the two; if the lake reaches far enough in the downstream direction for the level of the river to be exceeded by the water level of the lake, an exchange flow in the opposite direction from the lake to the river results. An example of this principle can be observed at "Le Rosel" (km 37–38; Figure 64a). At "Les Iles" (km 60–62; Figure 64c), only an infiltration flow at the upstream part of the lakes occurs. In the example of "Pouta-Fontana" (km 72; Figure 64e), an infiltration can only be observed at the most downstream of the lakes. It shall be reminded, that the ponds are not simulated as surface waters in the model but are part of the aquifer. As stated above, the occurrence of these exchange flows requires a well-established hydraulic connectivity between the river and the ponds. The reason why such connectivity should have developed is not yet fully understood.

An obvious explanation for high exchange flows occurring at the sites within the model area, at which gravel is excavated from the streambed, is that digging works have increased the streambed conductivity at these sites. It should be mentioned, that high groundwater levels observed at these sites – which are at the origin of high infiltration rates in the model – could possibly also be reproduced by other parameter combinations, as for instance by a zone of low hydraulic conductivity downstream of the sites in question. Although the given explanation is appealing, it is difficult to understand, why PEST favored a high exchange flow over alternative solutions.

The remaining places with high infiltration rates (km 56–57 and km 68–70) interestingly correspond to areas where the groundwater table lies above the streambed during HW and below it during LW, as can be seen from a comparison of the top and

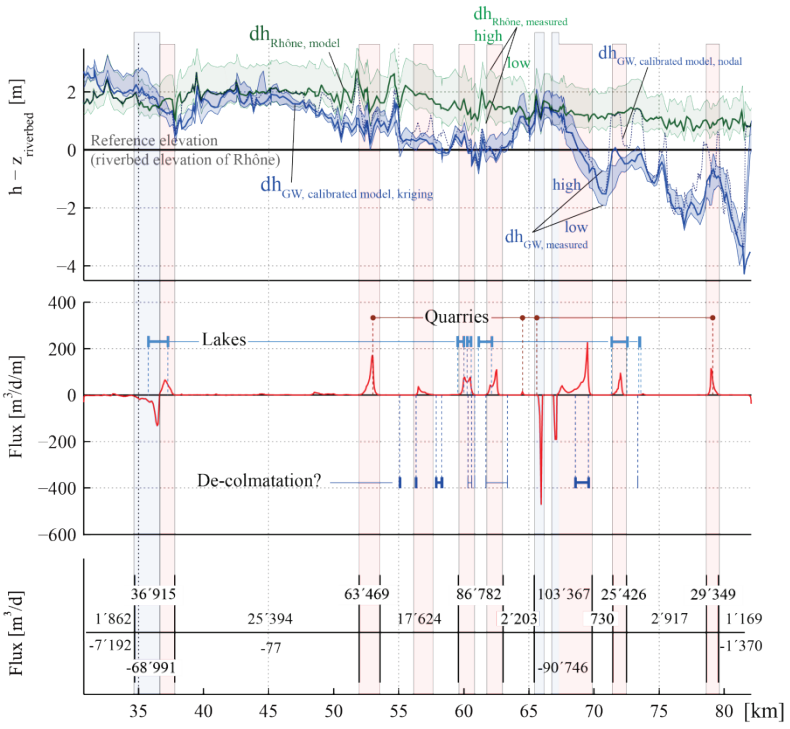

Figure 76 : *Top plot*: Comparison of water levels at the Rhône River (measured and as used in the model) as well as measured and modeled groundwater heads along the Rhône River; Values are relative to the elevation of the streambed (data from PR3); *Central plot*: SW-GW exchange rates at the Rhône River resulting in the calibrated model and tentative explanations; *Bottom plot:* Cumulated exchange rates per section.

central plots in Figure 76. While the detailed processes are not understood, it is conceivable that in these transitional zones, a de-clogging of the streambed takes place. A considerable alternative explanation for high inflows on the stretch running through the alluvial fan of the Borgne River would be a recharge of the aquifer by infiltration of the Borgne River.

As shown by the bottom plot in Figure 76, considerable exchange flow occurs on stretches outside of the areas with very high exchange rates, contrary to what may be judged from the central plot of Figure 76.

As for the Rhône River, specific exfiltration rates at ditches are at some places high, too. It is at this point worth underlining that the drainage ditches considered in the model are a surrogate of a dense system of smaller ditches and buried drainage pipes, whose positions are often unknown [160]. Therefore high specific flow rates may result at places where many drains converge.

Model-calculated flow rates at Canal du Syndicat, Canal de Leytron-Saillon-Fully and Canal de Vissigen were found to compare satisfyingly well to estimations based on measurements. As stated above, this confirms estimated parameters to be in the right range. This is also indicated by results of a simulation of annual head changes in a transient model.

As described in Doherty [119], the NSMC procedure can be implemented at two levels of detail: At the level of parameters used for parameter estimation, and at the level of the model grid. Although both approaches were tested, the analysis of parameter uncertainty as presented herein is restricted to the outcomes of the first approach. The reason for this is that in applying the second approach, simultaneously noise was added to model outputs ahead of the post null space projection re-calibration step. This is theoretically correct and has been proven to be necessary in order to correctly sample the posterior parameter distribution in the context of a synthetic example (see Chapter 3). In this real-world case, however, this strategy was found to introduce a bias in parameter estimates, in that mean values of the resulting parameter distributions differed considerably from the calibration solution. Possibly, poor estimates of the magnitude and especially the structure of measurement noise are at the origin of the observed bias. This issue is however not well understood and requires further investigation. It should be mentioned, that parameter uncertainties resulting from the second method were considerably higher. Uncertainties given herein need therefore to be treated with some caution.

An important observation of the parameter estimation exercise is the fact that parameters relatively often run into bounds. One reason for this might be that parameter bounds were placed too close to each other. Care was taken to choose large ranges in order to avoid such an interference of the estimation by parameter bounds, in particular because when SVD-assist is used as an inversion mechanism, parameters stuck at their bounds, once they hit them [47]. This possibility can nonetheless not be completely excluded. For instance for transfer rates, valid bounds are difficult to provide, given that this model parameter depends on several real-world parameters, whose estimates are all subject to uncertainty.

Extreme values of model parameters may also be a consequence of overfitting. Overfitting may occur due to an underestimation of the magnitude of the expected noise in the data. What has been considered as data to condition the calibration in such a case is in fact partly noise. If a complex model with many parameters is used, it is generally not too difficult to attain (too) good a fit between model outputs and field measurements contaminated by noise, sometimes at the cost of lack of meaning of parameters.

Another cause for extreme values may be the presence of structural noise, i.e. the presence of inconsistencies between the model structure and the simulated system. In

the model presented herein, parameterization schemes are employed that represent heterogeneity at a scale which is larger than typical scales of field data (see section 5.2.4). It is therefore also conceivable that parameters take extreme values in an attempt to compensate for model inadequacies. The fact that extreme values of hydraulic conductivity mainly occur in the upper part of the study area (Figure 57), where low permeable deposits of the Sierre landslide are intercalated with alluvial deposits, is in line with this hypothesis.

It is clear that where uninformed parameters have been constrained by regularization of the preferred state type (e.g. lateral influxes), their adherence to the prior estimate along the optimization process does not necessarily mean that the prior estimate was particularly well, but must rather be interpreted as a consequence of the influence of regularization constraints on the estimation.

Plausibility of lateral inflows is assured by the fact that apart from the inflow at Conthey, calibrated values are within the specified range. However, it is suspected that other conceptual models, with flow boundaries specified at different locations, should also be valid.

Testing of different conceptual models against each other has not been undertaken herein, but would be interesting. Besides locations of lateral flow boundaries this would concern the assumptions on the structure of spatial correlations of hydraulic properties, which here in a simplified view is considered to be multi-Gaussian, or even the parameterization of the inverse problem (pilot point density, choice of variogram, different initial values etc.). It is to be assumed that parameter uncertainty would increase, if many conceptual models would be included in the test and the uncertainty as quantified herein can therefore be regarded as not exhaustive.

The approach of using a highly parameterized model seems to be justified by the correspondence of modeling results with local phenomena such as aquifer heterogeneity as well as by the possibility that a dense parameterization offered to simulate small scales processes, such as is seemingly the case for SW-GW exchange flow.

Chapter 6

Assessing the impact of the Third Rhône correction on groundwater

6.1 Introduction

In Chapter 5, an estimation of model parameters of the numerical groundwater flow model introduced in Chapter 4 has been presented along with a quantification of parameter uncertainty. Based on these results, a predictive model was created to study the influence of the PR3 project on groundwater. This chapter describes the setup of the predictive model and discusses modeling results.

The impact of the PR3 is first examined in terms of induced head changes, alterations of flow rates and of changes to the SW–GW relationships that are expected to occur in the long term. A sensitivity analysis of model predictions to streambed conductance (transfer rate) is carried out in order to assess predictive uncertainties arising from the uncertain evolution of streambed properties in the restored state. The uncertainty of the model-predicted impact is furthermore quantified based on parameter uncertainties derived in Chapter 5.

Following the estimate of the long-term system state in section 6.2, which is made at the scale of the study area, an estimate of short-term changes associated with local restoration measures is presented (section 6.3). The chapter closes with a discussion of modeling results.

6.2 Long-term impact of the PR3 on groundwater

6.2.1 Introduction

In the first approach, in which the long-term impact of the PR3 is assessed at the scale of the flow model, river stages as expected after completion of the restoration works are assigned to the boundary condition at the Rhône River all along its course through the model domain. All other boundary conditions are borrowed from the calibrated solution. In a first simulation, calibrated model parameters are used to simulate the future state. This simulation refers to a long-term future state in which alterations, which are possibly induced by construction works or by changes in the morphology of the streambed, have been reversed again (see section 6.2.2.1).

This implies for instance that a clogging layer, thought to be present in the current Rhône streambed, develops in the restored state, too. This assumption may be defended by the hypothesis that the sediment load of the Rhône River in the future state will be similar to that of today, involving the transport of suspended fine-grained sediments, which is a requirement for a mechanical clogging based on “the intrusion and the deposition of suspended fine particles in (or on) the top layer of the streambed [31, p. 196]” to take place. The assumption is furthermore supported by the work of Fette [14], who found that in the Rhône River, clogging of the streambed is increased by hydropeaking. Although not being unfounded, the assumption of a future streambed, which is identical to the current one, is of course simplistic. The restora-

tion will for instance most probably trigger off geomorphological changes of the streambed giving rise to a variable streambed geometry, which reduces the development of a clogging layer [31]. In order to account for the uncertainty related to the evolution of the streambed properties in the long term, a sensitivity analysis of predicted head changes to transfer rates is carried out. The sensitivity analysis in section 6.2.2.2 consists in multiplying calibrated transfer rates uniformly by factors between 0.1 and 1000.

The outcome of the parameter uncertainty analysis undertaken in Chapter 5 is a series of parameter sets that reproduce conditioning data and that are in agreement with prior information. These parameter sets are used in section 6.2.2.3 to examine how the parameter uncertainty leads predictions of the system state uncertain.

As for the simulation of the current state, water stages along the Rhône River are represented by outcomes of a one dimensional hydraulic model [1]. Analogous to the current state model (section 4.5.2.1), mean values were calculated as the weighted sum of water levels during low and during high water conditions (using 2/3 and 1/3 as weighting factors for LW and HW respectively).

6.2.2 Head changes induced by the PR3

6.2.2.1 Predictions using calibrated parameters

Figure 77a represents a map view of the long-term impact of PR3 on water levels in the aquifer as estimated using calibrated parameters. As stated above, due to the uncertain evolution of the streambed properties in the restored streambed, this estimate is only one possible prediction amongst many. Head changes here are calculated as heads in the restored state minus heads in the current state. In Figure 77b, head changes in the aquifer underneath the Rhône River are shown in a profile view. A representation of changes in river stages in the Rhône River is included in this plot for comparative purposes. Figure 77c and d represent map views of head changes resulting for transfer rates that are 10 and 100 times higher than calibrated values. These simulations conceptually stand for the scenario of a restored streambed with an increased streambed conductance.

In response to the predominant lowering of river stages caused by the general widening of the streambed, water levels in the aquifer are mostly lower in the future state compared to the current state (Figure 77a). Exceptions to this are the regions close to the up- and downstream model limits, where the water level in the aquifer is expected to rise as a consequence of increasing river stages.

Figure 77a shows that the induced head changes in the area between Fully and Riddes (km 40–52) are largely limited to a strip along the Rhône River. The small extent of the influenced zone can be explained by the rather low to moderate hydrau-

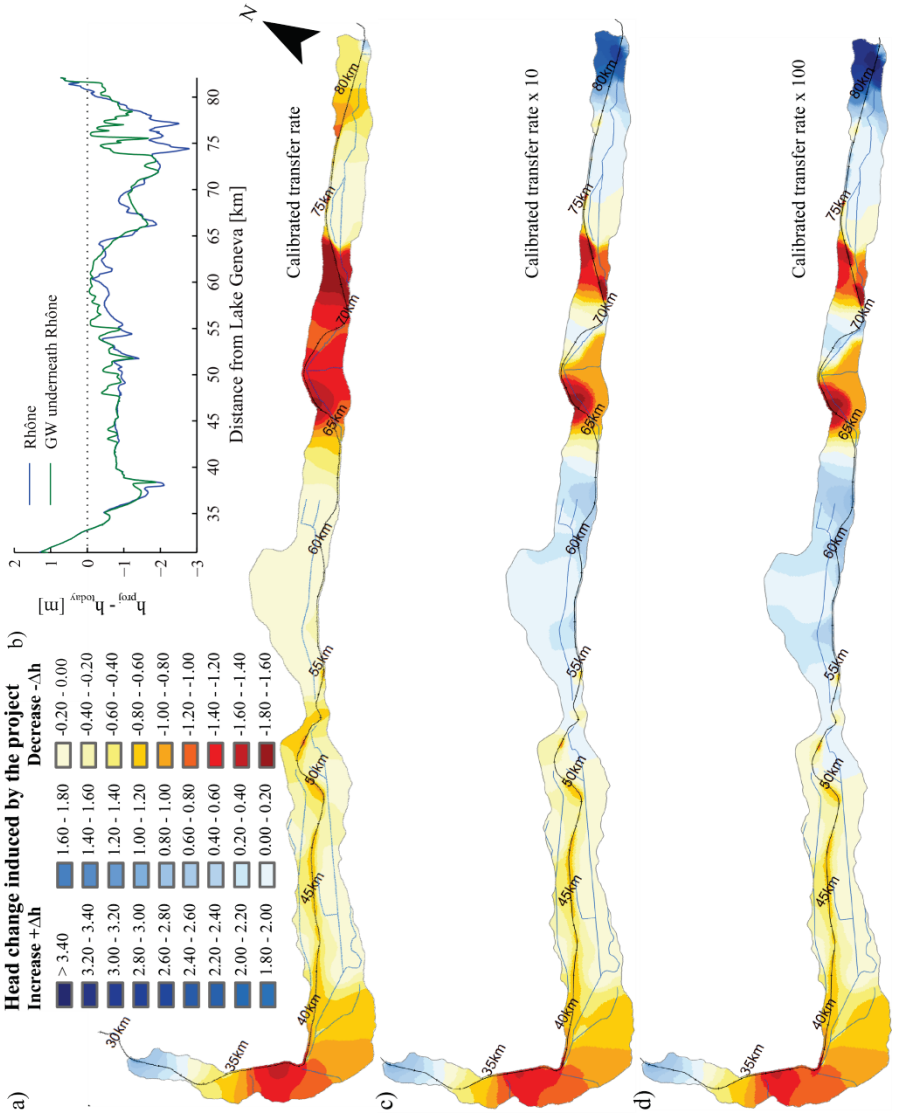

Figure 77 : Long-term impact of PR3 on water levels in the alluvial Rhône aquifer as estimated using calibration parameters; in a) a map view and b) in a profile view of the aquifer underneath the Rhône River; Impact of PR3 on water levels in the aquifer as estimated using calibration parameters and transfer rates which are c) 10 and d) 100 times the calibrated values.

lic conductivity of this area (see section 5.7.1). Despite the lowering of the water table in the aquifer, exfiltrating conditions are present on stretches of the Canal de Leytron-Saillon-Fully[47] (north of the Rhône River, Figure 84a) and are – as in the current state – predominant at the Canal du Syndicat (south of the Rhône River; Figure 84a). The weak impact to the north and to the south of the Rhône River is seen as an effect of the drainage ditches. The same explanation holds for the stretch at km 55-62. Because in the model, the exfiltrating Canal de Sion-Riddes is hydraulically better connected to the aquifer than the Rhône River[48], it controls heads in the aquifer on this stretch and mostly prevents the influence of the project from being propagated beneath it. Figure 77b reveals that changes of river stages do not necessarily have an impact on water levels in the aquifer: Obviously, large changes in river stages on the stretch between km 74–77 are not fully propagated to the aquifer. This is on the one hand explained by the presence of low values of calibrated transfer rates on this stretch (Figure 54). Furthermore, stretches with exfiltrating conditions on the Canal de Chalais and the Rhône River are thought to stabilize the water level in the aquifer.

Large drawdowns of more than 1.5 m resulting for the region immediately downstream of the "neck" at Martigny (km 36–38) and for the region between Sion and Grône (km 65–74) are an immediate consequence of the large lowering of river stages on these stretches (Figure 77b).

6.2.2.2 Sensitivity of predictions to transfer rates

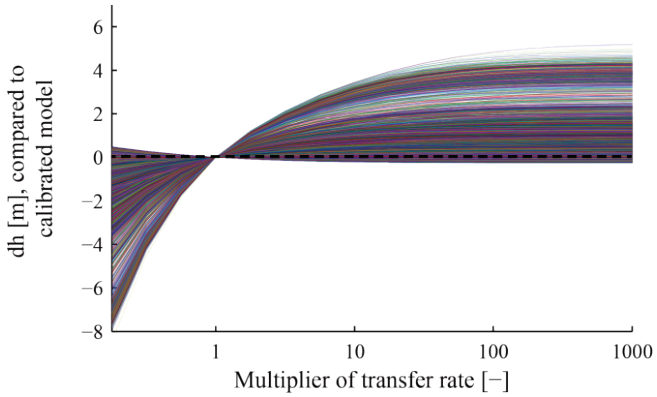

Figure 78 : Difference to head changes as predicted by the calibrated model (multiplier = 1) using multiples of calibrated transfer rates (head changes at the model grid level).

[47] Including the small stretch of Canal de Gru.
[48] See parameter values of transfer rates and hydraulic conductivities in Figure 54.

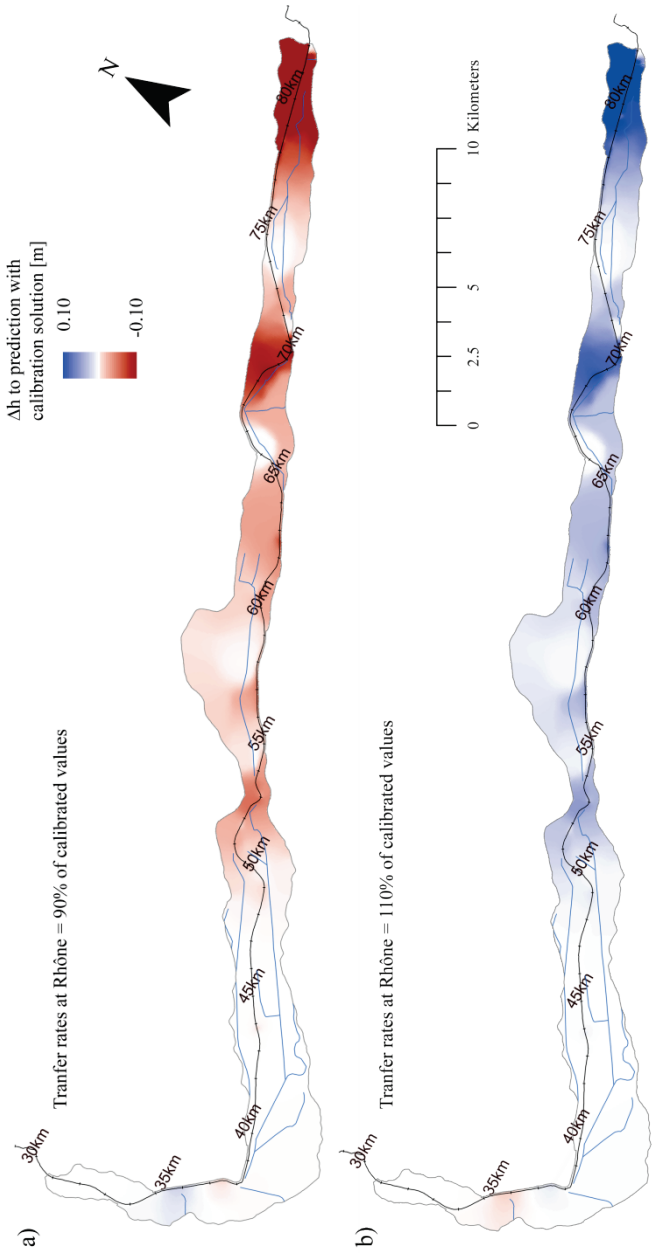

Figure 79 : Sensitivity of predictions to the transfer rate: Difference to head changes as predicted by the calibrated model when using transfer rates that are a) 90% of the calibrated values and b) 110% of the calibrated values.

This subsection presents the results of the sensitivity analysis of the predicted impact by PR3 with regard to streambed conductance. Inspection of Figures 77a, c and d and Figure 78 indicates that an increase in streambed conductance, as it may be induced by digging works or by geomorphological changes, has important consequences on model predictions. As indicated by Figure 78, predicted head changes depend nonlinearly on transfer rates. Figure 79 shows differences in induced head changes arising from a variation of calibrated transfer rates by +/- 10%. The figure indicates that upstream of about km 50, a decrease of the calibrated transfer rate leads to a more pronounced drawdown (Figure 79a) while increasing transfer rates has the opposite effect (Figure 79b). Sensitivity to changes of transfer rates is highest in the uppermost part of the model (east of km 77) and in the upstream stretch of the alluvial fan of Borgne River (km 67–71). Sensitivity is small at stretches where exfiltration conditions are prevailing at the Rhône River or at drainage ditches. Sensitivity to changes of the transfer rate tends to decrease in the downstream direction. Downstream of about km 50, model predictions are little sensitive to streambed conductance.

This may be explained by the trend of head losses between the Rhône River and the aquifer to decrease in the downstream direction: Around km 45–50, the water table in the aquifer approaches the water level of the Rhône River (see Figure 76 for the measurements in the current state or Figure 80 for model results of both the current and the future state). This implies that transfer rates are poorly identifiable from measurements in the current state and that they are hence uncertain (e.g. Figure 66a). The fact that head differences between the Rhône River and the aquifer are small in the future state, too, and hence parameter uncertainties are not propagated into predictions, is seen as a result of the regional control of the aquifer in this area, i.e. heads are mainly determined by levels of surface waters.

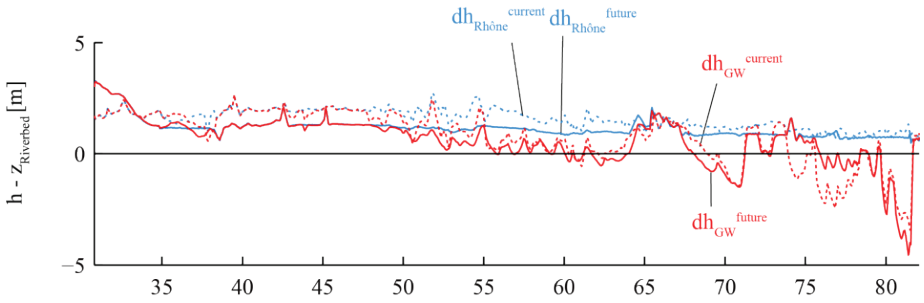

Figure 80 : Average heads in the Rhône River and in the aquifer (simulated using calibrated parameters) for the current and the long-term future state. Curves are drawn relative to the elevation of the streambed.

6.2.2.3 Predictive uncertainty due to parameter uncertainty

This subsection presents the results of the predictive uncertainty which arises from the parameter uncertainty. In Figure 81, predictive uncertainty is illustrated as the difference between the 10% and the 90%-percentiles of predicted head changes. This representation was used because compared to a representation using standard deviations (as chosen for parameter uncertainties), it is considered to facilitate the thinking in hazard scenarios (flooding by groundwater, settlements etc.).

Amounting at 6.25% of the mean predicted head changes, the uncertainty on this prediction can in general be considered small compared to absolute values[49]. A comparison of Figure 81 with Figure 84a reveals that uncertainty in absolute terms is very low (< 2.5 cm) where exfiltrating conditions exist. On stretches with infiltration, the estimated uncertainty tends to be lower where exchange rates are high (e.g. km 53, km 72, km 79).

Compared to other places, predictive uncertainties are large in the area south of the mounding of the Canal du Syndicat (south of Branson; km 39), at Fully (km 41), in the region around "Pouta-Fontana" (km 72–73) and in the uppermost part of the model close to the upper model limit (Figure 81), as a consequence of relatively high parameter uncertainties in these areas. In absolute values, uncertainty in these areas is still small, 80% of simulated heads resulting from the 535 accepted NSMC realizations being within a range of 0.20 m. In contrast, the strip between the alluvial fan of the River Losentse and Conthey (km 55–60) is obviously weakly influenced by the Rhône River such that the relatively high parameter uncertainty in this area is not propagated into predictions.

A detailed analysis of the sources of predictive uncertainty was not made herein due to lack of time. Such an analysis could for instance be undertaken in an approximate manner using methods based on linear uncertainty analysis available in PEST [119]. In order to analyze which parameters are responsible for predictive uncertainties at the locations cited above, where uncertainty is highest (near Branson, at Fully, at "Pouta-Fontana" and near the upstream model limit) here, a qualitative assessment is provided based on a sensitivity analysis of predicted head changes with regard to model parameters. To the end of this sensitivity analysis, a PEST problem is prepared in which predicted head changes are considered as the model outcome[50].

Predictions near the most upstream part of the model are found to be dominated by

[49] With a mean head change of -0.48 m and a mean standard deviation on head changes of 0.03 m.

[50] The computation of the sensitivity of observations to one specific parameter requires two forward model runs, one using boundary conditions for the current state and one using boundary conditions for the future state.

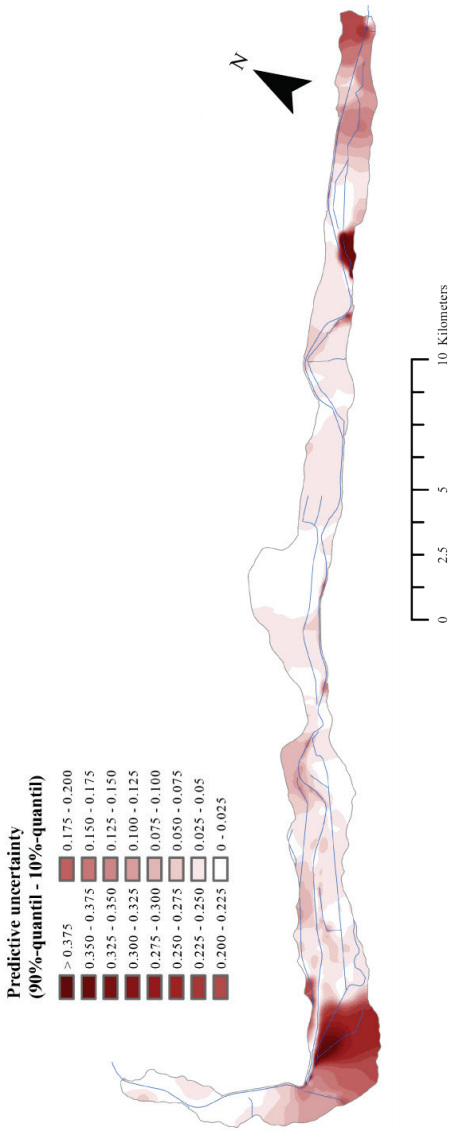

Figure 81 : Estimation of predictive uncertainty arising from parameter uncertainty.

the influx at the upstream model limit, as an inspection of the sensitivity matrix at the calibrated solution reveals. In this area, the uncertainty of calibration data was estimated to be high, mainly due to large variations which the water table undergoes here. This influx at the upstream limit being well defined (Figure 59), it is thought that the influx parameter would be even better defined, and hence the predictive uncertainty lower, if the measurement uncertainty could be lowered, e.g. by having longer time

series at disposition or by considering continuous measurements instead of bi-annual measurement for the calculation of mean values. Also, applying a more severe criterion in accepting NSMC simulations would result in a lower estimate of uncertainty.

In contrast, at other places with high predictive uncertainty, there is not one single but various parameters that are at the origin of predictive uncertainty. This is suggested by Figure 82 which shows contributions made by different parameter groups to composite observation sensitivities of the areas with high predictive uncertainty. Composite observation sensitivity is a measure of the sensitivity of an observation to all estimated parameters [47]. Here it is calculated for each parameter group separately. Figure 82 then shows how sensitive predictions in a given area are, with regard to different parameter groups. It is clear, that measures of streambed hydraulic conductivities of the Rhône River on the stretch at Fully would not help in reducing the predictive uncertainty, because as shown in Figure 82, predictions for this area are not sensitive to the transfer rates at the Rhône River.

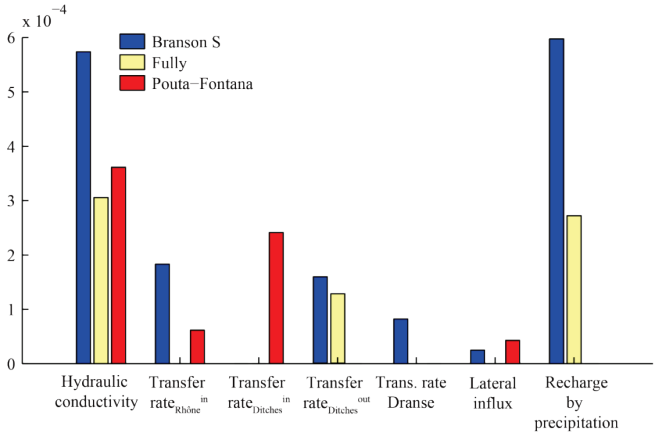

Figure 82 : Contributions to composite observation sensitivities made by different parameter groups (for locations with high predictive uncertainty).

6.2.3 Water balance

Figure 83 gives a representation of the water balance of the long-term future state as calculated using the calibrated parameters and the parameter sets resulting from the NSMC analysis. A comparison with the representation of the water balance for the current state, which is included in the plots, illustrates that flow across the model is smaller in the future state than in the current state. This can be seen as a consequence of the reduction of head losses between the Rhône River and the groundwater that comes along with the lowering of the streambed. The total flow in the future state model amounts to 91% of the flow in the current state.

It is distributed in a similar manner amongst the different hydrological elements of the system as in the current state; the contribution of the Rhône River to outflow is somewhat higher, though, and the one of the drainage ditches is lower.

Similar to the current state, the uncertainty on total flow through the aquifer arising from the non-uniqueness of the solution to the inverse problem is estimated to about 5% of the total flow[51].

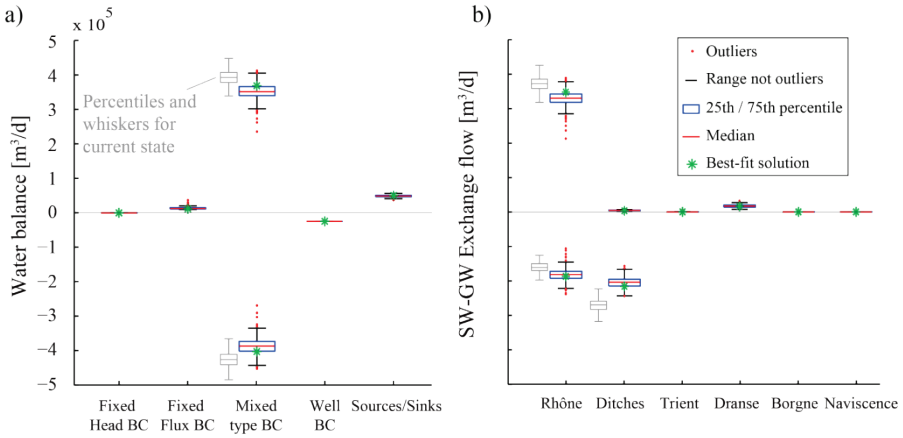

c)

Boundary Type	Inflow		Outflow	
	[m³/d]	[% in]	[m³/d]	[% out]
Downstream head	0 ± 0	0	-782 ± 115	0.2
Fluxes at model limits	13'070 ± 3'246	3.2	-	-
Rivers	352'087 ± 20'334	85.2	-387'515 ± 21'111	93.8
Rhône River	329'878 ± *19'371*	*79.8*	-182'393 ± *15'290*	*44.1*
Ditches	4'499 ± *921*	*1.1*	-205'122 ± *13'539*	*49.6*
Tributaries	17'715 ± *4'074*	*4.3*	-	-
Well boundary conditions	-	-	-25'040 ± 0	6.1
Recharge by precipitation	48'165 ± 2'808	11.7	-	-
Total	413'325 ± 21'111	100.0	-413'337 ± 21'109	100.0
Imbalance	-	-	-12 ± 36	0.002

Figure 83 : Simulated water balance for the future state resulting from the calibration solution and from NSMC realizations; a) Flux according to boundary condition types; b) Detail of fluxes at mixed type boundary conditions (rivers); c) Table of fluxes resulting from NSMC realizations.

[51] Uncertainty here is expressed by one standard deviation of total flows as computed based on the accepted NSMC realizations. The uncertainty arising from the uncertain evolution of streambed conductance in the future state is not quantified because multiplying streambed conductances by uniform factors is considered a too rough approach to yield reasonable volumes of water balances.

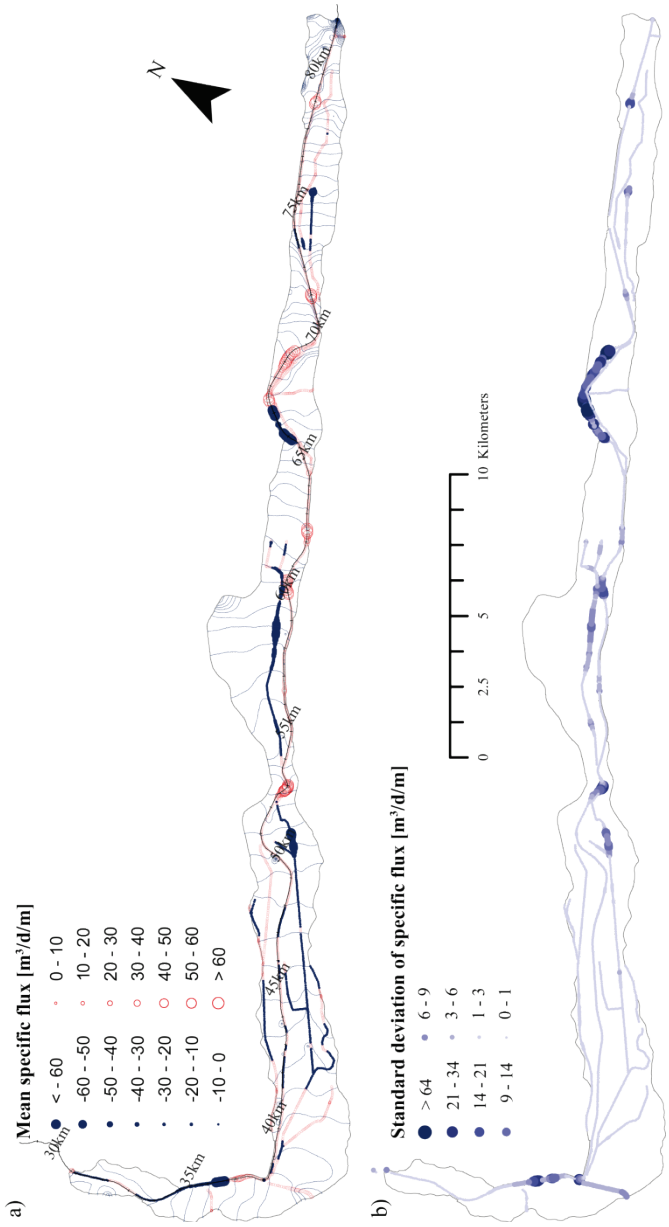

Figure 84 : Mean (a) and standard deviation (b) of specific flow rates (flux per meter of surface water body).

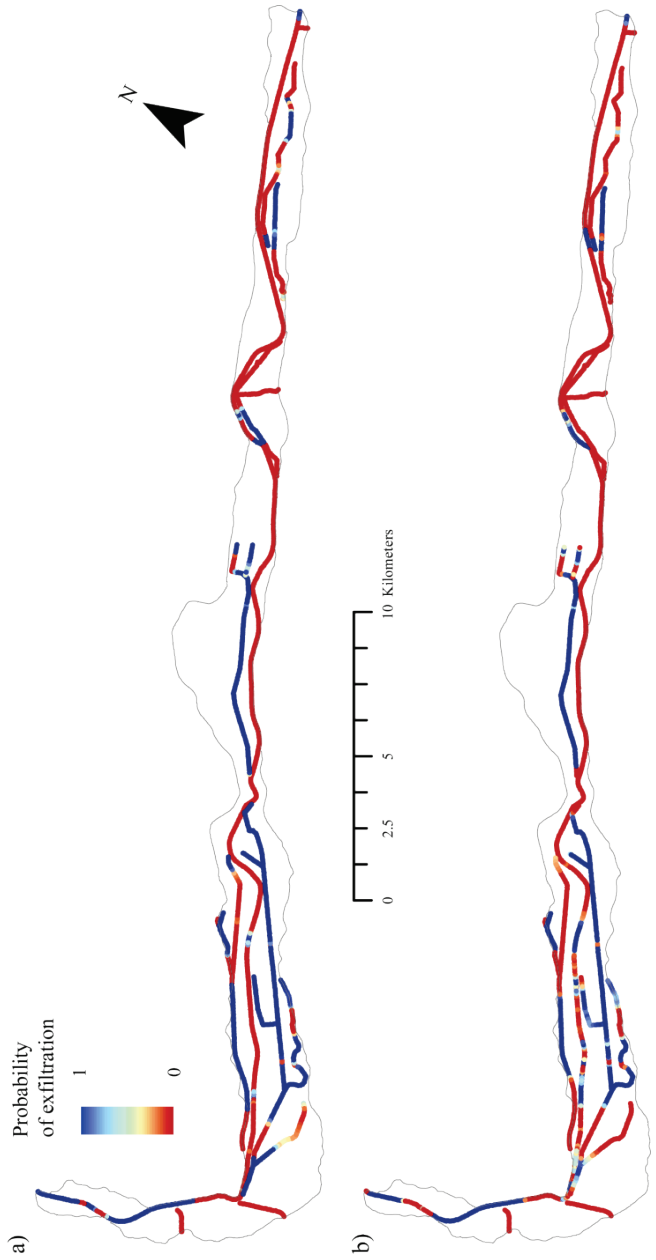

Figure 85 : Probability for conditions to be exfiltrating; a) Current state; b) Future state.

6.2.4 GW-SW interaction

Compared to SW-GW exchange flow in the current state (Figure 65a), a very similar picture emerges for exchange flows in the future state as calculated using the calibrated parameters (Figure 84a). As might be expected, the stretches with exfiltrating conditions are in general a little shorter in the future state. In the area between Fully and Saillon (km 40–50), the tendency toward exfiltrating conditions increases. The stretch running through the downstream part of the Borgne alluvial fan at Sion – displaying a transitional character in terms of GW-SW interactions in the current state model – changes to a zone where exfiltrating conditions prevail. Near Granges (km 74), a short stretch with exfiltrating conditions is indicated by the future state model. The Canal de Vissigen near Sion and the Canal du Toléron (south of km 40) are expected not to drain the groundwater any longer once the Rhône River has been restored. As in the current state, uncertainty in absolute terms is highest at locations with high exchange rates (Figure 84b).

Probabilities for conditions at a surface water to be exfiltrating are shown for the current and for the future state in Figures 85a and b respectively. The "exfiltration probability" at a given location is calculated based on the number of occurrences of exfiltrating conditions at that location throughout the accepted NSMC realizations divided by the total number of accepted realizations. In addition, to confirm the finding mentioned above that hydraulic relations between surface waters and groundwater are not expected to be affected substantially by the PR3, the figure indicates that the SW-GW relations vary little throughout the NSMC simulations.

6.3 Impact of local measures

6.3.1 Introduction

In the first assessment of the impact of PR3 on groundwater, the fact that the project consists of a series of successive stages is neglected. In a second approach, the influence of the PR3 is examined at the scale concerned by individual stages of the project in order to account for this factor.

It is assumed, that in the short term, the streambed conductance will be increased by the restoration works. Similar to the sensitivity analysis at the scale of the study area, different values of transfer rates are thus considered for simulating the impact of the PR3, in order to take into account for the uncertainty of streambed conductance in the restored future state. Transfer rates are varied between calibrated values and an assumed maximum value. The maximum value is chosen so that conceptually a declogging of the streambed is ensured, i.e. such that SW-GW exchange flow is solely controlled by head losses between the Rhône River and the groundwater and by the hydraulic conductivity of the aquifer. This case can be regarded as the worst case scenario regarding the risk of potential rising groundwater problems. The maximum potential drawdown, on the other hand, is in the given context of a permeable aquifer at most places given by the simulation with minimum values of transfer rates, i.e. by the calibration solution. The exception to this is the very location with the maximum lowering of river stages. At that location, the maximum drawdown is given by the simulation using maximum values of transfer rates.

It should be noted that in none of these variants, the widening of the streambed entailed by the PR3 is explicitly considered. In principle, a widening causes higher exchange rates between the Rhône River and the aquifer due to the increased contact surface area. The increase of the leakage coefficient in the second variant can conceptually be regarded as partly being caused by the widening.

The second approach is applied to reaches affected by measures of high priority near Sion and Vernayaz. These sites were chosen in agreement with Alexandre Vogel, who is in charge of hydrogeological studies at PR3. The reaches are simulated in the sequence given above, according to the planning of the restoration. At both reaches, future state river stages are assigned to the boundary condition at the Rhône River. Except from the site simulated before, boundary conditions outside of the reach are kept at the value for the current state. At both reaches, transfer rates are progressively increased from calibrated values to the assumed maximum value in four steps. On short zones to the left and the right of the reaches, transfer rates were interpolated between increased values on the reach and calibrated values outside the reach, in order to avoid a sharp transition.

6.3.2 Results

On the following pages, results of the second approach taken to assess the impact of PR3 on groundwater are presented. For both sites, water levels in the river and heads in the aquifer in the current and the future state are first shown in a profile view. Then the impact induced by the local restoration measure as estimated using calibrated parameters is presented in a map view of induced head changes. As mentioned above, this represents the map of maximum potential drawdown at most locations of a given site, the exception being the area in which the lowering of water levels in the river is maximal. Afterwards the results of a sensitivity analysis, in which transfer rates are varied, are presented in a figure that includes longitudinal profiles of transfer rates, of hydraulic heads resulting for the five simulations made at both sites as well as profile views of induced head changes.

The intended restoration measures on the reach near Sion (km 60.2–71) are expected to result in a lowering of river stages (Figure 86a). This induces a drawdown in the aquifer, if no alteration of the streambed conductivity is assumed (Figures 86b and 87). Maximum drawdowns of about 1.6 m observed in the area around km 66 are related to the largest depletions of river stages (of about 1.9 m) occurring in this area. Head changes induced by the local restoration measures as predicted based on calibration parameters are very similar to those found when evaluating the impact at the scale of the entire model (Figure 77). However, an increase of transfer rates (Figure 88a), results in a dramatically different prediction: in all simulations using increased values of transfer rates, a rising of the groundwater table is observed in large parts of the area. Only in a zone in the central part of the reach at km 66, a drawdown is predicted in all simulations, independently of the values of transfer rates. As soon as the clogging layer is removed, heads underneath the Rhône River are close to or at the level of the Rhône River, as shown by the results of simulation 4 in the top plot in Figure 88b[52]. In this scenario, the most important groundwater rise occurs in the region of "Les Iles" at km 62 and around km 70, where water levels in the aquifer are predicted to rise by about 1 m (Figure 88c). In these areas, predictions based on calibrated parameters indicate a drawdown of about 0.15 m and 0.90 m respectively. The only "inundated" areas, i.e. locations with negative values of water table depths in Figure 88d, correspond to the flooded gravel pits at "Les Iles".

On the reach near Vernayaz (km 35–38.5), river stages as planned in the PR3 are significantly lower than in the current state (max. of 2.1 m; Figure 89a). They induce a drawdown of the groundwater table in this area, with maximum values of about

[52] Simulations 2–3 yield practically the same results.

1.4 m in the area of "Le Rosel" (Figures 89a and 90). Flooding by groundwater is therefore unlikely to occur. Predicted drawdowns induced by the local measures are very similar to those induced by changes in river stages on the scale of the study area. Contrary to the site at Sion, an increase of transfer rates has almost no effect on predictions.

This is explained by the fact that the model is largely driven by regional controls in this area (see section 6.2.2.2) and that calibrated transfer rates are already large enough for a hydraulic connection to exist between the Rhône River and the aquifer.

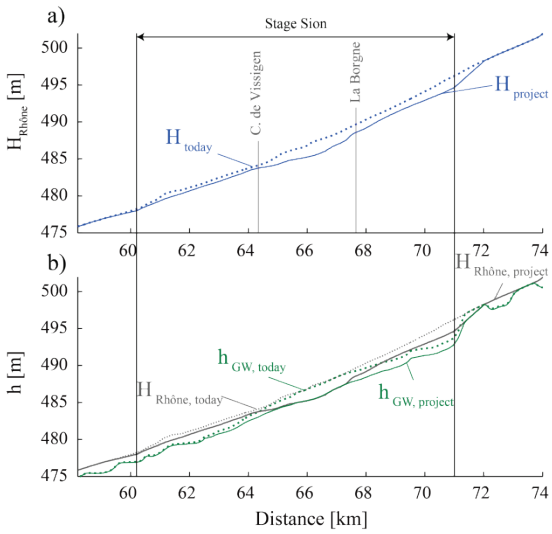

Figure 86 : a) Profile view of river stages near Sion for the current state (H_{today}) and the project state ($H_{project}$); b) Heads in the aquifer for the future state ($h_{GW,\ project}$) compared to heads in the current state ($h_{GW,\ today}$) (both resulting from calibration parameters).

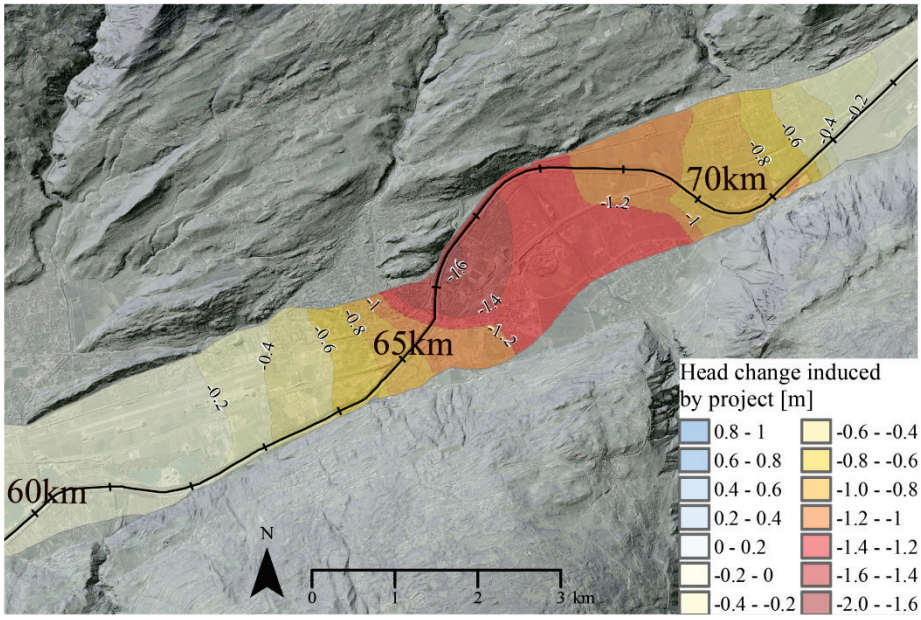

Figure 87 : Head changes induced by local restoration measures near Sion as predicted by using calibration parameters (background map: hillshade of DTM [144] and orthophotos SWISSIMAGE (source: Federal Office of Topography)).

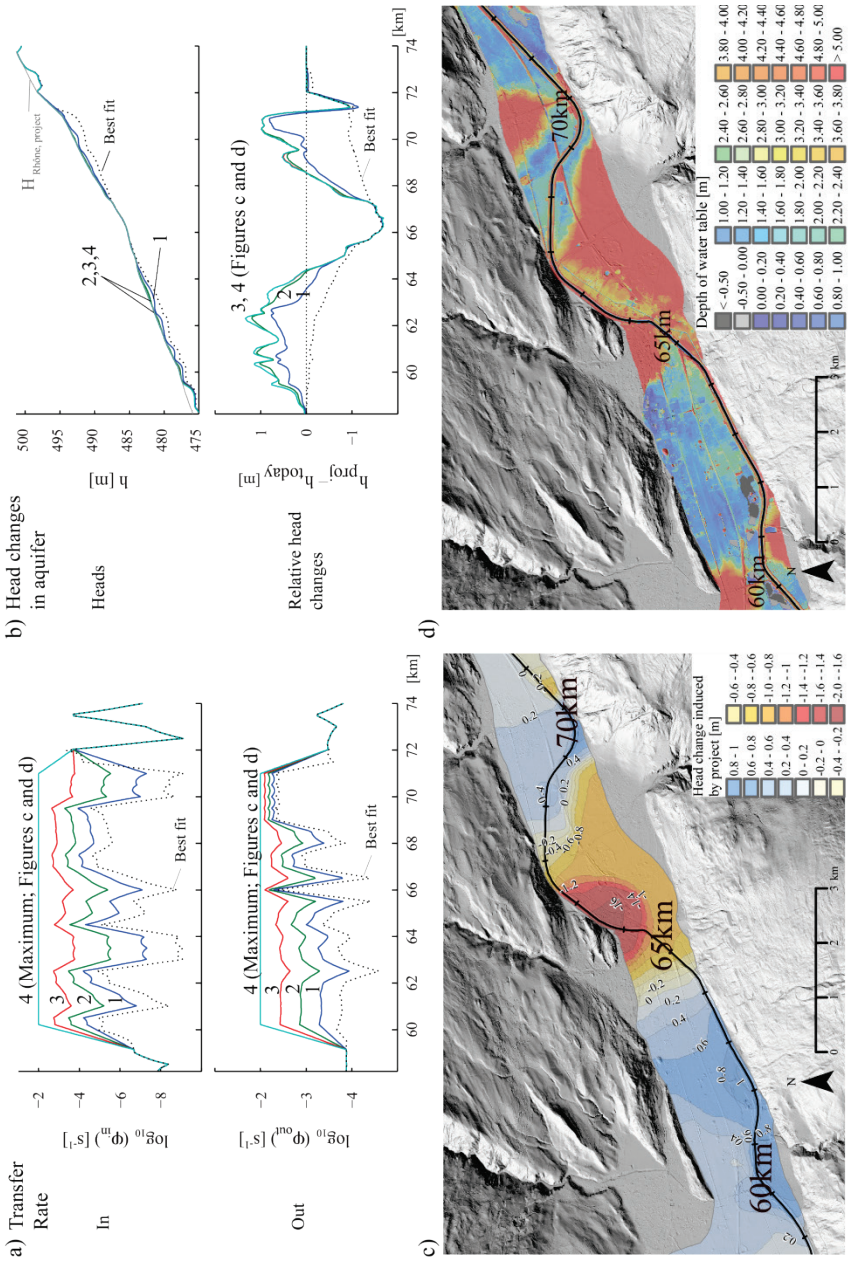

Figure 88 : Head changes induced by local restoration measures near Sion: Sensitivity to transfer rates: a) Values of transfer rates considered in the test; b) resulting heads (above) and head changes (below) in the aquifer underneath the Rhône River; c) Head changes resulting with maximum transfer rates; d) Depth of water level in aquifer resulting with maximum transfer rates.

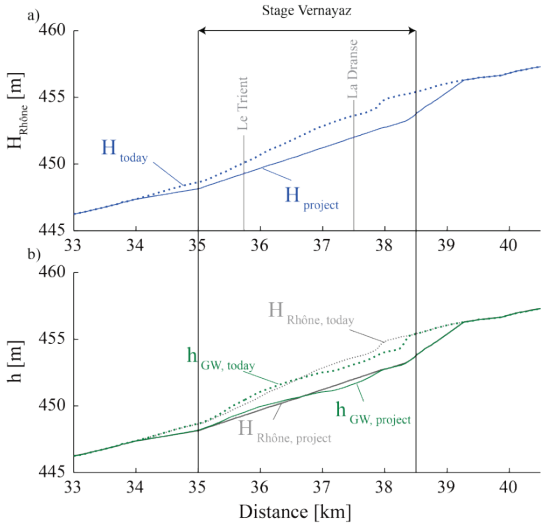

Figure 89 : Profile view of river stages near Vernayaz for the current state (H_{today}) and the project state ($H_{project}$); b) Water levels in the aquifer resulting from local measures ($h_{GW, project}$) compared to water levels in the current state ($h_{GW, today}$).

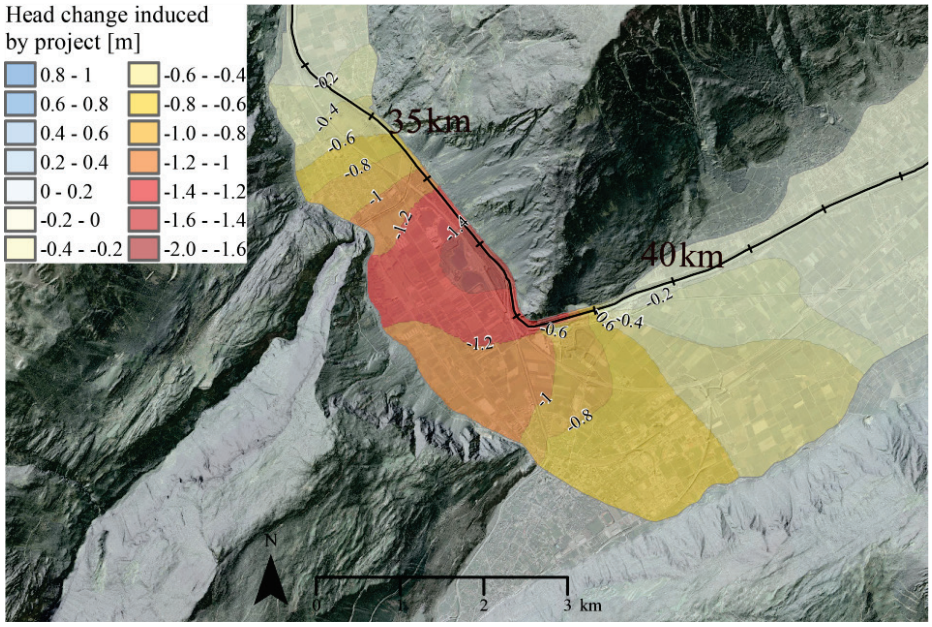

Figure 90 : Head changes induced by local restoration measures near Vernayaz as predicted by using calibration parameters.

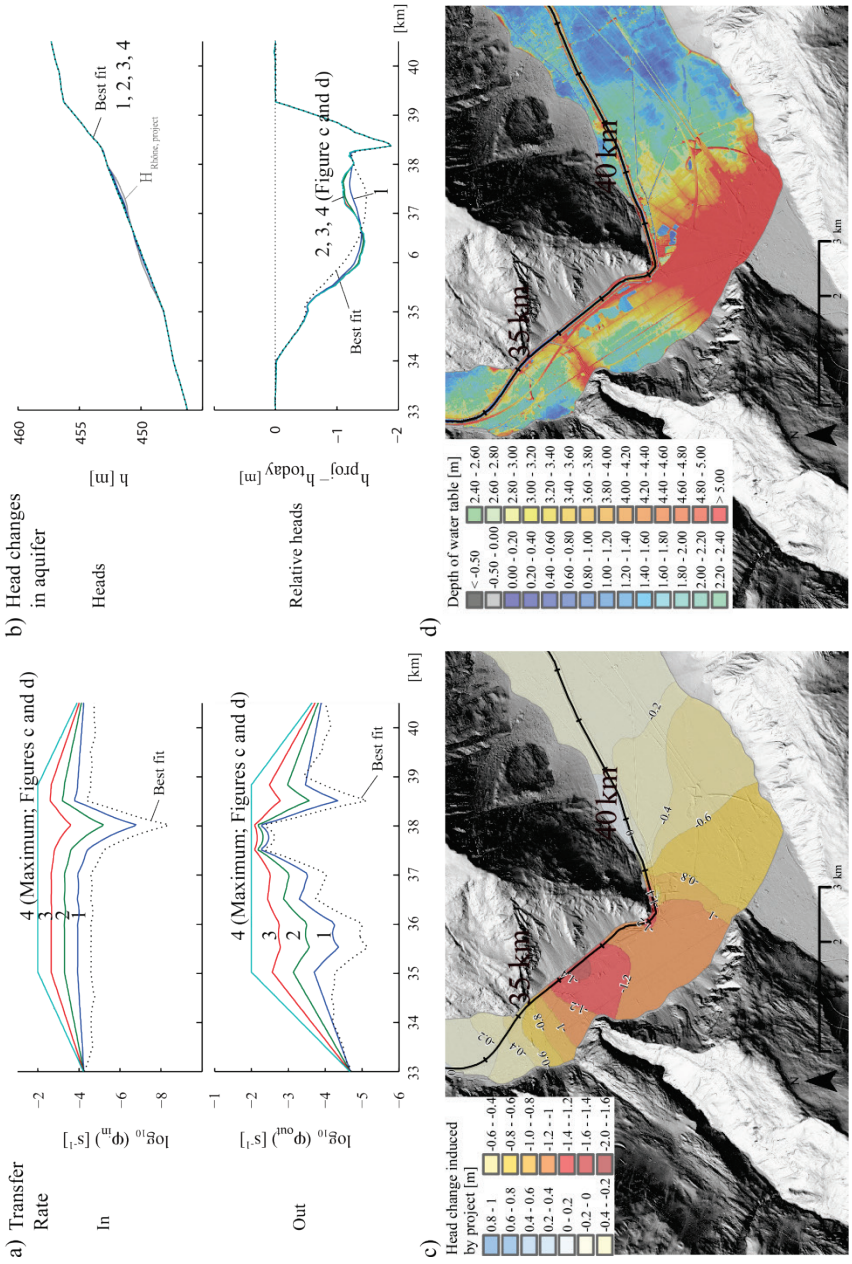

Figure 91 : Head changes induced by local restoration measures near Vernayaz: Sensitivity to transfer rates: a) Values of transfer rates considered in the test; b) resulting heads (above) and head changes (below) in the aquifer underneath the Rhône River; c) Head changes resulting with maximum transfer rates; d) Depth of water level in aquifer resulting with maximum transfer rates.

6.4 Comparison of model predictions to predictions by a method using coupling factors

In the planning phase of the project, the impact of the PR3 on groundwater was estimated based on a semi-quantitative method[53]. In this method, induced water level changes in the Rhône River were multiplied by a coupling factor depending on the SW-GW interaction type. For each SW-GW interaction type, a coupling factor was determined by comparing time series of water levels in the Rhône River with time series of hydraulic head in the aquifer. Four interaction types were differentiated [3]:

1. Exfiltration (Gaining river):
   - The water level in the aquifer is higher than in the river, $h_{gw} > h_{Rh}$.
   - A coupling factor of 0.6 is used to link changes in water levels in the Rhône River to the head changes in the aquifer.

2. Infiltration (Losing river) of type I:
   - The water level in the aquifer is lower than in the river, $h_{gw} < h_{Rh}$.
   - The water level in the aquifer lies above the streambed, $h_{gw} > z_{Rh}$.
   - Coupling factor: 0.6.

   In general, the hydraulic conductivity of the levees is presumably higher than the one of the streambed. Therefore, SW-GW exchange is thought to occur predominantly as bank infiltration for this interaction type.

3. Infiltration (Losing river) of type II:
   - The water level in the aquifer is lower than in the river, $h_{gw} < h_{Rh}$.
   - The water level in the aquifer lies below the streambed, $h_{gw} < z_{Rh}$.
   - Coupling factor: 0.4.

   SW-GW exchange occurs as flux across the streambed and as bank infiltration.

4. Infiltration (Losing river) of type III:
   - The water level in the aquifer is lower than in the river, $h_{gw} < h_{Rh}$.
   - The water level in the aquifer lies much below the streambed, $h_{gw} << z_{Rh}$.
   - Coupling factor: 0.2.

   SW-GW exchange occurs as flux across the streambed.

[53] In the final predictions made in the planning phase of the PR3, the values calculated in this manner were slightly adapted in Sion and near Vernayaz according to expert knowledge.

Head changes induced by the PR3 as predicted by the above method using coupling factors (CF method) are shown in Figure 92a along with induced water level changes in the Rhône River. In the planning phase of the project, the impact of the PR3 was evaluated for high waters (HW) and for low waters (LW). In order to establish a comparison with model results, herein, an annual average was calculated based on values for HW and for LW[54]. Figure 92b presents the interaction types for HW and LW.

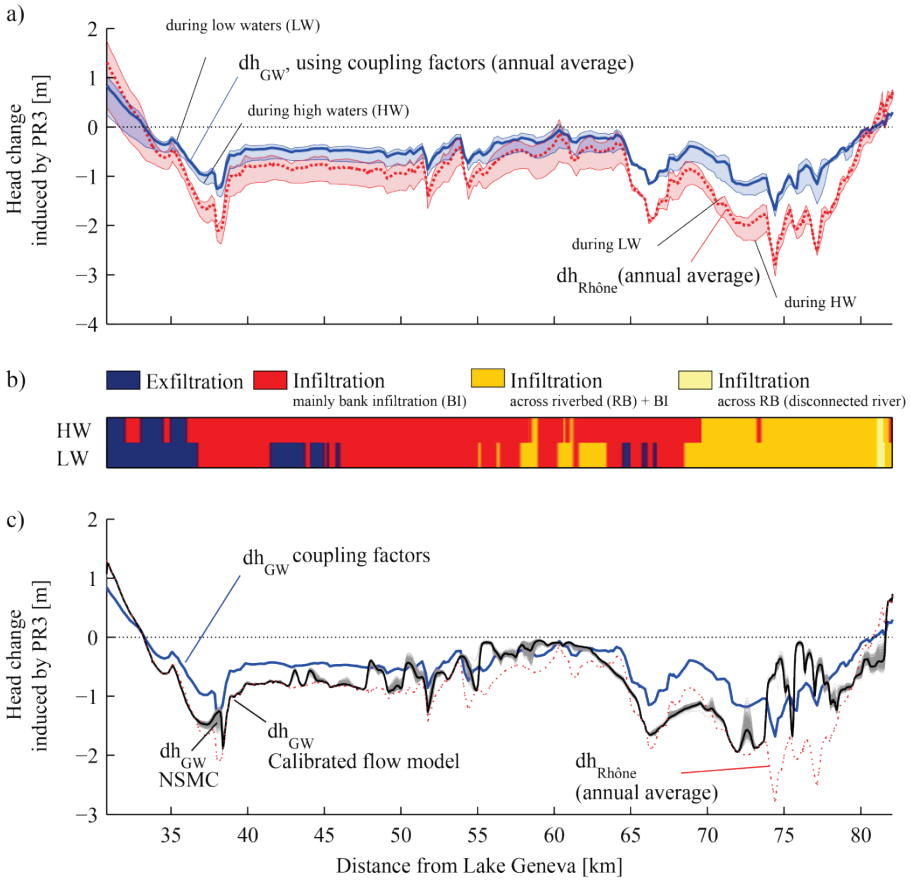

Figure 92: a) Longitudinal profile of changes in river stages and in heads in the aquifer induced by the PR3; head changes in the aquifer were computed by multiplying changes in river stages by coupling factors (data: [3], see text for details); b) SW-GW interaction types used for the definition of the coupling factors; c) Comparison of model predictions to predictions made by the method using coupling factors.

[54] As earlier (Eq. 4.5 and 5.1), a weighted average based on values for HW and for LW was calculated, using as weights the factors derived in section 4.5.2.1 for the Rhône River (0.6666 for LW, 0.3333 for HW) and in section 5.3.1 for heads in the aquifer (0.7411 for LW, 0.2588 for HW).

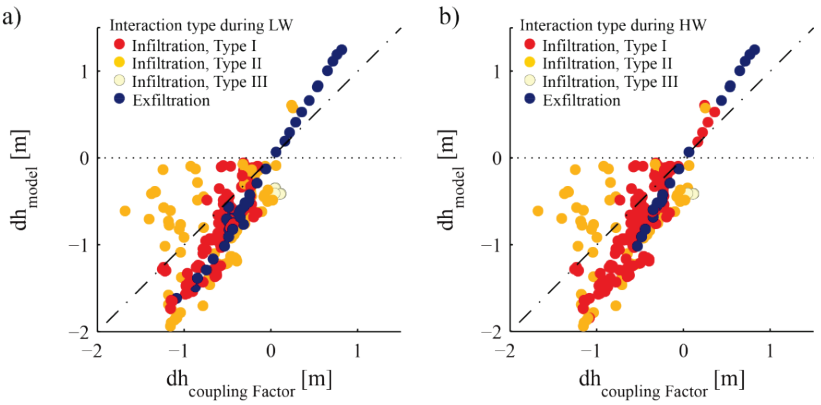

Figure 93 : Comparison of model predictions (head changes induced by PR3 on an annual average) made with the calibrated model to predictions made by the method using coupling factors (data: [3]; annual average acc. to [52]) in a scatterplot; Dots are colored according to the interaction type during low waters (a) and high waters (b).

Induced head changes in the aquifer as predicted by the model are compared to predictions made by the CF method in a profile view in Figure 92c, in scatterplots in Figure 93c and d and in a map view in Figure 95a and b.

As far as head changes at locations with infiltrating conditions of type I and especially with exfiltrating conditions are considered, a linear relationship exists between model predictions and predictions made by the CF method (Figure 93). From this, one may conclude that for these interaction types, water levels in the aquifer are dominated by river stages. On the other hand, the fact that points for infiltrating conditions of type II display a larger scatter (Figure 93) may be taken as an indication that for this interaction type, aquifer and streambed properties as well as the hydrogeological context play a more important role than for the above types. The fact that model predictions and predictions made by the CF method display a different match for infiltrating conditions of type I and of type II justifies the classification of interaction types into these two categories.[55]

Head changes predicted by the model are in general higher than those predicted by the CF method (Figures 92c and 93). Model predictions as displayed in Figures 92c and 93 apply to the aquifer located directly underneath the Rhône River, whereas the results of the CF method apply strictly speaking only to the close vicinity of the Rhône River, the area where piezometers, from which the coupling factors were de-

[55] There are too few locations in order to analyze the behavior at locations with infiltrating conditions of type III.

rived, are located. This may possibly explain the methodological bias, as it is clear that head changes in the aquifer induced by PR3 are highest underneath the Rhône River and decrease with increasing distance from the Rhône River.

Contrary to this general trend, there are places at which the CF method predicts a larger impact than the model. The locations correspond almost always to places with an infiltration of type II (Figure 93). The most import overestimation of the impact by the CF method, compared to model predictions, is observed on the section between km 73.7 and km 78.6 (Figure 92c, Figure 95). This may be explained on the one hand by the fact the river stages around km 74.5 are lowered to the point that the SW-GW interactions at the Rhône River locally change to exfiltrating conditions (Figures 84a and 94). This exfiltration zone stabilizes the water table in the surroundings. On the other hand, already in the current state, the water table on this stretch lies at a relatively large depth as a result of the low streambed conductance (Figure 52). In this context, the lowering of river stages has obviously little effect on the water table in the aquifer.

This example illustrates two evident differences between the two methods: First, the CF method neglects the influence of system parameters, contrary to the flow model. Apparently, this simplification does not apply in all cases. Second, model predictions are placed in a context by the flow model, contrary to the CF method, where predictions are independent from each other. Another apparent difference is that the CF method neglects the influence of all elements of the hydrosystem other than the Rhône River. As Figure 95 demonstrates, the CF method for instance misses the dampening effect that drainage ditches have on the impact of PR3 on groundwater (e.g. the section on km 74 – 77).

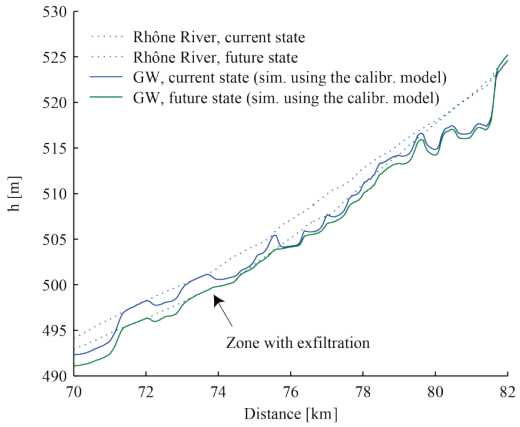

Figure 94 : Water levels in the Rhône River (data: [3]; annual average [52]) and in the aquifer for the current state and the restored future state; water levels in the aquifer are computed by the calibration model.

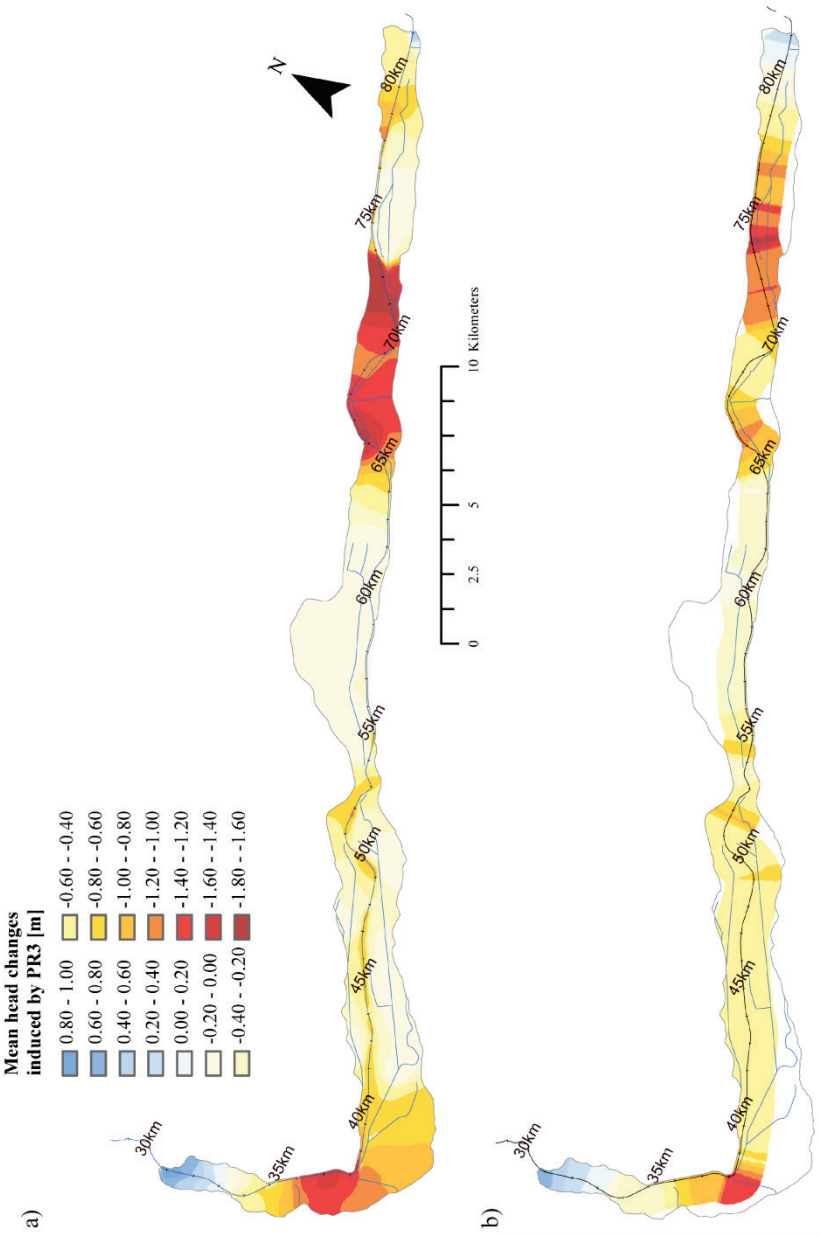

Figure 95 : Comparison of a) predicted head changes in the aquifer as calculated with the calibrated model to b) predictions made by the method using coupling factors (data of water level changes at the Rhône River: [3]; annual average [52]) in a map view.

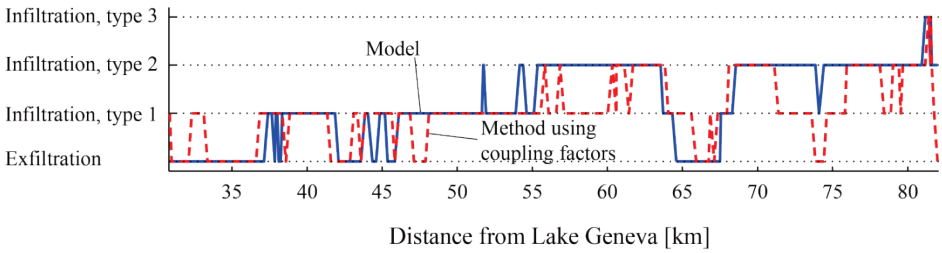

Figure 96 : Comparison of interaction types in the restored state as derived by the method using coupling factors [3] and the model.

Figure 96 compares the interaction types as predicted by the CF method and by the model. On 63% of the distance along the Rhône River across the study area, the predicted interaction types are in agreement. The downwards shift of the curve resulting from the CF method can be explained by the trend of the CF method to underestimate the impact of the PR3 compared to model predictions.

Due to the fact that SW-GW interactions between the Rhône River and the aquifer play an important role for the aquifer, the CF method yields results that are satisfactory well to be used as an approximation to estimate the impact by PR3 in the vicinity of the Rhône River. If the method should be used to predict the impact along the very axis of the Rhône River, coupling factors of 0.95 and 0.82 can – according to model predictions – be used for stretches with exfiltrating conditions and with infiltrating conditions of type 1, respectively. For the other interaction types, the definition of a coupling factor is not possible based on the modeling results.

6.5 Discussion

Qualitatively, model predictions are in agreement with common hydrogeological sense: Modeling results indicate that in the long-term, induced head changes in a given area are at large proportional to changes in river stages on the corresponding river stretch, provided the river is hydraulically connected to the aquifer. Furthermore it is shown that the presence of stretches with exfiltrating conditions – whether on the Rhône River or at ditches – may attenuate the influence of the PR3 on groundwater. A slight decrease in groundwater flow rates is to be expected for the long-term future state, if the same values of streambed conductance are considered in the future state as in the current state.

Transfer rate is found to be an important control of groundwater flow, especially in the upstream part of the model. Modeling of local restoration measures at Sion as well as results of a sensitivity analysis of model predictions with respect to transfer rates indicate that in this area, predictive uncertainty arising from the uncertain evolution of streambed properties is generally far larger than parameter uncertainty due to

the non-uniqueness of the inverse problem in the short-term. The capacity of the calibrated model to make short-term predictions for the upper part of the study area is hence limited. In the long-term, this issue is thought to be less important, because the streambed properties are considered, if not the same as in the current state, to be at least less uncertain than in the short-term. According to the sensitivity analysis of predictions to transfer rates, this assessment applies for the part upstream of about km 50 (Saillon).

In the lowermost third of the model, the situation is exactly the opposite: Both in modeling of local restoration measurements near Vernayaz (km 37) and in the sensitivity analysis on the model scale, predictions did not depend on transfer rates. Predictive uncertainties that are present within this area must therefore be considered to result from other variables.

Apart from areas near the upstream model limit, at "Pouta-Fontana", south of Branson (km 39) and at Fully (km 41), predictive uncertainties that emanate from parameter uncertainties are considered insubstantial. Outside of the cited areas, in the downstream area, the model can be considered to yield a reliable estimate of the impact by PR3.

It may be notable that predictive uncertainties arising from the second implementation of the NSMC procedure tested herein, in which small-scale heterogeneity and measurement noise were accounted for, are higher than the ones presented in this chapter (inter-percentile of 0.26 m on average between the 10% and the 90%-percentiles of predicted head change), and seem more realistic than low values found in using the standard approach as presented herein. It should nevertheless be mentioned again that the second implementation of the NSMC yielded results that were inconsistent with outcomes of the calibration. This consistency is a requirement to be able to claim with integrity that predictions made by the calibrated model are of minimum error variance [118].

It should be mentioned again that only major drainage ditches have been considered in the model. For instance, the drainage ditch Canal d'Uvrier running across the downstream part of the alluvial fan of Lienne River at St-Léonard has not been accounted for in the model. This ditch drains the alluvial aquifer during HW, while it lies above the water level in the aquifer during LW. If the temporary occurrence of exfiltrating conditions should persist in the future state, the extent of the zone with large head changes predicted for this area might possibly be limited. A similar scenario is conceivable for the area downstream of the "neck" at Martigny, where several exfiltrating gravel pits ("Le Rosel") are present that are not represented as surface waters in the model but that pertain to the aquifer.

In the light of the stated "barrier effect" that drainage ditches may have on the impact of the PR3, uncertainty related to surface water levels may be particularly rele-

vant. It is however clear, that the influence of surface water levels is masked by the presence of a streambed with unknown properties. Ideally, an assessment of the effect of uncertain surface water levels should be carried out. This would however require a re-calibration of transfer rates for each tested scenario, which was considered computationally too expensive.

Within this work, considerations regarding uncertainty always refer to uncertain parameters. Other sources of uncertainty which possibly are sometimes even more important for predictions of the impact of PR3 on groundwater have not been considered. For instance:

- No evaluation of the uncertainty of surface water levels or of abstraction rates has been undertaken.
- More importantly, one single conceptual model has been considered, whereas often, several conceptual models are capable to match the available field measurements. Moreover, the conceptual understanding of the Rhône aquifer used as a basis for the model relies on steady state data. It is clear that the transient character of possibly important system processes (such as the de-clogging of the streambed during flood events cannot be captured by the model). It must be admitted that it is not clear in how the inclusion of transient data would require a revision of the conceptual model and what the effect on model predictions would be.
- To my knowledge, the influence of climate changes has not been considered in the modeling of future state discharge of the Rhône River. This may be an important factor in the near future, as changes in the amount and seasonality of precipitation, and in the response of snow and glaciers induced as a consequence of a warming climate are expected to trigger off substantial changes to the flow regime of the Rhône River [161].
- The long-term response of the alluvial aquifer is to an important degree influenced by the evolution of the streambed conductance in the restored streambed, at least in the upper part of the model.

Chapter 7

Conclusions and future work

7.1 Project insights and future prospects

7.1.1 System understanding

The main objective of this thesis was the quantitative evaluation of the impact of the Third Rhône correction (PR3) on groundwater within the alluvial Rhône aquifer. The first aim consisted in a hydrogeological study of the area and in synthesizing the understanding in a conceptual aquifer model. Here, the most important findings from the data analysis are summarized:

1) Surface water – groundwater (SW–GW) interactions are the major driving force of the subsurface hydrology of the Rhône alluvial aquifer. This can safely be concluded by the analysis of groundwater flow patterns, of the distribution of hydrophysical and hydrochemical parameters and by the dynamics of the aquifer, imitating variations of river stages in the Rhône River. Besides the Rhône River, drainage ditches are seen as an important element of the SW–GW system.

2) At and near the upstream limit, on the stretch between Charrat and Riddes, at Saillon, at Martigny, at Conthey and at four other places with minor contributions, recharge of the aquifer by lateral inflows from valley slopes and small lateral alluvial aquifers is indicated by piezometric, hydrochemical and hydrophysical data.

3) The system is driven by regional controls, with low water tables in the aquifer downstream of the low permeable Illgraben fan and increasing heads in the downstream direction due to recharge by the Rhône River and due to the presence of the low permeable alluvial fan of St-Barthélémy.

This conceptual understanding formed the base for the construction of a steady state groundwater flow model. The model was calibrated against average hydraulic heads. The calibrated model was able to reproduce the observation data satisfactory and estimated parameters lie within the expected range. An independent assessment of the degree of realism of the model can be elaborated by comparing the model behavior to hydrogeological features observed in the model area. For example:

1) The fact that modeled exchange flow rates at drainage ditches are consistent with measured flow rates provides evidence that the underlying modeling assumptions are correct. These flow rates have not been accounted for in the calibration process.

2) The systematic occurrence of high exchange flow in areas where the Rhône River passes by a pond is a sign that the model is able to capture the dominant aspects of SW-GW interaction.

3) The systematic occurrence of high exchange flow in areas where material is excavated from the streambed of the Rhône River indicates that patterns of SW-GW interaction are significantly affected by changes to the streambed and can be taken as a further indication, that the model is a robust description of the physical environment along the Rhône River.

Besides this, modeling results provide further insights to the functioning of the alluvial aquifer:

4) Modeling results suggest a clogging of the streambed in large part.

5) Modeling results suggest that areas, in which the water table in the aquifer fluctuates around the elevation of the streambed on a seasonal time scale, are characterized by high exchange flows. It is speculated that in these transitional zones, a de-clogging of the streambed takes place.

6) Even if the alluvial aquifer is driven by regional controls, human influence constitutes an important factor of the hydrosystem: drainage of the alluvial plain by ditches, hydropeaking resulting from the exploitation of hydropower and related to it, clogging of the streambed are important characteristics of the SW-GW system which are man-made.

7) A comparison of the estimated hydraulic conductivity field with historic maps of the region suggests that inverse modeling permitted to roughly identify geomorphic features such as historic river beds. This finding may be interesting for paleoenvironmental studies in a similar hydrogeological setting.

Regarding predictions of the impact by PR3, modeling results are qualitatively in agreement with common hydrogeological sense. Results show that:

1) On the condition that the streambed properties will return to a stable state identical to the current state in the long term, induced head changes in a given area are at large proportional to changes in river stages on the corresponding river stretch, if the river is hydraulically connected to the aquifer.

2) In the short term, a rise of the water table in the aquifer may be expected at places where a clogging layer is removed by restoration works and where the streambed incises in a permeable aquifer.

3) The presence of stretches with exfiltrating conditions – whether on the Rhône River or at ditches – may attenuate the influence of the PR3 on groundwater.

4) Streambed conductance was found to be an important control for the understanding of the surface water – groundwater system of the alluvial Rhône aquifer and for the prediction of the impact by the PR3. Especially in the upstream part of the model, the response of the alluvial aquifer is to an important degree influenced by the evolution of the streambed conductance in the restored streambed. In contrast, the downstream part of the model (downstream of about km 48) is largely driven by regional controls and the response of the aquifer depends hence little on the streambed conductance.

7.1.2 Remaining challenges and future work

1) Changes to the streambed significantly affect SW-GW interactions, as indicated by the occurrence of high exchange rates near quarries within the streambed; the understanding of sedimentation transport processes is crucial to predicting the evolution of streambed properties after restoration works, and hence to predicting the impact of restoration measures in the long term. This item has not been addressed herein and should be tackled in future work.

2) The relation between SW-GW interactions and sedimentation processes is possibly an important element of the SW-GW system, as indicated by the hypothesized de-clogging of the streambed by fluctuations of the groundwater table. This relation remains an unaddressed issue and deserves attention.

3) Infiltration through the riverbank has been suggested to be an important mechanism of aquifer recharge in the Rhône alluvial aquifer. As this process cannot explicitly be accounted for in a 2D model, it could be treated in future modeling studies involving a 3D model.

4) The transience of the system was disregarded in the present steady state model and should receive attention, e.g. in regard of the presumably transient character of streambed properties on a restored reach.

5) The high density of the parameterization has proven to be important in that it enables the identification of local-scale processes (exchange flow at quarries; identification of buried paleochannels etc.). In the uppermost part of the model, an even denser parameterization of hydraulic conductivity would be a promising approach to better account for the local hydrogeology (low permeable hills formed by rockslide deposits) and to hopefully face structural noise that is thought to be present in that area in the model presented herein.

6) Testing of different conceptual models against each other has not been undertaken herein, but would be interesting. Testing might include locations of lateral flow boundaries, the parameterization of the inverse problem (pilot point density, choice of variogram, different initial values etc.), or assumptions on the structure of the spatial correlation of hydraulic properties. For instance, recent geostatistical methods allow the generation of realistic aquifer and streambed – connectivity [162, 163], an issue that is evidenced to be important by exchange flows occurring on a small scale.

7) Other types of observation data could potentially better identify the system. For instance, measurements of SW-GW exchange rates, be it local measurements or values integrated over a certain distance (e.g. at drainage ditches), would certainly help to further constrain parameter values.

8) Lithological data would merit to be analyzed in more detail. For instance, vertical proportion curves of the lithological composition seem to provide information for an exciting analysis of the formation history of the Rhône alluvial aquifer.

7.2 Conclusions regarding the null space Monte Carlo method

In Chapter 3, PEST's null space Monte Carlo (NSMC) methodology for the assessment of parameter uncertainty has been tested on a synthetic model. Three specific points have been examined: (1) the technique to sample the null space about a calibrated solution, (2) the performance of NSMC in the context of a nonlinear model and (3) the inclusion of measurement noise prior to the re-calibration step that is innate to the NSMC methodology in the context of a nonlinear model. The main findings of this test are:

1) The null space is not necessarily sampled in a homogeneous way, when using the standard sampling method as implemented in the suite of PEST's utility programs, i.e. if sampling is undertaken by projection of random parameter sets onto the null space. We suggest to directly sampling the null space instead. The method proposed herein has been tested for a low dimensional problem solely and needs further testing.

2) In the context of a nonlinear model, the NSMC method may underestimate parameter uncertainty, if the uncertainty analysis is based on a single calibrated model only. This issue may in principle be overcome by performing the uncertainty analysis about several calibrated solutions, which can for instance be found by starting the estimation process from different initial solutions. In an alternative method presented herein, the NSMC procedure is de-

signed as a sequence of null space projection and re-calibration steps. In principle, this approach has the advantage to release the modeler from the task of choosing appropriate initial values, such that a full exploration of uncertainty is ensured. While the proposed strategy yielded promising results in the simple synthetic case considered herein, further testing is required to assess its practical usability.

3) Including measurement noise in the post-null-space-projection-re-calibration step proved to be necessary in order to correctly propagate measurement noise into parameters. In the model of the Rhône alluvial aquifer, however, this strategy was found to introduce a bias in parameter estimates, in that mean values of the resulting parameter distributions differed considerably from calibrated values. This behavior was unexpected and would be worth be addressing in future research.

In view of the high computational cost associated with other methods of uncertainty estimation, the NSMC methodology can – despite the issues related to the method – be seen as an approximate, but valid approach to assess parameter uncertainty.

References

1. Canton du Valais, P. *Rapport de synthèse du plan d'aménagement de la 3ème correction du Rhône - PA-R3.* Département des transports, de l'équipement et de l'environnement, 2008.
2. Géoval. *Rapport après 3 ans d'obsérvation - Paliers 1-7*. Sion: Hydro-Rhône SA, 1986.
3. Rovina, H., D. Glenz, and S. Volken. (2008). *Beurteilung der GW-Beeinträchtigung auf Stufe Generelles Projekt*. Projet Rhône 3.
4. Rovina, H. and D. Glenz. (2007). *Versuchsstandort Rhonebrücke Lalden, Durchlässigkeitsbestimmung der Rhonesohle*. Projet Rhône 3.
5. Badertscher, C. (2008). *Détermination de la conductivité hydraulique de la couche de colmatage du Rhône, Mesure prioritaire de Fully - Pont de Solverse*. Projet Rhône 3.
6. Schmalzried, R. and H. Rovina. (2010). *Baggerschlitze / Volumenproben - Kurzbericht zur Probenahme und Dokumentation der Analytik der Korngrössenverteilung*. Projet Rhône 3.
7. Murisier, L. *Etude de la typologie des principaux canaux de la plaine entre Riddes et Martigny*. Projet Rhône 3, 2009.
8. Badertscher, C. (2011). *Jaugeages du canal de Vissigen du 13.09.2011*. Projet Rhône 3.
9. Marquis, F.-X. and Y. Borle. (2011). *Canaux du Syndicat et de Leytron-Saillon-Fully: Campagnes de jeaugeage et charactérisation des relations nappe - canal*. Projet Rhône 3.
10. Magnard, A. (2006). *Mesures d'infiltration et modélisation des écoulements dans deux profils transversaux représentatifs*. Master thesis, Univerité de Neuchâtel.
11. Cochand, F. (2006). *Modélisation de la nappe alluviale du Rhône au niveau du coude de Fully*. Master thesis, Univerité de Neuchâtel.
12. Meile, T., M. Fette, and P. Baumann. *Synthesebericht Schwall/Sunk (Publikation des Rhone-Thur Projektes)*. Eawag, WSL, LCH-EPFL, Limnex, 2004.
13. Meile, T., J.L. Boillat, and A.J. Schleiss, *Hydropeaking indicators for characterization of the Upper-Rhone River in Switzerland.* Aquatic Sciences, 2011. **73**(1): p. 171-182.
14. Fette, M.W. (2005). *Tracer Studies of River-Groundwater Interaction under Hydrospeaking Conditions*. PhD thesis, Swiss Federal Institute of Technology.

15. Wüest, A., *Alpine hydroelectric power plants and their "long-range effects" on downstream waters.* EAWAG news, 2002. **55e**: p. 18-20.

16. Meier, W., M. Frey, L. Moosmann, S. Steinlin, and A. Wüest. *Wassertemperaturen und Wärmehaushalt der Rhone und ihrer Seitenbäche.* Rhone-Thur Projekt, EAWAG, WSL, 2004.

17. Frey, M. (2003). *Temperaturmodellierung - Auswirkungen von Kraftwerken auf das Temperaturregime in Zuflüssen der Rhône.* Master thesis, ETH Zürich.

18. Portmann, M., P. Baumann, and B. Imhof. *Schwebstoffhaushalt und Trübung der Rhone.* Rhone-Thur Projekt, EAWAG, WSL, 2004.

19. Brögli, M. (2001). *Geochemische und wasserisotopische Untersuchungen im Rhoneabschnitt zwischen Sion und Branson.* Master thesis, ETH Zürich.

20. Steiner, R. (2004). *Untersuchungen im Pfynwald (Wallis) zu Wechselwirkungen zwischen Rhône und Grundwasser mittels Tracern und Modellrechungen*. Master thesis, ETH Zürich.

21. Peter, A., F. Kienast, and S. Nutter, *The Rhone-Thur River project: a comprehensive river rehabilitation project in Switzerland.* Large Rivers, 2005. **15**: p. 643-656.

22. Loizeau, J. and J. Dominik, *Evolution of the Upper Rhone River discharge and suspended sediment load during the last 80 years and some implications for Lake Geneva* Aquatic Sciences, 2000. **62**(1): p. 54-67.

23. Bernard, R., R. Perraudin - Kalbermatter, and M. Bernard. *Observation de la qualité des eaux de surface du canton du Valais - Le Rhône et neuf de ses affluents*. 1994.

24. Fleckenstein, J.H., S. Krause, D.M. Hannah, and F. Boano, *Groundwater-surface water interactions: New methods and models to improve understanding of processes and dynamics.* Advances in Water Resources, 2010. **33**(11): p. 1291-1295.

25. Winter, T.C., J.W. Harvey, O.L. Franke, and W.M. ALLEY, *Ground Water and Surface Water A Single Resource*. 1998, Circular 1139. Denver, Colorado.: USGS.

26. Woessner, W., *Stream and Fluvial Plain Ground Water Interactions: Rescaling Hydrogeologic Thought.* Ground Water, 2000. **38**(3): p. 423-429.

27. Sophocleous, M., *Interactions between groundwater and surface water: the state of the science.* Hydrogeology Journal, 2002. **10**(2): p. 52-67.

28. Kalbus, E. (2009). *Spotlight on heterogeneity: measuring and modelling stream-aquifer interactions*. PhD thesis, Université de Neuchâtel.

29. Käser, D.H., A. Binley, and A.L. Heathwaite, *On the importance of considering channel microforms in groundwater models of hyporheic exchange.* River Research And Applications, 2012.

30. Kasahara, T. and A.R. Hill, *Modeling the effects of lowland stream restoration projects on stream-subsurface water exchange.* Ecological Engineering, 2008. **32**(4): p. 310-319.

31. Schaelchli, U., *The Clogging of Coarse Gravel River Beds by Fine Sediment.* Hydrobiologia, 1992. **235**: p. 189-197.

32. Wroblicky, G.J., M.E. Campana, H.M. Valett, and C.N. Dahm, *Seasonal variation in surface-subsurface water exchange and lateral hyporheic area of two stream-aquifer systems.* Water Resources Research, 1998. **34**(3): p. 317-328.

33. Zlotnik, V.A., M.B. Cardenas, and D. Toundykov, *Effects of Multiscale Anisotropy on Basin and Hyporheic Groundwater Flow.* Ground Water, 2011. **49**(4): p. 576-583.

34. Irvine, D.J., P. Brunner, H.-J.H. Franssen, and C.T. Simmons, *Heterogeneous or homogeneous? Implications of simplifying heterogeneous streambeds in models of losing streams.* Journal of Hydrology, 2012. **424–425**(0): p. 16-23.

35. Huggenberger, P., E. Hoehn, R. Beschta, and W. Woessner, *Abiotic aspects of channels and floodplains in riparian ecology.* Freshwater Biology, 1998. **40**(3): p. 407-425.

36. Fleckenstein, J.H., R.G. Niswonger, and G.E. Fogg, *River-Aquifer Interactions, Geologic Heterogeneity, and Low-Flow Management.* Ground Water, 2006.

37. Schneider, P., et al., *Towards improved instrumentation for assessing river-groundwater interactions in a restored river corridor.* Hydrol. Earth Syst. Sci., 2011. **15**(8).

38. Tague, C., S. Valentine, and M. Kotchen, *Effect of geomorphic channel restoration on streamflow and groundwater in a snowmelt-dominated watershed.* Water Resources Research, 2008. **44**(10): p. W10415.

39. Brunke, M. and T. Gonser, *The ecological significance of exchange processes between rivers and groundwater.* Freshwater Biology, 1997. **37**(1): p. 1-33.

40. Kalbus, E., F. Reinstorf, and M. Schirmer, *Measuring methods for groundwater - surface water interactions: a review.* Hydrology and Earth System Sciences, 2006. **10**(6): p. 873-887.

41. de Marsily, G., J.P. Delhomme, F. Delay, and A. Buoro, *40 years of inverse problems in hydrogeology.* Comptes Rendus de l'Academie des Sciences Series IIA. Earth and Planet Science, 1999. **329**(2): p. 73-87.

42. Carrera, J., A. Alcolea, A. Medina, J. Hidalgo, and L.J. Slooten, *Inverse problem in hydrogeology.* Hydrogeology Journal, 2005. **13**: p. 206 - 222.

43. Renard, P., *Stochastic Hydrogeology: What Professionals Really Need?* Ground Water, 2007. **45**(5): p. 531-541.

44. Cardenas, M.B. and J.L. Wilson, *Hydrodynamics of coupled flow above and below a sediment-water interface with triangular bedforms.* Advances In Water Resources, 2007. **30**(3): p. 301-313.

45. Cardenas, M.B., J.L. Wilson, and R. Haggerty, *Residence time of bedform-driven hyporheic exchange.* Advances In Water Resources, 2008. **31**(10): p. 1382-1386.

46. Kasahara, T. and S.M. Wondzell, *Geomorphic controls on hyporheic exchange flow in mountain streams.* Water Resources Research, 2003. **39**(1).

47. Doherty, J. (2011). PEST: Model—Independent parameter estimation, user manual (5th ed.). Brisbane, Australia: Watermark Numerical Computing.

48. Labhart, T.P., *Geologie der Schweiz*. 2001, Thun: Ott Verlag. 211.

49. Reynard, E., M. Evéquoz-Dayen, and P. Dubuis, *Le Rhône alpin vu sous l'angle de la géomorphologie: état des lieux.* Cahiers de Vallesia, 2009. **21**: p. 75-102.

50. Champagnac, J.-D., C. Sue, B. Delacou, and M. Burkhard, *Brittle deformation in the inner NW Alps: from early orogen-parallel extrusion to late orogen-perpendicular collapse.* Terra Nova, 2004. **16**(4): p. 232-242.

51. Preusser, F., J. Reitner, and C. Schlüchter, *Distribution, geometry, age and origin of overdeepened valleys and basins in the Alps and their foreland.* Swiss Journal of Geosciences, 2010. **103**(3): p. 407-426.

52. Hubbard, M. and N.S. Mancktelow, *Lateral displacement during Neogene convergence in the western and central Alps* Geology, 1992. **20**(10): p. 943-946.

53. Jaboyedoff, M., F. Baillifard, and M.-H. Derron, *Preliminary note on uplift rates gradient, seismic activity and possible implications for brittle tectonics and rockslide prone areas: The example of western Switzerland.* Bull. Soc. Vaud. SC. nat., 2003. **88.3**: p. 393-412.

54. Pfiffner, O.A., P. Lehner, P. Heitzmann, S. Mueller, and A. Steck, *Deep Structure of the Swiss Alps - Results from NRP 20*. 1997, Basel: Birkhäuser Verlag.

55. Valla, P.G., et al., *Late Neogene exhumation and relief development of the Aar and Aiguilles Rouges massifs (Swiss Alps) from low-temperature thermochronology modeling and 4He/3He thermochronometry.* J. Geophys. Res., 2012. **117**(F1): p. 23.

56. Finckh, P. and W. Frei, *Seismic reflection profiling in the Swiss Rhone valley. I, Seismic reflection field work, seismic processing and seismic results of the Roche-Vouvry and Turtmann and Agarn lines.* Eclogae Geologicae Helvetiae, 1991. **84**(2): p. 345-357.

57. Besson, O., R. Marchant, A. Pugin, and J.-D. Rouiller, *Campagne de sismique-réflexion dans la vallée du Rhône entre Sion et St-Maurice: Perspectives d'exploitation géothermique des dépôts torrentiels sous-glaciaires.* Bulletin du Centre d'Hydrogéologie, Université de Neuchâtel, 1993. **12**: p. 39 - 58.

58. Rosselli, A. and O. Raymond, *Modélisation gravimétrique 2.5D et cartes des isohypses au 1:100'000 du substratum rocheux de la Vallée du Rhône entre Villeneuve et Brig (Suisse).* Ecolgae geol. Helv., 2003. **96**: p. 399-423.

59. Roten, D., D. Fäh, K.B. Olsen, and D. Giardini, *A comparison of observed and simulated site response in the Rhône valley.* Geophysical Journal International, 2008. **173**(3): p. 958-978.

60. Havenith, H.-B., D. Fäh, S. Alvarez-Rubio, and D. Roten, *Response spectra for the deep sediment-filled Rhône Valley in the Swiss Alps.* Soil Dynamics and Earthquake Engineering, 2009. **29**(1): p. 17-38.

61. Finger, W. and M. Weidmann, *Quelques données géologiques nouvelles sur la vallée du Rhône entre Sierre et le Léman.* Bulletin de la Murithienne, 1987. **105**: p. 27-40.

62. Badoux, H., *Le glacier du Rhône au Pléistocène.* Bulletin de la Société Vaudoise des Sciences Naturelles, 1995. **83**: p. 245-292.

63. Maurer, H.R., M. Burkhard, N. Deichmann, and A.G. Green, *Active tectonism in the central Alps: contrasting stress regimes north and south of the Rhone Valley.* Terra Nova, 1997. **9**(2): p. 91-94.

64. Marchant, R. and O. Besson (1986). *Etude gravimétrique des collines de Chiètres*. Master thesis, Lausanne.

65. Lugeon, M. and N. Oulianoff, *L'alluvion du Rhône valaisan. Essai de détermination de l'épaisseur par méthode électrique.* Bulletin des Laboratoires de Géologie, Géographie Physique, Minéralogie et Paléontologie de Lausanne, 1939. **64**: p. 1-26.

66. Clavien, B. *Hydrogeologische Studie. Bericht zur Tiefbohrung Brigerbad (TB)*. Service des routes nationales, 1988.

67. Burri, M., *La géologie du Quaternaire aux environs de Sierre.* Bulletin de la Société Vaudoise des Sciences Naturelles, 1955. **66**(288): p. 141-154.

68. Summermatter, S., *Die erste Rhonekorrektion und die weitere Entwicklung der kantonalen und nationalen Wasserbaupolitik im 19. Jahrhundert.* Vallesia, 2004. **59**: p. 199-224.

69. Pasche, L., *Travaux de correction des cours d'eau en Valais et dans la région de Conthey (1860-1900).* Vallesia, 2004. **59**: p. 225-246.

70. Stäuble, S. and E. Reynard, *Evolution du paysage de la plaine du Rhône dans la région de Conthey depuis 1850.* Vallesia, 2005. **60**: p. 433-456.

71. Zanini, F., E. Zanini, and C. Weber, *Analyse de la dynamique du paysage de la plaine du Rhône de 1850 à 2003 sur la base de cartes topographiques.* Bulletin de la Murithienne, 2006. **124**: p. 89-98.

72. Laigre, L., G. Arnaud-Fassetta, and E. Reynard, *Cartographie sectorielle et dynamique de la plaine alluviale du Rhône suisse (Tourtemagne-Sierre) depuis la fin du Petit Age Glaciaire*, in *La géomorphologie alpine : entre patrimoine et contrainte. Actes du colloque de la Société Suisse de Géomorphologie, 3-5 septembre 2009, Olivone*, C. Lambiel, Reynard, E., Scapozza, C., Editor. 2011, Université, Institut de géographie: Lausanne. p. 79 - 97.

73. Baumann, P. *Revitalisierung und Benthos der Rhone*. Rhone-Thur Projekt, EAWAG, WSL, Limnex AG, 2004.

74. Mariétan, I., *Le Rhône. La lutte contre l'eau en Valais.* Editions du Griffon, Neuchâtel, 1953: p. 22 pp.

75. Bragg, O.M., A.R. Black, R.W. Duck, and J.S. Rowan, *Approaching the physical-biological interface in rivers: a review of methods for ecological evaluation of flow regimes.* Progress in Physical Geography, 2005. **29**(4): p. 506-531.

76. Cushman, R.M., *Review of Ecological Effects of Rapidly Varying Flows Downstream from Hydroelectric Facilities.* North American Journal of Fisheries Management, 1985. **5**(3A): p. 330-339.

77. Bradford, M.J., G.C. Taylor, J.A. Allan, and P.S. Higgins, *An Experimental Study of the Stranding of Juvenile Coho Salmon and Rainbow Trout during Rapid Flow Decreases under Winter Conditions.* North American Journal of Fisheries Management, 1995. **15**(2): p. 473-479.

78. Schaelchli, U. *Kolmation: Methoden zur Erkennung und Bewertung*. Bericht im Auftrag von Fischnetz c/o EAWAG, Dübendorf, 2002.

79. Crealp, *Données hydrogéologiques cantonale REGIS*, 2010.

80. FOEN. *Hydrological data, Rhône - Branson*. 2011; Available from: http://www.hydrodaten.admin.ch/de/2024.html#historische_daten.

81. FOEN. *Hydrological data, Rhône - Sion*. 2011; Available from: http://www.hydrodaten.admin.ch/de/2011.html#historische_daten.

82. Weingartner, R. and A. Hugo, *Discharge Regime - the Basis for the Estimation of Average Flows, Plate 5.2*, in *Hydrological Atlas of Switzerland,* 1992, Federal Office for the Environment FOEN: Bern.

83. Bernard, M., R. Bernard, and D. Theler. *Qualité des cours d'eau en Valais.* 2007.

84. Gurnell, A., D.M. Hannah, and D. Lawler. *Suspended sediment yield from glacier basins*. In: Proceedings of *Erosion and Sediment Yield: Global and Regional Perspectives*. 1996. Exeter, UK: IAHS Publ. 236.

85. Tockner, K., U. Karaus, A. Paetzold, and S. Blaser, *Ökologischer Zustand der Rhone: benthische Evertebraten und Uferfauna.* Wasser Energie Luft, 2004. **96**(11/12): p. 315-317.

86. Weber, C. (2007). *River rehabilitation and fish. The challenge of initiating ecological recovery.* PhD thesis, Swiss Federal Institute of Technology.

87. Roulier, C. and G. Vadi, *Erfolgskontrolle der Vegetationsdynamik Rhone: Stand der Forschung 2004.* Wasser, Energie, Luft 2004. **11/12**: p. 309-314.

88. Vogel, A. (2011). Personal communication on: *Composition of river bed sediments in tributaries between Sierre and St-Maurice (Canton of Valais).*

89. Fibicher, A., *Walliser Geschichte: Die Neuzeit / Ereignisse und Entwicklungen 1520 - 1991*. 1993: Erziehungsdepartement d. Kantons Wallis.

90. Crealp. *Exploitation et valorisation des données piézométriques de la nappe alluviale - Plaine du Rhône entre Brig et le Léman, Cartes de la nappe phréatique*. Sion: Crealp, Centre de recherche en environnement alpin, 2008.

91. Schürch, M. (2000). *Détermination des paramètres hydrauliques et hydrochimiques d'un aquifère alluvial dans une vallée alpine (Valais, Suisse)*. PhD thesis, Université de Neuchâtel.

92. Brunner, P., C. Simmons, and P. Cook, *Hydrogeologic controls on disconnection between surface water and groundwater.* Water Resources Research, 2009. **45**(1): p. 13.

93. Freeze, R.A.a.C., J.A., *Groundwater*. 1979, Englewood Cliffs, NJ.: Prentice-Hall Inc.

94. Hoehn, E. and A. Scholtis, *Exchange between a river and groundwater, assessed with hydrochemical data.* Hydrol. Earth Syst. Sci., 2011. **15**(3).

95. Granges, M. (2009). *Etude hydrogéologique et géochimique du système hydrothermal de Saxon, Valais*. thesis, Université de Neuchâtel.

96. Vuataz, F., J.D. Rouiller, J.D. Dubois, G. Bianchetti, and O. Besson, *Programme GEOTHERMOVAL. Résultats d'une prospection des ressources géothermiques du Valais, Suisse.* Bulletin du Centre d'hydrogéologie de Neuchâtel, 1993. **12**: p. 1-37.

97. Bernard, R., R. Perraudin - Kalbermatter, and M. Bernard, *Observation de la qualité des eaux de surface du canton du Valais - Le Rhône et neuf de ses affluents (Campagne 1993)*. Rapp. Comm. int. prot. eaux Léman contre pollut., 1994: p. 197-240.

98. Canton du Valais. (2010). *BD-for, Borehole database*.

99. Matheron, G., H. Beucher, C. de Fouquet, and A. Galli, *Conditional Simulation of the Geometry of Fluvio-Deltaic Reservoirs*, in *SPE Annual Technical Conference and Exhibition,* 1987, Society of Petroleum Engineers Dallas, Texas. p. 591-599.

100. Rovina, H. and D. Glenz. *Versuchsstandort Rhonebrücke Lalden, Durchlässigkeitsbestimmung der Rhonesohle*. Projet Rhône 3, 2007.

101. MeteoSwiss, *Climate norm values 1961 - 1990*, 2010, Federal Office of Meteorology and Climatology MeteoSwiss.

102. FOEN, *Mean Annual Corrected Precipitation Depth 1951-1980, Plate 2.2*, in *Hydrological Atlas of Switzerland,* 2010, Federal Office for the Environment FOEN: Bern.

103. Neuman, S.P., *Calibration of distributed parameter groundwater flow models viewed as a multiple-objective decision process under uncertainty.* Water Resources Research, 1973. **9**(4): p. 1006-1021.

104. Doherty, J.E., *Approaches to highly parameterized inversion - A guide to using PEST for groundwater-model calibration: U.S. Geological Survey Scientific Investigations Report 2010–5169*, ed. R.J. Hunt. 2010, Reston, Va.: U.S. Dept. of the Interior, U.S. Geological Survey.

105. Fuhry, M. and L. Reichel, *A new Tikhonov regularization method.* Numerical Algorithms, 2012. **59**(3): p. 433-445.

106. Yeh, W.W.-G., *Review of Parameter Identification Procedures in Groundwater Hydrology : The Inverse Problem.* Water Resources Research, 1986. **22**(2): p. 95-108.

107. Marsily, G.d. (1978). *De l'identification des systèmes hydrogeologiques*. pHD thesis, Ecoles des Mines de Paris.

108. Marsily, G.d., C. Lavedan, M. Boucher, and G. Fasanino, *Interpretation of interference tests in a well field using geostatistical techniques to fit the permeability distribution in a reservoir model. In: Verly G et al., editors. Geostatistics for natural resources characterization. Part 2. D. Reidel Pub Co.* 1984: p. 831–849.

109. LaVenue, A.M., B.S. RamaRao, G. De Marsily, and M.G. Marietta, *Pilot Point Methodology for Automated Calibration of an Ensemble of Conditionally Simulated Transmissivity Fields: 2. Application.* Water Resources Research, 1995. **31**(3): p. 495-516.

110. RamaRao, B.S., A.M. LaVenue, G. De Marsily, and M.G. Marietta, *Pilot Point Methodology for Automated Calibration of an Ensemble of conditionally Simulated Transmissivity Fields: 1. Theory and Computational Experiments.* Water Resources Research, 1995. **31**(3): p. 475-493.

111. Alcolea, A., J. Carrera, and A. Medina, *Pilot points method incorporating prior information for solving the groundwater flow inverse problem.* Advances in Water Resources, 2006. **29**(11): p. 1678-1689.

112. Doherty, J., *Ground water model calibration using pilot points and regularization.* Groundwater, 2003. **41**(2): p. 170-177.

113. Kowalsky, M.B., S. Finsterle, and Y. Rubin, *Estimating flow parameter distributions using ground-penetrating radar and hydrological measurements during transient flow in the vadose zone.* Advances in Water Resources, 2004. **27**(6): p. 583-599.

114. Oliver, D.S., A.C. Reynolds, and N. Liu, *Inverse Theory for Petroleum Reservoir Characterization and History Matching*. 2008: Cambridge University Press.

115. Hu, L., G. Blanc, and B. Noetinger, *Gradual Deformation and Iterative Calibration of Sequential Stochastic Simulations.* Mathematical Geology, 2001. **33**(4): p. 475-489.

116. Caers, J., *History matching under training-image based geological model constraints.* Society of Petroleum Engineers Journal, 2003. **8**(3): p. 218-226.

117. Kirkpatrick, S., C.D. Gelatt, and M.P. Vecchi, *Optimization by simulated annealing.* Science, 1983(220): p. 671–680.

118. Doherty, J.E., *Approaches to highly parameterized inversion - Pilot-point theory, guidelines, and research directions: U.S. Geological Survey Scientific Investigations Report 2010–5168*, ed. R.J. Hunt. 2010, Reston, Va. :: U.S. Dept. of the Interior, U.S. Geological Survey. 36.

119. Doherty, J.E., *Approaches to highly parameterized inversion - A guide to using PEST for model-parameter and predictive-uncertainty analysis: U.S. Geological Survey Scientific Investigations Report 2010–5211*, ed. R.J. Hunt. 2010, Reston, Va.: U.S. Dept. of the Interior, U.S. Geological Survey. 71.

120. Paige, C.C. and M.A. Saunders, *LSQR: An Algorithm for Sparse Linear Equations and Sparse Least Squares.* ACM Trans. Math. Softw., 1982. **8**(1): p. 43-71.

121. Moore, C. and J. Doherty, *The cost of uniqueness in groundwater model calibration.* Advances in Water Resources 2005. **29**: p. 605-623.

122. Aster, R., B. Borchers, and C. Thurber, *Parameter Estimation and Inverse Problems - 2nd ed.* 2012: Elsevier Academic Press.

123. Tonkin, M.J. and J. Doherty, *A hybrid regularized inversion methodology for highly parameterized environmental models.* Water Resources Research, 2005. **41**(10): p. W10412.

124. Tonkin, M., J. Doherty, and C. Moore, *Efficient nonlinear predictive error variance for highly parameterized models.* Water Resources Research, 2007. **43**(7): p. W07429.

125. Tonkin, M. and J. Doherty, *Calibration-constrained Monte Carlo analysis of highly parameterized models using subspace techniques.* Water Resources Research, 2009. **45**(12): p. W00B10.

126. Herckenrath, D., C.D. Langevin, and J. Doherty, *Predictive uncertainty analysis of a saltwater intrusion model using null-space Monte Carlo.* Water Resources Research, 2011. **47**(5): p. W05504.

127. Tarantola, A., *Inverse Problem Theory and Methods for Model Parameter Estimation*. 2005, Philadelphia: Society for Industrial and Applied Mathematics.

128. Ginn, T., J. Cushman, and M. Houck, *A Continuous-Time Inverse Operator for Groundwater and Contaminant Transport Modeling: Deterministic Case*, in *Water Resour. Res.*1990. p. 241-252.

129. McLaughlin, D. and L.R. Townley, *A Reassessment of the Groundwater Inverse Problem.* Water Resources Research, 1996. **32**(5): p. 1131-1161.

130. TZ, I. and S. ND, *Noninformative Priors Do Not Exist: A Discussion with Jose M. Bernardo.* 1997.

131. Mariéthoz, G., P. Renard, and J. Caers, *Bayesian inverse problem and optimization with Iterative Spatial Resampling.* Water Resources Research, 2010.

132. Martino, L. and J. Miguez. *A novel rejection sampling scheme for posterior probability distributions*. In: Proceedings of *2009 IEEE International Conference on Acoustics, Speech and Signal Processing*. 2009. Taipei, Taiwan: IEEE Computer Society.

133. Ballio, F. and A. Guadagnini, *Convergence assessment of numerical Monte Carlo simulations in groundwater hydrology.* Water Resources Research, 2004. **40**(4).

134. MATLAB. (2012) (Version Version 7.14). Natick, Massachusetts: The MathWorks Inc.

135. Doherty, J. and D. Welter, *A short exploration of structural noise.* Water Resources Research, 2010. **46**(5).

136. Keating, E.H., J. Doherty, J.A. Vrugt, and Q. Kang, *Optimization and uncertainty assessment of strongly nonlinear groundwater models with high parameter dimensionality.* Water Resources Research, 2010. **46**(10).

137. Yoon, H., D.B. Hart, and S.A. McKenna, *Parameter estimation and predictive uncertainty in stochastic inverse modeling of groundwater flow: Comparing null-space Monte Carlo and multiple starting point methods.* Water Resources Research, 2013.

138. Cornaton, F.J. (2007). Ground Water : A 3-D Ground Water and Surface Water Flow, Mass Transport and Heat Transfer Finite Element Simulator.

139. Bear, J., *Hydraulics of groundwater*. 1979, New York ; London: McGraw-Hill. xiii, 567p.

140. Anderson, M.P. and W.W. Woessner, *Applied groundwater modeling*. 1992: Acad. Press.

141. Rushton, K. and L. Tomlinson, *Possible mechanisms for leakage between aquifers and rivers.* Journal of Hydrology, 1979. **40**: p. 49-65.

142. Shewchuk, J.R. (2005). Triangle - A Two-Dimensional Quality Mesh Generator and Delaunay Triangulator (Version 1.6).

143. Schäppi, B., P. Perona, P. Schneider, and P. Burlando, *Integrating river cross section measurements with digital terrain models for improved flow modelling applications.* Computers and Geosciences, 2010. **36**(6): p. 707-716.

144. Swisstopo. *Digitales Terrain Modell - Amtliche Vermessung (DTM-AV)*.

145. Swisstopo. *DTM-AV + DOM Verfügbarkeit*. 2012; Available from: http://www.swisstopo.admin.ch/internet/swisstopo/de/home/products/height/dom_dtm-av.html.

146. Vogel, A., *Relations entre le lac de la gravière des Epines et la nappe phréatique de la plaine alluviale du Rhône (Valais, Suisse).* Bulletin du Centre d'hydrogéologie, 2005. **No. 21**: p. 165-166.

147. Osman, Y.Z. and M.P. Bruen, *Modelling stream-aquifer seepage in an alluvial aquifer: an improved losing-stream package for MODFLOW.* Journal of Hydrology, 2002. **264**(1-4): p. 69-86.

148. Brunner, P., P.G. Cook, and C.T. Simmons, *Hydrogeologic controls on disconnection between surface water and groundwater.* Water Resources Research, 2009. **45**(1).

149. Fuhrer, J. *Abschätzung des Bewässerungsbedarfs in der Schweizer Landwirtschaft*. Forschungsanstalt Agroscope Reckenholz-Tänikon ART - Forschungsgruppe Lufthygiene/Klima, E.V. EVD; 2010.

150. Fuhrer, J. (2011). Personal communication on: *Contribution of groundwater to cover the agricultural water demand in Valais*.

151. Capilla, J.E., J.J. Gomez-Hernandez, and A. Sahuquillo, *Stochastic simulation of transmissivity fields conditional to both transmissivity and piezometric data 2. Demonstration on a synthetic aquifer.* Journal of Hydrology, 1997. **203**(1): p. 175-188.

152. Calver, A., *Riverbed permeabilities: Information from pooled data.* Ground Water, 2001. **39**(4): p. 546-553.

153. Engeler, I., H.J. Hendricks Franssen, R. Müller, and F. Stauffer, *The importance of coupled modelling of variably saturated groundwater flow-heat transport for assessing river–aquifer interactions.* Journal of Hydrology, 2011. **397**(3–4): p. 295-305.

154. Vogel, A. (2011). Personal communication on: *Composition of river bed sediments in drainage ditches between Sierre and Martigny (Canton of Valais).*

155. FOEN, *Mean Annual Actual Evaporation 1973-1992, Plate 4.1*, in *Hydrological Atlas of Switzerland*2010, Federal Office for the Environment FOEN: Bern.

156. Taylor, J.R., *An Introduction Error Analysis: The Study of Uncertainties in Physical Measurements*. 1997: Univ Science Books.

157. Thurgau, A.f.U.K., et al. *Grundwassermodell Thurtal - Schlussbericht*. K.T. Departement für Bau und Umwelt; 2008.

158. Laigre, L., E. Reynard, G. Arnaud-Fassetta, L. Baron, and D. Glenz, *Caractérisation de la paléodynamique du Rhône en Valais central (Suisse) à l'aide de la tomographie de résistivité électrique.* Géomorphologie : relief, processus, environnement, 2012(4): p. 405-426.

159. Hoehn, E., *Hydrogeological Issues of Riverbank Filtration — A Review*, in *Riverbank Filtration: Understanding Contaminant Biogeochemistry and Pathogen Removal*, C. Ray, Editor. 2002, Springer Netherlands. p. 17-41.

160. Vogel, A. (2010). Personal communication on: *Drainage system of the alluvial plain of the Rhône River.*

161. Beniston, M., *Impacts of climatic change on water and associated economic activities in the Swiss Alps.* Journal of Hydrology, 2012. **412–413**(0): p. 291-296.

162. Mariethoz, G., P. Renard, and J. Straubhaar, *The Direct Sampling method to perform multiple-point geostatistical simulations.* Water Resources Research, 2010. **46**(11): p. W11536.

163. Straubhaar, J., A. Walgenwitz, and P. Renard, *Parallel Multiple-Point Statistics Algorithm Based on List and Tree Structures.* Mathematical Geosciences, 2013. **45**(2): p. 131-147.